Semiconductor photoelectrochemistry: multi-electron transfer processes at illuminated semiconductor-electrolyte interfaces

Jimenez, David Jesus Fermin

Award date:
1996

Awarding institution:
University of Bath

SEMICONDUCTOR PHOTOELECTROCHEMISTRY:

Multi-Electron Transfer Processes At Illuminated Semiconductor-Electrolyte Interfaces

Submitted by David Jesús Fermín Jiménez
for the degree of PhD
of the University of Bath
1996

COPYRIGHT

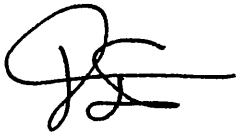

David J. Fermín

ProQuest LLC
789 East Eisenhower Parkway
P.O. Box 1346
Ann Arbor, MI 48106-1346

University of Bath

School of Chemistry

Doctor of Philosophy

SEMICONDUCTOR PHOTOELECTROCHEMISTRY: MULTI-ELECTRON TRANSFER PROCESSES AT ILLUMINATED SEMICONDUCTOR-ELECTROLYTE INTERFACES

by

David Jesús Fermín Jiménez

ABSTRACT

The mechanism of multi-electron transfer processes at illuminated semiconductor electrodes were studied by steady state and dynamic measurements. The steady state analysis was based upon photocurrent potential curves, while dynamic measurements involved Intensity Modulated Photocurrent Spectroscopy (IMPS) and Photoelectrochemical Impedance Spectroscopy (PEIS). The theoretical framework for these techniques is described for multi-electron transfer processes involving surface bound intermediates.

The theoretical analysis of steady state photocurrent potential curves showed that, if photogenerated intermediates species are involved in the surface recombination reaction, the photocurrent onset is affected by the illumination intensity. It is also demonstrated that the surface accumulation of charged intermediates can induce changes in the potential drop across the Helmholtz layer. This photopotential can alter the band bending under potentiostatic conditions, and consequently the kinetics of recombination. The dependence of the photocurrent-potential relationship with light intensity is sensitive to the charge transfer mechanism.

A *phenomenological* approach for the analysis of IMPS and PEIS responses is developed. This approach allow the use of expressions of IMPS and PEIS for a single electron transfer process in order to analyse the responses of multi-electron transfer reactions. The relation between the *phenomenological charge transfer and*

recombination parameters and real rate constants are derived for two general mechanisms. Periodical perturbations of the band bending associated with the surface accumulation of charged intermediates are also derived. Diagnostic criteria based on the potential and light intensity dependence of the phenomenological parameters are considered.

The mechanisms of photodissolution of CdS single crystal, photo-oxidation of SO_3^{2-} on CdS electrodes and photo-oxidation of water and organic species on rutile TiO_2 electrodes are studied within the framework of the model presented. It is proved that steady state and dynamic measurements can provide useful kinetic information about the elementary steps in each of these processes. Finally, fundamental aspect about surface recombination and charge transfer at the semiconductor electrolyte interface are discussed.

Acknowledgements

I am most grateful to Professor Laurence M. Peter for his enthusiastic, patience and encouraging supervision throughout these three years in the University of Bath. I am also thankful to Dr Evgueni Ponomarev for the numerous and enlightening discussion and for providing the heart of the model developed in this thesis.

I would like to thank the School of Chemistry, especially to Dr Adrian Fisher, Dr D. Jason Riley, Dr Steve Roser, Dr Gareth Price and Dr. Paul Bartlett who, in one way or another, provided the help that is always needed. A very especial thanks to Dr Mike Bailes for his outstanding technical support. Also I would also like to mention Mrs Pam Croft for her kind assistance.

It is always difficult to mention all the present and past members of our group who somehow contribute to my work, however, I will give it a try: Günther, Magda, Laurent, Eric, Greg, Rachel, Mark, Pete, Rob, Siva, Mallika, Nicola, Fulian, Anthony and more recently Gabriella and Gareth. My apologies for this important acknowledgement in my mother tongue, un agradecimiento muy especial a mis queridos amigos (doctores todos) Sabino Menolasina, José Miguel Ortega, Carlos Ponce de León y Enrique Millán por estár siempre ahi; eso nunca se olvidará. I hope I have not missed anyone.

I also appreciate the technical support by Mr Mike Lock, Mr Les Steele and the member of the Science Workshop at the University of Bath.

Without the support that I received every time that I stepped out the University, I would not be able to finish this thesis. My beloved Family was always behind me from the other side of the Atlantic, to them my eternal gratitude. Also to the love and support of my dearest Joanne Morris and her wonderful and warmth family.

Finally I would like to thank Professor Benjamín Scharifker for presenting me the opportunity of continue my career in Chemistry at Bath. I am also grateful to Prof. Zunilde de Arenas from the Dirección de Desarrollo Profesoral de la Universidad Simón Bolívar and to the Concejo Nacional de Investigaciones Científicas y Tecnológicas de Venezuela (CONICIT) for the financial support through the Programa Nuevas Tecnologías.

To all, many thanks

David

To My Precious

Latin America

List of symbols

Main Symbols and units

C_H	Space charge capacitance	F cm^{-2}
C_{SC}	Capacitance of the space charge region	F cm^{-2}
E	Applied potential	V
E_{CB}	Energy of the conduction band (normally refer against SHE)eV	
E_F	Fermi energy level	eV
E_{FB}	Flat band potential	V
E_g	Bandgap, CdS = 2.4 and TiO_2 (rutile) = 3.0	eV
E_{VB}	Energy of the valence band	eV
g	Hole flux to the surface	cm^{-2} s^{-1}
j	current density	A cm^{-2}
j_{ch}	Interfacial charging current density	A cm^{-2}
j_{photo}	Photocurrent density	A cm^{-2}
k	Boltzmann constant, 1.38 10^{-23}	J K^{-1}
k_{tr}	Phenomenological charge transfer parameter	s^{-1}
k_{rec}	Phenomenological recombination parameter	s^{-1}
L_p	Diffusion length of holes	m
N_{SC}	Semiconductor doping density	m^{-3}
$_pE_{decomp}$	Energy level for decomposition via valance band holes	eV
q	Electron charge, 1.602 10^{-19}	C
S	Electrode surface area	m^2
T	Temperature	K
W	Width of the space charge region	m
α	Absorption coefficient	m^{-1}
β	Ideality factor to account for Femi-level pinning effects, i.e. $\Delta\phi_{SC}$ / ($E-E_{FB}$)	-
ΔV_H	Potential drop across the Helmholtz layer	V
$\Delta\phi_{SC}$	Potential drop across the space charge region	V
δ	Surface reaction length, ~ 10^{-9}	m

ε_0	Permitivity of free space, $8.85\ 10^{-12}$	$C^2\ N^{-1}\ m^{-2}$
ϕ	Potential	V
Φ	Conversion efficiency	-
κ	Dielectric constant, CdS = 8.5 and TiO_2 (rutile) = 173	-
λ	Reorganisation energy	eV
υ	thermal velocity	$cm\ s^{-1}$
σ	Capture cross section	cm^2
ω	Frequency of modulation	s^{-1}
ψ	$\frac{q^2}{(C_{SC} + C_H)kT}$	-

Abbreviations

CT	Charge transfer
SR	Surface recombination
IMPS	Intensity Modulated Photocurrent Spectroscopy
PEIS	Photoelectrochemical Impedance Spectroscopy
SCR	Space charge region
CBD	Chemical Bath Deposition

Table of contents

SEMICONDUCTOR PHOTOELECTROCHEMISTRY:
Multi-Electron Transfer Processes At Illuminated Semiconductor-Electrolyte Interfaces.

INTRODUCTION

Research on electrochemical processes at semiconducting materials has undergone a change in direction in the last few years. In 1972, when Honda and Fujishima reported the photo-splitting of water on TiO_2 electrodes [1], a large amount of research was triggered towards solar energy conversion in photo-electrochemical cells (PEC) [2]. However, despite the enormous efforts to enhance the efficiency of PEC's, light energy conversion is still dominated in the technological world by the more efficient solid states photovoltaic cells.

An outstanding feature of the semiconductor-electrolyte interface, in comparison with solid state or solid-gas junctions, is the versatility of the contact between both phases. In principle, interfacial properties can be modified by just changing the composition or nature of the electrolyte. Etching and surface processing [3], photocatalytic oxidation of electrolyte species [4], colloidal and quantum sized particles [5-7], luminescence [7,8] and sensing devices are some of the areas where semiconductor electrochemistry remains as the central element. Nonetheless, the importance of semiconductors as electrodes lies not only in technological aspects, but also in fundamental concepts of solid-liquid interfaces. In this respect, electrochemistry, solid state physics, catalysis and material sciences have been linked together, and more encouragingly, each of them has profited from the extensive research.

From the electrochemical point of view, semiconductors have made an important contribution to the understanding of charge transfer mechanisms. Some of the major contribution have been reviewed by Gerischer [9], Peter [10] and Koval and Howard [11]. More extensive discussion can be found in textbooks by Pleskov [12] and Morrison [13]. Nevertheless, three or four decades after it was recognised that semiconductors electrodes have different properties than metals, controversy still remains about elementary aspects of interfacial reactions.

The first attempts to describe the illuminated semiconductor-electrolyte interface were based on extrapolation of the p-n and metal-semiconductor junction models from solid state physics [14,15]. This approach is built upon the principle that charge transfer between two materials in contact reaches equilibrium when their Fermi energies are equal. Although this thermodynamic criterion is applicable for any sort of interface involving electronic equilibrium, the chemistry of the semiconductor-electrolyte junction is completely ignored. Therefore, it is not surprising that this model fails to describe the basic features of "simple" electrochemical processes.

Indeed, one of the major problems in semiconductor electrochemistry is the relatively complicated chemistry that these materials usually exhibit. In many cases, electron transfer to the electrolyte species competes with the decomposition of the semiconductor, and very often more than one intermediate can be involved. Another source of difficulties in modelling these interfaces is the presence of so-called surface states, which lead to important effects on potential distribution, charge transfer and surface recombination of charge carriers.

The studies described in this thesis contrast the "steady state"[1] and dynamic (based on periodic perturbations) descriptions of photoelectrochemical processes. The steady state analysis involves classical photocurrent and capacitance measurements, while dynamic studies are based on Intensity Modulated Photocurrent (IMPS) and Photo-Electrochemical Impedance Spectroscopy (PEIS). Fundamental aspects of frequency response of interfaces under periodical perturbation are reviewed and extended to multi-electron transfer reactions. Diagnostic criteria for mechanisms involving surface intermediates are presented, and several photo-electrochemical reactions are described which were studied in order to provide experimental tests of the theoretical description.

[1] The steady state condition is not rigorously established in the measurements considered (see chapter 3). In the case of photocurrent-potential curves the illumination is mechanically chopped at a frequency of c.a. 27 Hz, and the current is measured in phase to this perturbation. On the other hand, the capacitance is calculated from the quadrature component of the admittance in potential modulated experiments. However, in most cases these measurements correspond to the low frequency limit of the dynamic reponse [16].

References

1 K. Honda and A. Fujishima, Nature, **238** (1972) 37.

2 H. Tributsch, in J.O'M. Bockris, B. Conway and R.E. White (eds.) *Modern Aspects of Electrochemistry*, vol. 7, Plenum Press, N.Y. 1986, p. 303.

3 Gomes and Goosens, in H. Gerischer and C.W. Tobias (eds.), *Advanced in Electrochemical Science and Engineering*, Vol. 3, VCH, Weinheim, 1994.

4 Mario Schiavello (ed.), *Photocatalysis and Enviroment Trends and Aplications*, NATO ASI series C vol. 237, Kluwer Academic Publishers, Dordrecht, 1988.

5 A.J. Bard, Science **207** (1980) 139.

6 M. Grätzel in D. Reidel (ed.), *Photoelectrochemistry, Photocatalysis and Photoreactors*, NATO ASI series C, Doedrecht, 1985.

7 L.T. Canham, Appl. Phys. Lett., **57** (1990) 1046.

8 B. Smandek and H. Gerischer, Electrochim. Acta, **30** (1985) 1101.

9 H. Gerischer, Electrochim. Acta, **35** (1990) 1677.

10 L.M. Peter in D. Pletcher (ed.), *Specialist Periodical Report*, Vol. 9, The Royal Society of Electrochemistry, London, 1982.

11 C.A. Koval and J.N Howard, Chem. Rev. **92** (1992) 411.

12 Yu. V. Pleskov and Yu. Ya. Gurevich, *Semiconductor Photoelectrochemitry*, Consultants Bureau, N.Y., 1986.

13 S.R. Morrison, *Electrochemistry at Semiconductors and Oxidised Metal Electrodes*, Plenum Press, N.Y., 1980.

14 S.M. Sze, *Physics of Semiconductor Devices*, 2nd. edition, John Willey & Sons, N.Y., 1981.

15 H.M. Rosenberg, *The Solid Sate*, 3rd edition, Oxford Science Publications, 1988.

16 L.M. Peter, Chem. Rev., **90** (1990) 753

CHAPTER 1

An overview of the structure of the semiconductor-electrolyte interface

1.1 Introduction

The kinetics of interfacial processes are expected to be sensitive to the potential distribution across the semiconductor-electrolyte interface (SEI). Under *depletion conditions* (this concept is defined in the next section), the limited concentration of charge carriers introduces a potential drop that can extend from the surface up to few microns inside the semiconducting material. The properties of semiconductors as photoelectrodes are based on this potential drop. In the present chapter, the potential distribution in an electrochemical cell under potentiostatic conditions is briefly reviewed. The effect of the applied potential on the surface charge of the semiconductor in the dark and under illumination is also discussed.

1.2. Potential distribution across the SEI

Let us consider initially the case in which the semiconductor electrode is in *equilibrium* with a redox species in solution. For the sake of consistency, all discussions are developed for n-type semiconductors, although they can be extended to p-type by the appropriate sign reversal. The equilibrium is established when the Fermi level of the semiconductor is equal to the energy associated with the redox potential. This situation is depicted in **fig 1.1**, showing that the electron density is *depleted* toward the surface of the electrode. This depletion layer, also referred to as *space charge region (SCR)*, introduces a bending of the bands to higher energies.

In an electrochemical cell under potentiostatic conditions, the applied potential is established between *reference* and *working electrodes*. Considering an ideally polarisable interface, i.e. electrons cannot be exchanged with the electrolyte, the condition of zero bias can be represented as in **fig. 1.2**.

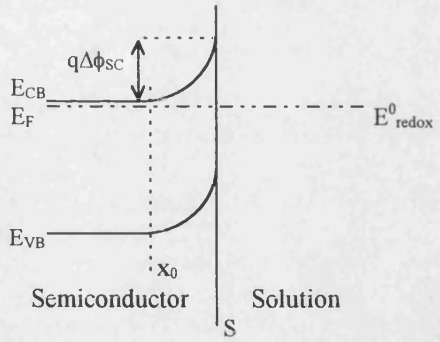

Fig. 1.1. Energy diagram of the Semiconductor-Electrolyte interface under equilibrium. The Fermi level energy (E_F) is equal to the redox potential energy (E^0_{redox})

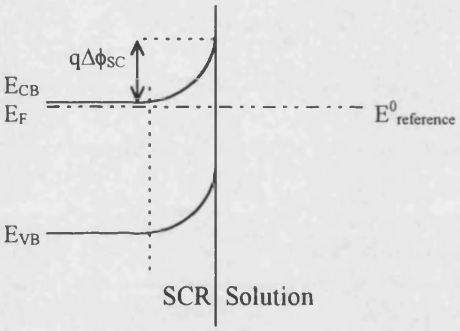

Fig. 1.2. Energy diagram of the ideally polarisable interface at zero bias. The Fermi level energy (E_F) is equal to the reference electrode energy ($E^0_{reference}$)

It is obvious from **fig. 1.2** that the concentration of the electrons in the space charge region is dependent on the potential difference between the reference and the semiconductor electrode. At this point is also necessary to consider the potential distribution at the other side of the junction, which is known as the *Helmholtz double layer*. In a simplified description, for high concentrations of supporting electrolyte, this region contains the nonadsorbed ions which represent the counter-charge. The thickness of the Helmholtz layer is considerably smaller than the space charge region. This is schematically shown in **fig. 1.3**. In **fig. 1.3a**, the potential distribution across the interface is shown taking the potential of the bulk of the solution as zero. It is seen that $\Delta\phi_{SC}$ occurs over a larger distance than ΔV_H, which is due to the fact that $\Delta\phi_{SC}$ arises

from the ionisation of donors in the solid, while ΔV_H is given by the ions accumulated few Ångstroms away from the surface. This becomes evident from the representation of the charge across the interface displayed in **fig. 1.3b**.

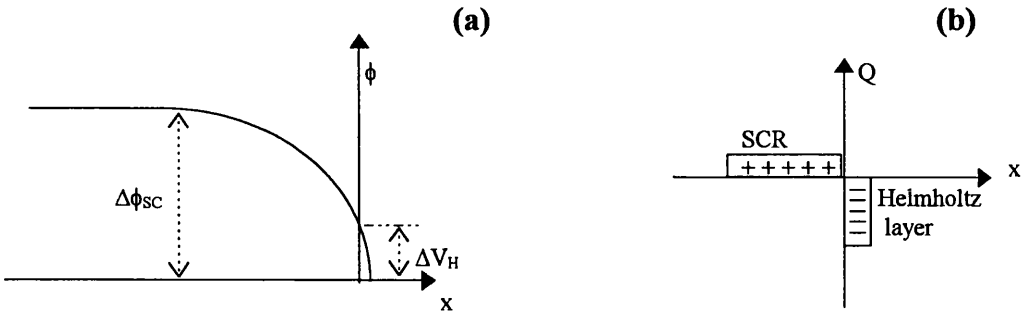

Fig. 1.3. Schematic representation of the potential drop (a) and charge across the semiconductor electrolyte interface under depletion conditions.

Since the charge in both region is equal but with opposite sign, the capacitance of the space charge region is generally negligible in comparison to the Helmholtz capacitance. Under this condition[1], ΔV_H is constant and any change in the applied potential between reference and working electrode will appear in $\Delta\phi_{SC}$ as

$$E = \Delta\phi_{SC} + E_{FB} \tag{1.1}$$

where E_{FB} is the *flat band potential*. At this potential, the surface concentration of electrons is equal to the bulk. At potentials more positive than E_{FB}, the surface concentration of electrons is decreased producing a depletion layer and a corresponding bending of the bands to higher energies. On the other hand, at potential more negative than E_{FB}, electrons generate an *accumulation layer*, bending the bands to lower energies. The potential dependence of the band bending is depicted in **fig. 1.4**.

[1] This condition is introduced in order to simplify the description of the potential dependence of the space charge region. However, as discussed in the subsequent chapters, charge accumulation at the surface may affect the potential drop across the Helmholtz layer. This effect is referred to as *Fermi level pinning*.

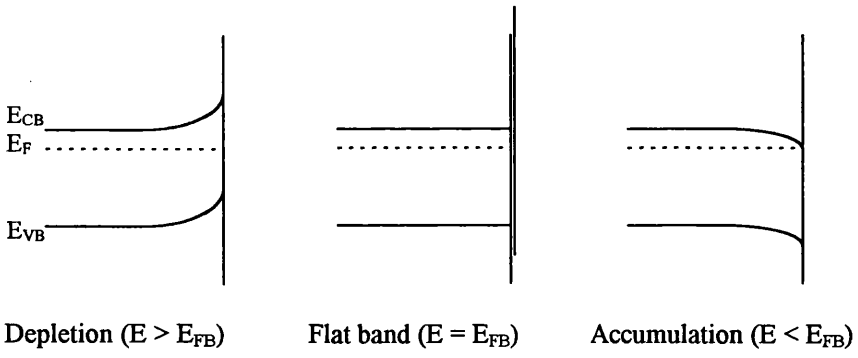

Fig. 1.4. Potential dependence of the band bending for a n-type semiconductor.

Before studying photo-effects on semiconductor electrodes, it is necessary to consider a more quantitative analysis of the band bending under depletion regime. The charge generated under this condition results from the ionisation of donors. If the density of charge is assumed constant in the SCR, Poisson's equation can be written as

$$\frac{d^2(\Delta\phi)}{dx^2} = \frac{qN_{SC}}{\kappa\varepsilon_0} \tag{1.2}$$

Upon integrating twice and assuming that the electric field ($d(\Delta\phi)/dx$) is zero at x_0 (the abrupt depletion approximation), and that $\Delta\phi$ is zero in the bulk of the semiconductor, the *Schottky* relation can be obtained

$$\Delta\phi_{SC} = \frac{qN_{SC}}{2\kappa\varepsilon_0} W^2 \tag{1.3}$$

where W is the width of the space charge region. The potential dependence of W is shown in **fig. 1.5** for a doping density of 10^{16} cm^{-3} and a dielectric constant of 10. It can be seen that the square root dependence corresponds to a strong potential dependence of W near E_{FB}.

Another useful relation can be obtained recalling Gauss's law:

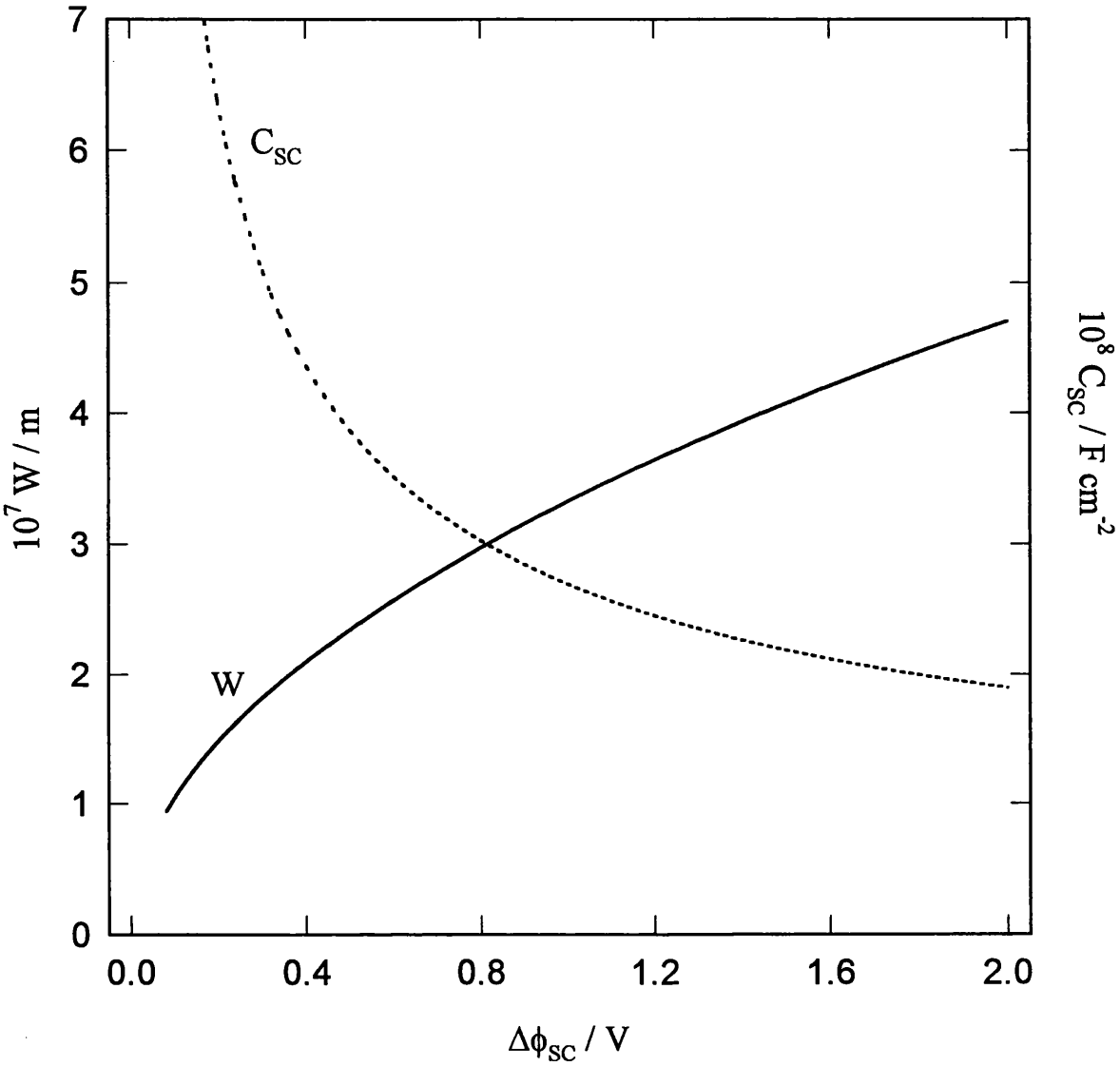

Fig.1.5. Thickness (W) and capacitance (C_{SC}) of the space charge region as function of the potential drop $\Delta\phi_{SC}$. Doping density 10^{16} cm^{-3}, relative permittivity κ 10.

$$\left(\frac{d(\Delta\phi)}{dx}\right)_{\Delta\phi=\Delta\phi_{SC}} = \frac{Q_{SC}}{\kappa\varepsilon_0 S} \tag{1.4}$$

Where S is the surface area of the electrode. Combining the integrated Poisson equation (including the effect of the electrons in the conduction band, $qN_{SC}/\kappa\varepsilon_0\, e^{-q\Delta\phi/kT}$) and eq. (1.4), the capacitance of the space charge region (C_{SC}) can be derived:

$$C_{SC}^{-2} = \left(\frac{2}{qN_{SC}\kappa\varepsilon_0 S^2}\right)\left(E - E_{FB} - kT/q\right) \tag{1.5}$$

This is the well known Mott-Schottky relationship. From eq. (1.5), C_{SC}^{-2} is linearly dependent on E, where the slope is inversely proportional to N_{SC} and E_{FB} can be obtained from the intercept. This representation of experimental capacitance data is referred to as the Mott-Schottky plot. The potential dependence of C_{SC} is also displayed in **fig. 1.5**.

The simple relations discussed in this section allow the determination of the potential drop across the SCR. A more complete description of the SEI structure is presented in several textbooks [1-3].

1.3. The SEI under illumination

It was considered previously that at potentials more positive than E_{FB} an electric field is generated in the space charge region. If the semiconductor is illuminated with radiation capable of exciting electrons from the valence to the conduction band (i.e. $h\nu > E_g$), the photo-generated carriers will be effectively separated by this electric field. This situation is depicted in **fig. 1.6**. As a result of this charge separation, holes will accumulate at the surface, and electrons will be driven to the bulk of the semiconductor. These valence band holes can react with either redox species in solution, or with the semiconductor lattice (decomposing the semiconductor). The rate at which holes are consumed in the surface determines the flux of electrons or *photocurrent* through the external circuit.

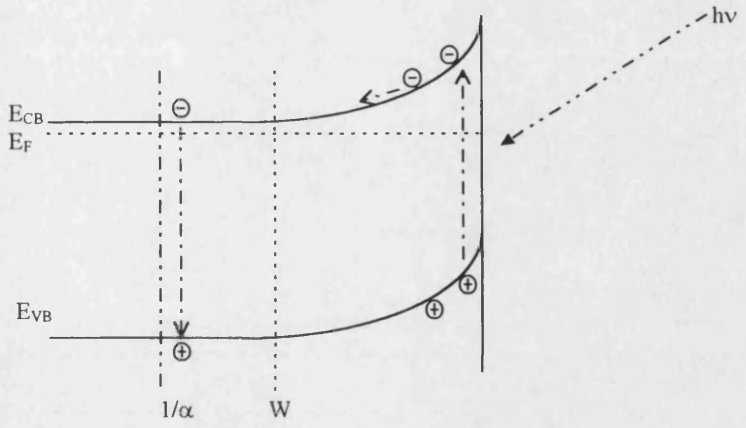

Fig. 1.6. Schematic diagram of the depletion layer under illumination $h\nu > E_g$. W is the width of the SCR and $1/\alpha$ defines the penetration depth of the incident light.

The flux of photogenerated holes to the surface will depend on the width of the SCR, the absorption coefficient of the semiconductor and the diffusion length of holes. The diffusion length of holes (L_p) is the average distance that holes can diffuse before recombining[2]. From **fig 1.6** it can be also seen that if light penetrates into the bulk of the semiconductor, holes can diffuse towards the SCR. Since the electric field is zero in the neutral region, photo-induced holes and electrons can effectively *recombine*. Gärtner [4] developed an expression which describes the flux of holes to the surface considering these parameters:

$$g = I_0\left(1 - \frac{\exp(-\alpha W)}{1+\alpha L_p}\right) \tag{1.6}$$

The potential dependence of g is shown in **fig. 1.7**. This useful expression provides the limiting photocurrent value in the absence of surface or space charge layer recombination losses. The effect of the absorption coefficient (**fig. 1.7a**) and the diffusion length of holes (**fig. 1.7b**) is also displayed.

[2] L_p is given by $(D_h\,\tau_h)^{1/2}$, where D_h is the diffusion coefficient of holes and τ_h is the carrier lifetime.

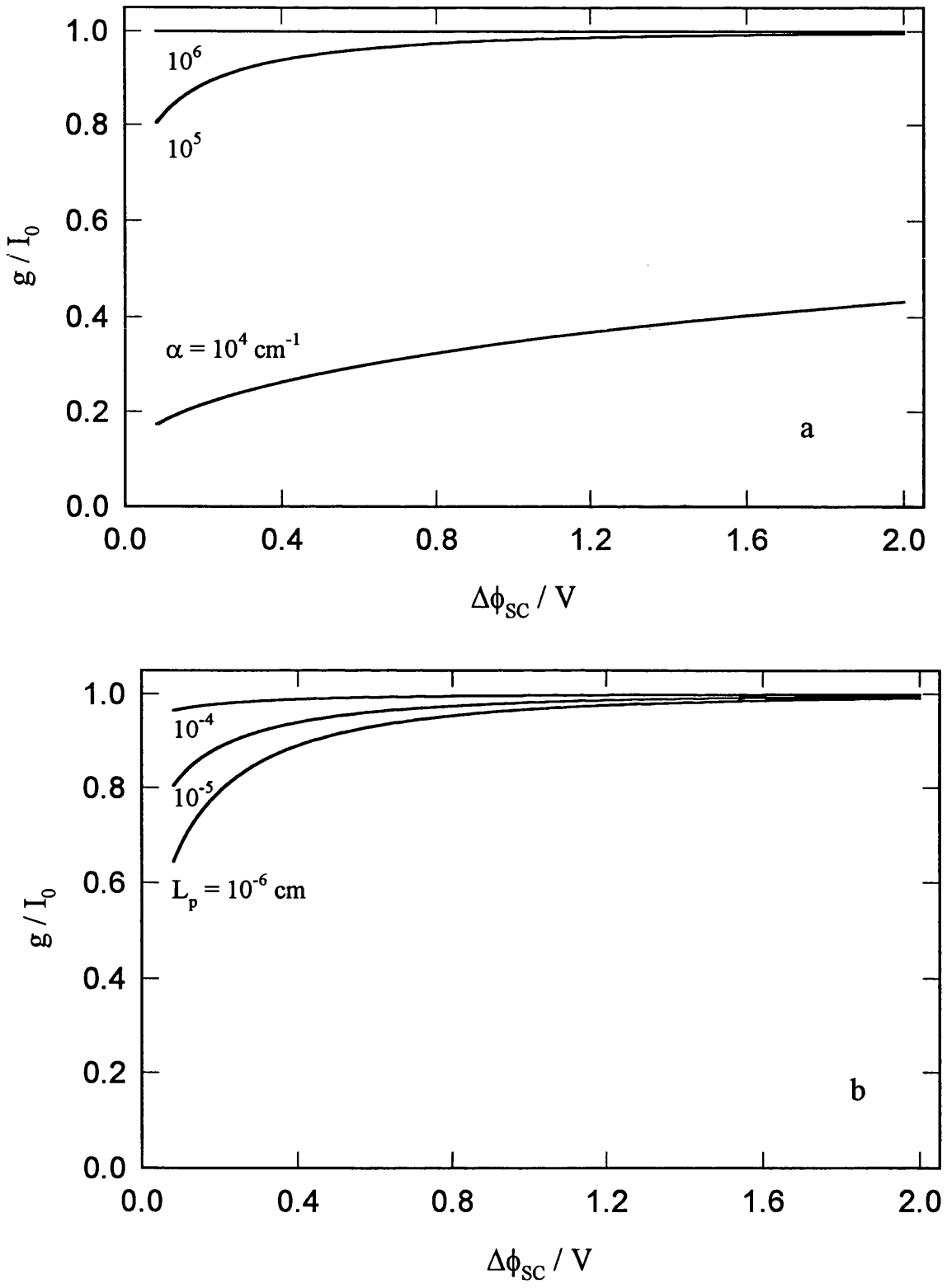

Fig.1.5. Normalised hole flux to the surface as a function of $\Delta\phi_{SC}$ predicted by the Gartner equation (1.6).(a) $L_p = 10^{-5}$ cm and various α, (b) $\alpha = 10^5$ cm^{-1} and L_p as indicated. Other parameters as in fig. 1.3.

Through the Gärtner expression (eq. 1.6) is possible to evaluate the flux of holes to the surface, however, the fate of the carriers at the surface will depend on the *charge transfer* (CT) and *surface recombination* (SR) rates. Chapter 5 considers a particular case of high CT rate where the effect of SR is almost negligible. In that case, eq. (1.6) describes the main features of the photocurrent-potential dependence. On the other hand, chapters 4 and 6 discuss cases where the photocurrent drops to lower values than predicted by eq.(1.6) at potentials near E_{FB}. In those cases, the competition between CT and SR will determine the behaviour of the photocurrent near E_{FB}.

1.4. Charge Transfer vs Surface Recombination

The ratio between these two processes is the determining factor behind the energy conversion efficiency of the SEI. Due to the complexity of the solid-electrolyte interaction, and the importance of these concepts, the CT vs SR relation is one of the most controversial issues in semiconductor electrochemistry. The objective of this section is to introduce these two physical phenomena, which are the focal point in the subsequent chapters of this thesis.

The theory of charge transfer proposed by Marcus, [5,6] and further developed by Hale and Gerischer [1,7], considers that the charge transfer rate depends largely on the degree of overlap between the fluctuating energy levels of the redox species and the electron energy band of the solid. This fundamental argument requires, obviously, an understanding of the energy level involved in the CT process, and the redox energy of the hole acceptor species. The fluctuating energy levels of the redox species are given by the *reorganisation energy* λ. This energy accounts for the changes in the inner and outer solvation shells of the hole acceptor species. In principle, if the energy level of the reduced species coincides with energy of the valence band (E_{VB}), "direct" transfer of the hole can occur. This situation is depicted in **fig. 1.8a**. On the other hand, if the energy of the reduced species lies above E_{VB}, the hole may be trapped initially in a energy level within the band gap before being transferred across (**fig. 1.8b**).

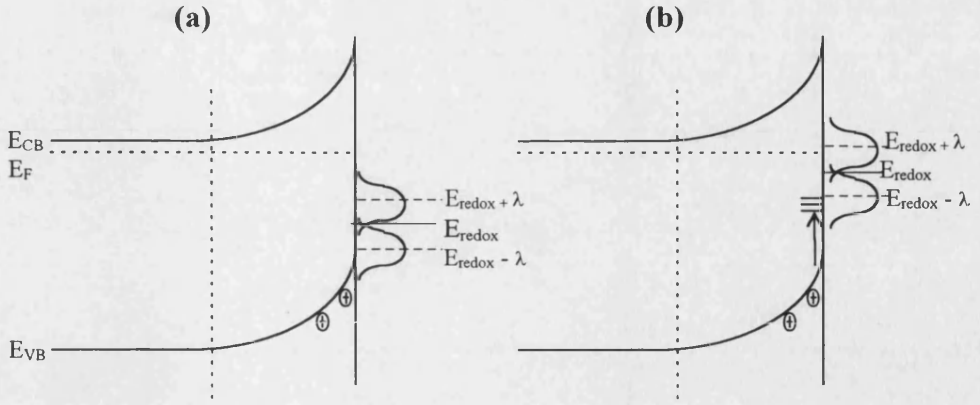

Fig. 1.8. Schematic representation of a hole transfer from the band edge (a) and via trapping in interface states (b). The arrow indicates the movement of holes.

Other complications may arise in the case of adsorption of redox species. The adsorbed species can introduce an energy level that is involved in CT as well as in SR. Another competing reaction that has to be considered in the CT mechanism is the photocorrosion of the semiconductor. From the thermodynamic point of view, photocorrosion will be determined by the position of the valence band and the *decomposition potential* [8]. In chapter 5, this topic is also reconsidered for the case of CdS photo-anodes. Morrison [1] and Pleskov [2] have also included extensive discussion of photocorrosion in their textbooks.

According to the previous arguments, the CT phenomenon will depend on the thermodynamics (redox potentials, adsorption, decomposition and traps energy levels) and the kinetics (reorganisation parameter - λ) of the processes involved. The rate of CT will be also influenced by the lifetime of the hole at the surface, which can be substantially decreased by SR.

The interfacial recombination of carriers has been studied extensively. These processes can occur either in the space charge region or at the semiconductor surface. Several approaches have been attempted to describe recombination in the SCR, however, most of them fail to describe the basic features of the photocurrent-potential dependence [9]. More recently, Vanmaekelbergh et al. [10,11] have studied the non-steady state response of the SCR and surface recombination. They provided diagnostic

criteria for both processes, in terms of IMPS and PEIS (see chapters 2 and 4). Their models have proved to be useful for the analysis of interfacial recombination, especially surface processes [12].

Previously in this section, we have mentioned briefly the possibilities of surface hole trapping at energy levels within the band gap, and also that adsorbed species may introduce such surface energy levels. These types of surface energy levels are commonly defined as *surface states* [13,14]. Depending on the degree of interaction between these states with the semiconductor or with the electrolyte, either charge transfer or recombination can be enhanced. In the case of adsorbed species, e.g. polysulfide on n-CdS single crystals [13-15], the states generated appears to have "strong" interaction with the electrolyte, and they enhance the CT rate from the semiconductor. On the other hand, dislocations and grain boundaries (see chapter 5) can play a role as charge trapping and recombination centres since they interact more with the semiconductor than with the electrolyte.

The schematic representation of **fig. 1.9** provides a summary of the above discussion [16]. The hole consumption at the surface is determined by the ratio of the charge transfer and surface recombination rates. CT can occur via the valence band or by surface states within the band gap. Surface states can also play a major role in the SR rate. We have associated kinetics factors with the reorganisation energy (λ), but this proves to be rather inconvenient in terms of experimental analysis. A more useful concept is the *capture cross section* of species or energy levels involved in the photoprocesses. For instance, the charge transfer velocity (s_h) is given by:

$$s_h = \sigma_h N_h \upsilon_h \tag{1.7}$$

where σ_h is the capture cross section of holes, N_h the surface density of the hole acceptor species and υ_h the thermal velocity of the minority carriers. In chapters 2 and 4, charge transfer and recombination rate constants are described in terms of this parameter. Capture cross sections involving emission, charged sites and several other factors have been estimated for bulk processes [17]. It is also expected that surface properties can also affect this parameter, and therefore, comparison between

experimental and theoretical estimation may provide additional information about electrolyte interaction and surface structure.

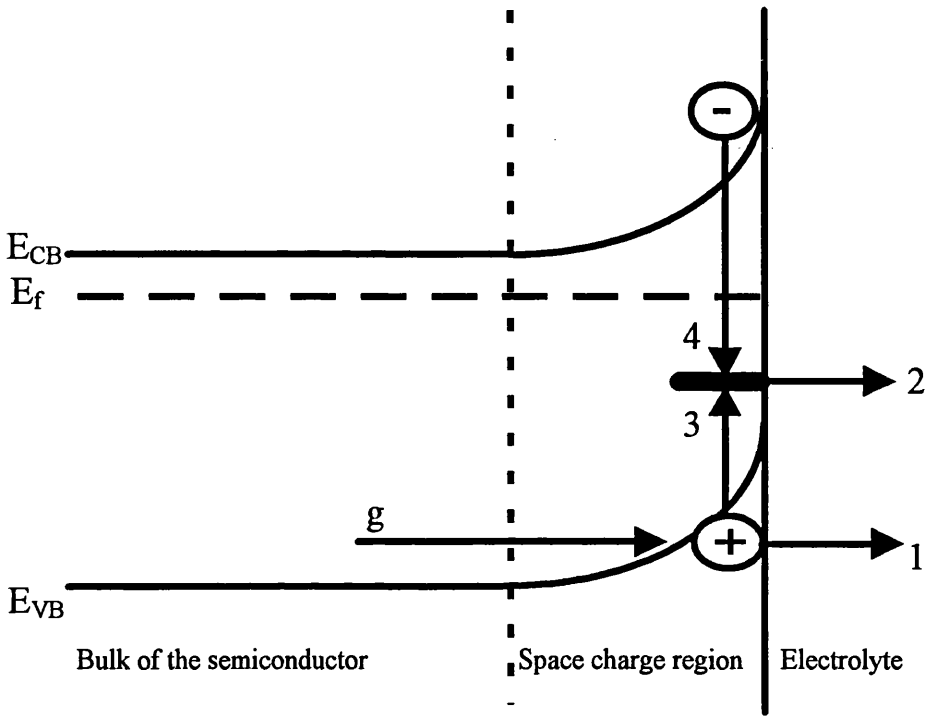

Fig. 1.9. Schematic representation of the interfacial processes at the semiconductor-electrolyte junction. Photogenerated holes can be consumed at the surface via charge transfer from the valence band edge (1) or via surface states (2). They can also recombine at interband states (3,4).

1.5. References

1 S.R. Morrison, *Electrochemistry at Semiconductors and Oxidized Metal Electrodes*, Plenum Press, New York, 1980

2 Yu. V. Pleskov and Yu. Ya. Gurevich, *Semiconductor Photoelectrochemitry*, Consultants Bureau, N.Y., 1986.

3 J.O'M. Bockris and S.U.M Khan, *Surface Electrochemistry, A Molecular Approach*, Plenum Press, N.Y., 1993.

4 W.W. Gärtner, Phys. Rev., **116** (1959) 84.

5 R.A. Marcus, J. Chem. Phys. **24** (1956) 966.

6 R.A. Marcus, J. Phys. Chem., **43** (1965) 679.

7 N.S. Lewis, Annu. Rev. Phys. Chem., **42** (1991) 543.

8 See ref 1 and also A.J. Bard and M.S. Wrighton, J. Electrochem. Soc., **124** (1977) 1706.

9 For a comparative review in this topic see L.M. Peter in D. Pletcher (ed.), *Specialist Periodical Report - Electrochemistry*, vol. 9, The Royal Society of Chemistry, London, 1984, ch.2, and references there in.

10 D. Vanmaekelbergh and F. Cardon, Electrochim. Acta, **37** (1992) 837.

11 D. Vanmaekelbergh, A.R. de Wit and F. Cardon, J. Appl. Phys. **73** (1992) 5049.

12 W.P. Gomes and D. Vanmaekelbergh, Electrochim. Acta, **41** (1996) 967

13 R.H. Wilson, J. Appl. Phys., **48** (1977) 4292

14 R.H. Wilson in A. Nozik (ed), *Photo-effects at Semiconductor-Electrolyte Interfaces*, ACS Symposium Series 146, ACS, Washington D.C., 1981, p. 103.

15 P. Herrasti and L.M. Peter, J. Electroanal. Chem., **305** (1992) 241.

16 E.A. Ponomarev and L.M. Peter, J. Electroanal. Chem., **396** (1995) 219

17 R.H. Bube, *Photoelectronic Properties of Semiconductors*, Cambridge University Press, Cambridge, 1992, ch.6.

CHAPTER 2

A phenomenological approach for the analysis of Intensity Modulated Photocurrent responses of multistep electron transfer mechanism

Abstract

The theoretical framework of Intensity Modulated Photocurrent Spectroscopy (IMPS) is extended to multi-electron transfer processes featuring a surface confined intermediate species (X). The general model considers the generation of X by a charge transfer step, which can react via subsequent charge transfer or via a second order reaction with another mobile surface intermediate. The recombination reaction was restricted to occur via electron capture through X. The intermediate was also considered to be charged, and the effect of this surface excess charge on the band bending is discussed. It was recognised that the accumulation of X introduces a potential drop across the Helmholtz layer, which decreases the band bending under potentiostatic conditions. This perturbation features a steady state and a dynamic component associated with the dc and modulated surface concentration of the intermediate. The modulated component of the photopotential also introduces a periodic change in the space charge capacitance, and consequently a charging current.

A phenomenological approach for the analysis of IMPS responses of multi-electron transfer process is introduced. This approach allows the use of the IMPS expression derived for the single electron transfer model. The parameters obtained from this analysis allow the access to the rate constants of each of the elementary steps. Diagnostic criteria for each of the mechanisms considered are discussed.

2.1 Introduction

The mechanisms involved in photoelectrochemical reactions have stimulated renewed interest in recent years in view of the technological impact of materials based on colloidal, dye sensitised, nano-porous and quantum sized semiconductors. Considerable progress towards the kinetic description of photoelectrochemical processes has been achieved by non-stationary techniques. Intensity Modulated Photocurrent Spectroscopy (IMPS) has proved to be a powerful technique for determining the interfacial kinetics of charge transfer, charge accumulation and surface recombination [1-4]. In IMPS, an ac perturbation of the light intensity is superimposed on the illumination of the interface, and the photocurrent response is measured as a function of the modulation frequency. As recombination has a finite velocity, the photocurrent at low frequencies is determined by the competition between charge transfer and recombination, while at high frequencies, recombination is effectively "frozen out" and only the response due to charge transfer is observed. The non-stationary approach can be extended to other techniques like Photoelectrochemical Impedance Spectroscopy (PEIS), where a modulated potential is superimposed on a constant potential under illumination [5, see also chapter 4]. Photo-modulated Microwave Reflectance Spectroscopy (PMMR) has also been successfully correlated to IMPS for the photo-evolution of hydrogen on p-InP [6]. Most of the theoretical descriptions of dynamic responses have been restricted to single charge transfer processes and to multi-step reactions involving majority carrier injection (photocurrent multiplication) [3,7-9]. However, essential aspects of minority carriers transfer in multi-electron processes remain to be addressed.

Many photoelectrochemical reactions of interest involve the transfer of more than one minority carrier. For instance, the photodissolution of CdS (chapter 4), sulfite photo-oxidation (chapter 5) and the photo-evolution of oxygen from n-TiO_2 (chapter 6) have been associated with multi-electron mechanisms, and a theoretical framework for the analysis of steady state and dynamic responses is required to allow further understanding of these mechanisms. These processes may also involved charged intermediates that can affect the potential distribution across the interface. Kelly and Memming [10] recognised this effect in the steady state photocurrent analysis on III-V semiconductors. More recently, de Wit et al. [11] introduced this effect in their IMPS

analysis of the CdS dissolution. However some aspects of their derivations are subject to debate. The steady state and dynamic effects of charged intermediates are considered in this chapter.

A typical complex representation of IMPS at potentials in the photocurrent onset region exhibits a semicircle in the first quadrant associated with the competition between interfacial minority carrier transfer and electron-hole recombination [1,6,7]. A second semicircle commonly observed in the fourth quadrant arises from the RC time constant of the system [4]. In the simplest case of single step one-electron charge transfer reactions, the frequency of maximum imaginary part (ω_{max}) corresponds to the sum of the charge transfer (k_{tr}) and recombination (k_{rec}) rate constants, and the normalised low frequency limit is given by the ratio $k_{tr}/(k_{tr} + k_{rec})$ [4]. These relations are depicted in **fig 2.1**. The rate constants k_{tr} and k_{rec} are therefore readily accessible. The theory has been extended to consider cases where the space charge capacitance (C_{SC}) is of the same order of magnitude as the Helmholtz layer capacitance (C_H), and to cases where charging of surface states leads to a redistribution of the potential drop across the interface [4].

Regardless of the mechanism of the photoelectrochemical process, a semicircular IMPS response can be described in terms of *phenomenological* rate parameters. In the case of a single electron transfer process, the phenomenological parameters are equivalent to the real rate constants. In multi-electron transfer reactions, the phenomenological parameters are functions of the real rate constant and the light intensity. In this chapter, the relation between phenomenological and real rate constants are considered for two different mechanisms. The perturbation of the potential distribution across the interface arising from the accumulation of charged intermediates is also analysed. The analysis of the phenomenological parameters as function of the potential and light intensity also provides useful diagnostic criteria for the understanding of the mechanism of photoelectrochemical processes.

2.2 The mechanistic model

The model is based on the n-type semiconductor/electrolyte interface under reverse bias, although all the relations are applicable for p-type with appropriate sign reversal. A general two hole transfer process is considered, where the surface recombination

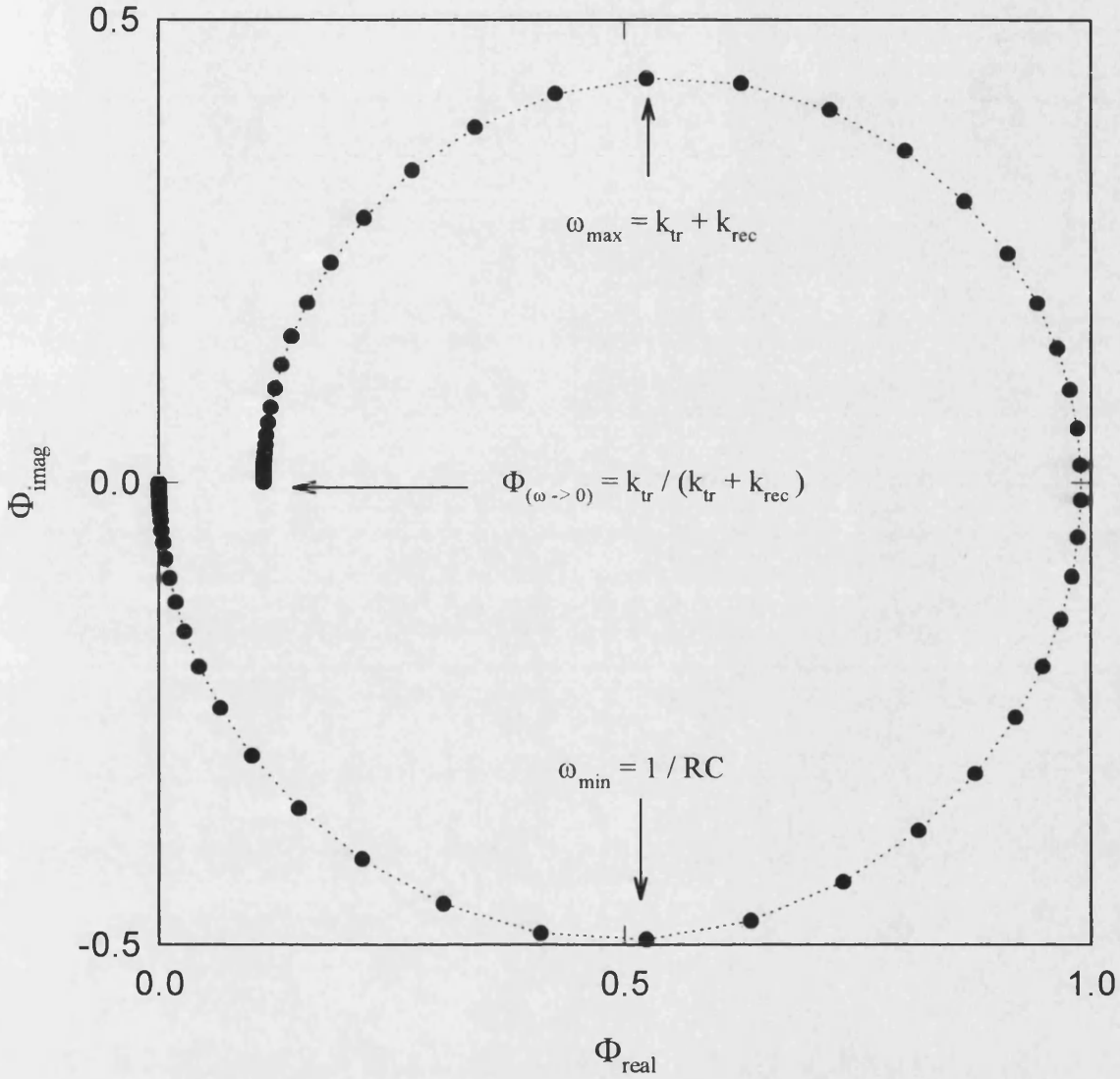

Fig. 2.1 Basic features of the complex representation of IMPS.
The lower quadrant exhibits the RC attenuation of the cell (this is shown only for illustration purposes, see chapter 6 for further details).

occurs via electron capture by the intermediate X^+. The mechanism can be completed by the second hole transfer to X^+ or by the reaction of two mobile intermediates at the surface. It can also be considered that redox species can interact with this intermediate, although for the sake of simplicity, this possibility is excluded from the model. The general mechanism can be represented as:

$$A + h^+ \xrightarrow{k_1} X^+ \quad (2.1)$$

$$X^+ + h^+ \xrightarrow{k_2} B^{2+} \quad (2.2)$$

$$X^+ + e^- \xrightarrow{k_3} A \quad (2.3)$$

$$X^+ + X^+ \xrightarrow{k_4} A + B^{2+} \quad (2.4)$$

For simplicity it is also assumed that the surface concentration of X^+ remains small relative to that of A, and k_1 is treated as a pseudo first order rate constant (s^{-1}). Another relevant assumption in this mechanism is the irreversibility of each step, and in particular the first hole transfer. In reaction 2.1, it is considered that there is a considerable activation energy for the regeneration of holes from X^+. Although this simplification is difficult to validate *a priori*, it is expected that the net charge associated with holes is stabilised more effectively at the surface than in the space charge region. In this sense, X^+ can be considered as a surface polaron with a confined two dimensional movement on the surface.

The pseudo first order rate constant k_3 for the recombination via X^+ depends on the potential drop across the space charge region ($\Delta\phi_{sc}$) as given by the Boltzmann distribution of electrons:

$$k_3 = k_3^0 \exp\left(\frac{-q\Delta\phi_{sc}}{kT}\right) \quad (2.5)$$

where k_3^0 is the value of k_3 at the flat band potential when $n_{surf} = n_{bulk}$. It is generally assumed that n_{surf} is constant at a given potential, however, the accumulation of positively charged species at the surface under illumination can perturb $\Delta\phi_{SC}$, and

therefore the recombination rate constant. This case will be considered in sections 2.3 and 2.4.

The differential equations describing the time dependence of the surface concentrations of holes (p) and intermediate (X) are

$$\frac{dp}{dt} = g - k_1 p - k_2 pX \tag{2.6}$$

$$\frac{dX}{dt} = k_1 p - k_2 pX - k_3 X - 2k_4 X^2 \tag{2.7}$$

Here g, the flux of holes into the surface, is defined by the Gärtner expression (eq. 1.6). For simplicity It is assumed that g is independent of the potential, which corresponds to the limiting case where the light absorption occurs very near to the surface ($W >> 1/\alpha$), or if the diffusion length of holes is large ($\alpha L_p >> 1$).

2.3. The steady-state solution

The steady state solution of eqs. (2.6) and (2.7) gives a cubic expression in X (cf. Appendix 2.1). Two limiting cases can be analysed separately in order to simplify the discussion; if the surface mobility of X^+ is small (*Case I*), then k_4 is effectively zero and the X^+ react via hole trap. On the contrary, if the surface diffusion of X^+ is fast or there is a considerable high energy barrier for the second hole transfer (see section 6.1), then the mechanism will follow predominantly the reaction between the two mobile X^+ (*Case II*).

2.3.1. Case I

Solution of eq. (2.6) and (2.7) gives the steady state concentrations of X and p:

$$X_0 = \frac{k_1 p}{k_2 p + k_3} \tag{2.8}$$

$$p_0 = \frac{g}{k_1 + k_2 X_0} \tag{2.9}$$

It follows that X_0 is given by

$$X_0 = \frac{-b + \sqrt{(b^2 - 4ac)}}{2a} \tag{2.10}$$

where $a = k_2k_3$, $b = (k_1k_3 + k_2g)$ and $c = -k_1g$. It is evident from eq. (2.8) that in the limit $k_3 \rightarrow 0$ (no recombination), the saturation value of X_0 corresponds to the ratio k_1/k_2.

In order to illustrate the behaviour of the steady state solution for *Case I*, the order of magnitude of the rate constants can be estimated from the thermal velocities for holes and electrons (υ_p and υ_n) and the corresponding capture cross sections of A and X for holes ($^A\sigma_p$ and $^X\sigma_p$) and of X for electrons $^X\sigma_n$:

$$k_1 = {}^A\sigma_p\, \upsilon_p\, A/\delta \sim 10^{-17}\ cm^2 \times 10^5\ cm\ s^{-1} \times 10^{15}\ cm^{-2}/10^{-7}\ cm = 10^{10}\ s^{-1} \tag{2.11}$$

$$k_2 = {}^X\sigma_p\, \upsilon_p/\delta \sim 10^{-15}\ cm^2 \times 10^5\ cm\ s^{-1}/10^{-7}\ cm = 10^{-3}\ cm^2\ s^{-1} \tag{2.12}$$

$$k^0_3 = {}^X\sigma_n \upsilon_n n_{bulk} \sim 10^{-16}\ cm^2 \times 10^5\ cm\ s^{-1} \times 10^{16}\ cm^{-3} = 10^5\ s^{-1} \tag{2.13}$$

Where A is the surface density of the initial reactive site and δ is a characteristic length of the order of few Ångstrom. In order to keep consistency with previous assumptions, the hole capture cross section of X will be assume higher than that of A, thus $X << A$.

The steady state photocurrent is obtained by noting that

$$j_{photo} = g - j_{rec} = g - k_3X_0 \tag{2.14}$$

It follows that the *steady state quantum efficiency* Φ_0 is given by

$$\Phi_0 = 1 - \frac{k_3X_0}{g} \tag{2.15}$$

The potential dependence of Φ calculated using these order of magnitude rate constants is illustrated for *Case I* in **fig. 2.2** as function of illumination intensity. It can be seen that the photocurrent onset shifts towards lower values of band bending as the light intensity is increased. The displacement of -59 mV per decade of hole flux

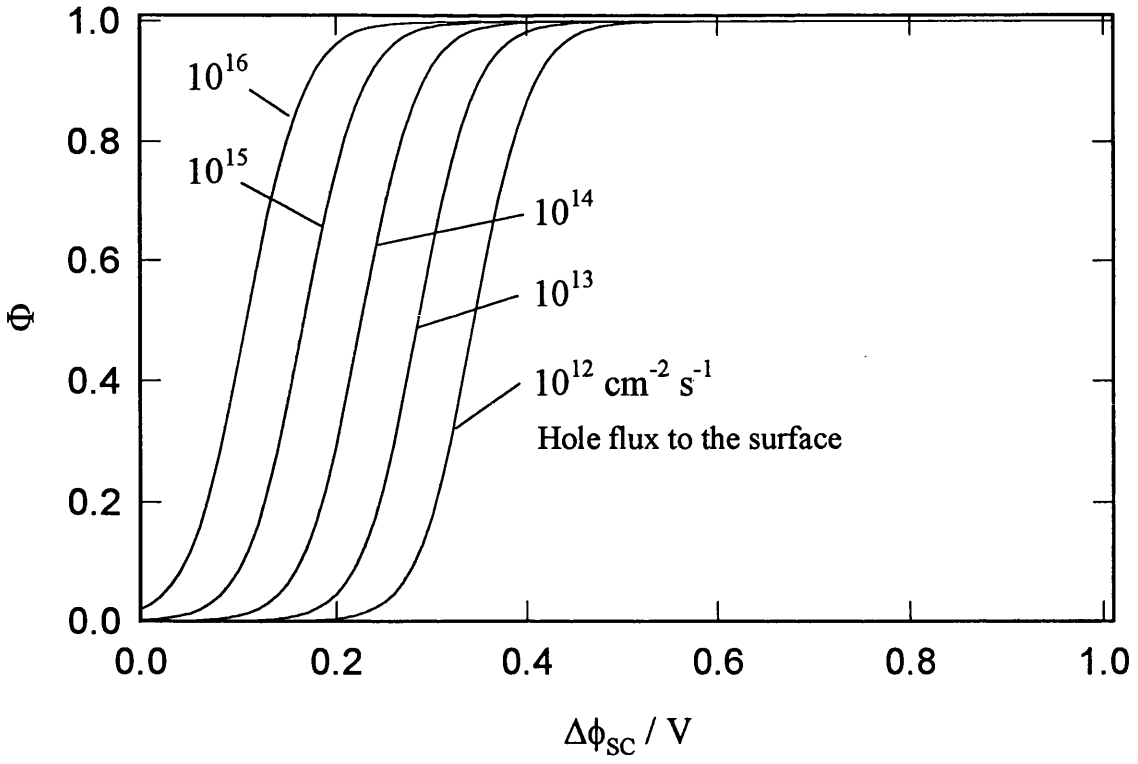

Fig. 2.2. Steady state photocurrent efficiency (Φ) as a function of the potential drop ($\Delta\phi_{SC}$) in the space charge region for *Case I*. Rate constants: $k_1 = 10\ s^{-1}$, $k_2 = 10^{-3}\ cm^2\ s^{-1}$, $k_3^0 = 10^5\ s^{-1}$.

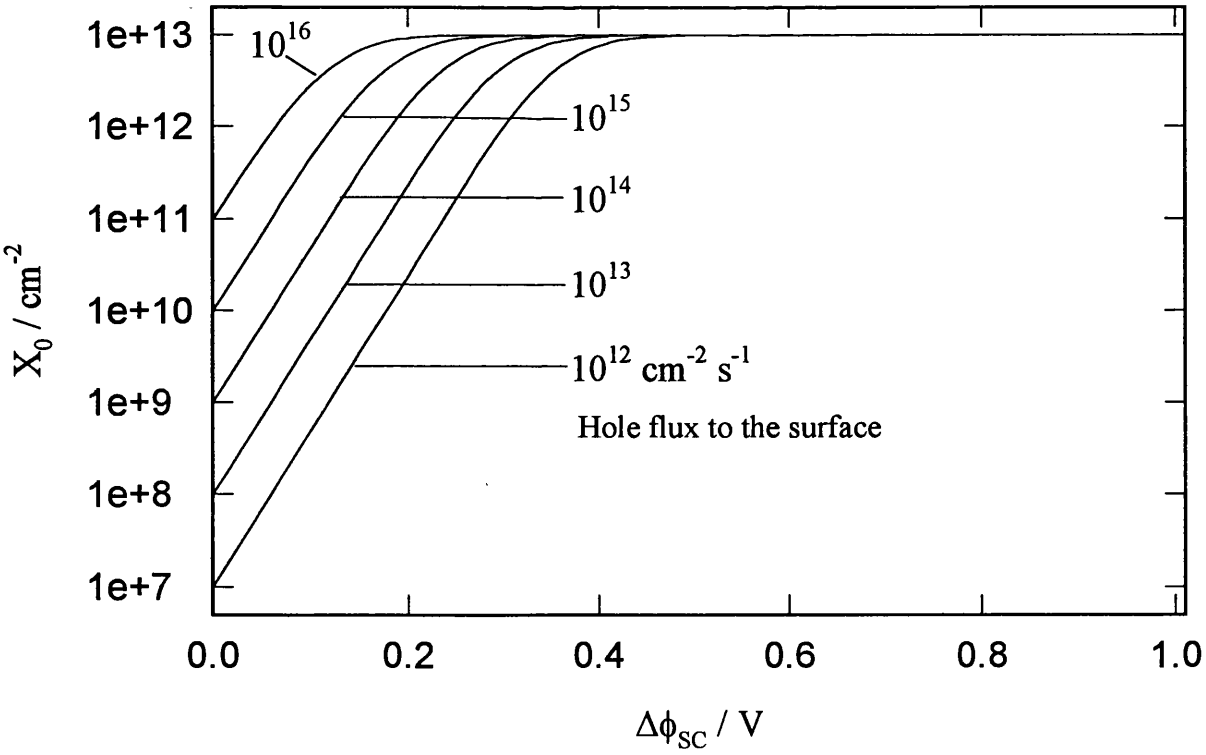

Fig. 2.3. Plots of the steady state concentration of X^+ as a function of $\Delta\phi_{SC}$ for *Case I*. Rate constants as for fig. 2.2.

reflects the potential dependence of k_3 (eq. 2.5). **Fig. 2.3** shows the corresponding potential dependence of the steady state surface concentration of intermediates (X_0) for the same range of illumination intensities. It is important to note that the limiting concentration is *independent of light intensity*.

The accumulation of X^+ (and of holes) leads to a redistribution of potential across the interface. The increase in potential drop across the Helmholtz layer is given by

$$\Delta V_H = q\frac{(X_0 + p_0)}{(C_{SC} + C_H)} \tag{2.16}$$

Fig. 2.4 shows the potential redistribution associated with the accumulation of X and p at the surface at various light intensities. This phenomenon appears experimentally in that only a fraction of the applied potential contributes to the band bending of the semiconductor. In some works, the term $\Delta\phi_{SC}$ in eq. (2.5) has been replaced by the product of an empirical "*ideality factor*" and the relation ($E - E_{FB}$) to account for this effect [12,13].

In **fig. 2.5**, photocurrent-potential curves are shown including the effect of surface charging. Note that the potential axis corresponds to the quantity $E - E_{FB}$. The most striking feature is the broadening of the photocurrent-potential curve in comparison with the case where surface charging is neglected. In **fig. 2.6**, it can be seen that this effect becomes more dramatic as the ratio k_1 / k_2 increases.

2.3.2 Case II

If the hole capture cross section of X^+ is small and the surface bound species is mobile, the decay of X^+ may take place predominantly via reaction 4. In this case, the steady state solutions for the concentrations of holes and X^+ are

$$p_0 = \frac{g}{k_1} \tag{2.17}$$

$$X_0 = \frac{-k_3 + \sqrt{(k_3^2 + 8k_4 g)}}{4k_4} \tag{2.18}$$

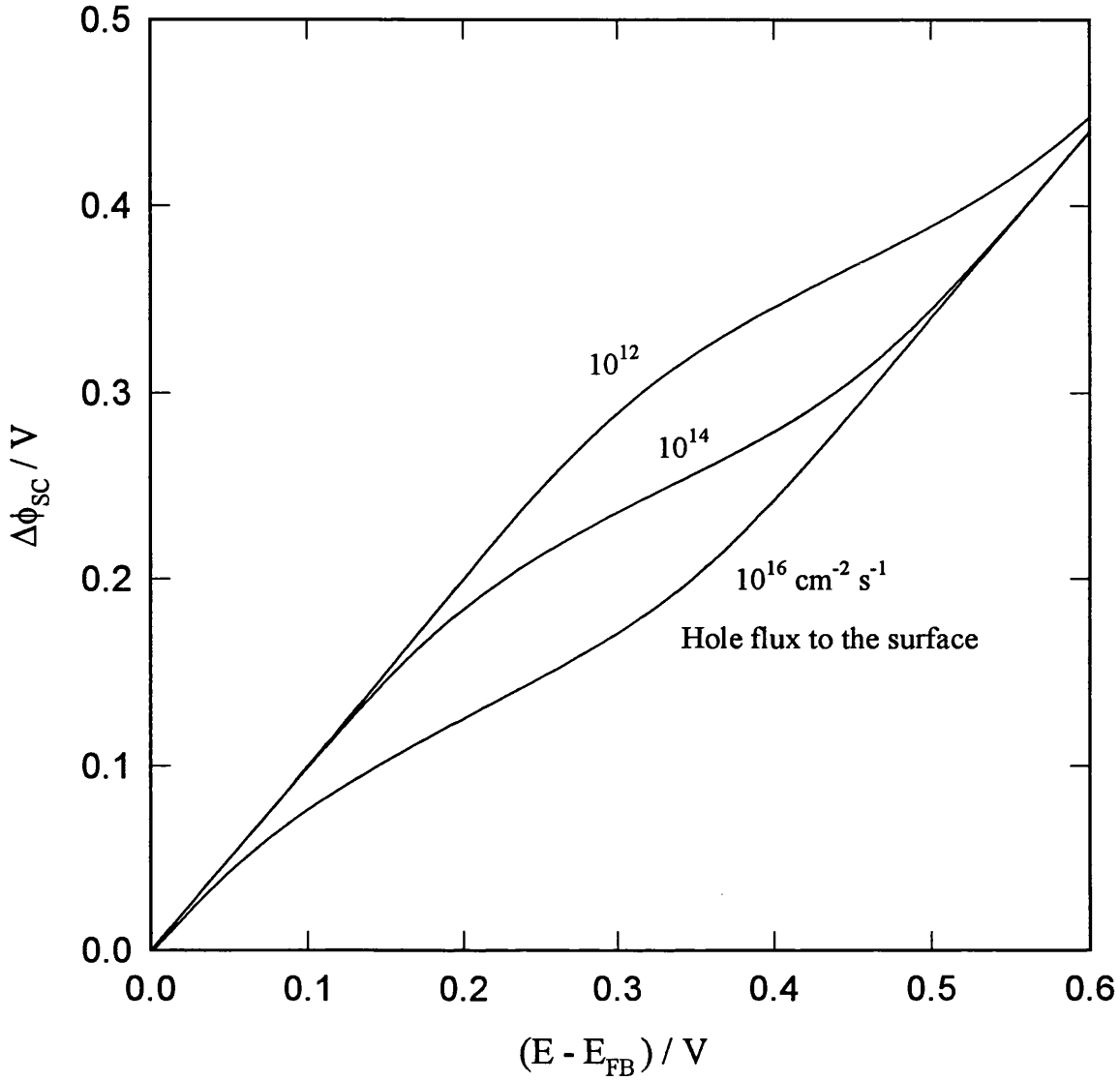

Fig. 2.4. Potential drop across the space charge region as a function of the measurable quantities E - E_{FB} for *Case I.* C_H = 10 μF cm^{-2} and rate constants as in fig. 2.1.

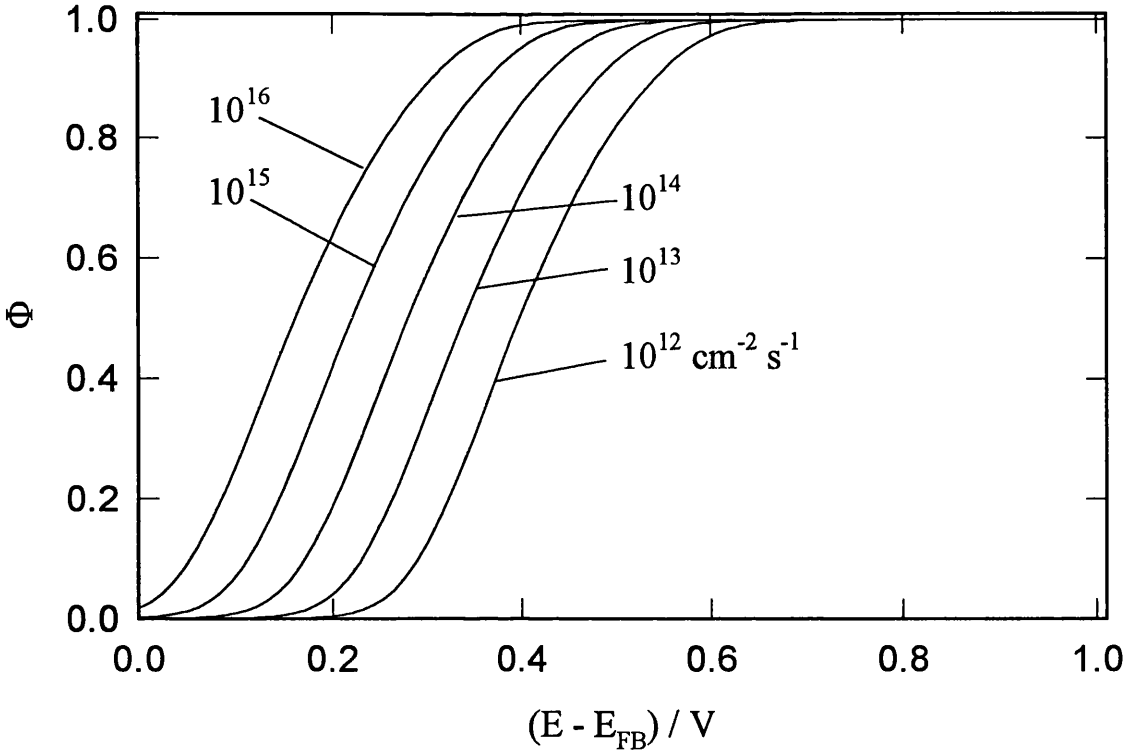

Fig. 2.5. Plots of Φ vs. $(E - E_{FB})$ for various hole fluxes showing the distortion due to surface charging for *Case I*. Rate constants as for fig. 2.2

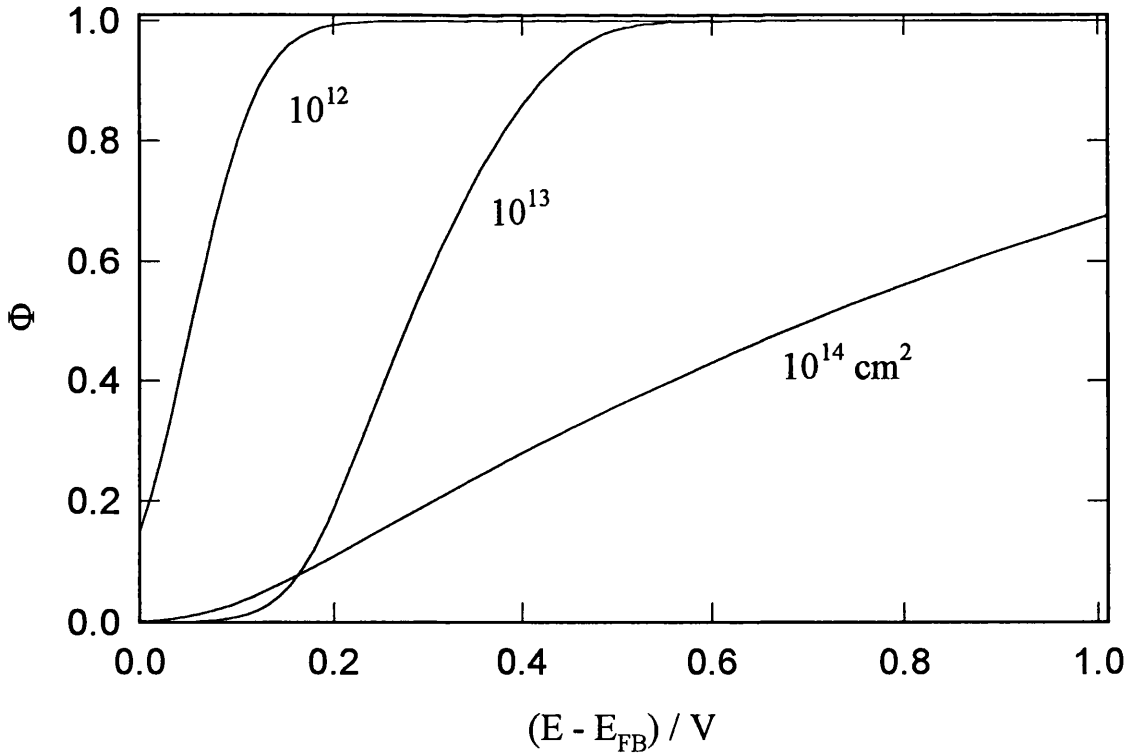

Fig. 2.6. Plots of Φ vs. $(E - E_{FB})$ for different ratios k_1/k_2 (k_2 varied, other rate constants as for fig. 2.2). $g = 10^{14}$ cm^{-2} s^{-1}.

Estimations of the order of magnitude of k_4 are rather more complicated. For instance, assuming that the reaction occurs when an "adatom" collides with a reactive neighbour, k_4 could be simply expressed as

$$k_4 = P_d \frac{\varsigma^2}{4\tau} \exp\left(-\frac{E_{diff}}{RT}\right) \exp\left(-\frac{E_d}{RT}\right) = k_4^0 \exp\left(-\frac{E_{2d}}{RT}\right) \qquad (2.19)$$

where P_d is the probability of desorption upon collision, ς is the mean free path (of the order of the lattice parameter~10^{-8} cm), τ is the mean free time (of the order of 10^{-12} s), E_{diff} is the diffusion barrier and E_d is the barrier of desorption upon reaction [14]. Assuming $P_d = 1$, it follows that $k_4^0 \sim 10^{-4}$ cm^2 s^{-1}. Values of $k_4 < 10^{-10}$ cm^2 s^{-1} have been reported for the photo-evolution of oxygen from n-TiO_2 electrodes [15], therefore it is not surprising to find high diffusion-desorption activation energies (E_{2d}) in this sort of reaction, especially if they involve surface charged intermediates. Consequently, in the rest of the discussion, values of k_4 are taken according to experimental evidence.

The photocurrent conversion efficiency can be calculated as before from eq. (2.17), and the redistribution of potential from eq. (2.16). **Fig. 2.7** illustrates the intensity dependence of the photocurrent potential response, and comparison with **fig. 2.2** shows that the shift per decade of hole flux is halved to -30 mV per decade. In **fig. 2.8**, the potential and light intensity dependence of the surface concentration of intermediate X^+ for *Case II* is presented. The most striking feature is observed in the saturation region where the steady state concentration of X^+ increases with the square root of the light intensity. This can be visualised from eq. (2.18) as $X_0 \rightarrow (g/(2k_4))^{1/2}$ when $k_3 \rightarrow 0$. Although the IMPS response is limited to a single point in the real axis under this condition, the dependence of X_0 on light intensity could be an interesting diagnostic criterion in studies based on microwave reflectivity measurements [6].

The fact that the steady state concentration of X is dependent on g determines that the steady state photopotential (ΔV_H) increases with increasing light intensities. **Fig. 2.9** shows ΔV_H as a function of potential and light intensity. For the set of parameters used in this simulation, more than 80% of the applied potential appears across the Helmholtz layer at an illumination level of 10^{16} cm^{-2} s^{-1}. The effect of charge

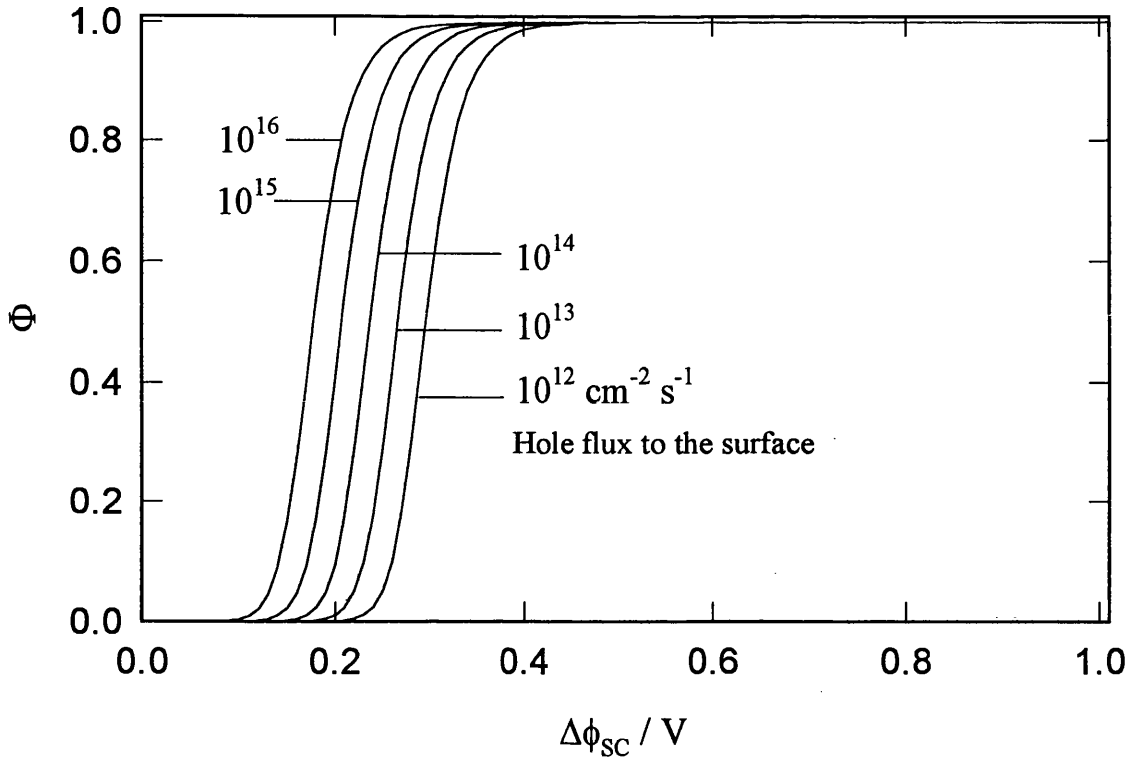

Fig. 2.7. Plots of Φ vs $\Delta\phi_{SC}$ for *Case II*. Rate constants: $k_1 = 10\ s^{-1}$, $k_3^0 = 10^5\ s^{-1}$, $k_4 = 10^{-12}\ cm^2\ s^{-1}$.

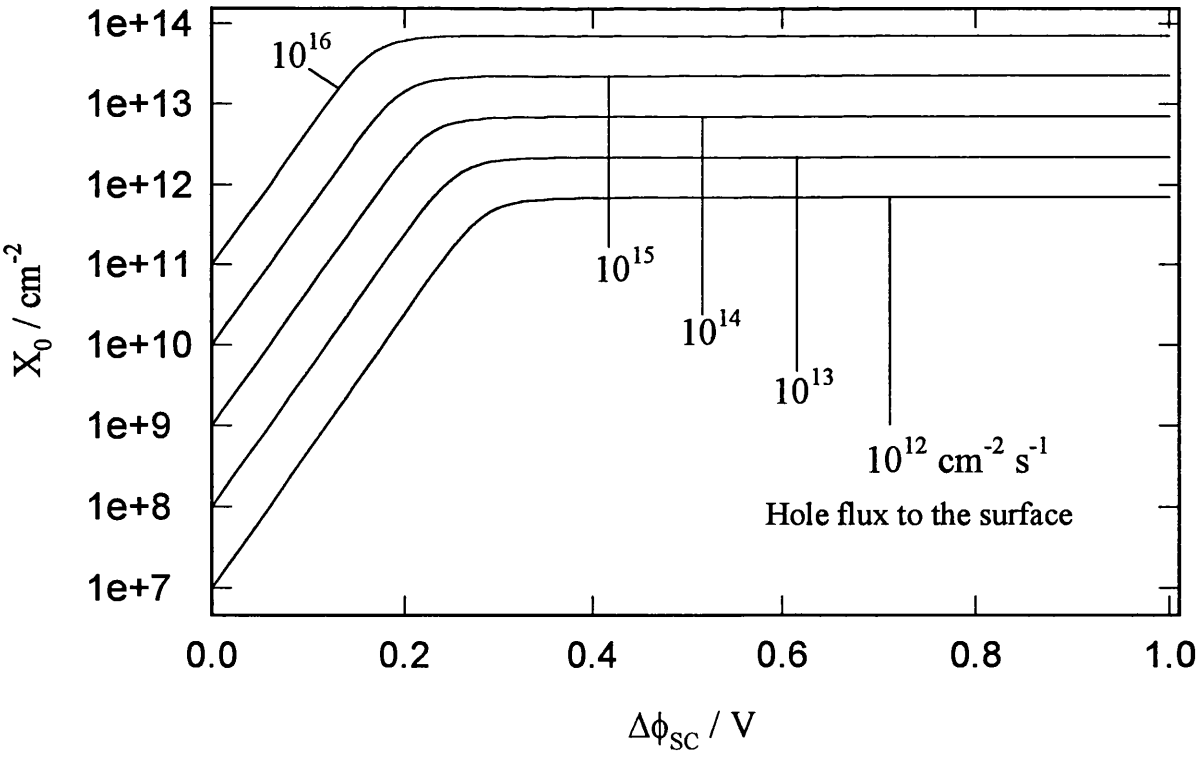

Fig. 2.8. Plots showing the build-up of X^+ as a function of $\Delta\phi_{SC}$ for *Case II* (contrast with fig. 2.3). Rate constants as for fig. 2.7.

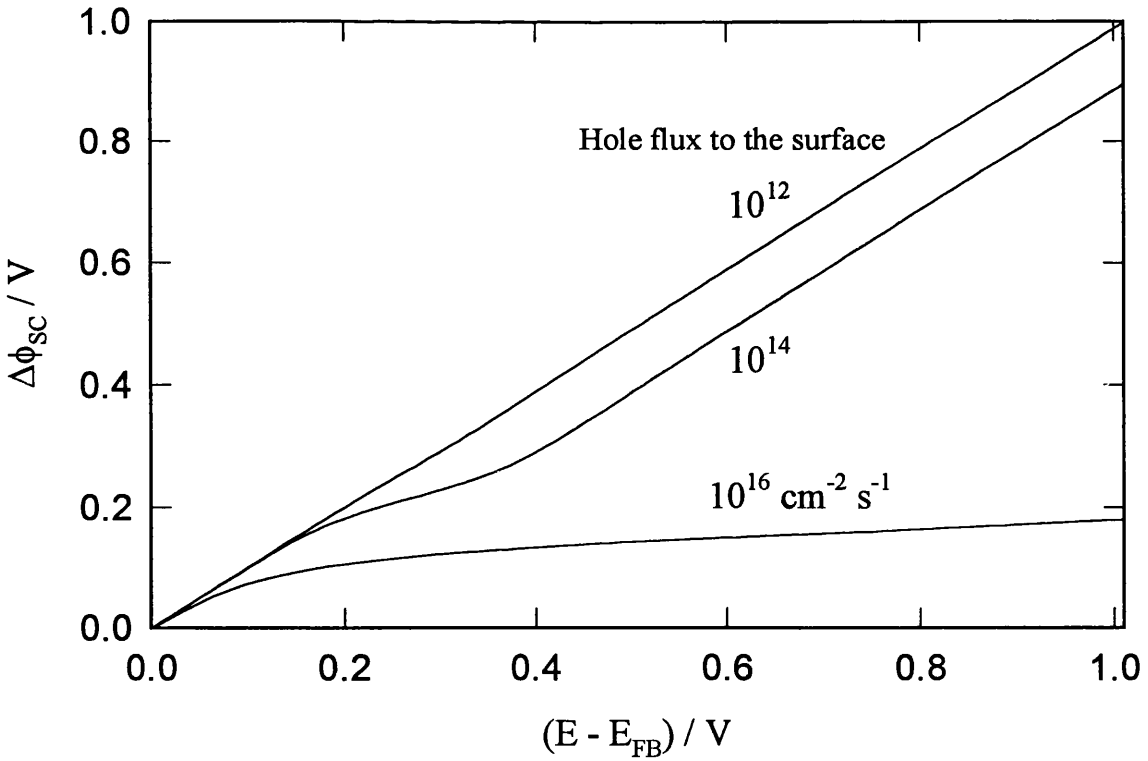

Fig. 2.9. Plots illustrating the steady state perturbation of $\Delta\phi_{SC}$ due to the accumulation of X^+ in *Case II*. Note that the magnitude of the perturbation depends on the hole flux.

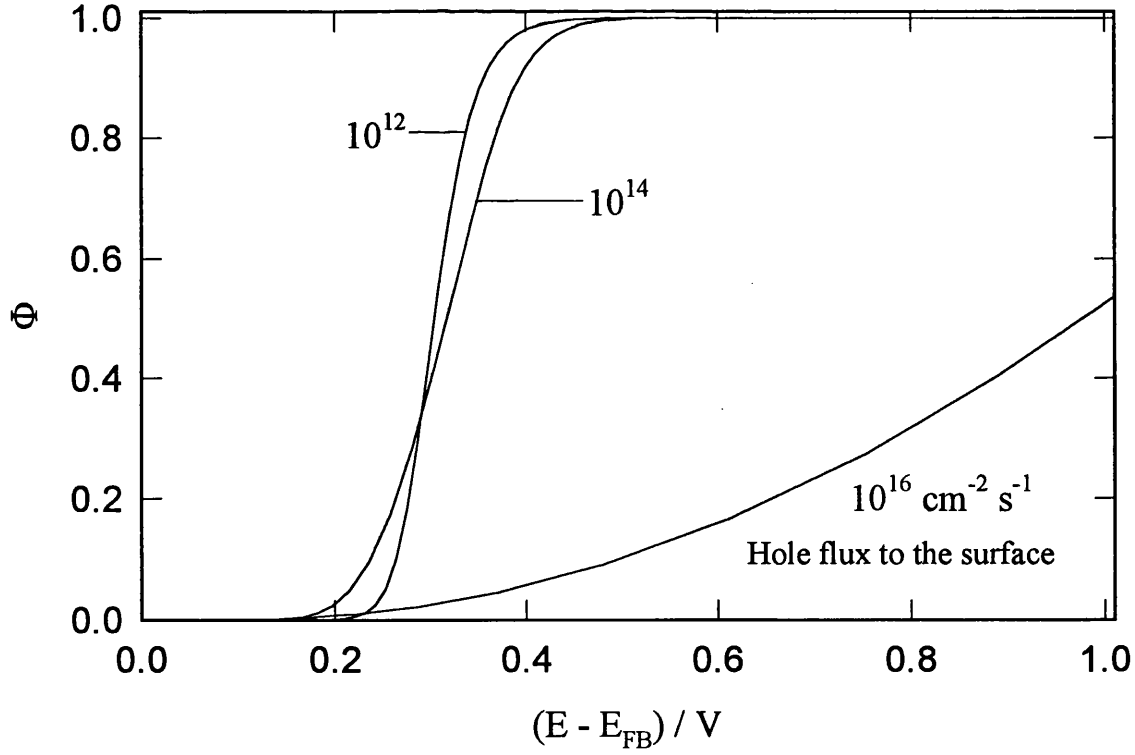

Fig. 2.10. Plots of Φ vs (E - E_{FB}) for *Case II*, illustrating the intensity dependent broadening due to the accumulation of X^+.

accumulation on the normalised photocurrent is shown in **fig. 2.10**. It is clear that this effect masks the shift of the photocurrent onset towards the flatband potential as the light intensity is increased. This behaviour should be quite distinguishable from that predicted for *Case I* (cf. **fig. 2.5**)

2.3.3 The general solution

The solution of eqs. (2.6) and (2.7) under steady state conditions is given in Appendix 2.2. X_0 as a function of the potential for the general case is shown in **Fig. 2.11**. It is observed that as k_4 increases the accumulation of X is decreased, especially at high band bending. Comparison of **fig. 2.3** with **fig. 2.11** reveals that at low coverage of X, the reaction occurs predominantly via *Case I*. This is clearly indicated in **fig. 2.12**, where the fraction of X reacting via the second order reaction is plotted vs. the band bending. For intermediates species with low surface mobility (small k_4), the probability of reacting with holes reaching the surface is very high and therefore the reaction will follow a *Case I* mechanism. However, if X is very mobile, the fraction of reacting via a *Case II* process will increase quite dramatically at high coverage of the intermediate.

2.4. Intensity Modulated Photocurrent Response

The attenuation introduced by the RC constant of the electrochemical cell is not considered in the following derivations, but it can be incorporated without difficulty if required [6]. In view of the complexity of the general solution under periodic conditions, we consider only the two limiting cases defined in the previous section.

2.4.1 Case I (X^+ not mobile)

As previously mentioned, in IMPS a sinusoidal light intensity is superimposed on a constant illumination level. This illumination will determine a total time dependent flux of holes of

$$g = g_0 + g_1 \exp(i\omega t) \qquad (2.20)$$

Eq. (2.15) can be rewritten to describe the periodic component of the photocurrent in the form

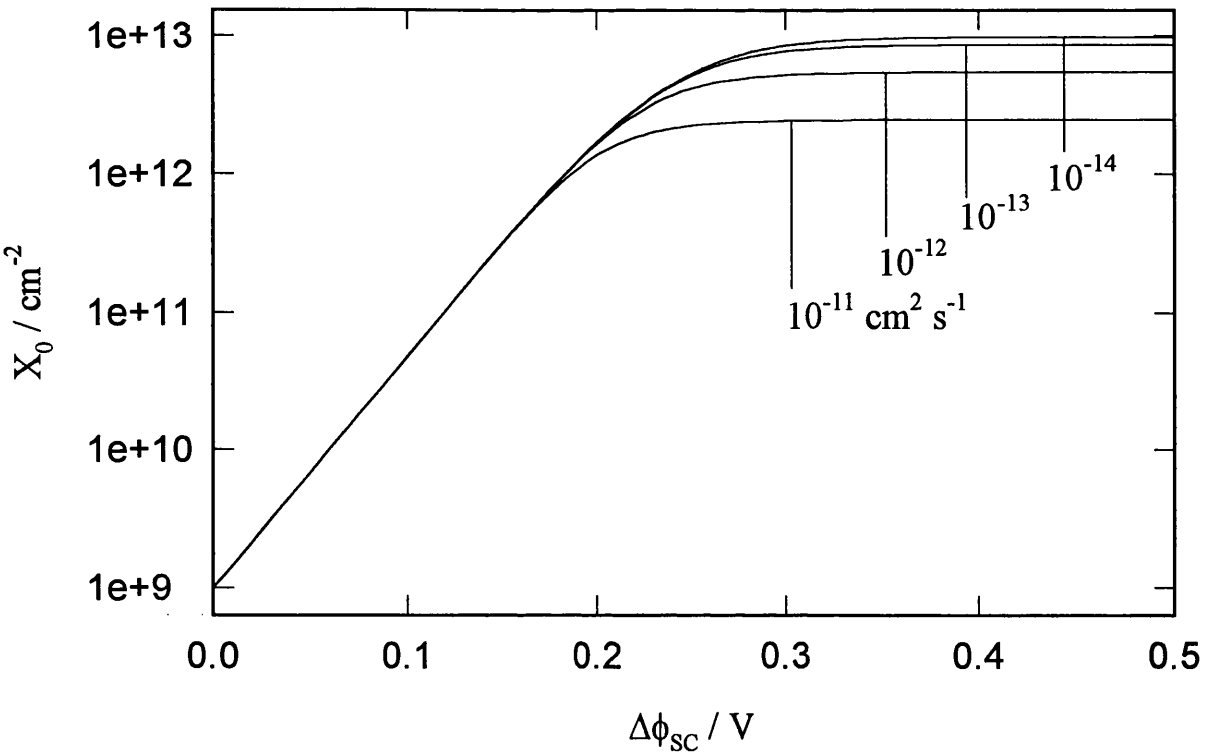

Fig. 2.11. Plots of X_0 vs $\Delta\phi_{SC}$ for the general case. Rate constants:
$k_1 = 10^{10}$ s^{-1}, $k_2 = 10^{-3}$ cm^2 s^{-1}, $k_3^0 = 10^5$ s^{-1}, k_4 as shown.
$g = 10^{14}$ cm^{-2} s^{-1}

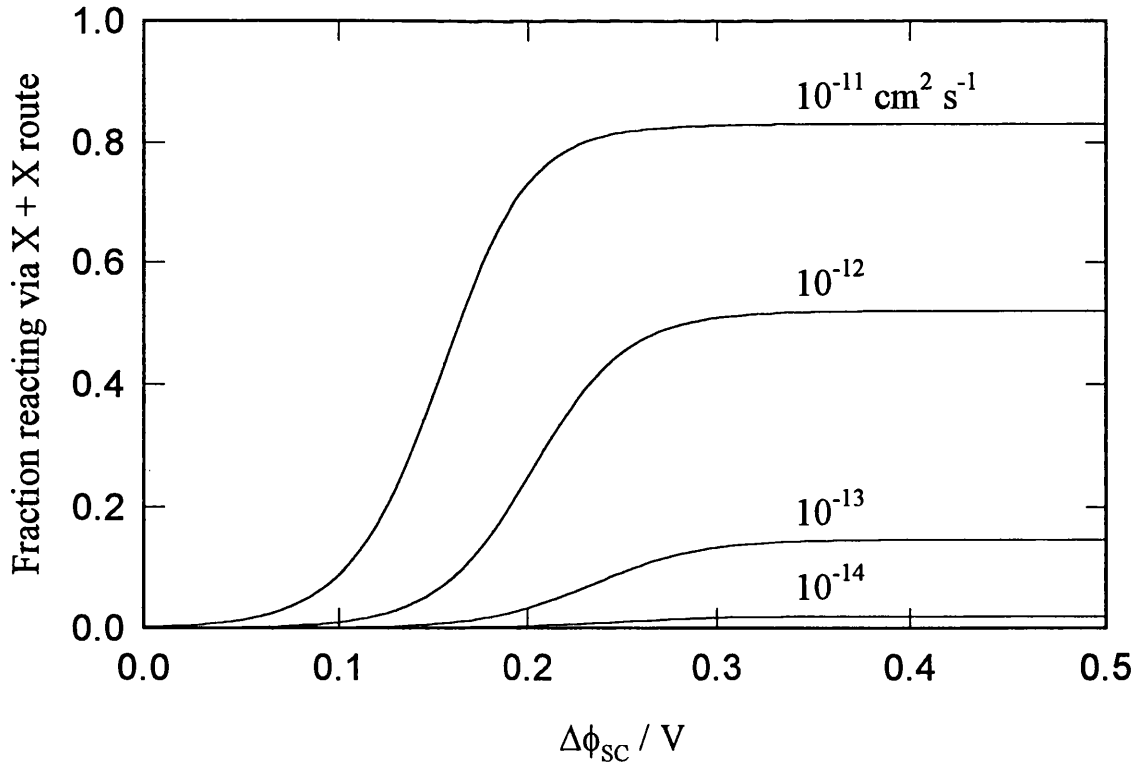

Fig. 2.12. Plots obtained from the general case showing the transition from *Case I* to *Case II* as a function of $\Delta\phi_{SC}$. Parameters as in fig. 2.11 and k_4 as shown.

$$\frac{j_{(\omega)}}{g_1} = 1 - \frac{k_3 X_1}{g_1} \tag{2.21}$$

where X_1 corresponds to the frequency dependent periodic component of the surface concentration of the X^+ species.

The total concentrations of intermediates and holes can be written by analogy with eq. (2.20) as

$$X = X_0 + X_1 \exp(i\omega t) \tag{2.22}$$

$$p = p_0 + p_1 \exp(i\omega t) \tag{2.23}$$

It follows that

$$p_1(k_1 + k_2 X_0 + i\omega) = g_1 - k_2 p_0 X_1 \tag{2.24}$$

$$X_1(k_2 p_0 + k_3 + i\omega) = (k_1 - k_2 X_0) p_1 \tag{2.25}$$

The *frequency dependent conversion efficiency*, $\Phi_{(\omega)}$, can now be derived for *Case I*. It is

$$\Phi(\omega) = \frac{j(\omega)}{g_1} = \frac{2(k_1 k_2 p_0 + k_2 k_3 X_0) - \omega^2 + i\omega(k_1 + k_2(p_0 + X_0) + k_3)}{2k_1 k_2 p_0 + k_1 k_3 + k_2 k_3 X_0 - \omega^2 + i\omega(k_1 + k_2(p_0 + X_0) + k_3)} \tag{2.26}$$

where X_0 and p_0 are the steady state surface densities of intermediate and of holes, which are given by eq. (2.9) and eq. (2.10) respectively.

The complex plane plot of eq. (2.26) is not always a semicircle since it contains quadratic terms. However, for rate constants consistent with the previous estimations (c.f. eqs. 2.11-13) and for modulation depth of ≤ 10 %, ω^2 can be neglected. Eq (2.26) then simplifies to

$$\Phi(\omega) = \frac{k_{tr} + i\omega}{k_{tr} + k_{rec} + i\omega} \tag{2.27}$$

where the *phenomenological rate constants* are defined as

$$k_{tr}^{I} = 2\frac{k_2(k_1 p_0 + k_3 X_0)}{k_1 + k_2(p_0 + X_0) + k_3} \tag{2.28}$$

$$k_{rec}^{I} = k_3\frac{(k_1 - k_2 X_0)}{k_1 + k_2(p_0 + X_0) + k_3} \tag{2.29}$$

These useful derivations indicate that the IMPS response for a two hole transfer reaction can be described by the same expression of the single hole transfer mechanism (eq. 2.27). *The link between phenomenological and real rate constants is given by expressions (2.28) and (2.29).*

In order to illustrate the main features of the IMPS response, calculations have been carried out using values of k_1 and k_2 chosen to minimise surface charging effects. The influence of surface charging is considered in section 2.6. **Fig. 2.13a** illustrates the dependence of the IMPS response on $\Delta\phi_{SC}$. Qualitatively, it is not possible to distinguish between the responses for a single or two hole transfer processes, since they are given by the same general equation. However, a distinctive behaviour is given by the comparison of the low frequency limit of the photocurrent and the steady state photocurrent. For the single charge transfer model, $\Phi_{(\omega\to 0)}$ and Φ_{dc} are identical. **Fig. 2.13b** shows that for *Case I* the low frequency intercept is higher than the steady state value in the photocurrent onset region. This behaviour was also recognised by de Wit et al. for a similar mechanism. The frequency of maximum imaginary part can be readily obtained from eqs. (2.28) and (2.29) as

$$\omega_{max} = \frac{2k_1 k_2 p_0 + k_1 k_3 + k_2 k_3 X_0}{k_1 + k_2(X_0 + p_0) + k_3} \tag{2.30}$$

Fig. 2.13c shows dependence of ω_{max} on the band bending. It is observed that the limit $(59\ mV)^{-1}$ slope in a semilogarithmic plot, which characterised the single charge transfer model, is only observed at very low band bending. Furthermore, **fig. 2.13d** illustrates the potential dependence of k_{rec}, which also approaches the same slope only

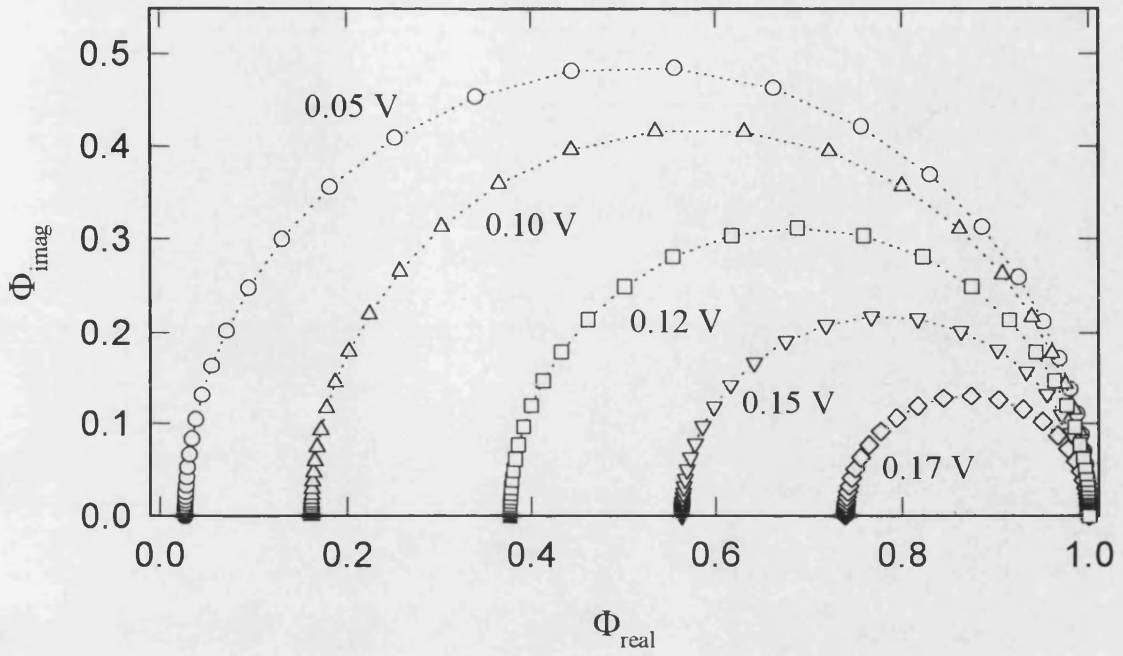

Fig. 2.13a. IMPS complex representation for *Case I* at various $\Delta\phi_{SC}$.
Rate constants: $k_1 = 10^{10}\ s^{-1}$, $k_2 = 10^{-2}\ cm^2\ s^{-1}$, $k_3^0 = 10^5\ s^{-1}$.
$g = 10^{14}\ cm^{-2}\ s^{-1}$

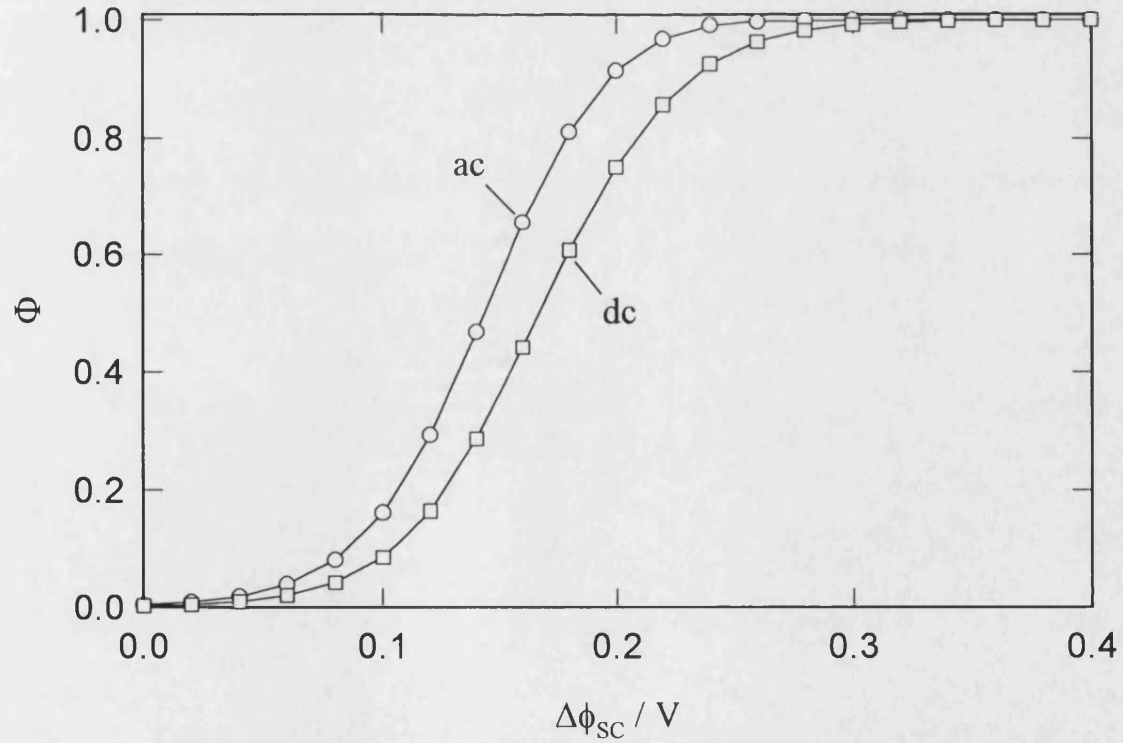

Fig. 2.13b. Plots of the steady state (dc) and limiting low frequency ac values of Φ for *Case I* as a function of $\Delta\phi_{SC}$.

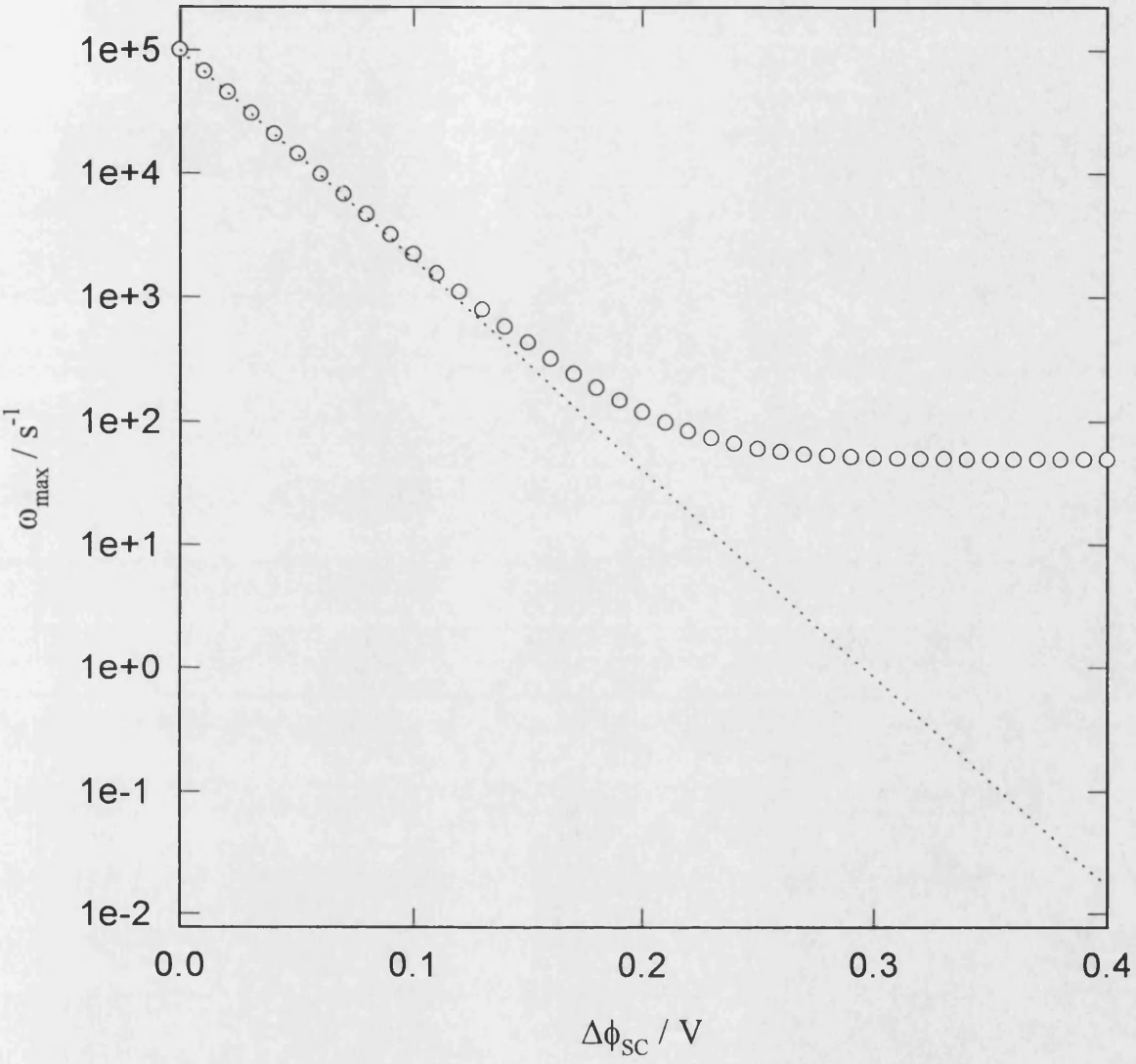

Fig. 2.13c. Semilogarithmic plot of ω_{max} vs $\Delta\phi_{SC}$ for *Case I*. The broken line shows the limiting slope of 59 mV/decade expected when ω_{max} is determined by k_3.

at low band bending. Under this conditions, X_0 is rather small and k_{rec} is mainly determined by k_3. The behaviour of k_{tr} is also interesting. In principle, in the single charge transfer model k_{tr} is independent of potential, since it is identical to the charge transfer rate constant. **Fig 2.13d** also shows that k_{tr} decreases as the band bending is decreased. This arises from the inclusion of k_3 in eq. (2.28).

2.4.2 Case II (mobile X^+ species)

If the $X^+ + X^+$ reaction predominates, a similar treatment yields an expression identical to eq. (2.26), but the phenomenological parameters have a different dependence on the real rate constants. In this case, the phenomenological charge transfer (k_{tr}^{II}) and recombination (k_{rec}^{II}) rate constants are given by:

$$k_{tr}^{II} = 4\frac{k_1 k_4 X_0}{k_1 + 4k_4 X_0 + k_3} \tag{2.31}$$

$$k_{rec}^{II} = \frac{k_1 k_3}{k_1 + 4k_4 X_0 + k_3} \tag{2.32}$$

As the complex IMPS representation of *Case I and II* is given by same general expressions (eq. 2.27), the general features are indistinguishable. The striking differences appear in the potential dependence of the phenomenological parameters. For a set of parameters which minimise surface charging effects, the potential dependence of k_{rec}^{II} and k_{tr}^{II} are displayed in **fig. 2.14a**. The slope of $(59\ mV)^{-1}$ observed for k_{rec}^{II} over the whole potential range contrasts with the behaviour obtained for k_{rec}^{I} (cf. **fig. 2.13d**). This arises from the fact that k_1 is the dominant factor in the denominator on eqs. (2.31) and (2.32), therefore k_{rec}^{II} is effectively equal to k_3. Even more interesting is the potential dependence of k_{tr}^{II}. *It is observed that k_{tr}^{II} increases as $\Delta\phi_{SC}$ increases until it reaches a plateau.* This trend contrasts quite clearly with the described in *Case I* (cf. **fig. 2.13d**), and it arises from the absence of the recombination term in the numerator of eq. (2.31). This feature provides a conclusive diagnosis for determining the nature of the last step in the two charge transfer mechanism. The increment of k_{tr}^{II} with $\Delta\phi_{SC}$ determine a distinctive behaviour of ω_{max}^{II} as shown in **fig. 2.14b**. The frequency of maximum imaginary part is given by:

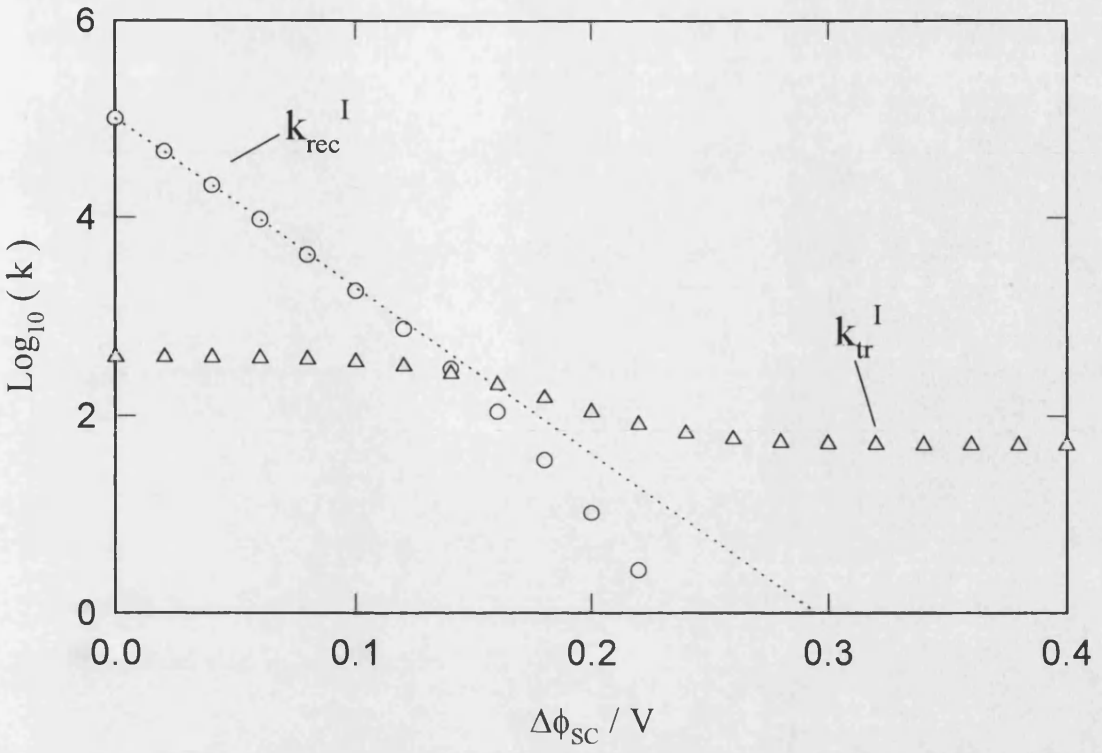

Fig. 2.13d. Semilogarithmic plot of k_{tr}^{I} and k_{rec}^{I} (*Case I*) vs $\Delta\phi_{SC}$

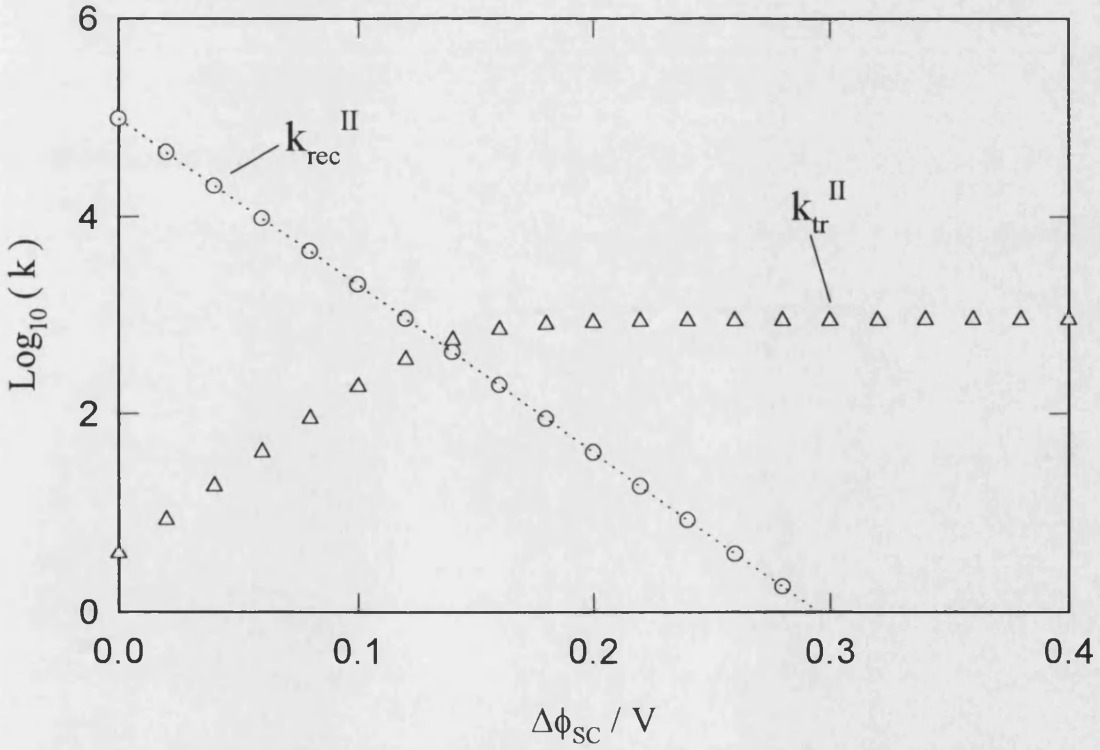

Fig. 2.14a. Semilogarithmic plot of k_{tr}^{II} and k_{rec}^{II} (*Case II*) vs $\Delta\phi_{SC}$.
$k_4 = 10^{-11}$ cm^2 s^{-1} (to minimise the effect of accumulation of X^+).
$k_1 = 10^{10}$ s^{-1}, $k_3^0 = 10^5$ s^{-1}. $g = 10^{14}$ cm^{-2} s^{-1}.

$$\omega_{max}^{II} = \frac{k_1(4k_4X_0 + k_3)}{k_1 + 4k_4X_0 + k_3} \qquad (2.33)$$

Fig. 2.14b shows a decrease of ω_{max}^{II} with the potential until $k_3 < 4k_4X_0$, where the contribution of the phenomenological charge transfer rate constant dominates in eqs. (2.33). This behaviour is also contrasted to the expected $(59\ mV)^{-1}$ slope. On the other hand, it is also observed that $\Phi_{(\omega\to 0)} > \Phi_{dc}$ as shown in **fig. 2.14c**.

2.5. Perturbation of the band bending due to accumulation of X^+ and p

At this point it is necessary to consider in more detail the influence of the accumulation of charged intermediates on the IMPS response. Two effects can be connected to the accumulation of X^+ and p: (i) a dc perturbation of $\Delta\phi_{SC}$ introduced by the steady state surface concentration of X^+ and p (X_0 and p_0 respectively) and (ii) a periodic perturbation in connection to the ac concentration of the charged species (X_1 and p_1). In this section, the effects of each of these perturbations on IMPS responses are analysed. Only the two hole transfer mechanism (*Case I*) is considered as an illustration.

2.5.1. Steady state perturbation of $\Delta\phi_{SC}$ by charged species

In section 2.3, the effect of X_0 and p_0 on the steady state photocurrent was discussed in terms of the perturbation of $\Delta\phi_{SC}$ given by the eq. (2.16). This phenomenon was also considered by Kelly and Memming [10]. It was shown that the increase of ΔV_H is compensated by a reduction in $\Delta\phi_{SC}$ under potentiostatic conditions. **Fig. 2.15a** contrasts IMPS spectra with and without considering the perturbation of $\Delta\phi_{SC}$. It is important to note that comparisons are made between calculations at constant $E - E_{FB}$, and that for the set of parameters used, the contribution of p_0 is negligible in comparison to X_0. A shift is observed of the low frequency limit towards the origin and an increment of ω_{max}, which is consistent with the broadening of the potential dependence of the steady state Φ shown in **fig. 2.5**. **Fig. 2.15b** illustrates the potential dependence of ω_{max} including the perturbation of X_0. It can be seen that the effect disappears at low band bending where the steady state concentration of X^+ is negligible due to recombination.

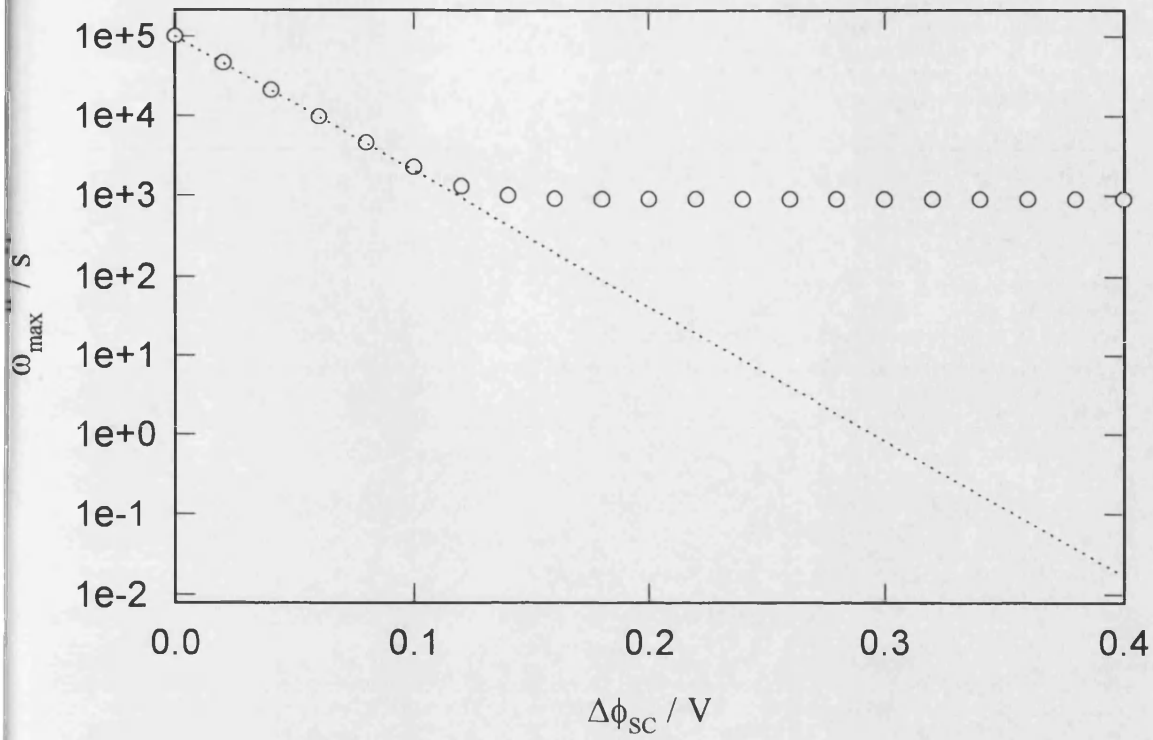

Fig. 2.14b. Semilogarithmic plot of ω_{max}^{II} vs $\Delta\phi_{SC}$. Note that k_{tr}^{II} dominates at high band bending.

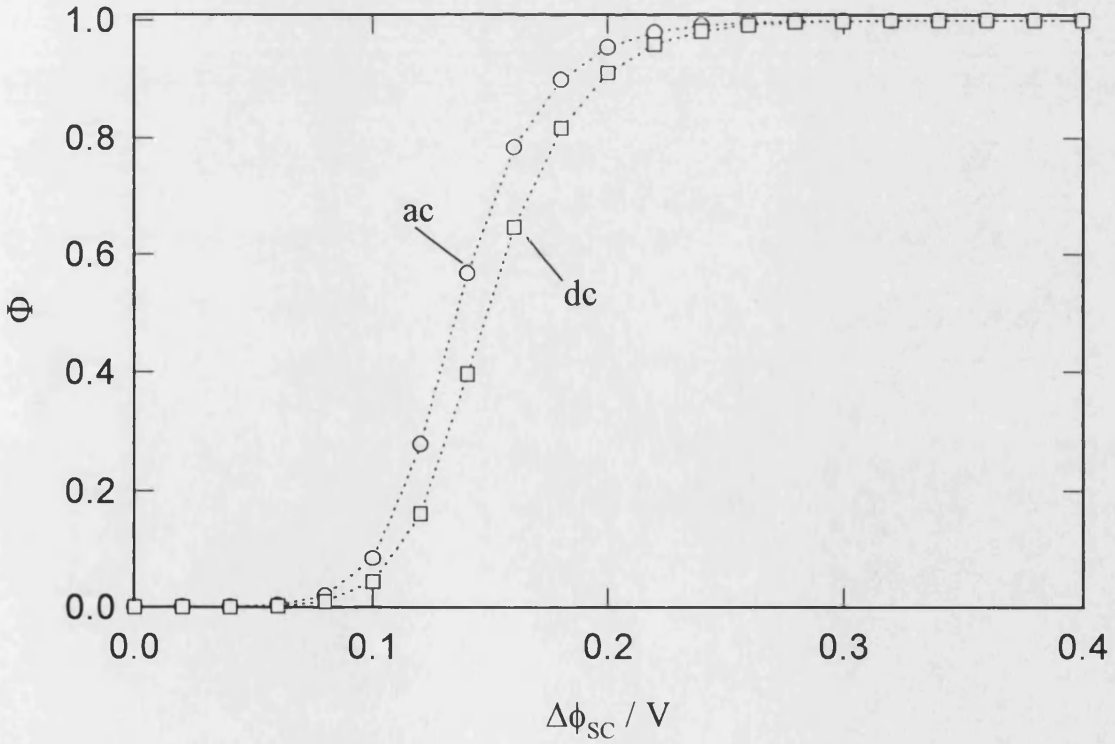

Fig. 2.14c. Plots of steady state and limiting low frequency ac values of Φ vs $\Delta\phi_{SC}$ for *Case II*.

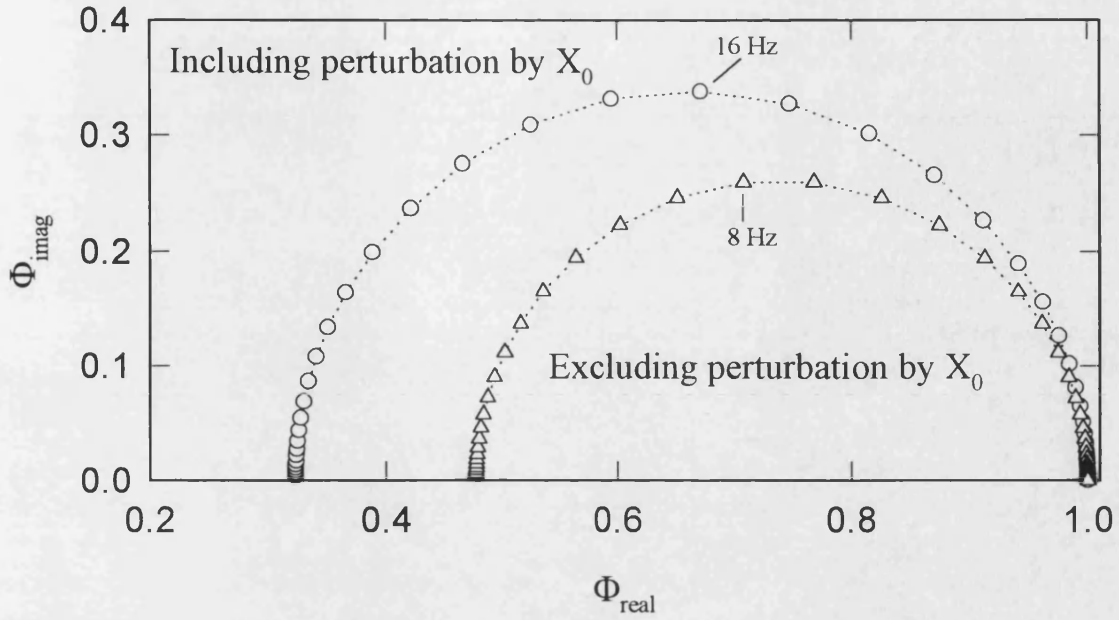

Fig. 2.15a. IMPS plots showing the effect of the steady state accumulation of X^+ (X_0) at E - E_{FB} = 0.20 V. Rate constants: $k_1 = 10^{10}$ s^{-1}, $k_2 = 10^{-3}$ cm^2 s^{-1}, $k_3^0 = 10^5$ s^{-1}. g = 10^{14} cm^{-2} s^{-1}

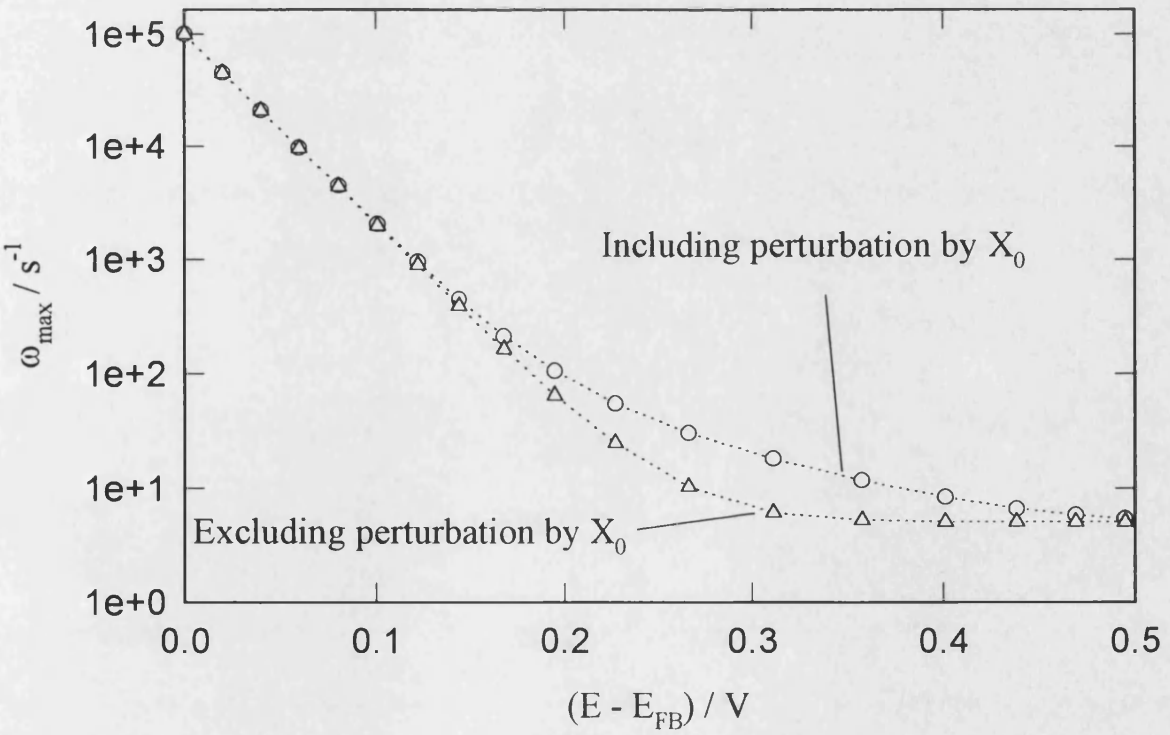

Fig. 2.15b. Plots of ω_{max} illustrating the perturbation by X_0 (dc effect) as a function of E - E_{FB} .Rate constants as in 2.15a.

Fig. 2.15c shows the potential dependence of k_{rec}. It is seen that the dc perturbation introduces a less steep relation with the applied potential. A similar effect is also observed for k_{tr} in **fig. 2.15d**. These trends can be rationalised in terms of a weaker potential dependence of k_3, noting that k_{tr} and k_{rec} are mainly linearly dependent on this rate constant (cf. eqs. 2.28 and 2.29). The effect of the dc perturbation on k_3 can be seen by comparing the dotted lines in **figs. 2.13d** and **2.15c**.

2.5.2. Periodic perturbation of $\Delta\phi_{SC}$ by charged species

It should be also considered that the periodic components X_1 and p_1 introduce an additional periodic perturbation of $\Delta\phi_{SC}$ of the form:

$$\partial V_H = -\partial(\Delta\phi_{SC}) = \frac{q}{C_{SC}+C_H}(X_1 + p_1) \tag{2.34}$$

This modulated photopotential will introduce an ac term in the recombination rate constant which becomes

$$k_3 + \partial k_3 = k_3^0 \exp\left(-q\left(\Delta\phi_{SC} + \partial(\Delta\phi_{SC})\right)/kT\right) \tag{2.35}$$

For small perturbations, i.e. $\partial(\Delta\phi_{SC}) << kT/q$, the *ac* component of k_3 can be simplified to

$$\partial k_3 = \frac{k_3 q^2}{(C_{SC}+C_H)kT}(X_1 + p_1) \tag{2.36}$$

This periodic recombination rate constant will affect the non-steady state concentration of X and p. The analysis shows that a cross term ($k_3X_1 + \partial k_3 X_0$) is introduced in eq. (2.25), changing the frequency dependence of X_1 and p_1. We will denote these new variables as X_1^{pert} and p_1^{pert} to avoid confusion.

The periodic component of X^+ is obtained from eqs. (2.6) and (2.7),

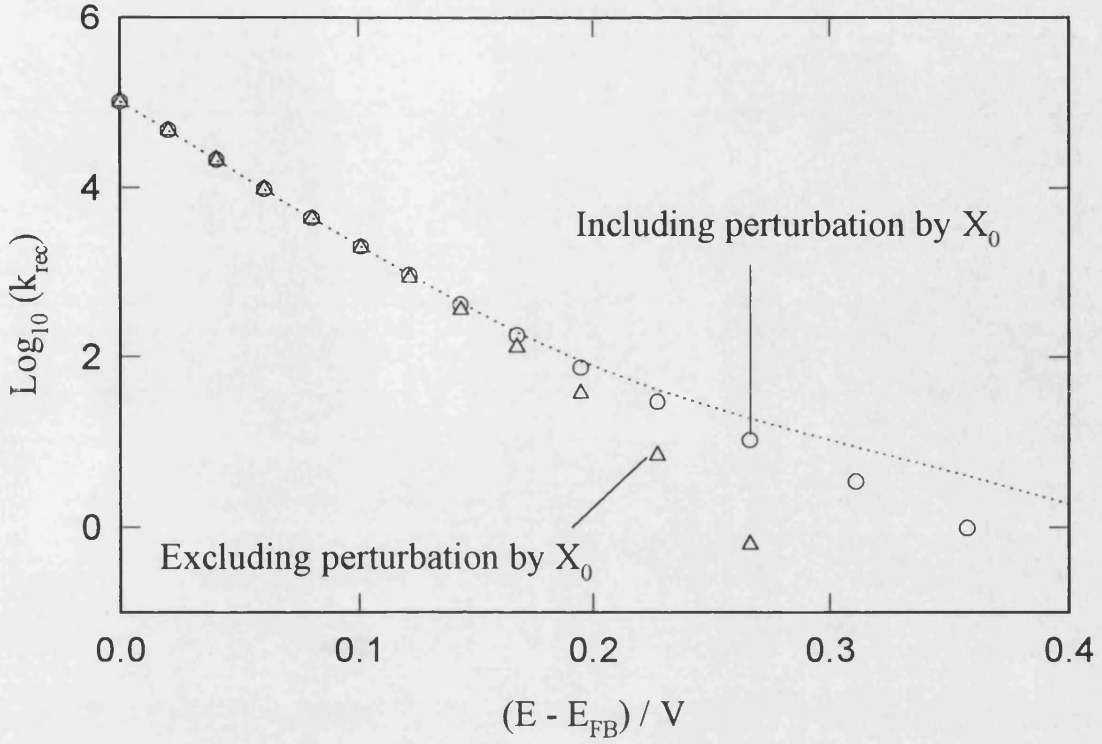

Fig. 2.15c. Semilogarithmic plot of k_{rec} as function of $E - E_{FB}$ including and excluding the steady state perturbation by X^+. Dotted line corresponds to k_3 as calculated from eq. (2.5).

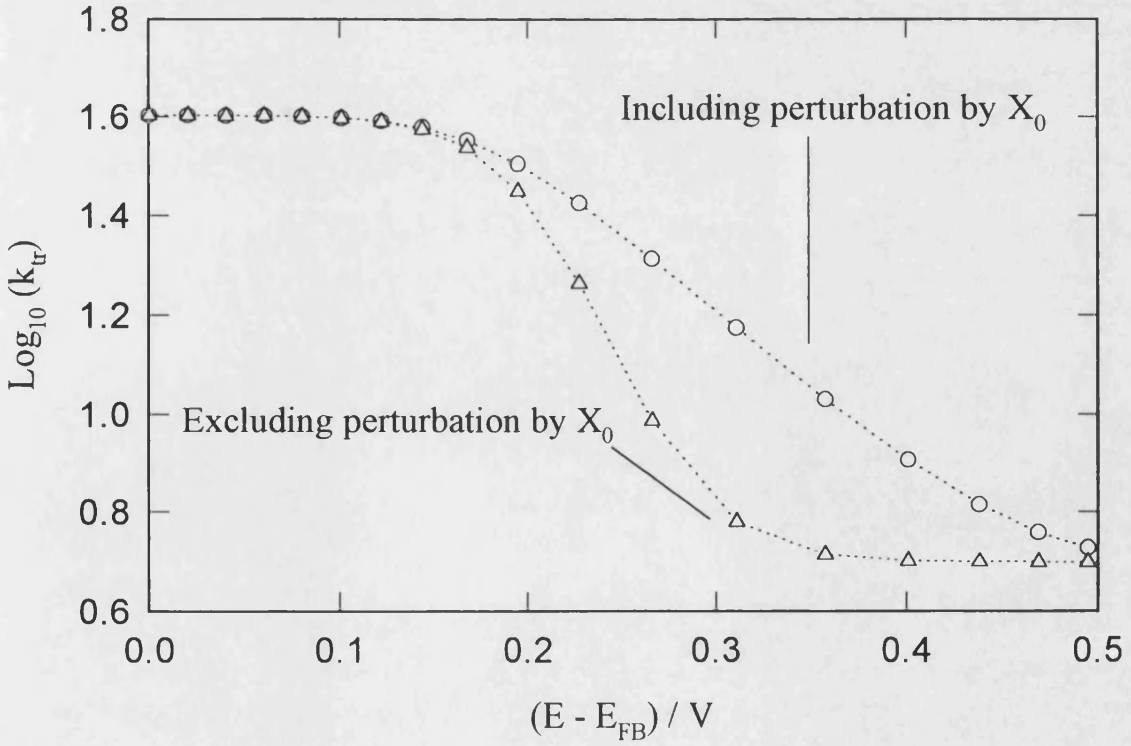

Fig. 2.15d. Semilogarithmic plot of k_{tr} as function of $E - E_{FB}$ including and excluding the steady state perturbation by X^+.

$$X_1^{pert} = \frac{g_1(k_1 - k_2 X_0 - \psi k_3 X_0)}{\eta} \tag{2.37}$$

where

$$\psi = \frac{q^2}{(C_{SC} + C_H)kT} \tag{2.37a}$$

and

$$\eta = 2k_1 k_2 p_0 + k_1 k_3 (1 + \psi X_0) + k_2 k_3 X_0 (1 + \psi(X_0 - p_0)) +$$
$$+ i\omega(k_1 + k_2(X_0 + p_0) + k_3(1 + \psi X_0) + i\omega) \tag{2.37b}$$

The expression for p_1^{pert} is given by eq. (2.24), but replacing X_1 by X_1^{pert}.

Having derived the ac concentration of X and p, the behaviour of ∂k_3 can be analysed from eq. (2.36). **Fig. 2.16a** shows the frequency dependence of $\partial k_3/k_3$ in the form of complex plane plot. It can be seen that the modulation attenuates as the frequency is increased. Further examination indicates that the maximum effect of $\partial k_3/k_3$ occurs at the "half wave potential" in the steady state photocurrent potential curve. The contribution of p_1^{pert} to ∂k_3 is negligible in comparison to X_1^{pert}. It is also observed that the frequency of minimum imaginary part increases as $\Delta\phi_{SC}$ decreases.

The frequency dependent current can be determined by eq. (2.21), but taking into account the ac component of the recombination rate constant,

$$j_{(\omega)} = g_1 - k_3 X_1^{pert} - \partial k_3 X_0 = g_1 - k_3 X_1^{pert}(1 + \psi X_0) - \psi k_3 p_1^{pert} X_0 \tag{2.38}$$

As shown in **fig. 2.16b**, a complex representation of eq. (2.38) also describes a semicircular response for the same set of parameters used in **fig. 15a**. However, it can be seen that the introduction of ∂k_3 originates further changes in the low frequency intercept as well as in ω_{max}. It is observed that low frequency limit moves towards the origin and ω_{max}^{pert} shifts to higher frequencies. These changes should come as a result of a different potential dependence of the phenomenological parameters.

The low frequency intercept and ω_{max}^{pert} can be obtained from previous relations, c.f. Appendix II, resulting in:

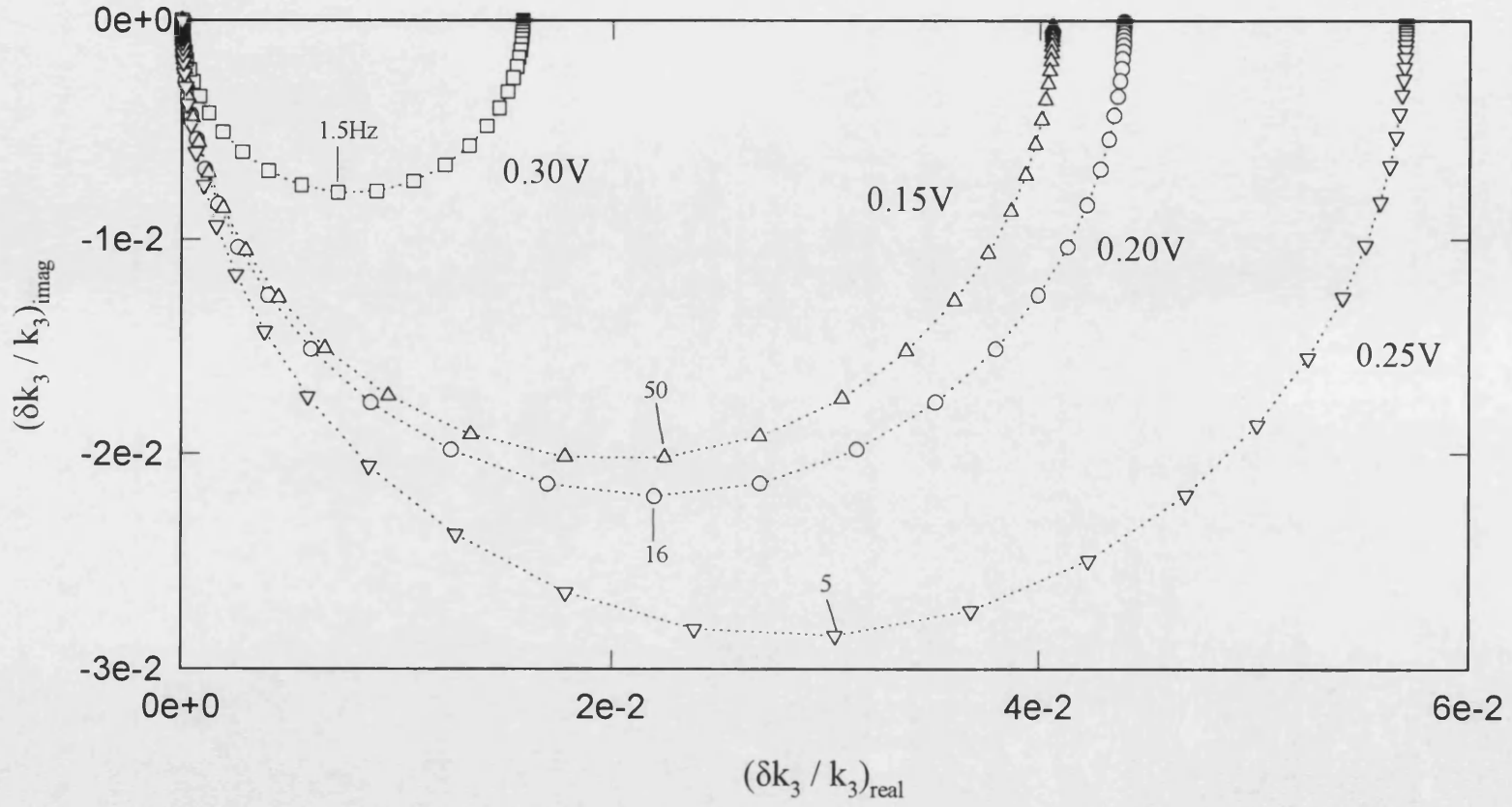

Fig. 2.16a. Complex plane plots of the ac component of k_3 normalised to the dc value at various $\Delta\phi_{SC}$. Rate constants: $k_1 = 10^{10}$ s^{-1}, $k_2 = 10^{-3}$ cm^2 s^{-1}, $k_3^0 = 10^5$ s^{-1}. $g = 10^{14}$ cm^{-2} s^{-1}. Note that the frequency of the minimum decreases as $\Delta\phi_{SC}$ increases.

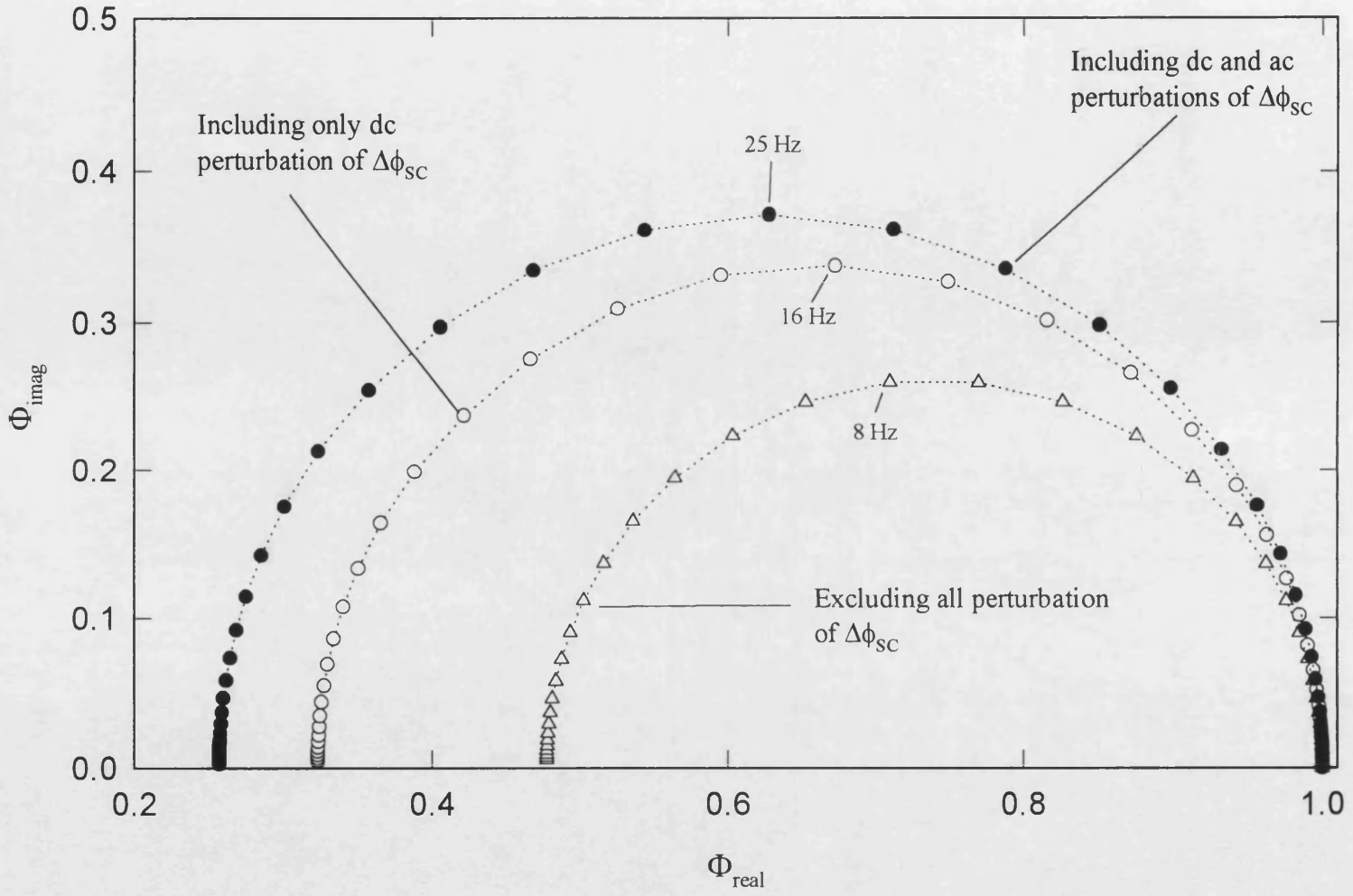

Fig. 2.16b. IMPS plots comparing the steady state and periodic perturbations associated with the accumulation of X^+ at $E - E_{FB} = 0.20$ V. Rate constants as in fig. 2.15a.

$$\Phi^{pert}_{(\omega\to 0)} = \frac{2k_1k_2p_0 + 2k_2k_3X_0(1+\psi X_0) + k_3^2\psi X_0(1+\psi X_0)}{2k_1k_2p_0 + k_1k_3(1+\psi X_0) + k_2k_3X_0(1+\psi X_0)} \tag{2.39}$$

$$\omega^{II}_{max} = \frac{2k_1k_2p_0 + k_1k_3(1+\psi X_0) + k_2k_3X_0(1+\psi X_0)}{k_1 + k_2X_0 + k_3(1+\psi X_0)} \tag{2.40}$$

The effect of the accumulation of X on the IMPS responses is clearly seen in the factor $(1 + \psi X_0)$, which appears associated with the recombination rate constant. If the concentration of $X \to 0$, eq. (2.40) is reduced to eq. (2.30) which defined the maximum imaginary part when the modulation of k_3 is excluded.

The phenomenological charge transfer (k_{tr}^{pert}) and recombination parameters (k_{rec}^{pert}) are obtained from eqs. (2.39) and (2.40),

$$k_{tr}^{pert} = \frac{2k_1k_2p_0 + 2k_2k_3X_0(1+\psi X_0) + k_3^2X_0\psi(1+\psi X_0)}{k_1 + k_2X_0 + k_3(1+\psi X_0)} \tag{2.41}$$

$$k_{rec}^{pert} = \frac{k_3(1+\psi X_0)(k_1 - k_2X_0 - \psi k_3X_0)}{k_1 + k_2X_0 + k_3(1+\psi X_0)} \tag{2.42}$$

Eqs. (2.41) and (2.42) are the link between phenomenological parameters and real rate constant for a two electron transfer process taking into account the modulation of the recombination rate constant by X_1. **Figs. 2.16c** and **2.16d** show the potential dependence of the phenomenological parameters illustrating the effect of dc and ac perturbations of the band bending. The periodical perturbation introduces an even weaker dependence of k_{rec}^{pert} with the applied potential in comparison to the steady state perturbation. However the most striking effect is seen in k_{tr}^{pert}, where a maximum is observed at the potential where the effect of $\partial k_3/k_3$ is maximum. For the set of parameters used, this maximum value of k_{tr}^{pert} is difficult to appreciate, however it becomes clear as X_1 is increased (e.g. increasing the ratio k_1/k_2).

de Wit et al. have studied the IMPS response for a mechanism similar to *Case I* (they also considered electron injection from the intermediate X) [11]. The general expression for $\Phi_{(\omega)}$ reported in their work is compatible with eq. (2.38), however their

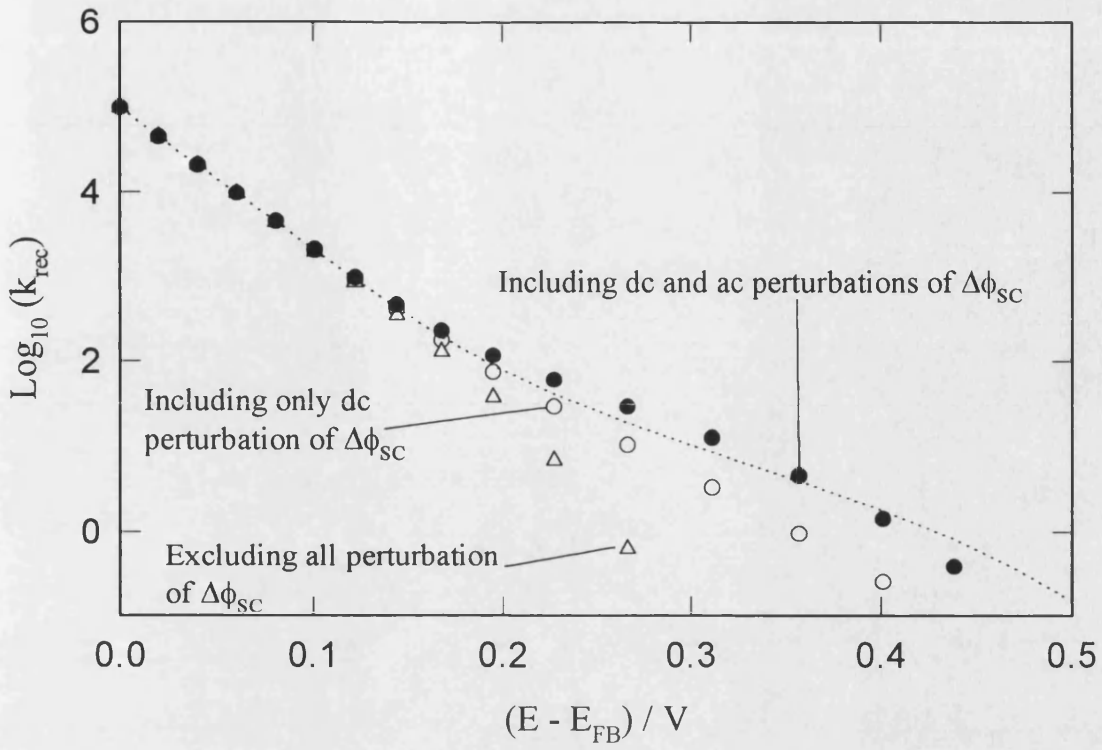

Fig. 2.16c. Semilogarithmic plot of k_{tr} as function of $E - E_{FB}$ illustrating the steady state and periodic perturbations by X^+. Dotted line corresponds to k_3 as calculated from eq. (2.5).

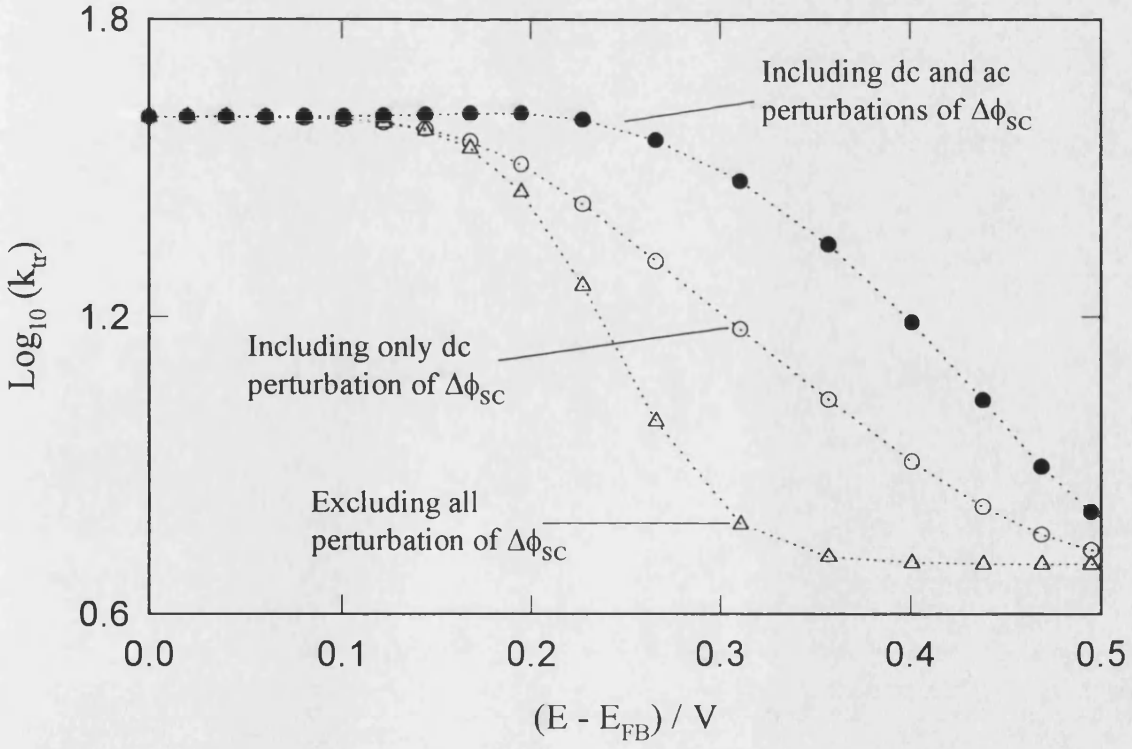

Fig. 2.16d. Semilogarithmic plot of k_{tr} as function of $E - E_{FB}$ illustrating the steady state and periodic perturbations by X^+.

analysis of ω_{max}^{pert} seems to show some inconsistency. They predicted a linear relationship between ω_{max}^{pert} and the hole flux, which is very unlikely as the dependence of X_1^{pert} upon g_1 is not linear. This inconsistency arises from the extrapolation of ω_{max}^{pert} expression obtained at the potential range where $j = j_{rec}$, to the region where Φ is effectively higher than zero. ($j > j_{rec}$) [11].

2.6. Charging current associated with the modulation of the band bending

The previous analysis shows that the modulation of the X^+ introduces a periodic perturbation in the potential drop across the space charge region. This perturbation generates a charging current of the C_{SC} which has the general form

$$j_{ch} = C_{SC}\frac{\partial(\Delta\phi_{SC})}{\partial t} \tag{2.43}$$

Under potentiostatic conditions, the redistribution of charge across the interface can be described by

$$\frac{dQ_{SC}}{dt} = g_0 + g_1\exp(i\omega t) - j - k_3X \tag{2.44}$$

$$\frac{dQ_H}{dt} = 2k_2pX - j \tag{2.45}$$

$$\frac{Q_H}{C_H} + \frac{Q_{SC}}{C_{SC}} = 0 \tag{2.46}$$

Taking into account that the eqs. (2.24) and (2.37), for p_1^{pert} and X_1^{pert}, are also valid under these conditions, the expression for the space charge charging current can be obtained as

$$j_{ch} = \frac{C_{SC}}{C_{SC}+C_H}\left(2k_2\left(X_0p_1^{pert} + p_0X_1^{pert}\right) - k_3X_1^{pert}\left(1+\psi X_0\right) + g_1 - \psi X_0k_3p_1^{pert}\right) \tag{2.47}$$

Normalised j_{ch} plots at various potentials are shown in **fig. 2.17a**. It can be seen that the charging current is negative (photocurrent to be taken positive), and therefore it

decreases the amplitude of the total current. As expected for a capacitive charging current, the low frequency limit is zero, while the high frequency limit corresponds to the ratio $C_{SC}/(C_{SC} + C_H)$. It was also verified that the normalised charging current is independent of the light intensity.

From eqs. (2.38) and (2.47), the total frequency dependent current is given by

$$j(\omega) = g_1 - k_3 X_1^{pert}(1 + \psi X_0) - \psi X_0 k_3 p_1^{pert} + j_{ch} \qquad (2.48)$$

Normalised IMPS spectra showing the effect of j_{ch} are shown in **fig. 2.17b**. The most interesting effect is observed in the high frequency limit where the response is smaller than unity. The effect is more noticeable at low band bending as the capacitance of the space charge region becomes larger. The effect of the charging current is even more evident if the doping density of the crystal is increased in one or two orders of magnitude as shown in **fig. 2.17c**.

The attenuation of the ac-photocurrent due to charging current is a particularly important consideration when the Gärtner hole flux is determined from the high frequency limit [11,15]. It is seen in **fig. 2.17** that the high frequency limit shifts toward higher photocurrent as the potential is increased. These results illustrate the requirement for independent measurements of the conversion efficiency in order to assure an appropriate normalisation of the IMPS responses.

2.7 Conclusions

IMPS responses for charge transfer mechanism involving surface bound intermediates can be described by a phenomenological approach based on two parameters which resemble the recombination and charge transfer rate constant in the single step model. The theoretical treatment shows that the potential dependence of k_{tr} and k_{rec} is very different for mechanisms involving hole capture by X (*Case I*) or coupling of two mobile intermediate species (*Case II*). In *Case I*, k_{tr} increases to a saturation value as the band bending is decreased, while in *Case II* it shows the opposite trend. It is also shown that k_{rec} decreases in different fashion as the band bending is decreased.

The steady state and periodic effects of the accumulation of charged surface bound intermediate on the potential across the space charge region is analysed. It

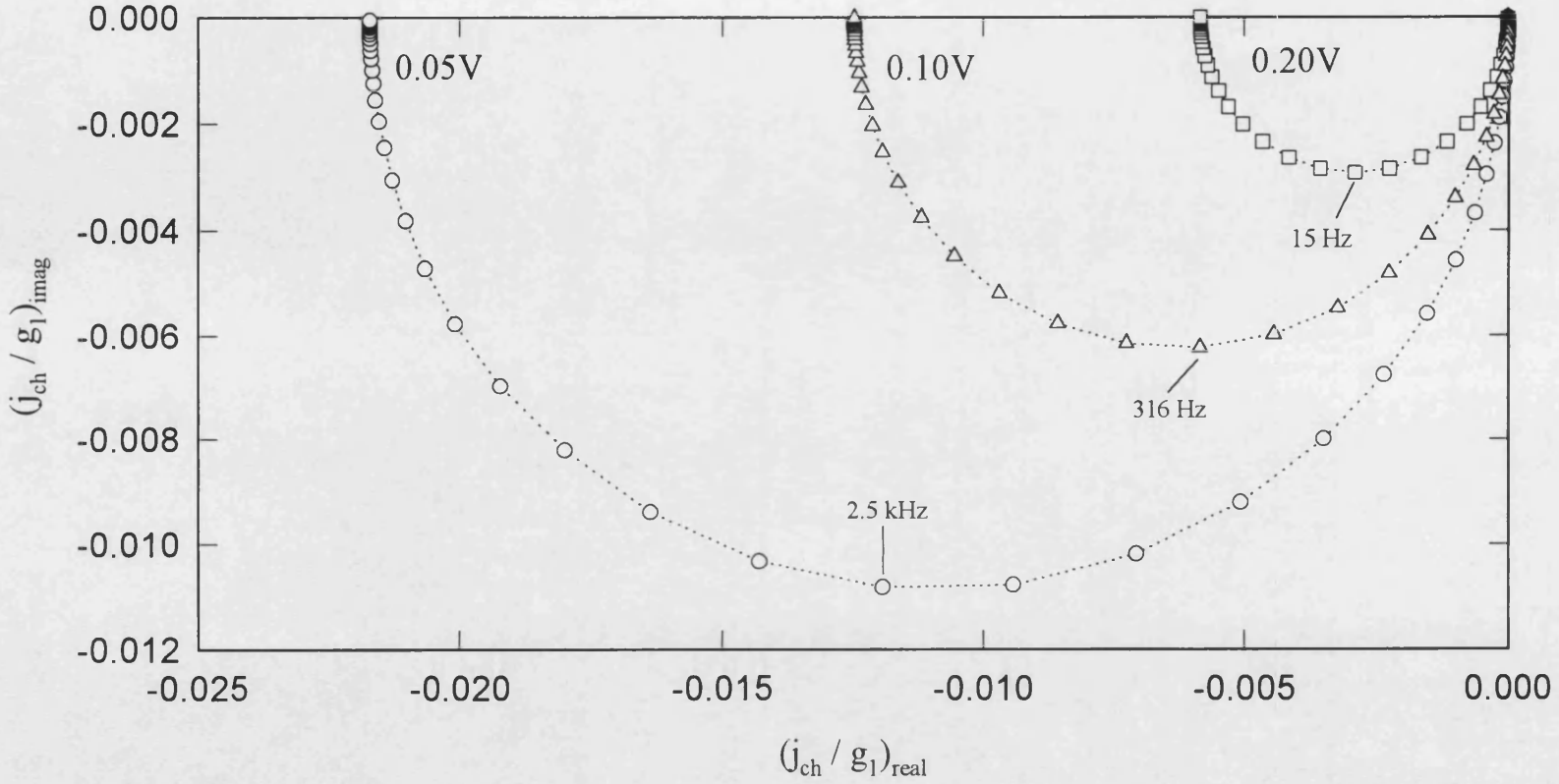

Fig. 2.17a. Complex representation of the ac component of the normalised charging current. Rate constants as in fig. 2.15a. Note that the frequency of the maximum increases as $\Delta\phi_{SC}$ decreases.

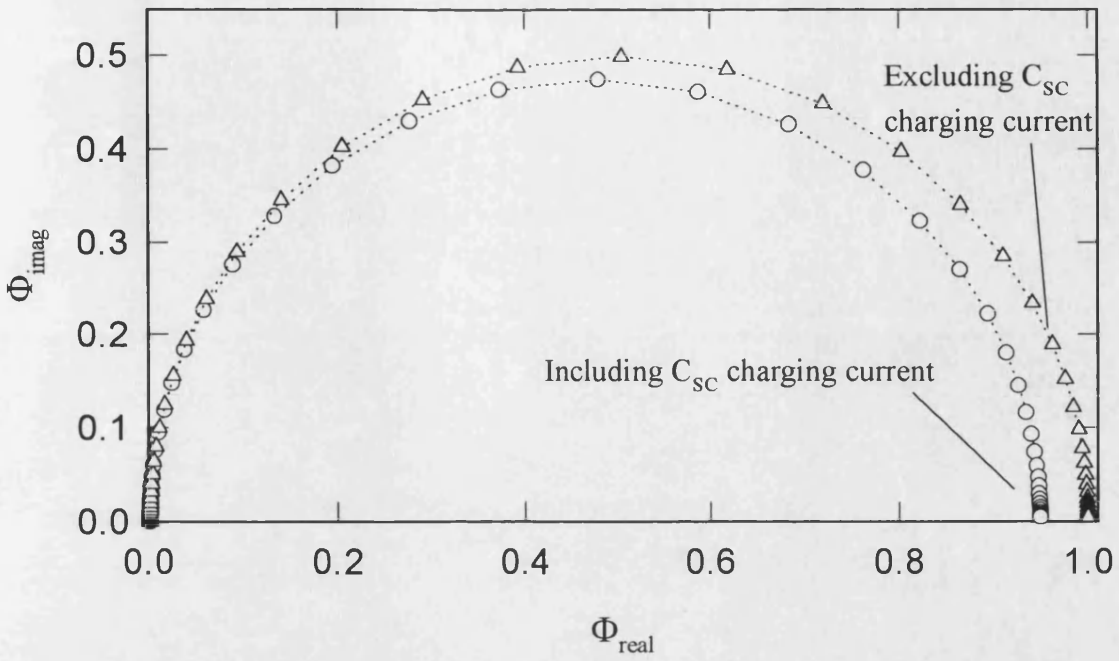

Fig. 2.17b. IMPS plots showing the effect of the C_{SC} charging current at $\Delta\phi_{SC} = 0.03$ V. Note that the high frequency limit is decreased by a factor of $C_{SC} / (C_{SC} + C_H)$.

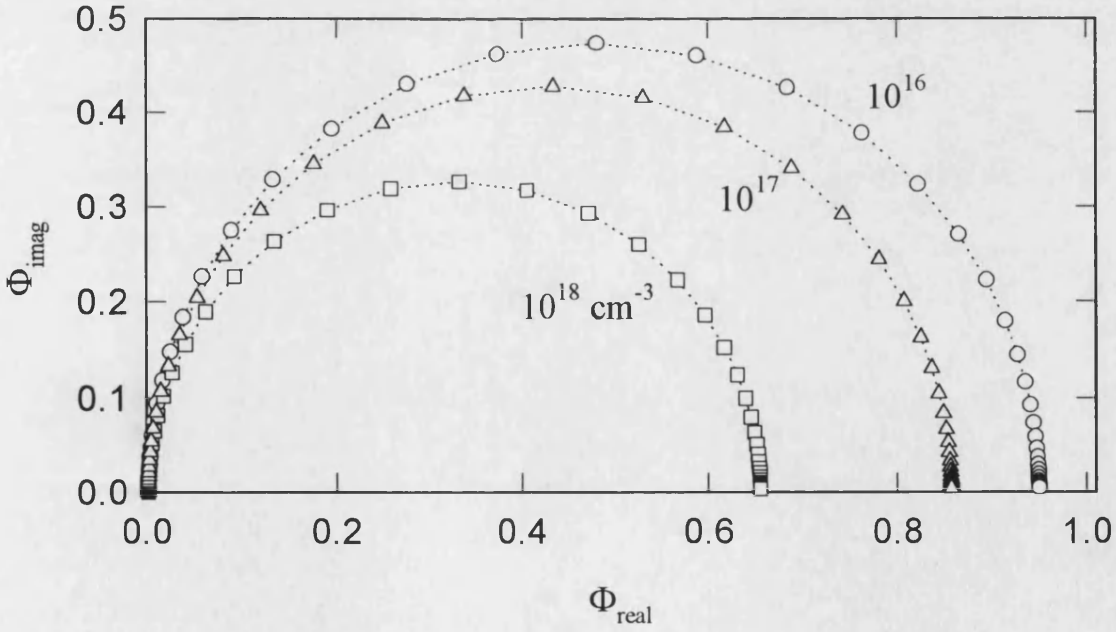

Fig. 2.17c. IMPS plots showing the effect of the C_{SC} charging current at $\Delta\phi_{SC} = 0.03$ V upon increasing doping density.

is shown that $\Delta\phi_{SC}$ is effectively a fraction of the parameter E - E_{FB}. This fraction, which corresponds to ΔV_H, depends on the steady state concentration of X^+. A dynamic photopotential is also associated with the periodic concentration of X^+. It is shown that k_{tr} and k_{rec} exhibits distinctive potential dependence upon considering the steady state and dynamic perturbations of the band bending. Analysis of the experimental steady state photocurrent and IMPS phenomenological parameters provides useful diagnostic criteria for kinetic study of processes at illuminated interfaces.

Finally, the effect of charging current, associated with the modulation of C_{SC} is evaluated. This charging current attenuates the high frequency IMPS response, leading to a limit lower than the unity.

Appendix 2.1

From eqs. (2.6) and (2.7), it follows that X_0 is a real root of:

$$X_0^3 + a_2 X_0^2 + a_1 X_0 + a_0 = 0 \tag{2.49}$$

where $a_2 = (2k_1k_4 + k_2k_3)/(2k_2k_4)$, $a_1 = (k_1k_3 + k_2g)/(2k_2k_4)$, $a_0 = - k_1g/2k_2k_4$. The solution is obtained by standard methods [16]. p_0 is obtained from eq. (2.6)

$$p_0 = \frac{g}{k_1 + k_2 X_0} \tag{2.50}$$

Appendix 2.2

The low frequency limit and the ω_{max}^{pert} can be obtain to a good approximation from eq. (2.38). Assuming that $k_2p_0 << k_1$, eq. (2.38) can be simplified to

$$j(\omega) = g_1 - g_1 \frac{\psi X_0 k_3}{k_1 + k_2 X_0 + i\omega} - k_3 X_1^{II}(1 + \psi X_0) \tag{2.51}$$

The contribution of the second term is very small in comparison to the third one, so that the frequency dependence of the photocurrent is determined by X_1^{pert}.

Consequently, the maximum of the photocurrent imaginary part will occur at the frequency where X_1^{pert} is minimum. This is consistent with the behaviour described by $\partial k_3/k_3$ as a function of the band bending (**fig. 2.14**).

In eq. (2.37), the term $i\omega$ can be neglected against k_1, obtaining

$$X_1^{pert} = \frac{g_1\left(k_1 - k_2 X_0 - \psi X_0 k_3\right)}{2k_1 k_2 p_0 + k_1 k_3\left(1+\psi X_0\right) + k_2 k_3 X_0\left(1+\psi X_0\right) + i\omega\left(k_1 + k_2 X_0 + k_3\left(1+\psi X_0\right)\right)} \tag{2.52}$$

The expression for ω_{max}^{pert} is derived directly from $(\partial X_1^{pert}/\partial\omega) = 0$. The low frequency limit is also obtained straightforward from eq. (2.51).

2.8 References

1 L.M. Peter, in Mario Schiavello (ed.), *Photocatalysis and Environment*, Kluwer Academic Publishers, London, 1988, 243.

2 J. Li and L.M. Peter, J. Electroanal. Chem., **193** (1985) 27.

3 R. Peat and L.M. Peter, J. Electroanal. Chem., **228** (1987) 351.

4 L.M. Peter, Chem. Rev., **90** (1990) 753.

5 D. Vanmaekelbergh, A.R. de Wit and F. Cardon, J. Appl. Phys., **73** (1993) 5049.

6 E.A. Ponomarev and L.M. Peter, J. Electroanal. Chem., **396** (1995) 219.

7 E.A. Ponomarev and L.M. Peter, J. Electroanal. Chem., **397** (1995) 45.

8 J. Schefold, J. Electroanal. Chem., **394** (1995) 35.

9 L.M. Peter, J. Li, R. Peat, H.J. Lewerenz and J. Stumper, Electrochim. Acta, **35** (1990) 1657.

10 J.J. Kelly and R. Memming, J. Electrochem. Soc., **129** (1982) 730.

11 A.R. de Wit, D. Vanmaekelbergh and J. Kelly, J. Electrochem. Soc., **139** (1992) 2508.

12 J. Schefold, J. Electroanal. Chem., **341** (1992) 837.

13 D. Meissner and R. Memming, Electrochim. Acta, **37** (1992) 799.

14 R.J. Madix, in D.A. King and D.P. Woodruff (eds.), *The Chemical Physics of Solids Surfaces and Heterogenous Catalysis*, Vol. 4, Elseiver Scientific Publishing Company, Amsterdan, 1982, ch.1.

15 P. Salvador, J. Phys. Chem., **89** (1985) 3863.

16 L. Poole and M. Borchers, *Some Common Basic Programs*, 3rd edition, Osborne/Mcgraw-Hill, Berkeley, 1977, p. 95.

CHAPTER 3

Etching and surface treatment of wurtzite n-CdS and rutile n-TiO_2 single crystal electrodes

Abstract

The effects of the surface treatment of the 0001 and $000\,\bar{1}$ crystal plane in wurtzite n-CdS, and highly hydrogen doped n-TiO_2 rutile single crystal were studied by steady state capacitance, photocurrent spectroscopy and photocurrent potential curves. A clear anisotropic behaviour of the Cd and S-face was observed upon etching in acid solutions. The Cd-face exhibits an optically flat surface, featuring well defined hexagonal pits after etching in a mixture of acetic and nitric acid. On the other hand, the S-face is covered by an amorphous sulfur film which strongly affects its photoelectrochemical properties. The sulfur film was removed in saturated Na_2S solutions. Consistent behaviour was observed for the two faces, although the flat band potential of the S-face appears to be displaced to more negative potentials. In the case of the n-TiO_2 electrodes, stable properties were observed for a crystal reduced in hydrogen at high temperature and etched subsequently in hot sulfuric acid. The crystal becomes considerably unstable in the presence of dilute sulfuric acid under illumination.

3.1. Introduction

The photoelectrochemical properties of semiconductors can be dramatically affected by their surface structure. Gerischer recognised that crystal surface orientation and structural imperfections, like grain boundaries or dislocations, can modify the energy barriers associated with interfacial processes, especially those which involve phase formation or dissolution [1]. The effect of crystal defects on the photocorrosion of semiconductors has also been analysed by Morrison, who evaluated the possibility of charge trapping and recombination events on these sites [2]. The strong accumulation of charge on these surface sites can also introduce perturbations in the potential drop of the Helmholtz layer, leading to Fermi level-pinning effects [3] (see also chapter 2). Some of these phenomena are discussed in this chapter.

In **Fig. 3.1**, the model of the unit cell for a wurzite crystal is shown, indicating the 0001 (cation rich) face and the $000\bar{1}$ (anion rich) face which are perpendicular to the c-axis. The structure of these faces has been extensively studied for CdS, ZnO, ZnS and CdSe [4,5]. Although very well defined structures can be obtained for single crystal of II-VI materials, *reconstruction forces* generate geometrical structures much more complicated than the ideal surface termination presented in **fig. 3.1**. The reconstruction of surfaces minimises the surface energy resulting from crystal cleavage. These processes are extremely complex and difficult to model [6]. Different reconstruction habits have been found for the two faces indicated in **fig. 3.1** in the absence of adsorbates [5]. For instance, the 0001 face seems always to reconstruct, but the $000\bar{1}$ shows higher stability depending on the pre-treatment [5]. Although reconstruction effects could be very different in the case of the SEI, it is expected nevertheless that some electrochemical properties will be different for the two crystal planes.

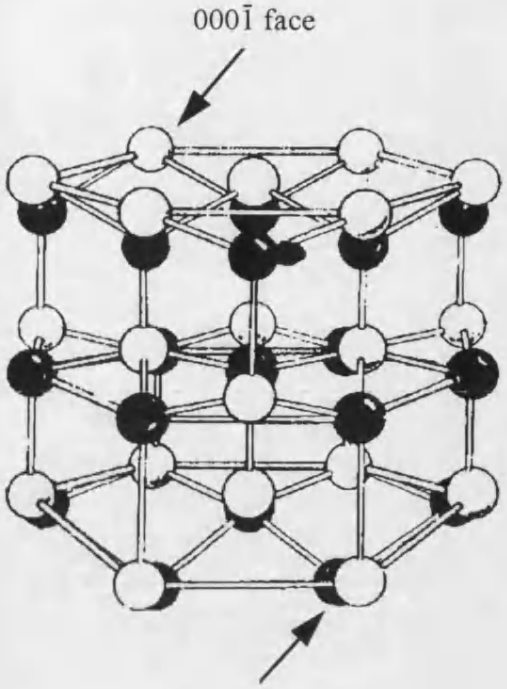

Fig. 3.1. Model of the II-VI wurtzite structure. The anion is represented by (●) and the cation by (○). The polar faces perpendicular to the c-axis are indicated. After ref. 7

Distinctive microscopic features have been reported for the two crystal faces perpendicular to the c-axis of wurtzite II-VI semiconductors [7]. **Fig. 3.2** shows the Zn-rich and the O-rich faces of a photo-electrochemically etched ZnO single crystal electrode [8]. The Zn-face (0001) exhibits well defined hexagonal pits and a rather "smooth" surface. On the contrary, the O-face (000 $\bar{1}$) appears more irregular with no definition of the crystal structure. Similar behaviour have been reported for n-CdS single crystal upon chemical etching. In the present chapter, the chemical etching of the two polar faces of n-CdS is related to their photo-electrochemical properties. The behaviour of mechanically damaged surfaces is also analysed in order to evaluate the effect of surface imperfection in the potential distribution and charge transfer processes at the illuminated SEI. Finally, the surface preparation of rutile n-TiO_2 single crystal electrodes is described and the behaviour in various electrolytes is briefly presented.

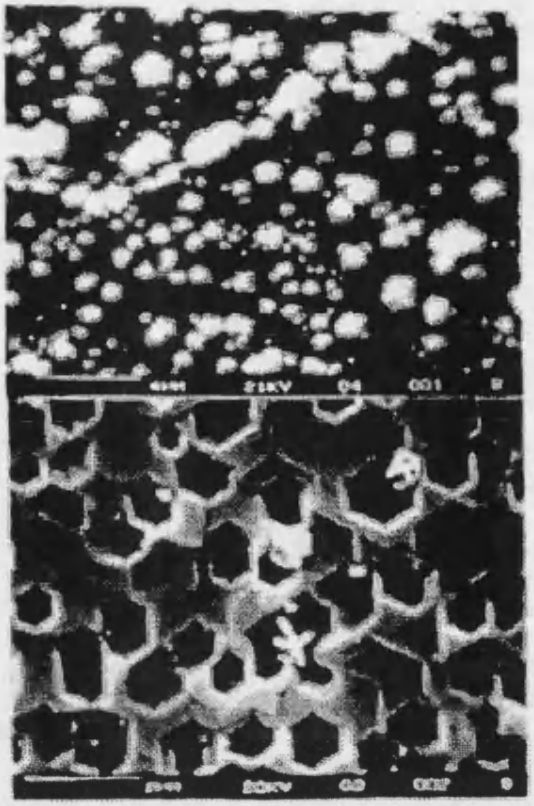

Fig. 3.2. SEM micrographs of the $000\bar{1}$ (O-face) and the 0001 (Zn-face) of a photo-electrochemically etched ZnO single crystal. After ref. 8.

3.2. Experimental

Solutions and cleaning procedure reported in this thesis are based on AnalaR grade reagents and purified water obtained from a Milli RO 6 plus - Milli Q 185 system (Millipore). The n-CdS single crystals (Eagle Picher Research Laboratory) were cut perpendicular to the c-axis exposing the Cd and S rich faces. The crystal were cleaned with 2-propanol in a Soxhlet for 24 hours, and subsequently rinsed with water. Both surfaces were polished to a mirror finish using alumina down to 0.3 μm size. A slight etching in dilute HCl was used in order to identify each of the faces under an optical microscope. The electrical contact was prepared by scratching Ga:In eutectic and attaching a platinum wire using electrically conducting epoxy to the opposite side of the face to be exposed to the electrolyte. The resistance of this back ohmic contact was in the order of 200 Ω according to impedance measurements in aqueous electrolyte.

The electrodes were mounted in 'Kel-F' rods and sealed with epoxy resin. The geometrical surface area was 0.28 cm^2. The subsequent treatment is discussed in the next sections.

Due to the severe etching treatment, the n-TiO_2 crystal surface were prepared before the electrode was assembled. The crystals (provided by Pikem) were cleaned following the same procedure mentioned previously, and reduced in a hydrogen atmosphere at 620°C for 90 min. They were subsequently etched in concentrated sulfuric at 240°C for three hours in accordance to published procedures [9]. The ohmic contact was also prepared with Ga:In eutectic, a platinum wire and conducting epoxy. The uncompensated resistance, mainly arising from the back ohmic contact, was estimated in 125 Ω from IR compensation measurements. The electrodes were mounted in 'Kel-F' rods and sealed with epoxy resin. The geometrical surface area exposed was 0.26 cm^2.

A three compartment photoelectrochemical cell provided with quartz windows was employed in all the measurements. The reference electrode was a standard Ag/AgCl electrode, to which all potentials are referred. A platinum disc was used as a secondary electrode. All solutions were purged with Ar inside the cell prior to all experiments.

The capacitance of the space charge region was derived from the quadrature (90° out of phase) component of the current with respect to a modulated potential input [2]. If the capacitance of the space charge region is considerably smaller than the Helmholtz capacitance, the imaginary component of the admittance is linearly proportional to C_{SC}. Consequently, for a given frequency and amplitude of modulation, the output of the cell can be calibrated using a decade capacitance box. The amplitude of modulation was ca. 5-10 mV. The experiment was performed using a home-built potentiostat connected to a 5210 EG&G PAR lock in amplifier.

The 'steady state' photocurrent was measured using low frequency (13-27 Hz) mechanical chopping and in-phase lock in detection. For the wavelength and potential dependence measurements, two illumination sources were employed: (i) Xe arc lamp set up with a f/3.4 monochromator from Applied Photophysics and (ii) a Liconix 4107 NB HeCd laser (λ = 442 and 325 nm).

3.3 Mechanically damaged CdS surfaces

The behaviour of mechanically polished electrodes is considered as a starting point in the comparison of various etching procedures. **Fig. 3.3** shows the capacitance voltage curve of the S and Cd face electrode in aqueous Na_2SO_4 pH 4.5 in the dark. The capacitance of the S-face exhibits considerable hysteresis in the forward and backward potential cycles. It is also seen in **fig. 3.3a** that the capacitance is only weakly dependent on the potential, becoming weaker as the frequency is increased. This effect is even more dramatic for the Cd-face electrode (cf. **fig. 3.3b**), where an almost flat response of the capacitance was recorded over more than 1 V.

The behaviour on both polished electrodes is far different from the expected capacitance voltage relationship described by eq. (1.5) (see also **fig. 1.3**). The weak potential dependence of the capacitance can be interpreted in terms of Fermi-level pinning associated with surface crystal dislocations. Defects at the surface can act as electron traps, and the net effect of the potential is to change the population of those traps. In this sense, the electrode behaves like a metal, keeping the bands relatively unpinned. The hysteresis in the signal during the potential cycles might be connected to slow charge trapping defects, i.e. changes in the potential drop across the interfaces relax more slowly than the scan rate. Gerischer et al. have determined that the extent of these defects is approximately of the same order of magnitude as the polishing grain size [10], therefore their description as "surface" defects is not completely accurate.

Fig. 3.4 displays the photocurrent spectra of polished surfaces in aqueous sulfate electrolyte. The reaction associated with the measured photocurrent is crystal dissolution, which is discussed in detailed in the next chapter. The low conversion efficiency and the intensity of the sub-band gap transitions are rather striking features for a single crystal electrode (the band gap for CdS is 515 nm), and resemble the response of anodically deposited CdS thin films [11]. The low conversion efficiency suggest that the defects behave as recombination centres which effectively consume the photogenerated holes at the surface. The sub-band gap peak observed at 540 nm is an interesting feature which indicates the presence of an energy level which contributes to the photocurrent process.

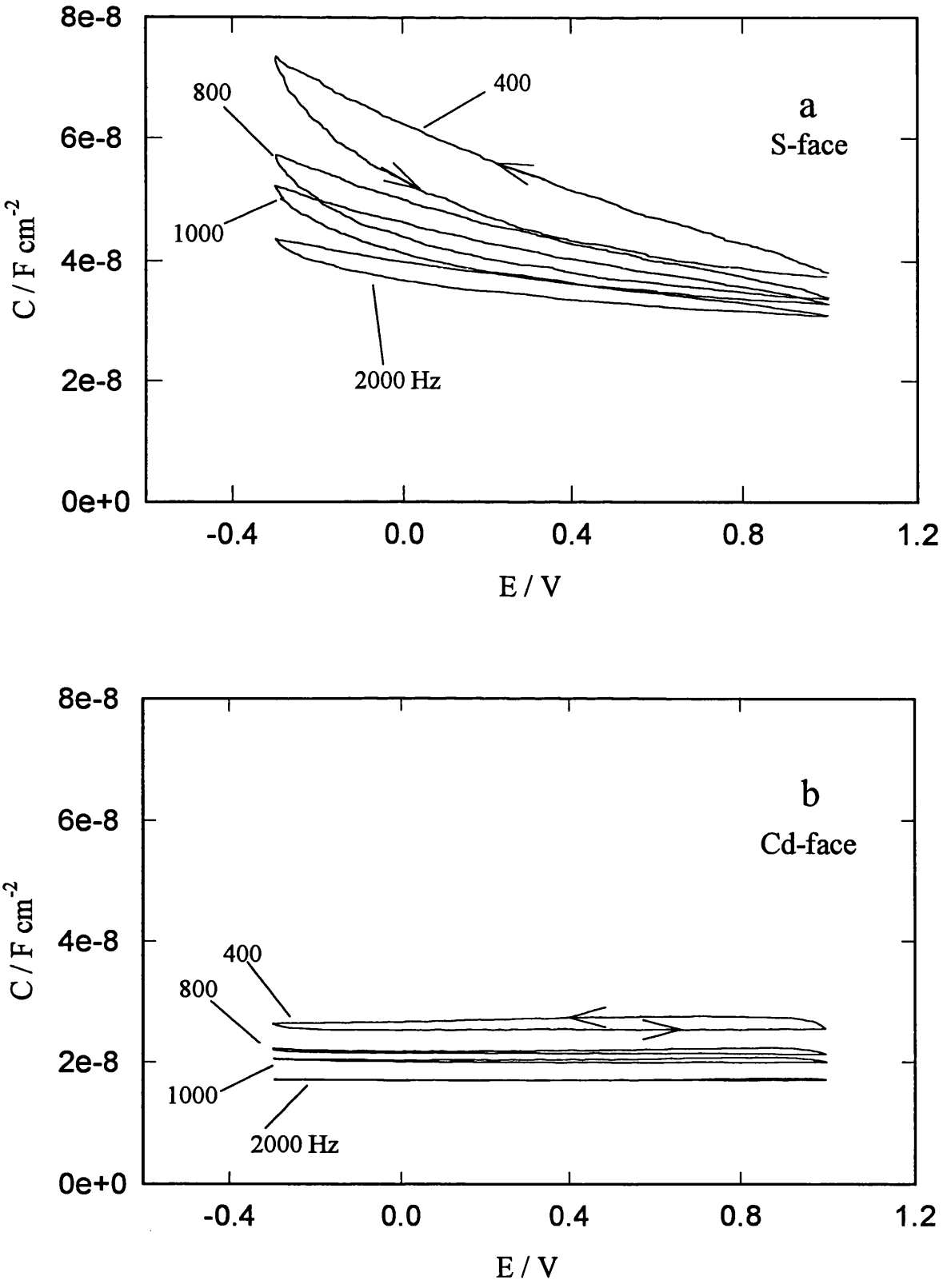

Fig. 3.3. Capacitance voltage curves of mechanically polished S-face (a) and Cd-face (b) electrodes in 0.1 mol dm^{-3} Na_2SO_4 pH 4.5 in the dark. Note that the capacitance is higher on the negative cycle than on the positive one. Scan rate 10 mV s^{-1}.

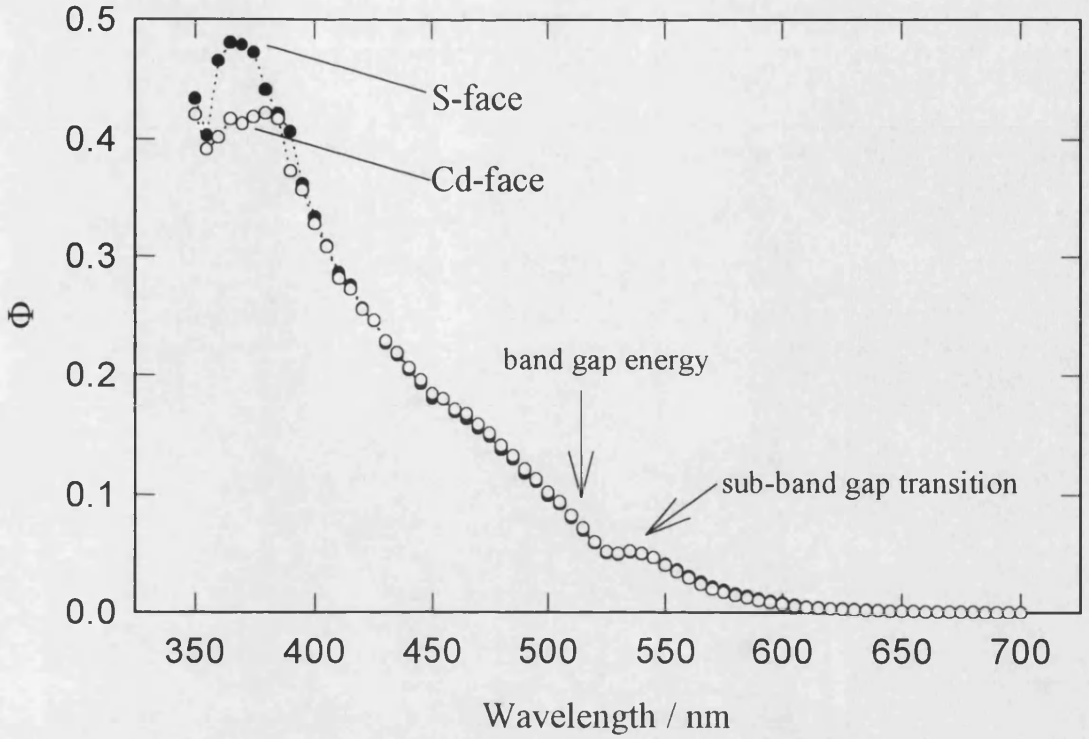

Fig. 3.4. Photocurrent spectra of the mechanically polished S and Cd-face electrodes in 0.1 mol dm^{-3} Na_2SO_4 pH 4.5 at 1 V. Note that the sub-band gap feature is common for both faces.

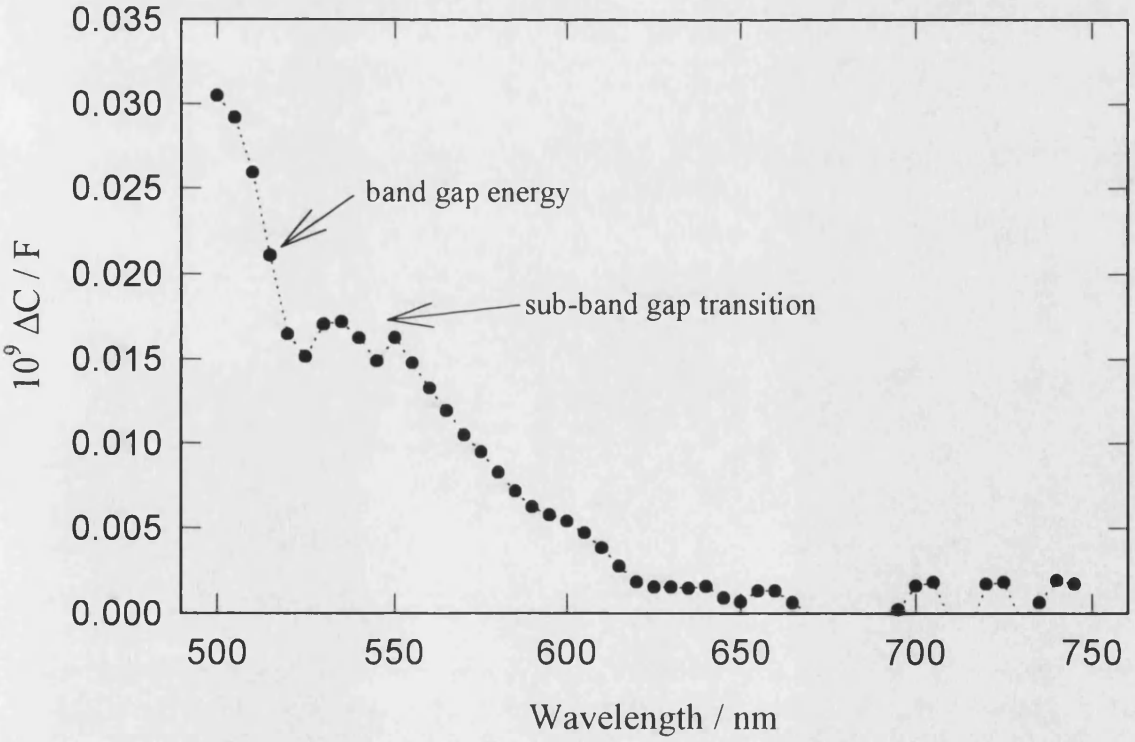

Fig. 3.5. Photocapacitance spectrum of the mechanically polished Cd-face electrode in 0.1 mol dm^{-3} Na_2SO_4 pH 4.5 at 1.0 V. Notice the sub-band gap peak at the same wavelength as the photocurrent transition (see fig. 3.4).

The nature of the sub-band gap transition can be studied by steady state photocapacitance spectroscopy [12,13]. **Fig. 3.5** shows a photocapacitance spectrum of the Cd-face electrode, where it is seen that the change in capacitance ΔC (i.e. $C_{SC(illumination)} - C_{SC(dark)}$) is positive. This result indicates that the sub-band gap excitation occurs from an occupied energy level in the band gap to the valence band. The same transition has been reported by Nakabayashi and Kira [14] for CdS crystals in Na_2SO_3, indicating that the surface treatment of their electrodes left substantial surface damage. In the next section, it is shown that these feature tend to disappear for "well etched" surfaces.

Fig. 3.6 shows a photocurrent-potential curve of a non-etched Cd-face electrode at 390 nm. The potential dependence of the photocurrent provides further evidence for the Fermi-level pinning effect observed in capacitance measurements.

3.4 Etching of CdS single crystal surfaces

The most common procedure for exposing well-defined II-VI semiconductor surfaces is chemical etching in acid solutions [4]. Hydrochloric acid, in a wide range of concentration and etching times, has been used for the elimination of surface defects induced by mechanical polishing in CdS and ZnO single crystals. This section describes the study of the surface properties of CdS, after *chemo-mechanical* and chemical etching in acid solutions, by photocurrent spectroscopy and capacitance potential curves.

Sullivan and Bracht mechanically polished CdS single crystal surfaces using a solution of 30 % HCl as a "lubricant" [15]. This method is referred to as chemo-mechanical polishing, and the main objective is to produce an optically smooth surface (especially the S-face) with a low density of defects by simultaneous etching. **Fig. 3.7** shows the capacitance-voltage curve for the Cd-face electrode after chemo-mechanical polishing using the same solution on a Nylon cloth (LECO). A decrease in the capacitance is observed with respect to the mechanical polished electrodes, however the hysteresis developed upon cycling indicates that considerable charge is still stored in surface defects. Different acid concentration and alternative procedures for chemical and chemo-mechanical polishing did not enhance the performance of the interface as far as the potential behaviour of the C_{SC} was concerned. A similar trend was observed

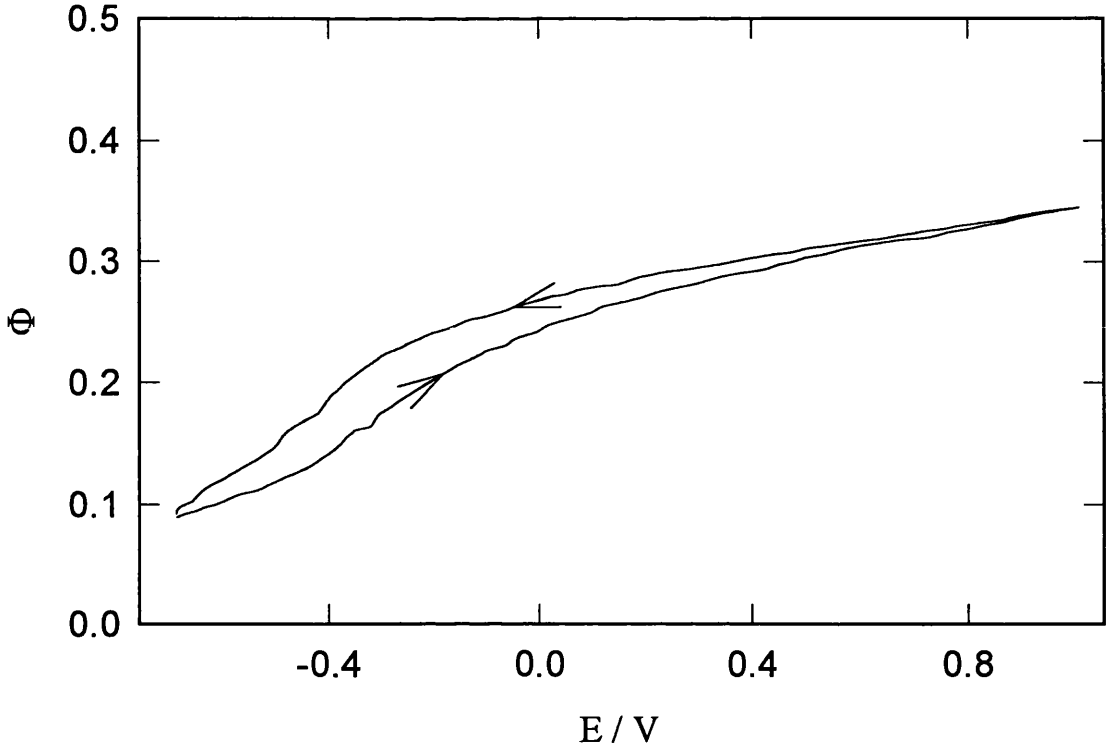

Fig. 3.6. Photocurrent-voltage curve of the mechanically polished Cd-face electrode in 0.1 mol dm^{-3} Na_2SO_4 pH 4.5 at 390 nm.

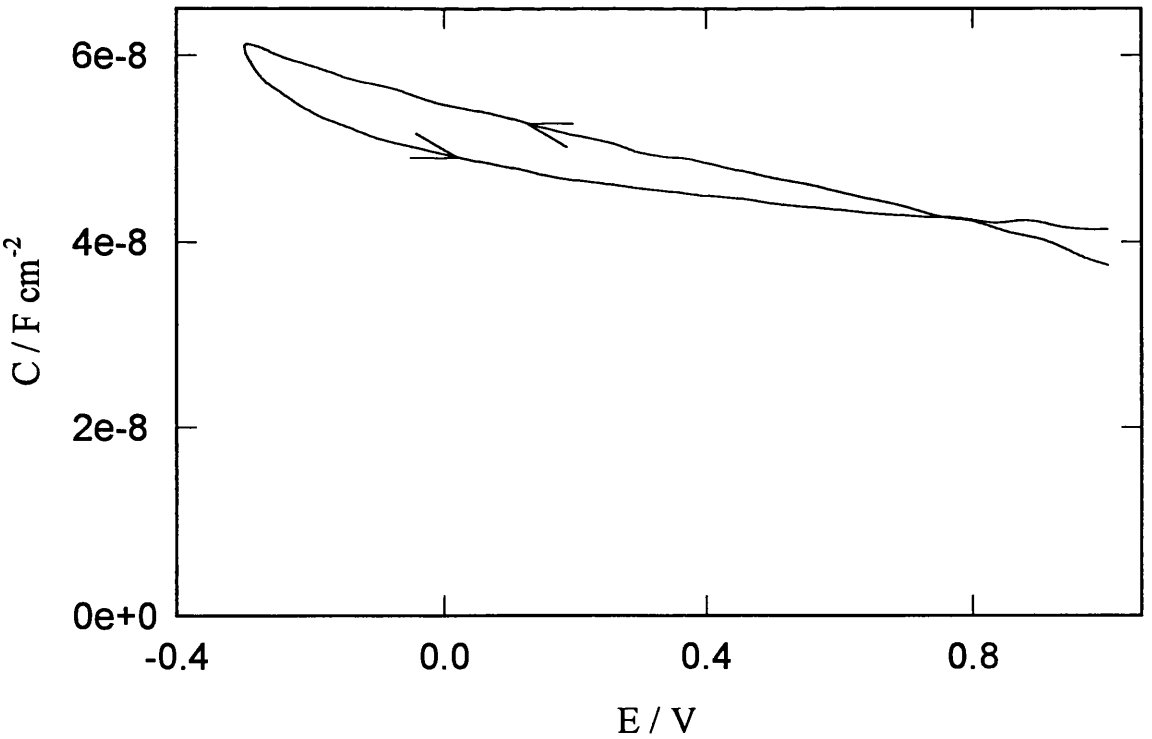

Fig. 3.7. Capacitance-voltage curve of a 5 min. chemo-mechanically polished Cd-face electrode at 400 Hz in 0.1 mol dm^{-3} Na_2SO_4 pH 4.5 in the dark.

for the Cd-face electrode. This result indicates that charge accumulation, and consequently the band bending, is very sensitive to surface dislocations.

An effective removal of mechanical defects was achieved by chemical etching in concentrated acid solutions. Warekois et al. [7] reported optically distinctive properties for Cd and S-faces after etching in a mixture 6:6:1 of acetic acid, nitric acid and water respectively. Both faces were etched for 1 min. with this mixture, and microscopic observations showed very similar features to those shown in **fig. 3.2**. The capacitance-voltage relationship for the S-face electrode changed dramatically after this treatment as shown in **fig. 3.8a**. Hysteresis disappeared at all frequencies, and the potential dependence of C_{SC} resembles the unpinned Fermi-level condition (cf. **fig. 1.3**). **Fig. 3.8b** shows the Mott-Schottky representation of the capacitance of the S-face electrode, featuring a rather negative flat band potential of (-1.15 ± 0.05) V in comparison to previous reports [16-18]. **Fig. 3.9a** displays the capacitance potential curve of the Cd-face electrode after identical treatment. A sharper dependence on potential is observed in comparison with the S-face (**fig. 3.8a**), and the capacitance is virtually independent of the frequency. The flat band potential calculated for the Cd-face from the Mott-Schottky plot in **fig 3.9b**, (0.73 ± 0.03) V, is in close agreement with reported data [16-18]. A smaller doping density is estimated for the S-face, (7.0 ± 0.3) 10^{15} cm^{-3}, in comparison to the Cd-face, (1.17 ± 0.02) 10^{16} cm^{-3}. These results point to differences in the surface structure of these faces as-etched.

Photocurrent spectra of both faces as-etched suggest that the difference in the capacitance is connected to a sulfur layer generated on the S-face electrode. This is clearly illustrated in **fig. 3.10**, where a considerable quenching of the photocurrent is observed for the S-face electrode, specially in the region of 350 - 450 nm. On the contrary, the Cd-face electrode exhibited quantum efficiencies close to unity after correction for reflection losses (estimated in about 10 %). The sulfur layer becomes visible to the naked eye if the S-face electrode is extensively etched for several minutes. Remarkably, even a similar treatment of the Cd-face electrode, no evidence of a sulfur layer is observed.

As a comparison, anisotropic etching behaviour is also noticed for the Zn and O-faces in ZnO single crystal electrodes. Well defined photocurrent and capacitance behaviour are recorded for the O-face electrode etched in aqueous solution of HCl 4:1

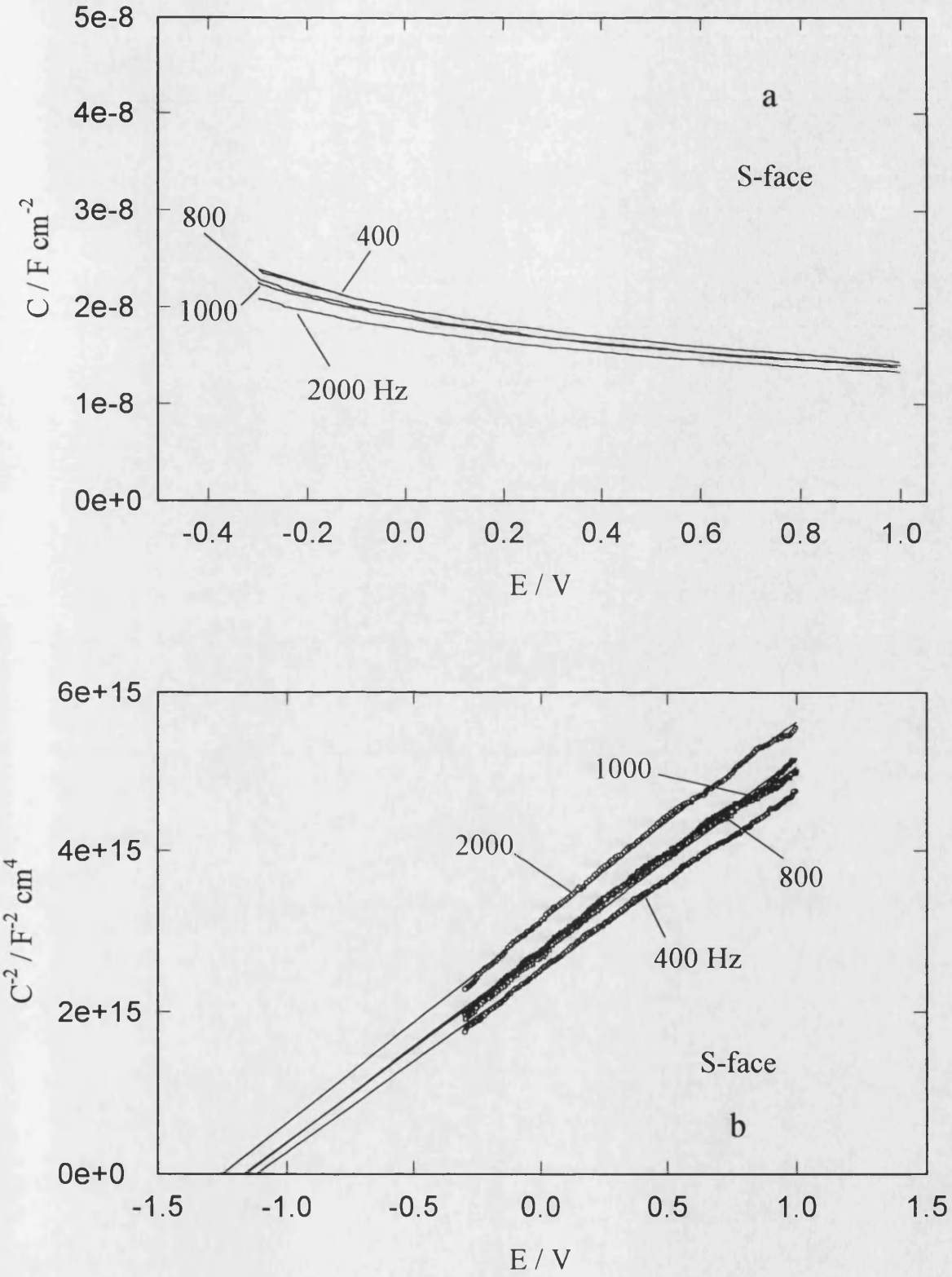

Fig. 3.8. Capacitance voltage curves (a) and Mott Schottky plots (b) of the S-face electrode after 1 min. chemical etching in 6:6:1 acetic acid, nitric acid and water. Note the disapperance of hysteresis upon consecutive cycles.

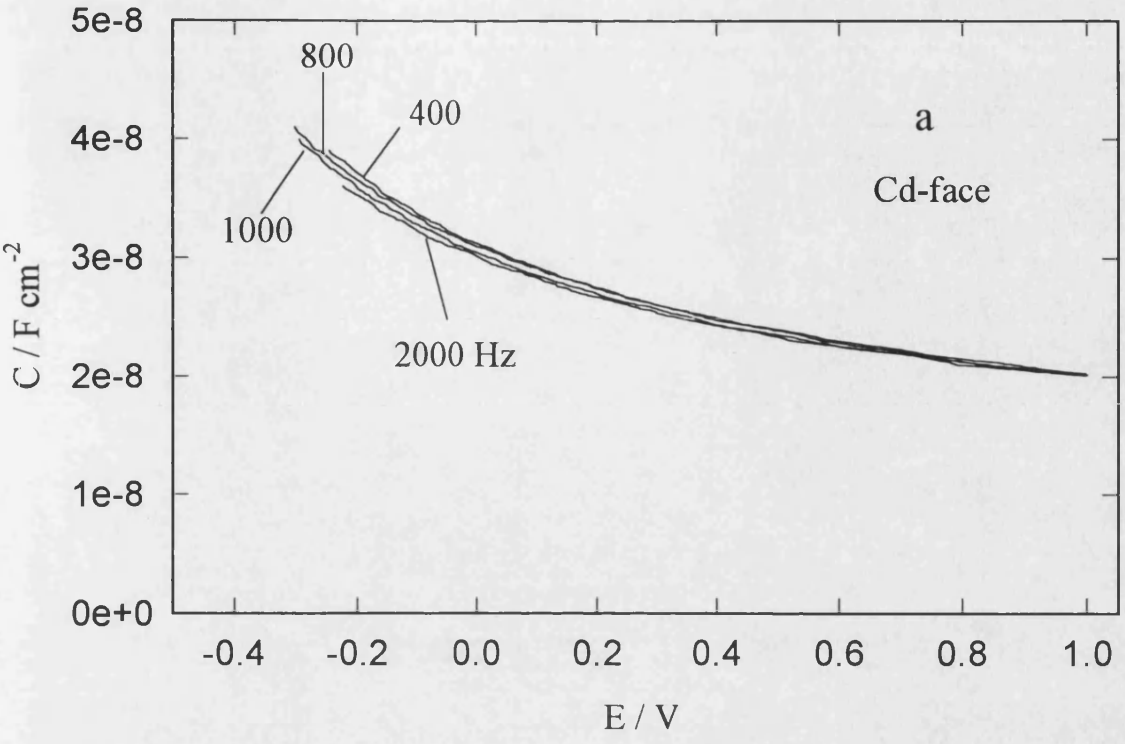

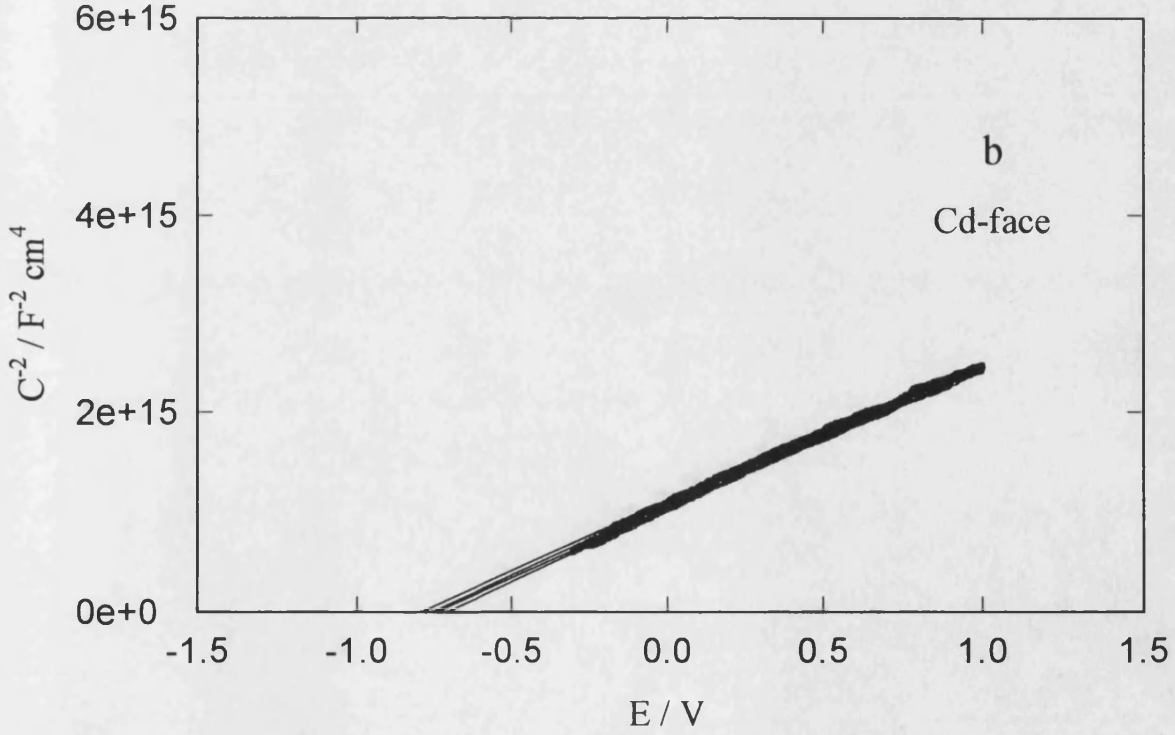

Fig. 3.9. Capacitance voltage curves (a) and Mott Schottky plots (b) of the Cd-face electrode after 1 min. chemical etching in 6:6:1 acetic acid, nitric acid and water. Note that the capacitance is almost independent of the frequency.

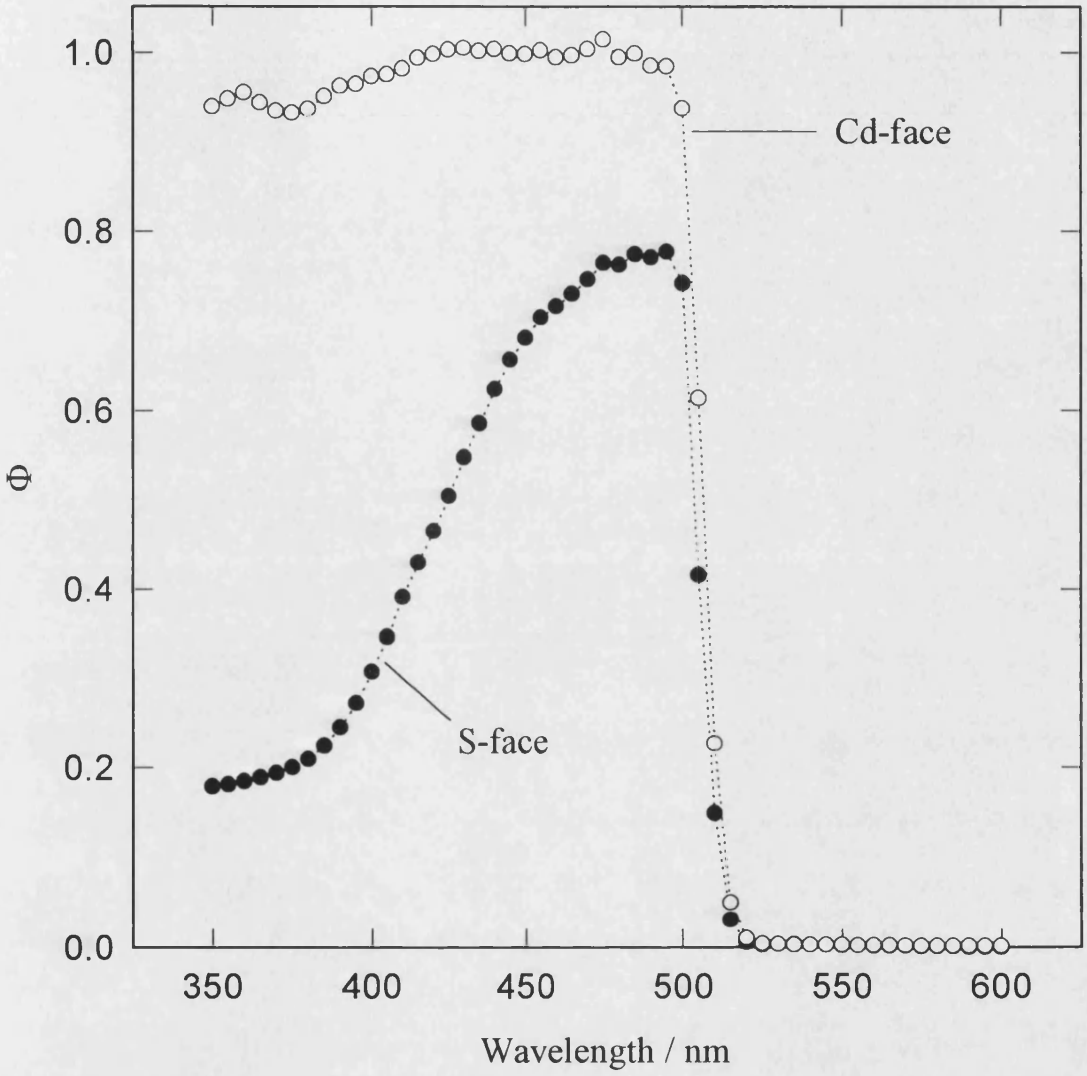

Fig. 3.10. Photocurrent spectra of the Cd and S-face electrodes as etched in 6:6:1 acetic acid, nitric acid and water for 1 min. The spectra were recorded at 1 V.

during 5 s. The surface looks optically rough and amorphous (see **fig. 3.2**). By contrast, Zn-face electrodes still exhibit a large density of surface defects after the same treatment. Only after photo-anodic dissolution in KCl, removing 1 to 2 μm from the crystal, does the Zn-face feature well defined hexagonal pits and reproducible photocurrent and capacitance behaviour.

The sulfur layer deposited on the as-etched S-face electrode was removed by immersion in a saturated alkaline solution of Na_2S for 5 min. The electrode was rinsed extensively with water, then with diluted HCl (5%), and finally with water just before being reintroduced into the cell. **Fig. 3.11** shows the photocurrent spectrum of the S-face electrode after being treated with Na_2S, featuring conversion efficiencies close to one at wavelengths above the band gap. Although the photocurrent response was greatly improved after this treatment, microscopic observation of the electrode still revealed an amorphous surface similar to that observed in **fig. 3.2**. It is also important to note that the sub-band gap response observed for polished electrodes (cf. **fig. 3.4**) is negligible with respect to the supra band gap features recorded in etched Cd-face (cf. **Fig. 3.10**) and S-face (**Fig 3.11**) electrodes spectra.

Capacitance voltage curves and Mott Schottky analysis of the treated S-face electrodes are illustrated in **fig. 3.12**. Although some frequency dependence of the capacitance-voltage response is observed, the doping density of the crystal, (1.0 ± 0.1) 10^{16} cm^{-3}, coincides with the value obtained for the Cd-face electrode. The flat band potential is still somewhat more negative in the S-face electrode, (-0.87 ± 0.02) V. It is difficult to provide a semi-quantitative explanation which accounts for the experimental difference in E_{FB} between both faces, in spite of evidence in the literature which suggests that their structures are not identical.

Surface termination can play an important role in the polarity of the surface. **Fig. 3.13** contrasts Mott-Schottky plots of the Cd and S-faces in 0.1 mol dm^{-3} Na_2S, featuring a large displacement of E_{FB} to more negative potentials. This displacement is interpreted by Wilson [19] in terms of an increase of the surface charge density associated with the adsorption of sulfide anions. Apart from the sulfide adsorption effect, the S-face electrode still showed a more negative potential than the Cd-face. This difference was in the order of 150 mV, which is similar to that observed in

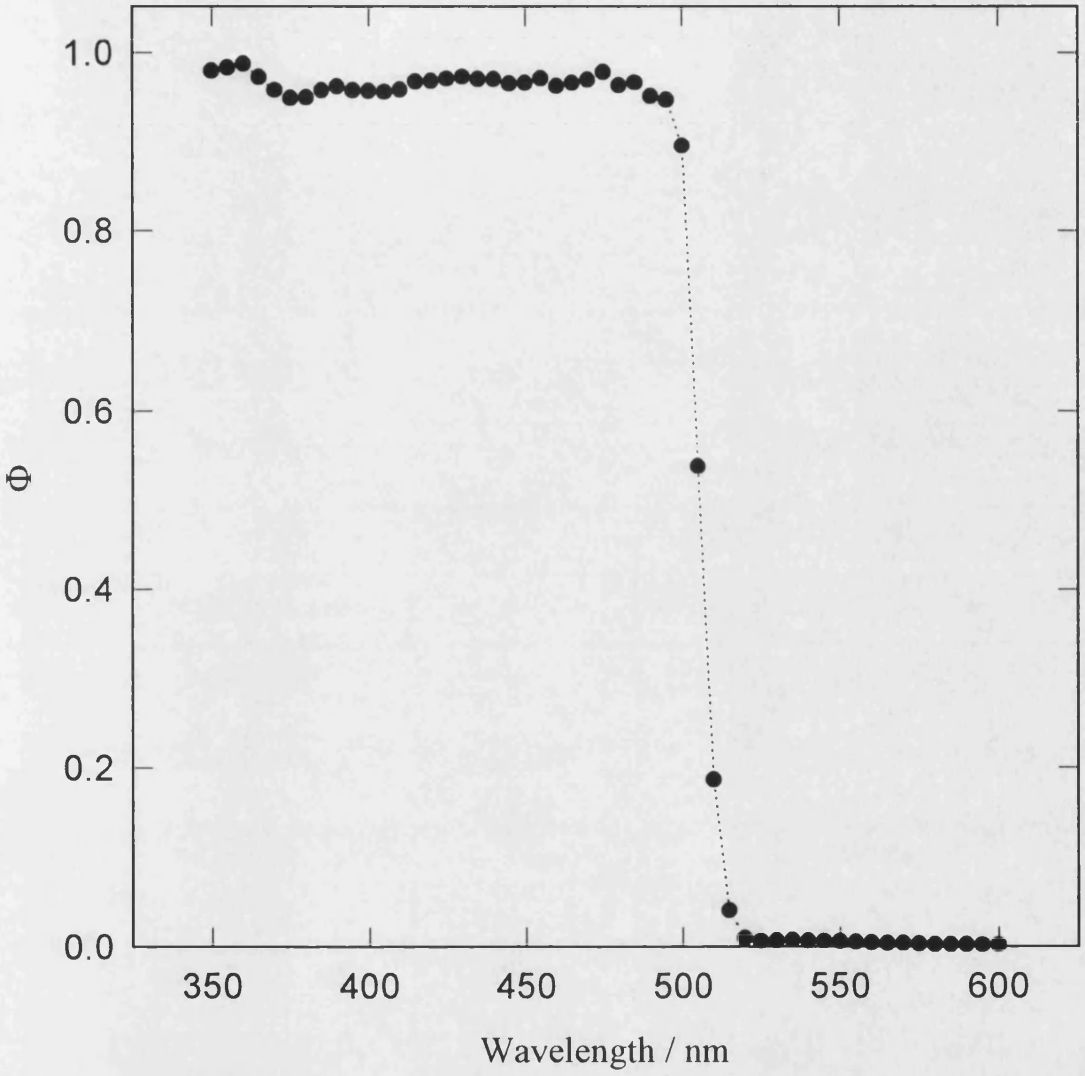

Fig. 3.11. Photocurrent spectrum of the S-face electrode after etching in 6:6:1 acetic acid, nitric acid and water for 1 min and treating with Na_2S.

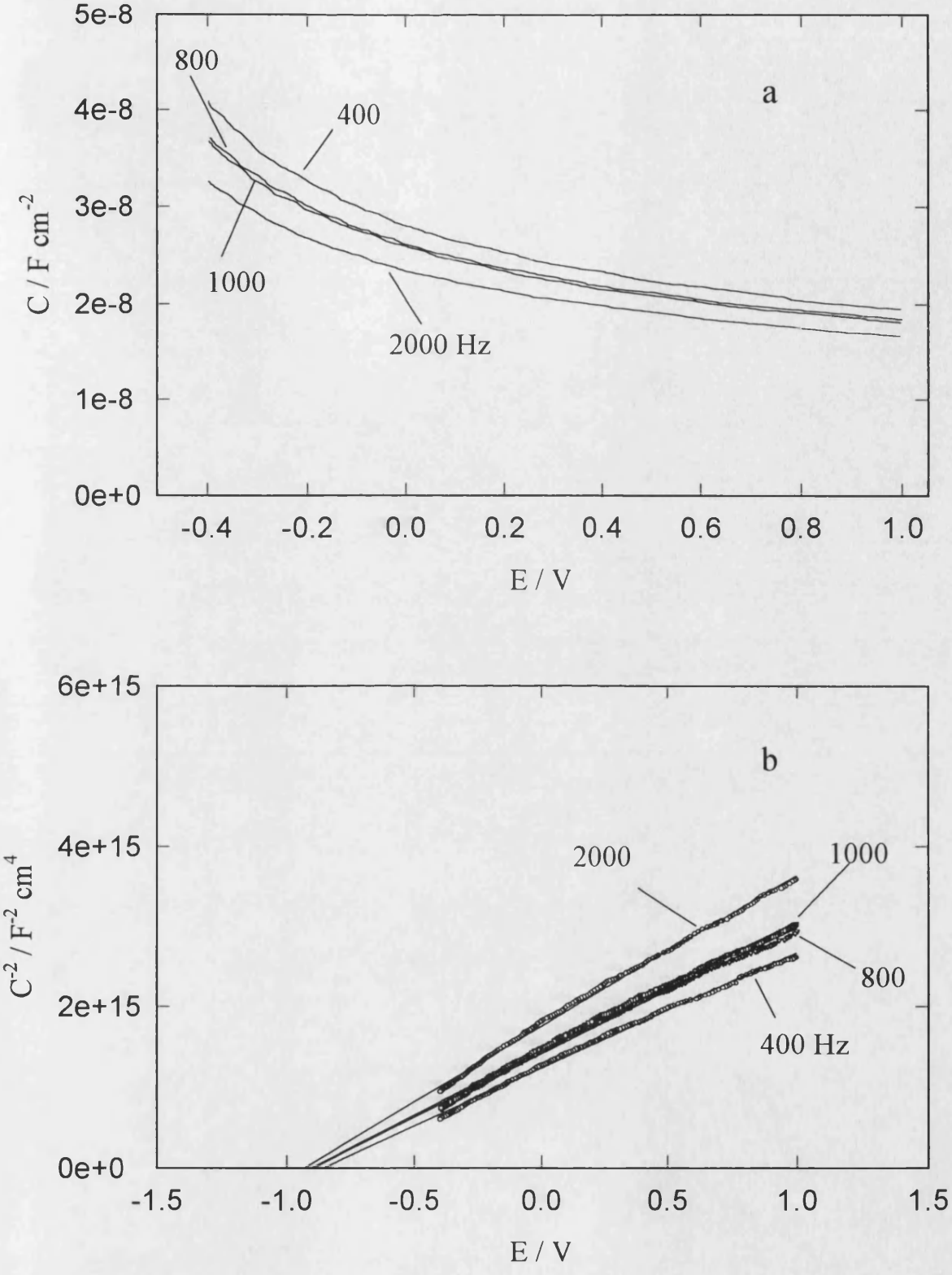

Fig. 3.12. Capacitance voltage curves (a) and Mott Schottky plots (b) of the S-face electrode after 1 min. chemical etching in 6:6:1 acetic acid, nitric acid and water and treated with Na_2S.

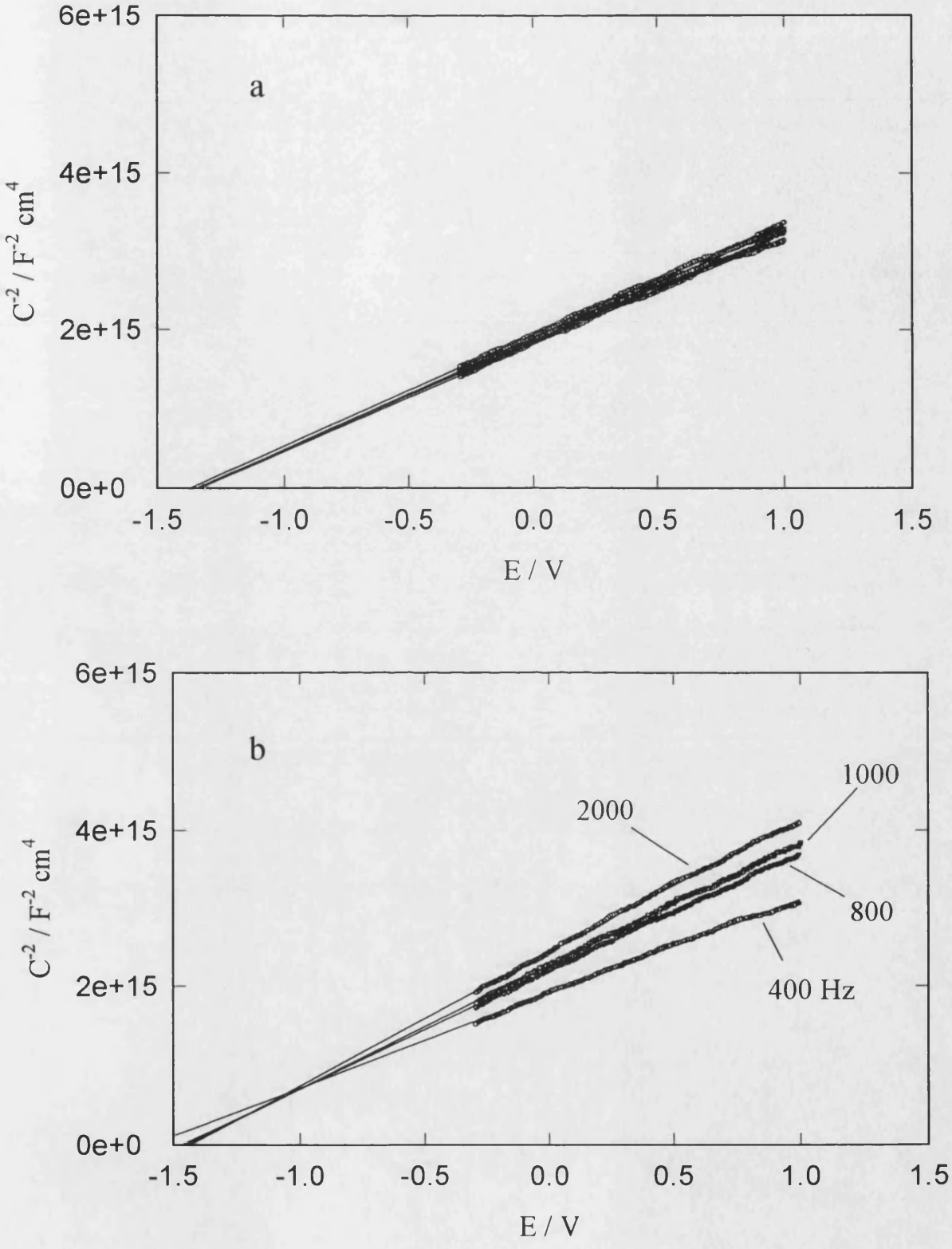

Fig. 3.13. Mott Schottky plots of the Cd (a) and S-face electrodes (b) in 0.1 mol dm^{-3} Na_2S. Note that the E_{FB} is 150 mV displaced to more negative potentials in the S-face electrode respect to the Cd-face.

Na_2SO_4. This suggests that there is a difference in the E_{FB} between the Cd and S-face which is determined by their surface structure.

The results presented in this section denote a marked anisotropic behaviour in the etching of the 0001 and $000\bar{1}$ crystal planes in wurtzite CdS. The most striking difference is connected to the generation of an amorphous sulfur layer in the S-face electrode after etching in acid solutions. This layer is not observed on the Cd-face under the analysis performed. The sulfur deposit can be removed by immersion in a saturated sodium sulfide solution without introducing substantial modification of the surface.

3.5 Brief comments on the photoresponse of rutile n-TiO_2 single crystal electrodes.

The stability of TiO_2 is one of the reasons behind the extensive studies of this material as photo-anode [2,20,21]. The photo-evolution of oxygen, firstly reported by Honda and Fujishima [20], is still a reaction of interest in the area of energy conversion. This reaction is discussed in chapter 6. In this section, the photo-stability of the rutile TiO_2 single crystal, treated by the procedure described in section 3.2, is assessed from photocurrent potential curves.

A typical Mott-Schottky plot of the n-TiO_2 electrode is displayed in **fig. 3.14**. The doping density was estimated to be $(2 \pm 1)\ 10^{19}$ cm^{-3} from studies in various electrolytes. Strong frequency dispersion of the capacitance was observed for all electrolytes, and deviations from the Mott-Schottky behaviour occur at frequencies higher than 1 kHz. The reasons for the complicated capacitance responses are discussed in chapter 6. The high density of donors is associated with oxygen vacancies formed during the reduction by hydrogen.

The high space charge capacitances can affect the determination of the flat band potential using eq. (1.5). When C_{SC} is no longer negligible respect to C_H, eq. (1.5) has the form:

$$C_{SC}^{-2} = C_H^{-2} + \frac{2}{qN_{SC}\kappa\varepsilon_0 S^2}\left(E - E_{FB} - \frac{kT}{q}\right) \qquad (3.1)$$

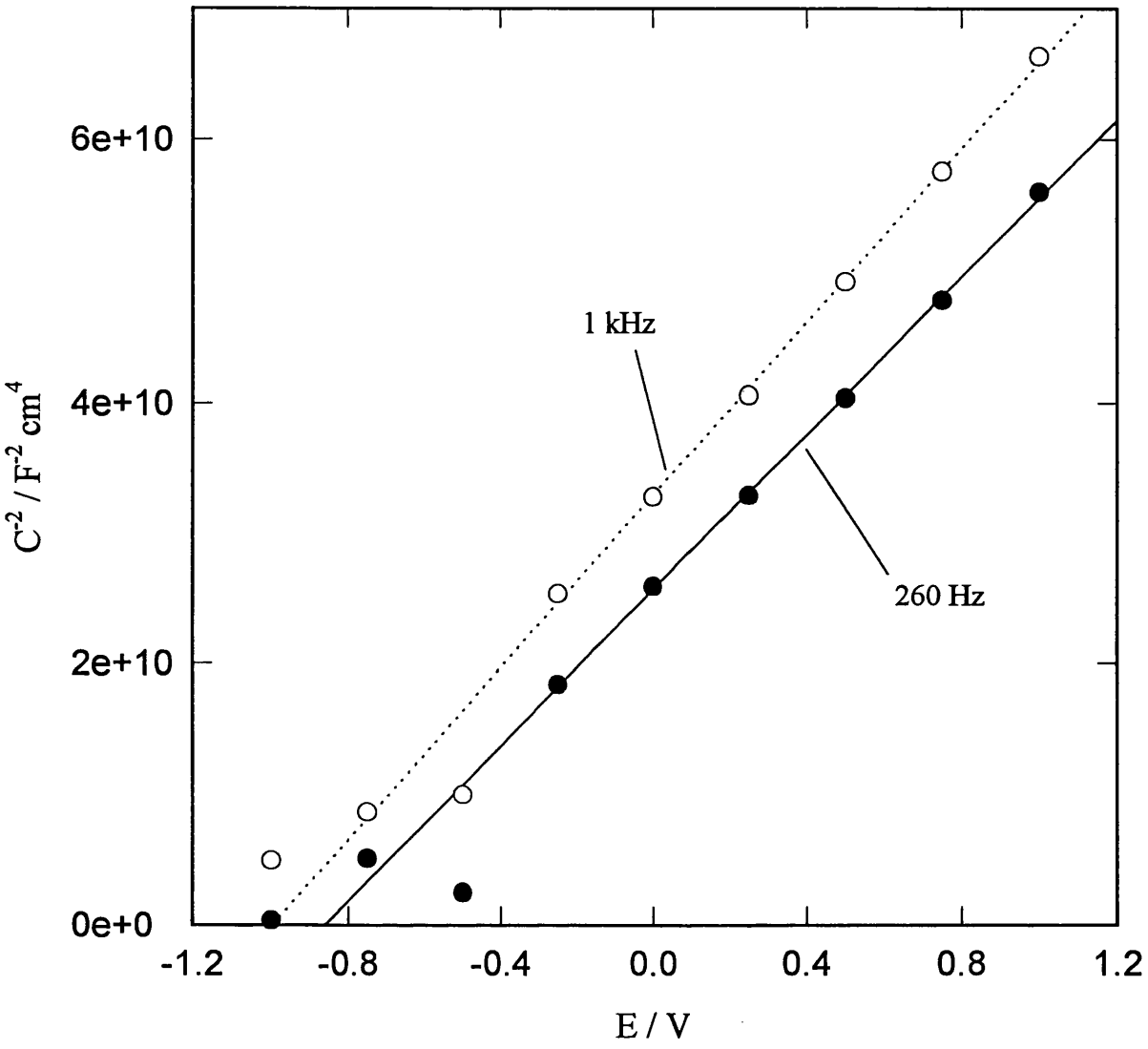

Fig. 3.14. Mott-Schottky plots of the n-TiO_2 single crystal electrode in 1.0 mol dm^{-3} Na_2SO_3 pH 9. Note that the E_{FB} is more negative at 1 kHz, which is attributed to the effect of the surface state capacitance (see chapter 6).

thus the intercept with the potential axis is displaced by a factor of $qN_{SC}\kappa\varepsilon_0/(2C_H^2)$. The determination of the E_{FB} from Mott-Schottky plots is complicated by two aspects: (i) the large dispersion of values of the Helmholtz capacitance in literature, and (ii) that the derivation of the C_{SC} from the admittance is very sensitive to the frequency of modulation. In chapter 6, C_H is estimated to be $(28 \pm 10)\ 10^{-6}$ F cm^{-2} from IMPS measurements. This value of C_H would cause a shift in the order of 30 mV in the Mott-Schottky intercept. This deviation is in the same order of the experimental error, therefore the effect of C_H is not considered further.

At this point, it is interesting to mention the approach by Redmond and Fitzmaurice to the measurement of E_{FB} in transparent TiO_2 thin films [22,23]. They measure the spectroscopic changes of the films which are associated with the accumulation of electrons at the surface. These electrons occupy empty states in the conduction band and in the interband region. This optical method proved to be more successful than the impedance techniques in the determination of the E_{FB}. Salvador has also considered spectro-electrochemical measurements for the determination of the flat band potential. Salvador's analysis is based on the change of the phase shift of the *electroreflectance* signal associated with the transition from depletion to accumulation [24].

Fig. 3.15 shows the normalised photocurrent-voltage curves obtained in three different electrolytes, aqueous 1.0 mol dm^{-3} sulfuric acid, 1.0 mol dm^{-3} sodium sulfite (pH 9) and 0.1 mol dm^{-3} $NaClO_4$ (pH 1). These curves were corrected for reflection losses estimated in (57 ± 1)% at 325 nm. The potential dependence of the photocurrent is rather different in all three electrolytes. In the case of sulfite, the photocurrent onset occurs at potentials close to E_{FB}, which contrasts with the behaviour observed in dilute sulfuric acid solutions. This is not surprising due to the excellent hole scavenging properties of sulfite, which are analysed in more detail in chapter 5. A sigmoidal behaviour is also observed in perchlorate containing solutions (oxygen evolution reaction), and this is typical of a competition between charge transfer and recombination reactions. This reaction is also discussed in chapter 6.

A wide range of light intensity was analysed, and the electrode showed stable photocurrent signal except in the presence of sulfate at low pH. In this electrolyte, the photocurrent at high band bending was found to decrease upon cycling, and the surface

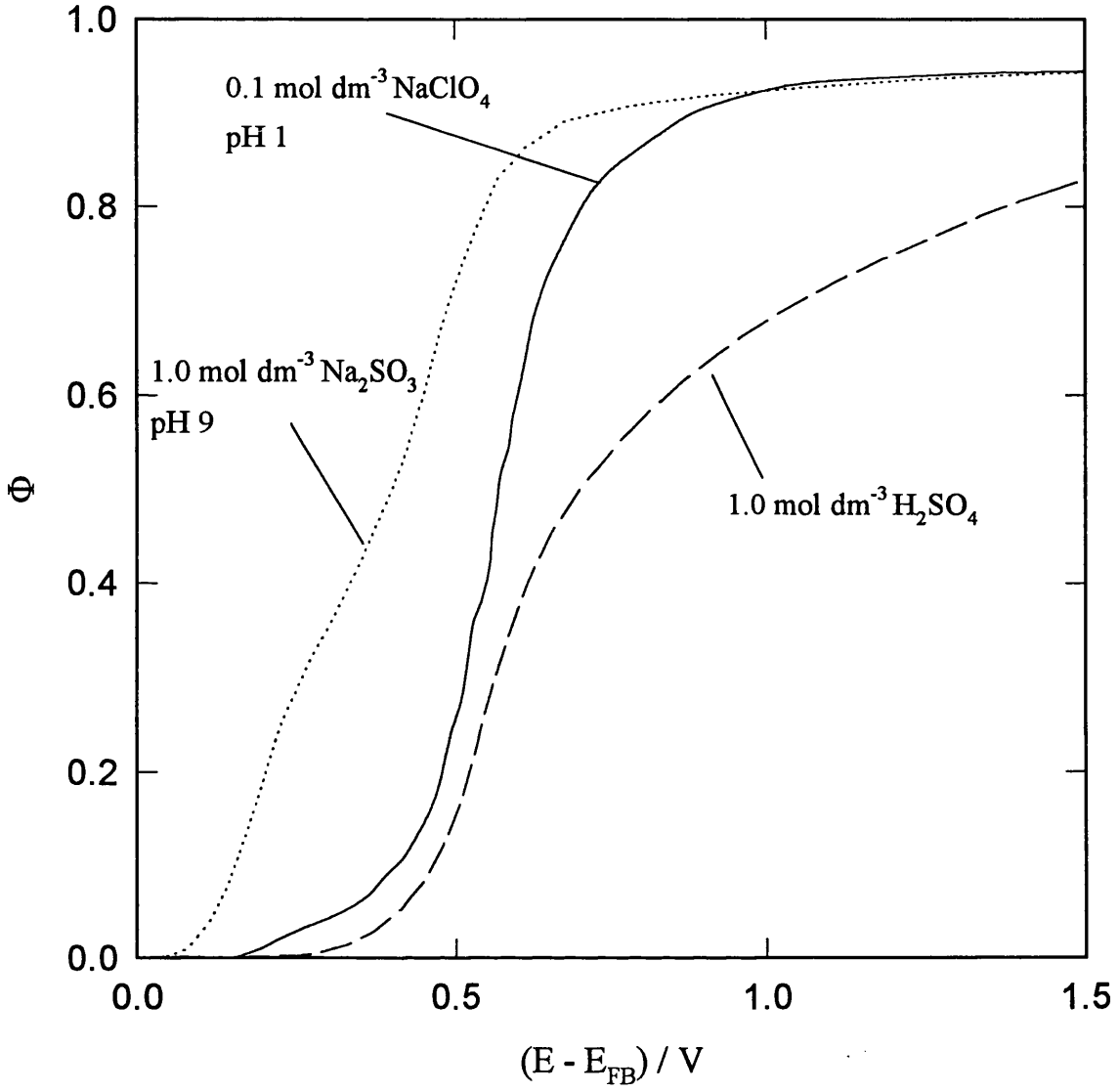

Fig. 3.15. Normalised photocurrent potential curves of the n-TiO_2 electrode in various electrolytes at 325 nm. Note that the potential dependence of the photocurrent in sulfuric acid is extended over a wider potential range.

progressively looked darker. This result clear indicates that the electrode surface is not stable in the presence of sulfate ions in acid solutions. A large amount of research has been devoted to the stability of TiO_2 towards the oxygen evolution reaction, however, there is still some controversy about the effect of the pH [21]. Harris et al. reported that the rate of photocorrosion is very high in dilute sulfuric acid [25]. However, they also obtained the same behaviour in diluted perchloric acid, which contradicts the results shown in **fig. 3.15** (see also chapter 6).

The surface modification detected in the presence of sulfate has been associated with the generation of micropores [21,26]. The photocorrosion mechanism is not well understood, however, it has been linked to the attack by $SO_4^{\bullet-}$ radicals formed at the surface. The decrease in the photocurrent upon cycling indicates that this process not only leads to surface roughening but to the formation of recombination sites.

3.6 Conclusions

Anisotropic etching behaviour was confirmed for the 0001 and $000\bar{1}$ crystal planes of wurtzite CdS. The Cd-face maintains a rather optically flat surface, exhibiting well defined hexagonal pits upon etching in a mixture of acetic and nitric acid. By contrast, an amorphous sulfur film is deposited on the S-face electrode during the same etching procedure. The sulfur film can be removed by saturated Na_2S solutions. The photoelectrochemical properties of both faces are extremely sensitive to surface dislocations. Although smooth surfaces were obtained by the chemo-mechanical polishing, electron-traps defect still perturb the charge accumulation and transfer properties.

Heavily hydrogen doped n-TiO_2 rutile single crystal exhibited poor stability in the presence of low pH sulfate solution under illumination. This result contrasted with the stable photocurrent measured in low pH sodium perchlorate and slightly alkaline sodium sulfite.

3.7 References

1 H. Gerischer, in A. Nozik (ed.), *Photoeffects at Semiconductor-Electrolyte Interfaces*, ACS Symposium Series, Vol. 146, American Chemical Society, Washington D.C., 1981, p. 1.

2 S.R. Morrison, *Electrochemistry at Semiconductors and Oxidised Metal Electrodes*, Plenum Press, N.Y., 1980.

3 E.A. Ponomarev and L.M. Peter, J. Electroanal. Chem., **396** (1995) 219.

4 B. Ray, *II-VI Compounds*, Pergamon Press, Edinburgh, Vol. 2.

5 S.R. Morrison, *The Chemical Physics of Surfaces*, Plenum Press, N.Y., 1977, Ch. 4.

6 A. Zangwill, *Physics at Surfaces*, Cambridge University Press, Cambridge, 1988.

7 E.P. Warekois, M.C. Lavine, A.N. Mariano and H.C. Gatos, J. Appl. Phys., **33** (1962) 690.

8 J.G. Li, *PhD Thesis*, University of Southampton, 1984.

9 M.P. Dare-Edwards and A. Hamnett, J. Electroanal. Chem., **105** (1979) 283.

10 H. Gerischer, F. Hein, F. Lübke, E. Meyer, B. Pettinger and H.R. Schöppel, Ber. Bunsengen. Phys. Chem., 77 (1973) 284.

11 L.M. Peter, Electrochim. Acta, **23** (1978) 1073.

12 R. Haak and D. Tench, J. Electrochem. Soc., **131** (1984) 275.

13 P. Allongue and H. Cachet, Ber. Bunsenges. Phys. Chem., **92** (1988) 566.

14 S. Nakabayashi and A. Kira, J. Phys. Chem., **94** (1990) 7571.

15 M.V. Sullivan and W.R. Bracht, J. Electrochem. Soc., **144** (1967) 295.

16 D. Meissner, R. Memming and B. Kastening, J. Phys. Chem., **92** (1988) 3476.

17 P. Salvador, J. Phys. Chem., **94** (1990) 4373.

18 A.R. de Wit, *PhD thesis*, University of Utrecht, 1992.

19 R.H Wilson, in A. Nozik (ed), *Photoeffects at Semiconductor-Electrolyte Interfaces*, ACS Symposium 146, American Chemical Society, Washington DC, 1981, p.103.

20 K. Honda and A. Fujishima, Nature **238** (1972) 37.

21 H.O. Finklea, in H.O. Finklead (ed), *Semiconductor Electrodes*, Studies in Physical and Theorethical Chemistry Vol. 55, Elseiver, Amsterdan, 1988, p. 43.

22 G. Redmond and D. Fitzmaurice, J. Phys. Chem., **97** (1993) 1426.

23 B. Enright, G. Redmond and D. Fitzmaurice, J. Phys. Chem., **98** (1994) 6195.

24 P. Salvador, Electrochim. Acta, **37** (1992) 957.

25 L.A Harris, D.R. Cross and M.E. Gerstner, J. Electrochem. Soc., **124** (1977) 839.

26 Y. Nakato, H. Akanuma, J.-I. Shimizu and Y. Magari, J. Electroanal. Chem., **396** (1995) 35.

CHAPTER 4

A kinetic study of the CdS photocorrosion by steady state photocurrent, Intensity Modulated Photocurrent and Photoelectrochemical Impedance Spectroscopy

Abstract

The kinetics of the elementary steps involved in the photodissolution of CdS single crystal were investigated by steady state photocurrent, intensity modulated photocurrent (IMPS) and photoelectrochemical impedance spectroscopy (PEIS). The potential dependence of the phenomenological charge transfer and recombination parameters show that the interfacial processes involve three elementary steps: (i) hole capture by a surface active site, (ii) capture of a second hole by the intermediate and crystal dissolution or (iii) capture of a conduction band electron by the intermediate, leading to surface recombination. Estimation of the capture cross section of the active site and intermediate species revealed that the first hole transfer involves a higher activation energy than the second. It was also found that the recombination process also involves an activated state. The kinetic results indicate that the generation of the intermediate (first hole transfer) involves partial bond breaking and cation solvation. The final dissolution step was also found to be affected by surface decomposition products. The theoretical analysis of PEIS for a two hole transfer process is derived and compared to IMPS responses.

4.1. Introduction

The energy conversion efficiency of Photo-Electrochemical Cells (PEC) is mainly determined by the competetion between the electron transfer and recombination of charge carriers. Analysis of the steady state photocurrent-voltage relation has been one of the classical approaches for the assessment of PEC performance. It has also provided valuable contributions to the understanding of the interfacial processes in semiconductor-electrolyte junctions [1-11]. The typical sigmoidal shape of the photocurrent at potentials near the flat band value (E_{FB}) has been interpreted in terms of competition between the charge transfer of minority carriers and the interfacial recombination processes. However, steady state measurements provide only limited mechanistic information regarding these processes. This is due to the fact that the contribution of each step cannot be reliably deconvoluted in the photocurrent onset region.

Recently, the study of the frequency dependent response to an ac perturbation has supplied a more direct approach to the kinetics of the elementary steps in photoelectrochemical processes [10]. Intensity Modulated Photocurrent (IMPS) [10,12-17], Photoelectrochemical Impedance (PEIS) [16,18-22] and Photomodulated Microwave Reflectance Spectroscopy (PMMRS) [23] are the most powerful techniques for the characterisation of charge trapping, recombination and charge transfer velocities. Schefold [21,22] proposed that PEIS and IMPS are complementary techniques which provide an overall kinetic description of illuminated interfaces. Schefold's description of the frequency response spectra obtained from both techniques is based on a model consisting of an equivalent circuit which involves two RC components connected in series. These components are related to the charge transfer and recombination rate constants. However, the physical interpretation of the "charge transfer resistance" in terms of the Butler-Völmer expression seems incorrect.

In principle, a similar approach is used by Vanmaekelbergh et al. in the description of the interfacial capacitance under illumination [14,19,20]. This model predicts a maximum in the potential dependence of the equivalent capacitance for processes controlled by surface recombination. This response can be distinguished from the expected for a space charge recombination process, where a monotonic increment of the capacitance occurs as the band bending is decreased. They have also

suggested that potential modulated and light intensity modulated analysis provide complementary kinetic information.

More recently, Ponomarev and Peter have introduced a model based on linear differential equations for each of the elementary steps involved at the illuminated interface [15,16]. This model is able to describe the basic features of IMPS, PEIS and PMMR. The charge distribution across the interface is defined by the space charge and Helmholtz capacitances and the uncompensated resistance between the reference electrode and the semiconductor back ohmic contact. This approach has also been compared to the two RC equivalent circuit model, and analogies between the circuit elements and physical parameters have been established [16]. In chapter 2, the theoretical description of IMPS responses within the framework of this model has been extended to mechanisms featuring two step minority carrier transfer.

Since the work of Gerischer and Mindt [24], the photodissolution of n-CdS has received particular interest as the reaction competing with the charge transfer to redox species [25-30]. However, basic aspects of the mechanisms are yet to be understood. de Wit et al. [14] studied the photodissolution of n-CdS single crystals by IMPS and capacitance under illumination. Based on the Vanmaekelbergh and Cardon model, they proposed that the photocurrent onset is dominated by surface recombination. They also suggested that the accumulation of charged intermediate introduces a potential drop across the Helmholtz layer which increases the interfacial concentration of majority carriers. Theoretical description of the band bending perturbation associated with charged intermediates is also discussed in chapter 2.

This chapter describes studies of the photodissolution of CdS by steady state photocurrent in conjunction with IMPS and PEIS measurements. Further aspects of the photocorrosion of CdS are briefly reviewed. Mechanistic considerations about the elementary steps involved in the process are discussed and related to estimations of charge transfer and recombination velocities.

4.2. Theoretical Model

4.2.1. Some mechanistic aspects of the CdS photodissolution

The photodissolution of CdS involves the reaction of two holes at the crystal surface producing, in acid electrolyte, cadmium dication and sulfur [24,31]. According to

photodissolution mechanisms previously proposed for various II-VI and III-V semiconductors [24,31-34], this process may include the following steps:

$$h\nu \longrightarrow h^+ + e^- \tag{4.1}$$

$$T + h^+ \xrightarrow{k_1^0} X \tag{4.2}$$

$$X + h^+ \xrightarrow{k_2} Cd^{2+} + S \tag{4.3}$$

$$X + e^- \xrightarrow{k_3^0} T \tag{4.4}$$

$$X + X \xrightarrow{k_4} T + Cd^{2+} + S \tag{4.5}$$

where T represents an active site at the surface and X is the intermediate species which can undergo several processes: (i) trapping a second hole to complete the crystal dissolution, (ii) trapping an electron leading to the surface recombination process, or (iii) reacting with another mobile X species. Steps (4.1)-(4.5) can be directly compared to the general mechanism discussed in chapter 2. For instance, steps (4.1)-(4.4) can be associated with *Case I*, while steps (4.1)-(4.2) and (4.4)-(4.5) described the limiting *Case II*. Reaction (4.5) appears to have been neglected in previous studies of the CdS photodissolution.

Photodissolution processes can be focused from the point of view of *thermodynamics* and *kinetics*. Thermodynamic aspects are discussed first. According to the concepts introduced by Gerischer [35], the dissolution induced by valence band holes will be favoured if the *Decomposition Energy Level*, $_pE_{decomp}$, lies above the valence band. For the photo-corrosion of CdS in KCl (electrolyte used in this work), $_pE_{decomp}$ with respect to the Standard Hydrogen Electrode (SHE) can be estimated from Gibbs free energy change ($\Delta G°$) of the following reaction:

$$CdS_{(s)} + 2H^+_{(aq)} \rightarrow Cd^{2+}_{(aq)} + S_{(s)} + H_2 \tag{4.6}$$

It follows that $\Delta G°$ can be calculated from the following free energy of formation:

$$Cd_{(S)} + S_{(s)} \rightarrow CdS_{(s)} \qquad \Delta G_f^{CdS} = -140.58 \text{ kJ mol}^{-1} \tag{4.7}$$

$$Cd^{2+}_{(aq)} + H_2 \rightarrow Cd_{(s)} + 2H^+ \qquad \Delta G^0_{Cd/Cd^{2+}} = -2\,F\,E^0_{Cd} = 77.18 \text{ kJ mol}^{-1} \qquad (4.8)$$

From these relations, it is found that the $_pE_{decomp}$ lies at 0.33 eV with respect to SHE. Assuming that the flat band potential does not vary from pH 2 to 0, the energy of the CdS bands can be estimated from the E_{FB} value reported later in section 4.4. These energies corresponds to -0.46 and 1.96 eV for the conduction and valence bands respectively. The $_pE_{decomp}$ is then situated between the valence and conduction bands. The energy level associated with the water decomposition is also located between the bands of the solid at 1.23 eV, however is considerably more positive than $_pE_{decomp}$. Therefore, from the thermodynamic point of view, valence band holes are expected to decompose the crystal rather than oxidise water. However, these energy relations do not offer any information about *how fast* this process will occur. In order to envisage the photocorrosion kinetics, some other aspects have to be considered.

The energy barrier that a charge has to overcome in order to be transferred to the electrolyte or to the crystal lattice will be determined by the *Reorganisation Energy* λ [36-38]. In the case of electrolyte species, λ may involve the energy of bond breaking and the re-accommodation of the first and external solvation shells due to the change in the charge of the central ion. It is obvious that in photo-corrosion induced by holes, the perturbation of the surface crystal structure and the cation solvation will contribute to λ. It can be also envisaged that the anion fate may also play a role in the corrosion kinetics. For instance, in step (4.3) a S atom is produced, which is an unstable form of this element. This S atom will stick to a larger clusters in order to form a more stable species, probably in a S_8 configuration. Indeed, evidence of the presence of S_8 species has been obtained by photocurrent spectroscopy [39]. In highly corroded CdS electrodes, it was observed that the conversion efficency at wavelength shorter than 300 nm was quenched, however, the photocurrent increases toward the band edge. The increment of the photocurrent coincided with the decreases of the absorption coefficient of S_8 species [40]. This behaviour is similar to that observed in S-face single crystal electrodes as etched (see **fig. 3.10**).

The species X generated in step (4.2) can be simply visualised as a radical $Cd^{+\bullet}S$. In terms of coulombic forces, the capture cross section for the second hole transfer, should be lower than for the first step, i.e. $^X\sigma_p < {}^T\sigma_p$, due to the net positive

charge of the trap site. If this is the only factor, reaction (4.3) would be the rate determining step. This argument based on coulombic effects is only valid if the holes transfer are non-activated processes. Albery et al [41] and Meissner et al. [42] have estimated the rate constants associated for the overall two hole transfer process, suggesting that the charge exchange occurs in sulfur species S^{2-}. Recently, Schoenmakers et al. [43] has estimated low values of the capture cross section for the recombination step in the photodissolution of ZnO single crystals, suggesting that the intermediate species is the negatively charged centre $O^{\bullet-}$. The critical aspect in these type of interpretations is that the nature of the II-VI compounds is partially covalent, therefore even if the intermediate is only represented in terms of the anionic species, the partial charge of the cation has to be considered, and therefore the *net* charge of the intermediate is positive.

The fact that the charge transfer occurs at the semiconductor/electrolyte interface indicates that activation barriers cannot be simply disregarded. Factors such as the complexation of corrosion species and the abrupt change in dielectric constant can affect the stability of the intermediate. The importance of these effects is illustrated, for example, by the work of Erbse et al. [44] who reported that Cl^- ions can increase the charge transfer velocity in the ZnO photodissolution.

A comprehensive model that includes all the possible factors involved in the photocorrosion reaction is outside the scope of this work. In the following section, the previous analysis of IMPS responses for a two hole transfer processes (chapter 2) is extended to PEIS. The analysis of the elementary rate constants obtained from these techniques has led to a better understanding of this complex mechanism.

4.2.2. Photoelectrochemical Impedance Spectroscopy of multi-electron charge transfer processes.

In section 2.4, it was concluded that the potential dependence of the phenomenological parameters is rather distinctive for mechanisms *I* (X + h reaction) and *II* (X + X reaction). **Table 4.1** summarises the fundamental expressions for IMPS associated with both mechanisms. A similar analysis can be carried out considering constant illumination and a modulated potential perturbation of the system. This is the basic principle of PEIS. The modulated photocurrent is measured as a function of the

frequency of potential modulation, and the results are represented in a complex plot of the real and imaginary impedance. The basic concepts on electrochemical impedance are discussed in the literature [45,46].

In the following derivations, it is assumed that the Helmholtz capacitance is infinite in comparison to the space charge region capacitance and that the uncompensated resistance is very small[1]. For a potential modulation of the form:

$$V = V_0 + V_1 \exp(i\omega t) \tag{4.17}$$

the charge stored across the depletion layer (Q) is given by:

$$\frac{dQ}{dt} = g - j_{photo} - k_3 X \tag{4.18}$$

and

$$\frac{Q_{(t)}}{C_{SC}} = -V_1 \exp(i\omega t) \tag{4.19}$$

The time dependent component of the recombination rate constant is associated with the accumulated charge by:

$$\Delta k_{3(t)} = A k_3 \frac{Q_{(t)}}{C_{SC}} \tag{4.20}$$

where $A = q^2 / kT$. Eqs. (4.17)-(4.20) describe the charge distribution across the SEI in the presence of a modulated potential. As presented in section 2.4 for IMPS, the expressions for PEIS of the limiting *Cases I* and *II* are considered separately.

4.2.2.1. PEIS for Case I

The general differential equations (2.6) and (2.7) can be reduced for *Case I* to:

[1] The assumption is not essential when considering the frequency response of the system. The uncompensated resistance (R) leads to an additional frequency independent impedance in the real component. Obviously, on steady state conditions, R will affect the potential drop across the band bending by (j_{photo} R).

$$\frac{dp}{dt} = g - k_1 p^{(I)} - k_2 p^{(I)} X^{(I)} \quad (4.21)$$

$$\frac{dX}{dt} = k_1 p^{(I)} - k_2 p^{(I)} X^{(I)} - k_3 X^{(I)} \quad (4.22)$$

Table 4.1. Phenomelogical parameters for IMPS for Cases I and II

Frequency dependent normalised photocurrent	$\Phi_{(\omega)} = \frac{k_{tr}^{IMPS} + i\omega}{k_{tr}^{IMPS} + k_{rec}^{IMPS} + i\omega}\left(\frac{1}{1 + i\omega R_u C_{SC}}\right)$ The second term corresponds to the RC attenuation of the interface [15]	(4.9)
	Case I, reactions (4.1)-(4.4)	
Charge transfer parameter	$k_{tr}^{IMPS(I)} = \frac{2k_1k_2p_0^{(I)} + 2k_2k_3X_0^{(I)}\left(1+\psi X_0^{(I)}\right) + k_3^2X_0^{(I)}\psi\left(1+\psi X_0^{(I)}\right)}{k_1 + k_2X_0^{(I)} + k_3\left(1+\psi X_0^{(I)}\right)}$ $\psi = \frac{q^2}{(C_{SC} + C_H)kT}$	(4.10)
Recombination parameter	$k_{rec}^{IMPS(I)} = \frac{k_3\left(1+\psi X_0^{(I)}\right)\left(k_1 - k_2X_0^{(I)} - \psi k_3X_0^{(I)}\right)}{k_1 + k_2X_0^{(I)} + k_3\left(1+\psi X_0^{(I)}\right)}$	(4.11)
Steady state density of X	$p_0^{(I)} = \frac{g_0}{k_1 + k_2X_0^{(I)}}$ $X_0^{(I)} = \frac{-(k_1k_3 + k_2g_0) + \sqrt{(k_1k_3 + k_2g_0)^2 + 4k_1k_2k_3g_0}}{2k_2k_3}$	(4.12) (4.13)
	Case II, reactions (4.1)-(4.2) and (4.4)-(4.5)	
Charge transfer parameter	$k_{tr}^{IMPS(II)} = \frac{4k_1k_4X_0^{(II)} + k_3X_0^{(II)}\psi(k_1 + k_3)}{k_1 + 4k_4X_0^{(II)} + k_3\left(1+\psi X_0^{(II)}\right)}$	(4.14)
Recombination parameter	$k_{rec}^{IMPS(II)} = \frac{k_3\left(k_1 - \psi k_3X_0^{(II)}\right)}{k_1 + 4k_4X_0^{(II)} + k_3\left(1+\psi X_0^{(II)}\right)}$	(4.15)
Steady state density of X	$X_0^{(II)} = \frac{-k_3 + \sqrt{k_3^2 + 8k_4g_0}}{2k_4}$	(4.16)

Keeping in mind that g is constant, the time dependent concentration of X_1 and p_1 are related by:

$$p_1^{(I)}\left(k_1 + k_2 X_0^{(I)} + i\omega\right) = -k_2 p_0^{(I)} X_1^{(I)} \tag{4.23}$$

$$X_1^{(I)}\left(k_2 p_0^{(I)} + k_3 + i\omega\right) = \left(k_1 - k_2 X_0^{(I)}\right) p_1^{(I)} - \Delta k_3 X_0^{(I)} \tag{4.24}$$

The derivation of the frequency dependent impedance from eqs (4.17)-(4.24) is included in **appendix 4.1**. Similarly to IMPS, the PEIS expression can be rewritten in terms of phenomenological parameters which resemble the general equation for the single hole transfer model [16]. These parameters are included in **table 4.2**. The complex plane representation of the PEIS according to eqs. (4.25) to (4.27) is shown in **fig. 4.1**. As the frequency is increased, two semicircles are developed in the lower quadrant. The two semicircles are only observed, within the experimental frequency range, in a rather narrow potential window. When the uncompensated resistance is not negligible, the high frequency limit is shifted from zero to the value R. Comparing **tables 4.1 and 4.2**, it is worth noting that the IMPS and PEIS parameters have different expressions. By contrast, in the single electron transfer case, the phenomenological parameters defined for both techniques are the same.

Fig. 4.2 illustrates the potential dependence of $k_{tr}^{peis(I)}$ amd $k_{rec}^{peis(I)}$ obtained from eqs. (4.26) and (4.27). It can be seen that the general features are similar to those observed for the IMPS parameters (cf. **fig. 2.13d**). For the set of parameters used in the calculation, it is seen that $k_{rec}^{peis(I)}$ is basically determined by k_3. Note that the dc potential perturbation of X_0 is included in the calculations.

4.2.2.2. PEIS for Case II

Following a similar argument, and considering that the differential equations defined for *Case II* are:

$$\frac{dp}{dt} = g_0 - k_1 p_0^{(II)} \tag{4.30}$$

$$\frac{dX}{dt} = k_1 p_0 - 2k_4{}^{(II)} X_0^2 - k_3 X_0^{(II)} \tag{4.31}$$

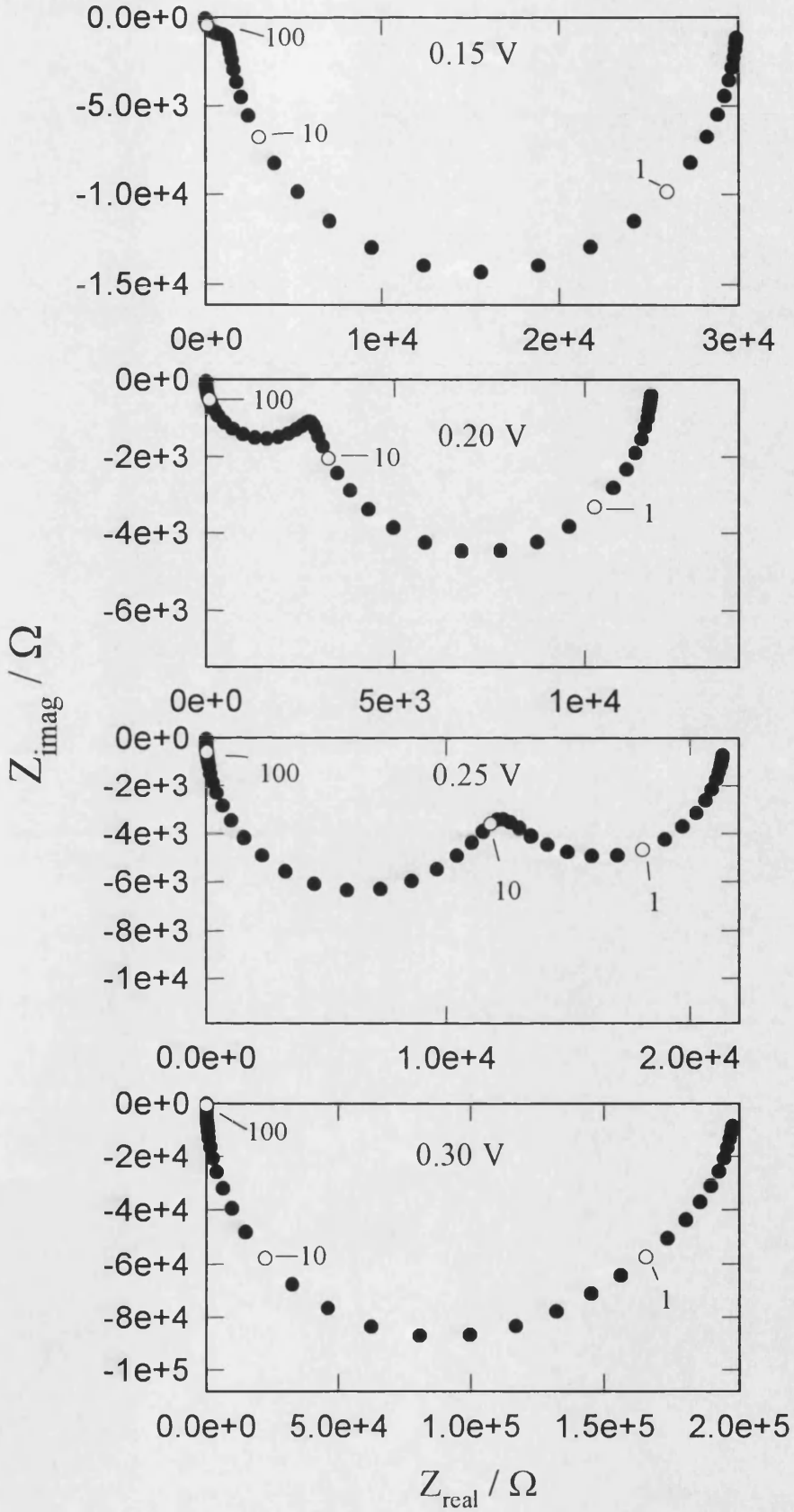

Fig. 4.1. Theoretical PEIS response for the two step photodissolution (*Case I*) at various $\Delta\phi_{SC}$. Rate constant: $k_1=10^{10}$ s^{-1}, $k_2=10^{-3}$ cm^2 s^{-1} and $k_3^0 = 10^5$ s^{-1}. The hole flux was 10^{14} cm^{-2} s^{-1}. C_{SC} was estimated from eq. 1.5 for $N_{SC}=10^{16}$ cm^{-3} and $\kappa= 8.5$

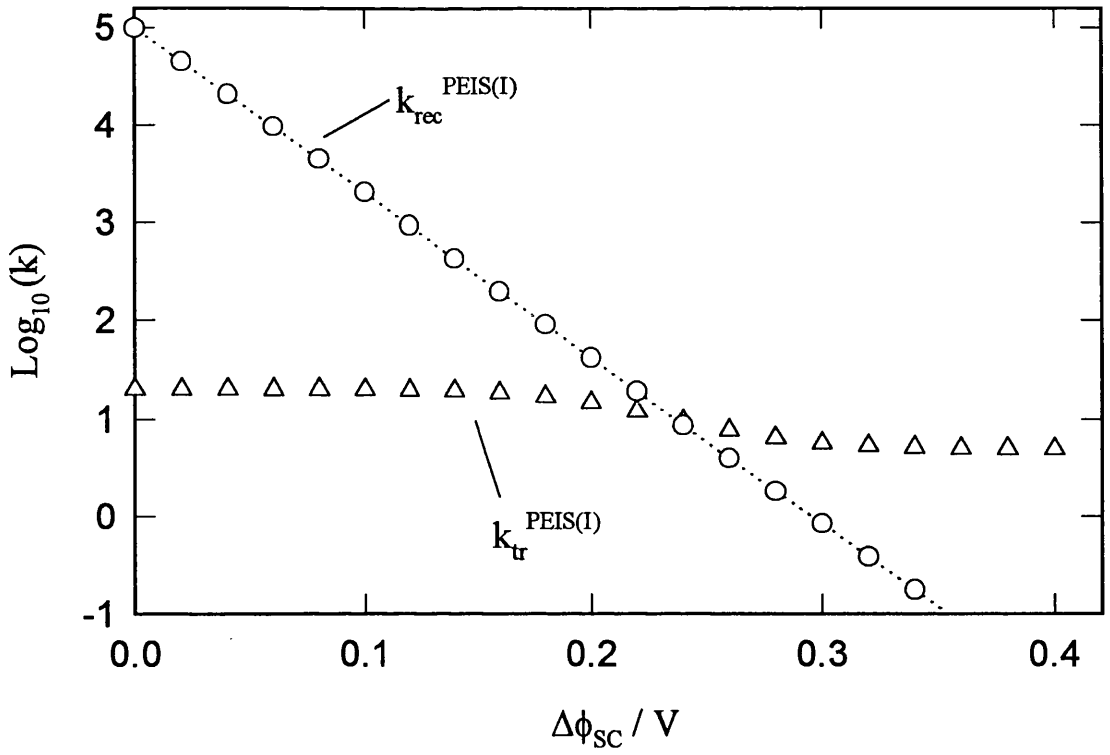

Fig. 4.2. Phenomenological $k_{tr}^{PEIS(I)}$ and $k_{rec}^{PEIS(I)}$ (*Case I*) as a function of the band bending. Rate constants and hole flux as in fig. 4.1. Compare with fig.2.13d.

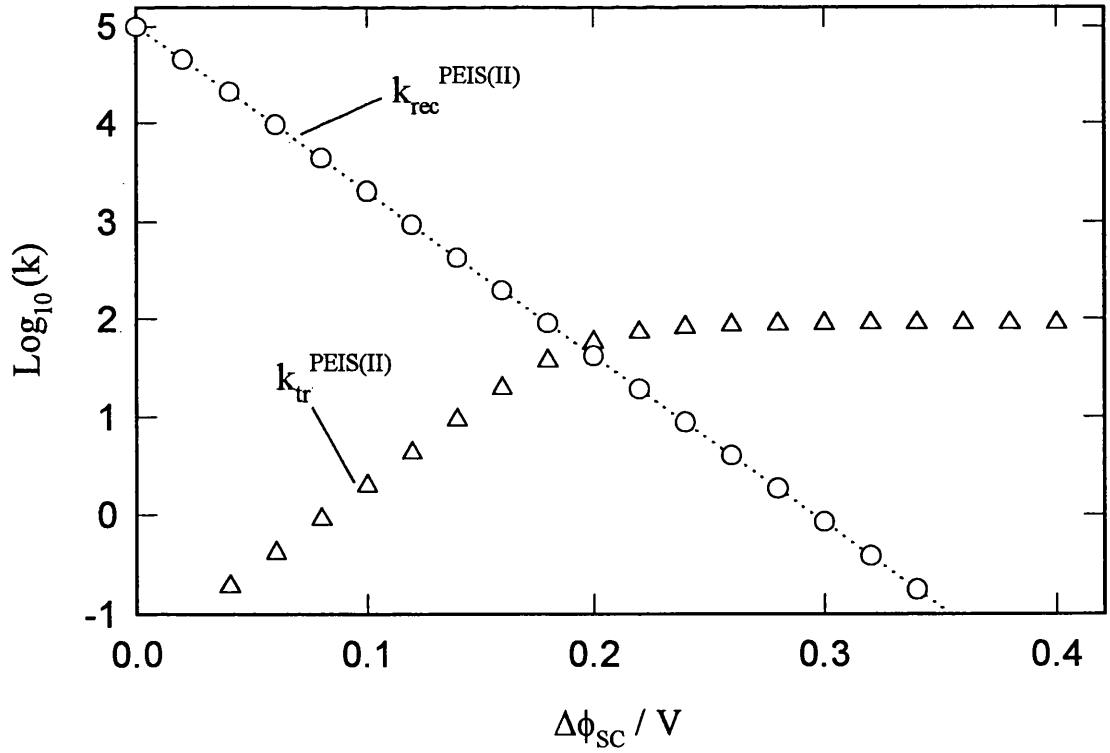

Fig. 4.3. Phenomenological $k_{tr}^{PEIS(II)}$ and $k_{rec}^{PEIS(II)}$ (*Case II*) as a function of the band bending. Rate constants: $k_1=10^{10}$ s^{-1}, $k_3^0=10^5$ s^{-1} and $k_4=10^{-12}$ cm^2 s^{-1}. Hole flux 10^{14} cm^{-2} s^{-1}. Compare with fig. 2.14a.

it can be shown that the frequency dependent concentration of X is:

$$X_1^{(II)} = \frac{-\psi k_3 X_0^{(II)} Q_{(t)}/C_{SC}}{k_3 + 4k_4 X_0^{(II)} + i\omega} \tag{4.32}$$

Table 4.2. Phenomelogical parameters for PEIS for Cases I and II

Frequency dependent normalised impedance	$Z_{(\omega)}^{(I)} = \frac{1}{i\omega C_{SC} + \frac{q^2}{kT} k_3 X_0^{(I)} \frac{k_{tr}^{PEIS(I)} + i\omega}{k_{tr}^{PEIS(I)} + k_{rec}^{PEIS(I)} + i\omega}}$	(4.25)
Case I, reactions (4.1)-(4.4)		
Charge transfer parameter	$k_{tr}^{PEIS(I)} = \frac{2k_1 k_2 p_0^{(I)}}{k_1 + k_2\left(p_0^{(I)} + X_0^{(I)}\right)}$	(4.26)
Recombination parameter	$k_{rec}^{PEIS(I)} = k_3 \frac{\left(k_1 + k_2 X_0^{(I)}\right)}{k_1 + k_2\left(p_0^{(I)} + X_0^{(I)}\right)} \approx k_3$	(4.27)
Case II, reactions (4.1)-(4.2) and (4.4)-(4.5)		
Charge transfer parameter	$k_{tr}^{PEIS(II)} = 4k_4 X_0^{(II)}$	(4.28)
Recombination parameter	$k_{rec}^{PEIS(II)} = k_3$	(4.29)

The impedance is calculated from eqs. (4.20) and (4.32) and the expression is also included in **table 4.2**. In this derivation it was assumed that $k_1 >> k_3$. It is worth noting that the IMPS and PEIS phenomenological parameters for *Case II* are equivalent, given a similar set of rate constants used previously (i.e. $k_1 \sim 10^{10}$ s^{-1}, $k_3^0 \sim 10^5$ s^{-1} and $k_4 \sim 10^{-12}$ cm^2 s^{-1}). The potential dependence of $k_{tr}^{peis(II)}$ and $k_{rec}^{peis(II)}$ is shown in **fig. 4.3**. As expected from the simple expressions (4.28) and (4.29), the phenomenological charge transfer parameter increases to reach a steady value as the potential is increased, and $k_{rec}^{peis(II)}$ is essentially given by k_3. The steady state perturbation of the band bending associated with $X_0^{(II)}$ is also included in this calculation.

The analysis of the PEIS for *Case I* and *Case II* predicts a different potential dependence for the phenomenological parameters. In contrast to *Case I*, k_{tr} and k_{rec} in *Case II* are equivalent for IMPS and PEIS. These relations provide further diagnostic criteria for multi-electron charge transfer mechanisms.

4.3. Experimental

The n-CdS 0001 electrode (Cd-face) was prepared according to the procedure discussed in section 3.4. The photo-dissolution of CdS in acid solution results in the formation of an amorphous sulfur film at the surface, therefore the polishing-etching procedure was repeated before each experiment to enhance the reproducibility of the conditions. The uncompensated resistance, mainly associated with the semiconductor ohmic contact, was in the order of 200 Ω according to impedance measurements in the dark. A donor density of $(1.5 \pm 0.5)\cdot 10^{16}$ cm^{-3} was also obtained from these measurements.

Experiments were carried out in aqueous 1.0 mol dm^{-3} KCl pH 2. The photo-electrochemical cell, reference and secondary electrodes are described in section 3.2. The IMPS and PEIS set ups have been described in detail previously [10,16]. An Isomet 1250C-2 acousto-optic modulator controlled by a Solartron 1250 FRA (Schlumberger) were used to modulate the light intensity produced by a HeCd laser (442 nm). The modulation depth of light was smaller than 10%. A fast home built potentiostat was also used for IMPS and PEIS measurements, allowing reliable spectra to be obtained at frequencies up to around 30 kHz. The modulation of light was referenced against a fast photodiode.

4.4. Results

Steady state photocurrent potential curves were recorded over a wide range of illumination intensity. **Fig. 4.4** displays the effect of the hole flux on the normalised photocurrent as a function of potential. Two striking features can be distinguished as the hole flux is increased: (i) a shift of the photocurrent onset toward more positive potentials, and (ii) a less steep increment of the photocurrent with increasing potential. These two features have an important effect on the IMPS responses shown later. It is also confirmed that the conversion efficiency was equal to one after correction for

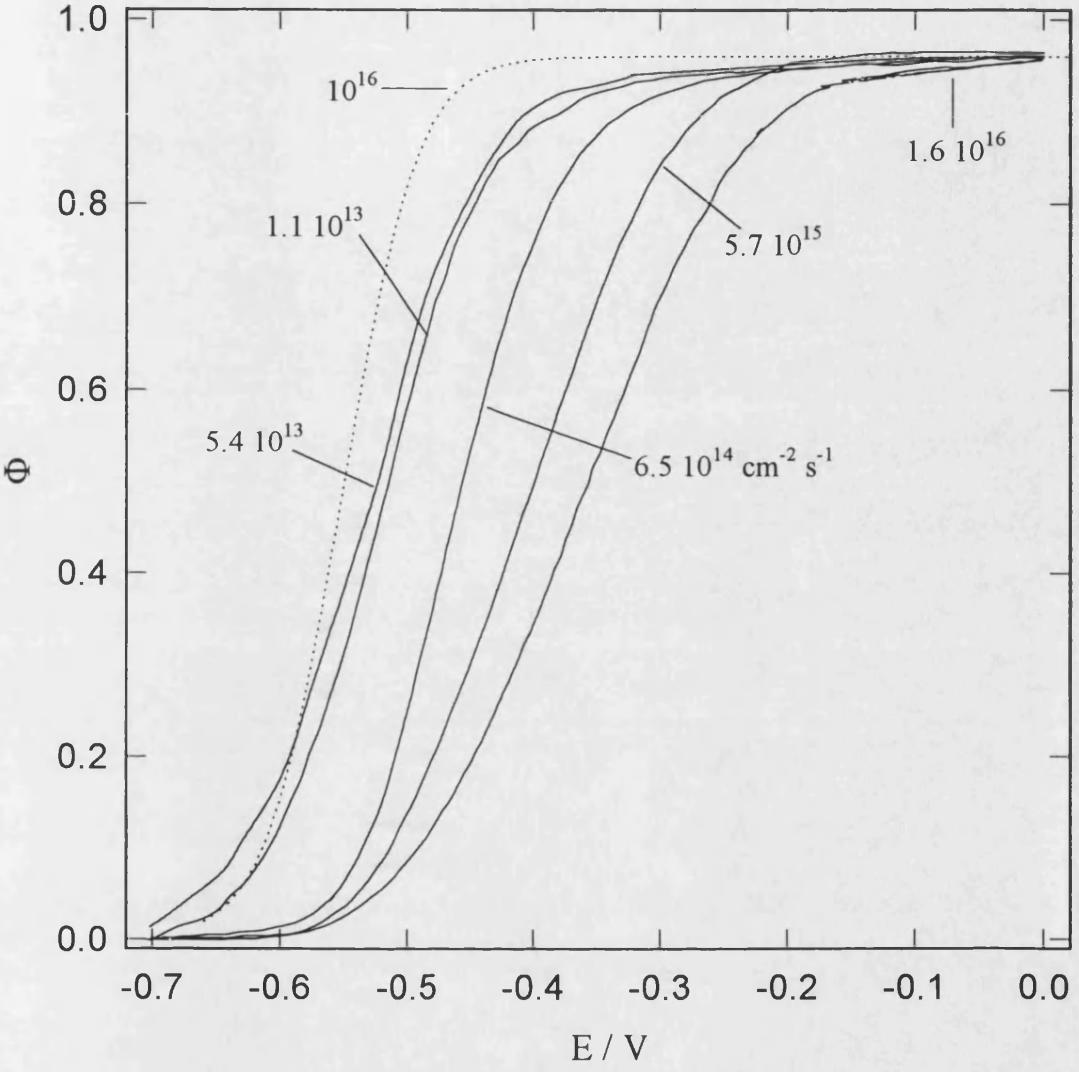

Fig. 4.4. Normalised photocurrent-potential curves of n-CdS (Cd-face) electrode in KCl pH 2 at various hole fluxes. Dotted line corresponds to the theoretical curve for a hole flux of 10^{16} cm^{-2} s^{-1} neglecting the surface charging effect (see eq. 2.15).

reflection losses in the photocurrent saturation region. No evidence of photocurrent multiplication was obtained, in contrast to previous reports [14].

Capacitance measurements were also performed at various light intensities. **Fig. 4.5** shows a small dispersion in the intercepts of the Mott-Schottky plot as the light intensity is increased. On the other hand, the slope consistently decreases as the hole flux is increased. This apparent change in the donor density is clearly related to a space charge-bulk process, since a similar effect is observed in the presence of other electrolytes such as alkaline Na_2SO_3 (see chapter 5) and Na_2S.

IMPS spectra at various potentials and light intensities are shown in **fig. 4.6**. At low hole flux, flattened semicircles were observed, especially at potentials near the saturation region. The low frequency response exhibited considerable deviation from the semicircular behaviour observed at frequencies above 900 Hz. As the flux of holes is increased, the spectra adopted a more semicircular shape, although complicated features at low frequencies were still observed. In some cases, at potentials near the photocurrent saturation region, a second response below 90 Hz was also recorded. A similar feature has been reported by de Wit et al. under similar conditions [14]. Another interesting effect of the increment of the hole flux is the wider range of potential where a semicircular IMPS signal can be detected. **Fig 4.6b** illustrates this phenomenon, where the ac photocurrent response decreases as the photon flux is increased at -0.4 V. These results are consistent with the shift of the photocurrent onset to more positive potentials (**fig. 4.4**).

PEIS spectra at various potentials are shown in **fig. 4.7**. These spectra were recorded at high light intensities, where the two semicircles predicted by eq. (4.25) were observed. At potentials close to E_{FB}, the high frequency semicircle shifts to frequencies beyond the experimental range. Additionally, at low light intensities, both signals become convoluted into a single broadened semicircle. As observed in the IMPS responses, the low frequency PEIS signal deviated considerably from the expected semicircular behaviour.

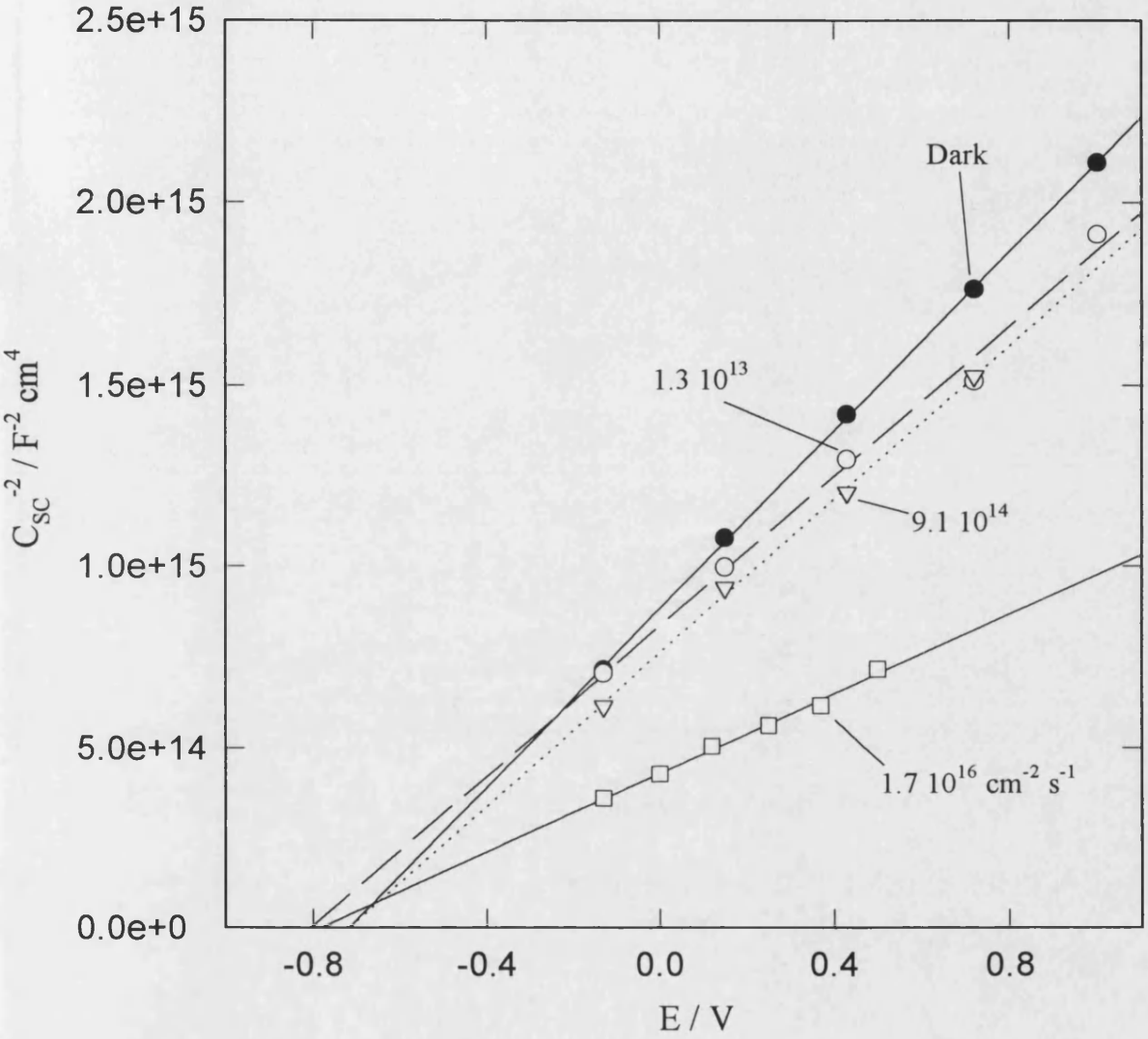

Fig. 4.5. Mott-Schottky plots of the Cd-face electrode in 1.0 mol dm^{-3} KCl pH 2 in the dark and at various hole fluxes. The frequency of potential modulation was 1 kHz. An E_{FB} of -0.66 V was estimated from the intercept of the experiment in the dark.

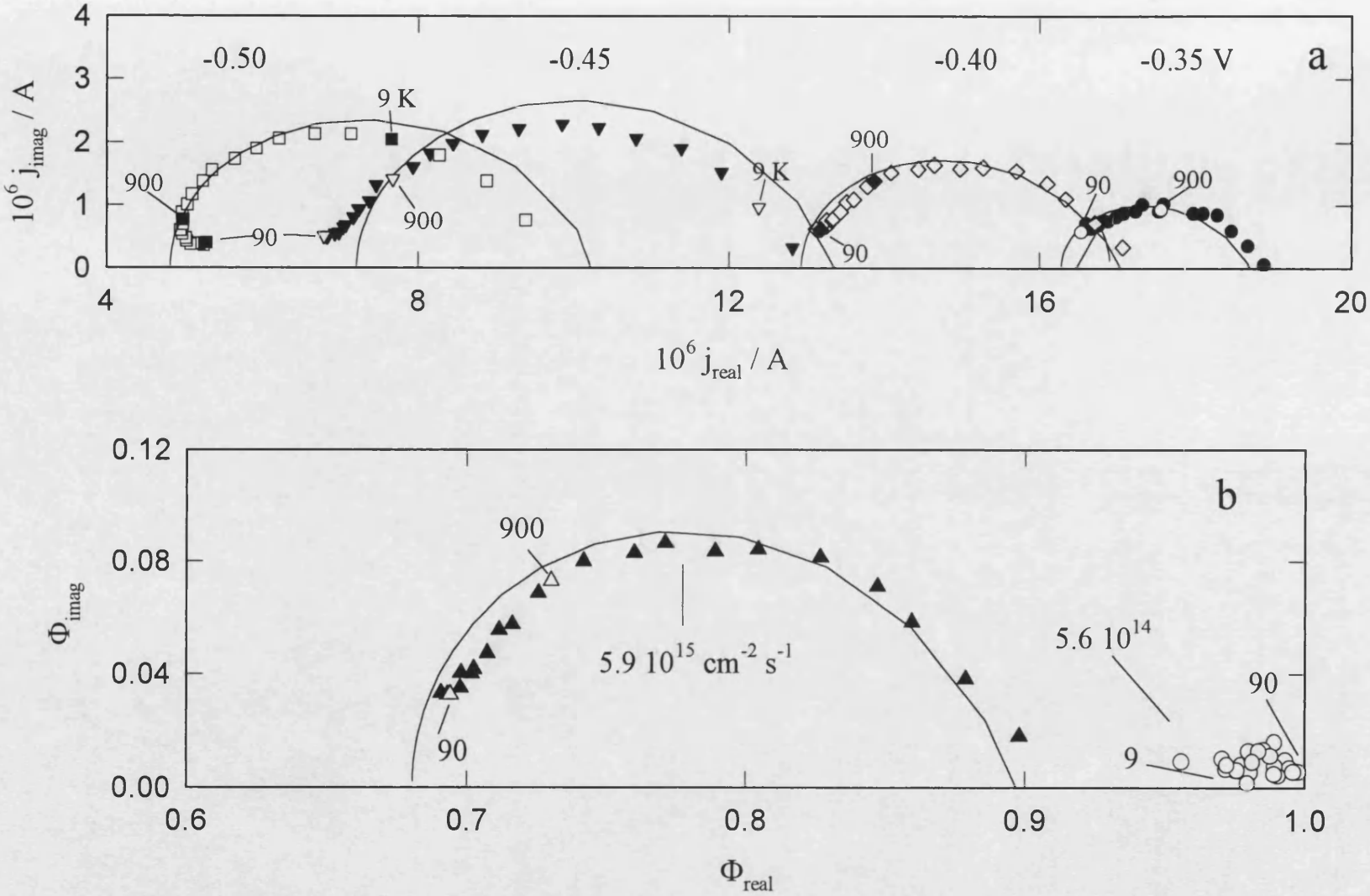

Fig. 4.6.(a) Complex plots of the IMPS responses at a hole flux of $5.9\ 10^{15}$ cm^{-2} s^{-1} and various potentials. Solid lines corresponds to the fits according to eq. (4.9). (b) Normalised IMPS spectra at -0.40 V and two different hole fluxes.

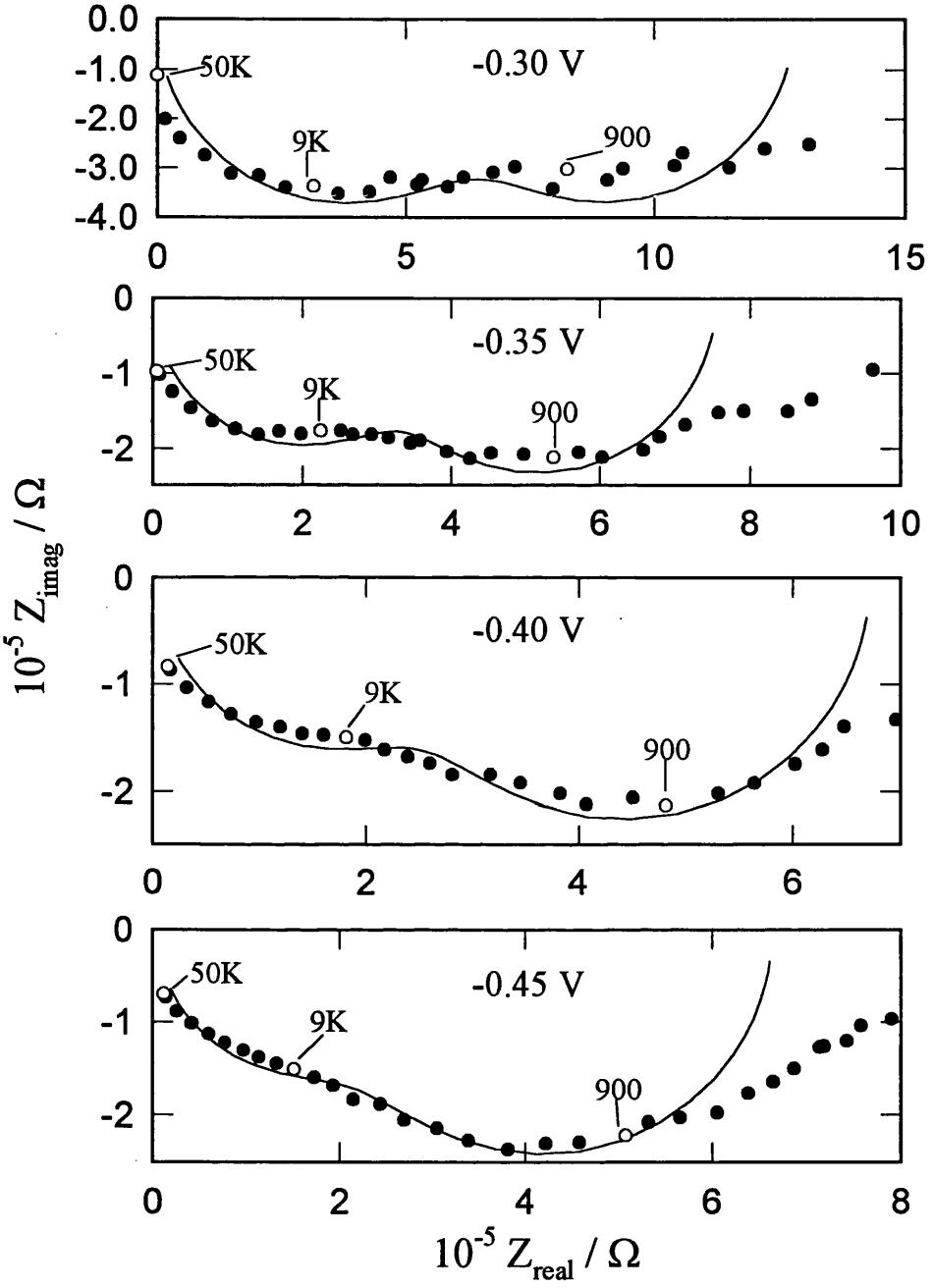

Fig. 4.7. Complex plot of the PEIS responses at 5.9 10^{15} cm^{-2} s^{-1} and various potentials. Solid lines corresponds to the fits according eq. (4.25).

4.5. Discussion

4.5.1. Steady state condition

In this section, the effect of the hole flux on the normalised photocurrent-potential curves (**fig.4.4**) is discussed. It was considered in section 2.3 that the accumulation of positive charge at the surface increases the potential drop across the Helmholtz layer. Consequently, this perturbation causes a decrease of the band bending and therefore an increase of the recombination rate. For the mechanism considered in chapter 2, this perturbation (photopotential) is mainly introduced by the steady state concentration of X. Therefore, as the band bending is increased, X_0 increases and the photopotential also increases. This effect accounts for the broadening of the photocurrent-potential relationship. As the dependence of X_0 upon light intensity is different for *Cases I* and *II*, photocurrent-potential curves are also distinctively affected (compare **figs. 2.5** and **2.10**).

In **fig. 4.4**, the photocurrent-potential curves become broader as the hole flux is increased. This effect indicates that the surface accumulation of X increases with increasing light intensity. This is the behaviour expected for a *Case II* type mechanism as depicted in **fig. 2.10** (see also section 2.3.2). For *Case I*, the slope of the photocurrent-potential curve is not affected by the light intensity; the plots only shift on the potential axis. Therefore, a first interpretation of the steady state behaviour indicates that the mechanism for the CdS photodissolution involves steps (4.2), (4.4) and (4.5).

Let us reconsider the effect of surface composition on the photocorrosion kinetics. In section 4.2, it was recognised that the interaction between the intermediate species and the electrolyte may affect the kinetics of the whole process. Assuming that the neutral sulfur forms a deposit at the surface, the access of the electrolyte to the active $Cd^{+\bullet}S$ centre will be hindered as the sulfur coverage increases. This effect will lead to a dependence of the rate constants on photocurrent. It is difficult to envisage a priori how the sulfur coverage will affect the kinetics of each of the steps. For instance, if the relation k_1/k_2 is decreased as the photocurrent is increased, the potential dependence of X_0 will depend on light intensity even for *Case I* (for an illustrative example see **fig. 2.6**). In view of the complications, it is not possible to qualitatively

attribute the photocurrent-potential behaviour at various light intensity to a *Case I* or *Case II* type of mechanism.

4.5.2 Non-steady state response of the photocurrent in the onset region

Phenomenological charge transfer and recombination parameters were accessed by non-linear fitting of eq. 4.9 (cf. **table 4.1**) to IMPS spectra recorded at various potentials and light intensities. Typical fittings are also illustrated in **fig. 4.6** (see continuos lines). In general, the quality of the fitting was rather poor at low frequencies due to the considerable distortion of the experimental responses. So far, the origin of these low frequency features is not clear, but it might reflect surface modifications occurring during the recording of the spectra. At high frequencies, the attenuation arose from the uncompensated resistante R_u (200 Ω) and the space charge capacitance shifts the interception with the real axis to lower photocurrents.

The potential dependence of k_{tr}^{IMPS} and k_{rec}^{IMPS} is displayed in **fig. 4.8**. It is observed that k_{tr}^{IMPS} increases slightly as the potential is decreased. *This trend provides strong evidence for a Case I type of mechanism.* In section 2.4, it was demonstrated that the potential dependence of k_{tr}^{IMPS} is a quite distinctive feature for both cases. According to the simulations presented (cf. **fig. 2.13d**), k_{tr}^{IMPS} increases as the potential is decreased due to the contribution of the recombination rate constant. The recombination parameter k_{rec}^{IMPS} exhibited the expected increase with decreasing potentials. In the light of these results, both phenomenological parameters were quantitatively analysed considering the expression for a *Case I* mechanism.

The quantitative analysis of the phenomenological parameters was done by fitting eqs. (4.10) to (4.13) to series of experiment at various light intensities. Typical fittings of k_{tr}^{IMPS} and k_{rec}^{IMPS} are also illustrated in **fig. 4.8**. Both parameters are displayed as function of $(E - E_{FB})$. This is done in order to account for the surface charging effect associated with the accumulation of X^+ (see section 2.4). The theoretical curves were constructed as follows:

(i) A set of values for k_1, k_2 and k_3^0 according to estimations from typical capture cross sections (cf. section 2.3.1) were introduced as a first approximation.

(ii) Values of X_0 and p_0 were calculated as a function of $\Delta\phi_{SC}$ from eqs. (4.12) and (4.13), assuming a C_H of the order of 2.5 μF cm^{-2} [14].

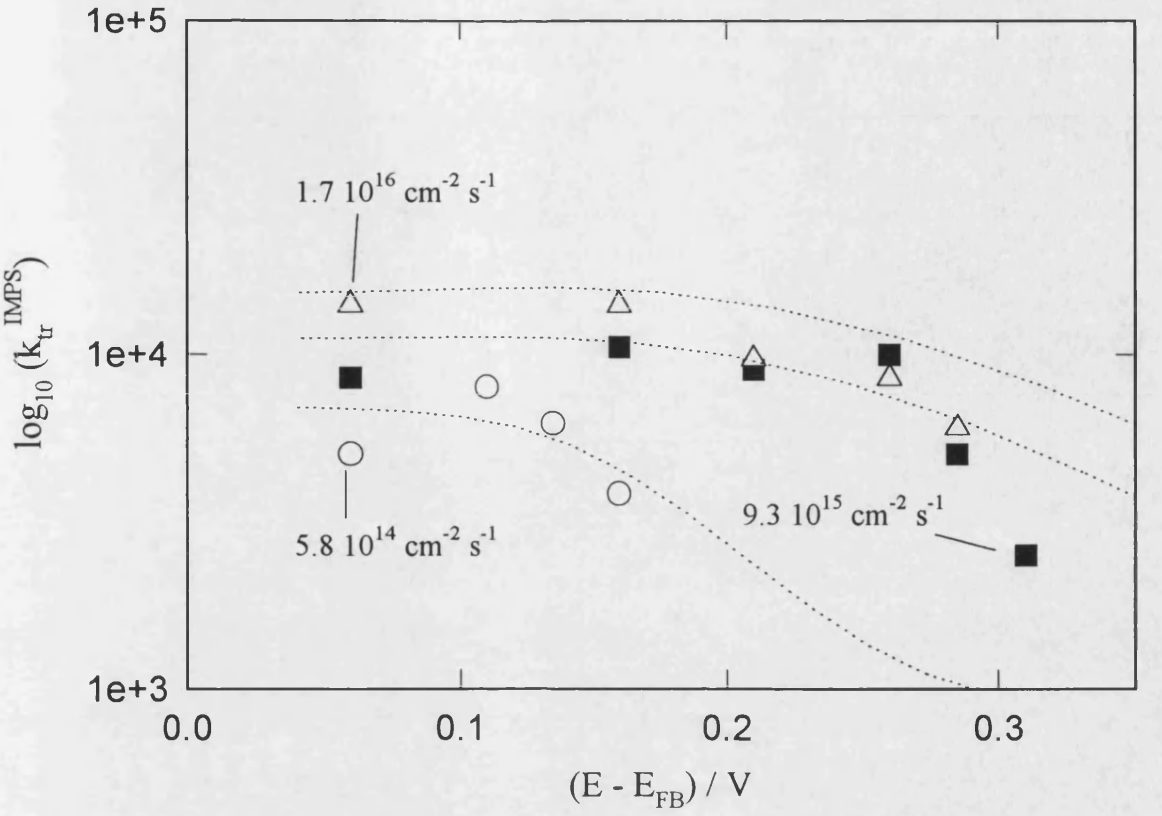

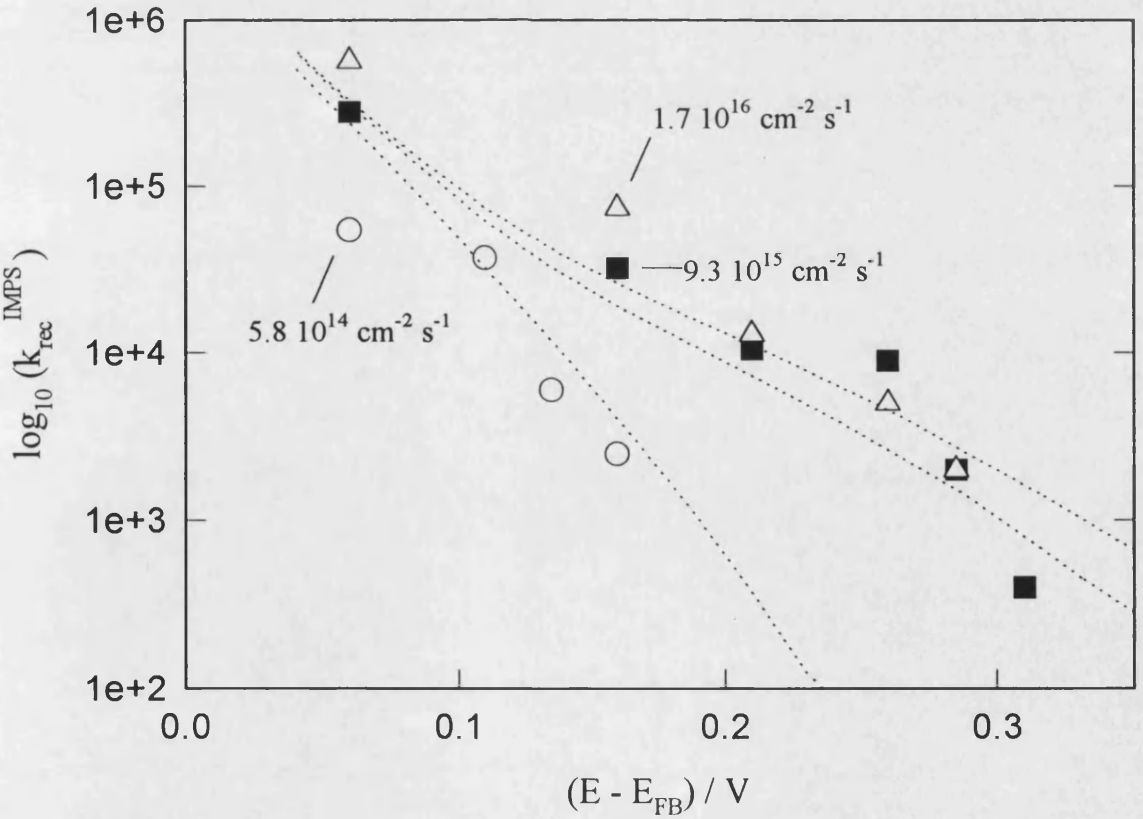

Fig. 4.8. Phenomenological (a) k_{tr}^{IMPS} and (b) k_{rec}^{IMPS} as a function of $(E - E_{FB})$ at various photon fluxes. Dotted lines correspond to the theoretical fittings according to eqs. (4.10) to (4.13). Rate constants are summarised in **table 4.3**.

(iii) The change in the potential drop across the Helmholtz layer was estimated using eq. (2.16), and the relation $E - E_{FB}$ was obtained directly from:

$$(E - E_{FB}) = \Delta\phi_{SC} + \Delta V_H \qquad (4.33)$$

(iv) The phenomenological parameters were calculated via eqs. (4.10) and (4.11). The best fit was obtained by adjusting the real rate constants. A closer examination of **table 4.1** reveals that k_{tr}^{IMPS} is particularly sensitive to k_2, while k_{rec}^{IMPS} is determined by k_3. The potential dependence of both parameters is very much affected by the ratio of k_1/k_2. Although some of the fittings were not quantitatively accurate, the potential dependence of k_{tr} and k_{rec} was reproduced.

Analysis at various light intensities showed that k_1 and k_3^0 remain constant, while k_2 *decreases monotonically as the hole flux is increased.* The results of the fittings at various hole fluxes are summarised in **table 4.3**. Although it is not clear which phenomenon is responsible for the light intensity dependence of k_2, it is reasonable to associate it with surface modifications during the crystal dissolution. The amorphous sulfur layer deposited under these conditions can effectively decrease the dissolution rate and therefore the rate of step (4.3).

From the data included in **table 4.3**, theoretical steady state photocurrent-potential curves can be constructed and compared with the experimental results (**fig. 4.4**). **Fig. 4.9** illustrates the potential dependence of the photocurrent as calculated from eqs. (2.8) and (2.15). The theoretical plots exhibits a broadening of the photocurrent-potential relation as the hole flux is increased, which resembles the behaviour observed experimentally. The decrease in k_2 with increasing hole fluxes generate a increasing surface accumulation of X, therefore the dc and ac perturbation of the band bending is more evident at high light intensity. The effect of the increasing accumulation of X is depicted in **fig. 4.10**, where the slope of $\Delta\phi_{SC}$ vs. $(E - E_{FB})$ decreases from one to nearly 0.5 in the potential dependence photocurrent range. All these calculations were done considering a *Case I* mechanism.

It is also shown in **fig. 4.9** that the decrease in the ratio of k_1/k_2 shifts the photocurrent onset towards more positive potentials. However, the experimental shift of the photocurrent onset is even more pronounced than that observed in **fig. 4.9**. This

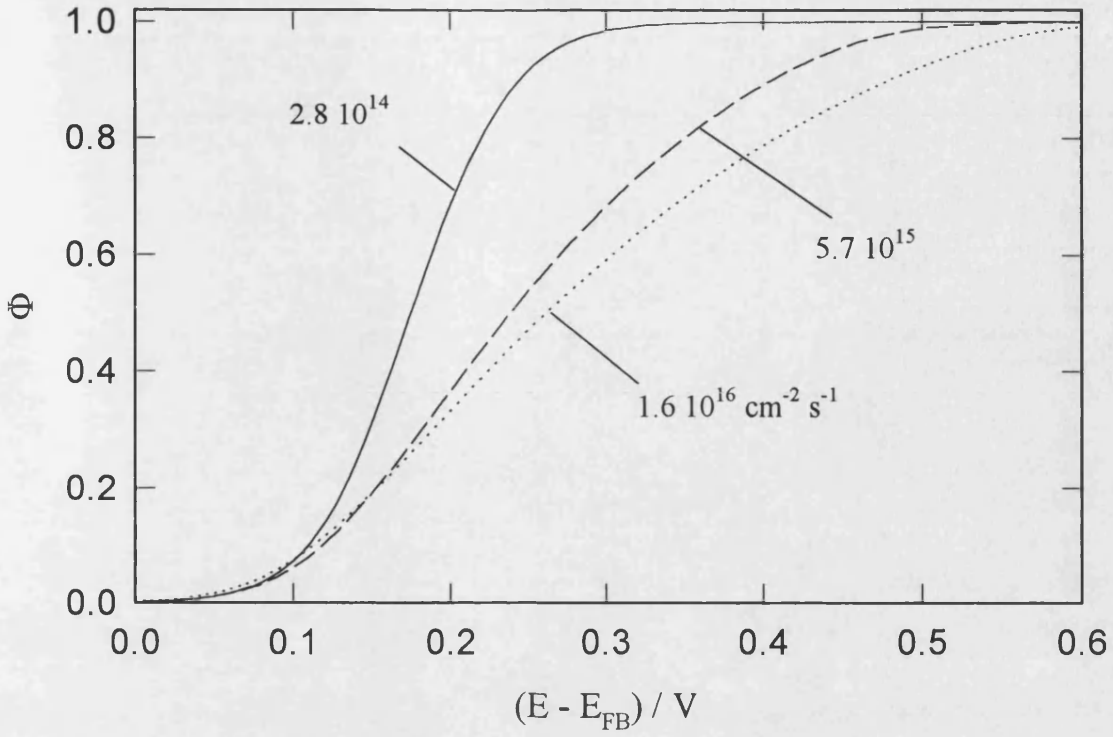

Fig. 4.9. Normalised photocurrent-potential curves at various photon fluxes calculated assuming a *Case I* type of mechanism with the rate constants obtained from IMPS spectra (see **table 4.3**).

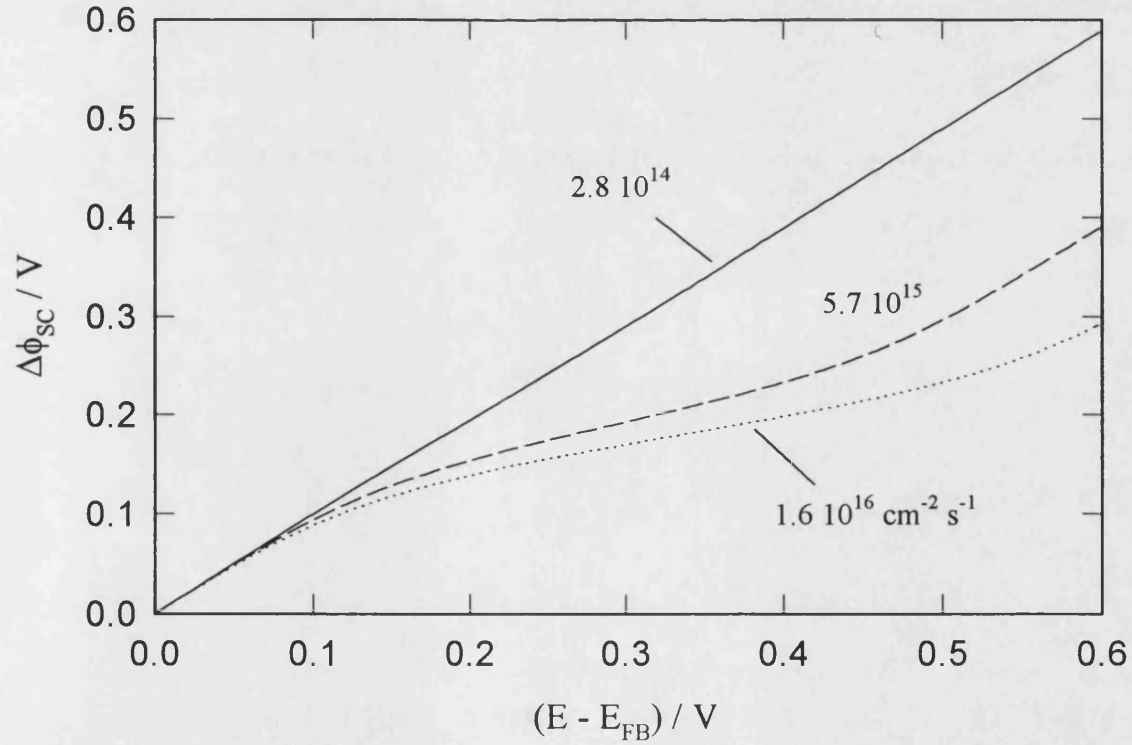

Fig. 4.10. $\Delta\phi_{SC}$ vs $(E - E_{FB})$ at various photon fluxes. Calculations were based upon a *Case I* type of mechansim and the rate constants summarised in **table 4.3**.

result suggests that other effects are involved in the photocurrent-potential relationship that cannot be explained simply in terms of surface charging.

Table 4.3. Elementary rate constants obtained from IMPS spectra

Mechanism step	*Rate constant / s^{-1}*
Step 4.2 (k_1)	$(1.0 \pm 0.1)\ 10^{10}$
Step 4.4 (k_3^0)	$(2 \pm 1)\ 10^{6}$
Hole flux to the surface / $cm^{-2}\ s^{-1}$	*Rate constants for step (4.3) k_2 / $cm^2\ s^{-1}$*
$2.8\ 10^{14}$	0.06 ± 0.01
$5.8\ 10^{14}$	0.03 ± 0.01
$5.9\ 10^{15}$	$(3 \pm 1)\ 10^{-3}$
$9.3\ 10^{15}$	$(3.0 \pm 0.3)\ 10^{-3}$
$1.7\ 10^{16}$	$(2 \pm 1)\ 10^{-3}$

PEIS spectra were analysed according to the general eq. (4.25). As observed in the IMPS results, the low frequency signal exhibited rather irreproducible features. Typical fits are included in **fig. 4.7**. The potential dependence of the PEIS phenomenological rate constant is displayed in **fig. 4.11**. *The decrease of* k_{tr}^{PEIS} *with increasing potential provides further evidence for a Case I type mechanism.*

In principle, the relations presented in **table 4.2** allow comparisons between the phenomenological IMPS and PEIS parameters for a given set of elementary rate constants. **Fig. 4.12** contrasts the potential dependence of k_{tr} and k_{rec} obtained from IMPS and PEIS relations for a given set of rate constants (see **table 4.3**). The theoretical PEIS curves reproduce the basic features of the experimental parameters, but the calculated values consistently underestimate the result obtained from the non-linear regression fits. This difference might be connected to a *cross-modulation* of the band bending associated with X_1. In eqs. (4.18) and (4.19) the interfacial charge Q is considered only through the space charge region (it was assumed that $C_H >> C_{SC}$). However, the IMPS responses at high illumination intensity show that the accumulation of X is high enough to induce perturbations of ΔV_H, and therefore C_H cannot be neglected from the PEIS analysis. The inclusion of this parameter introduces considerable complications and requires further investigation.

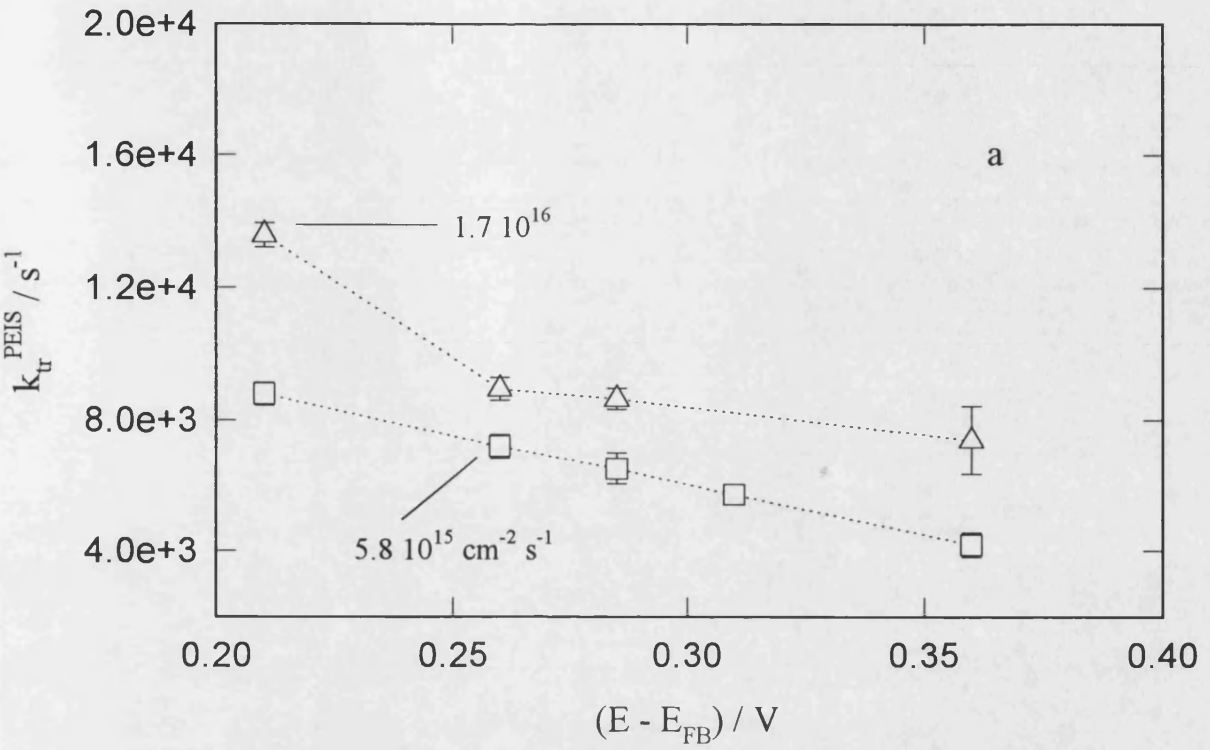

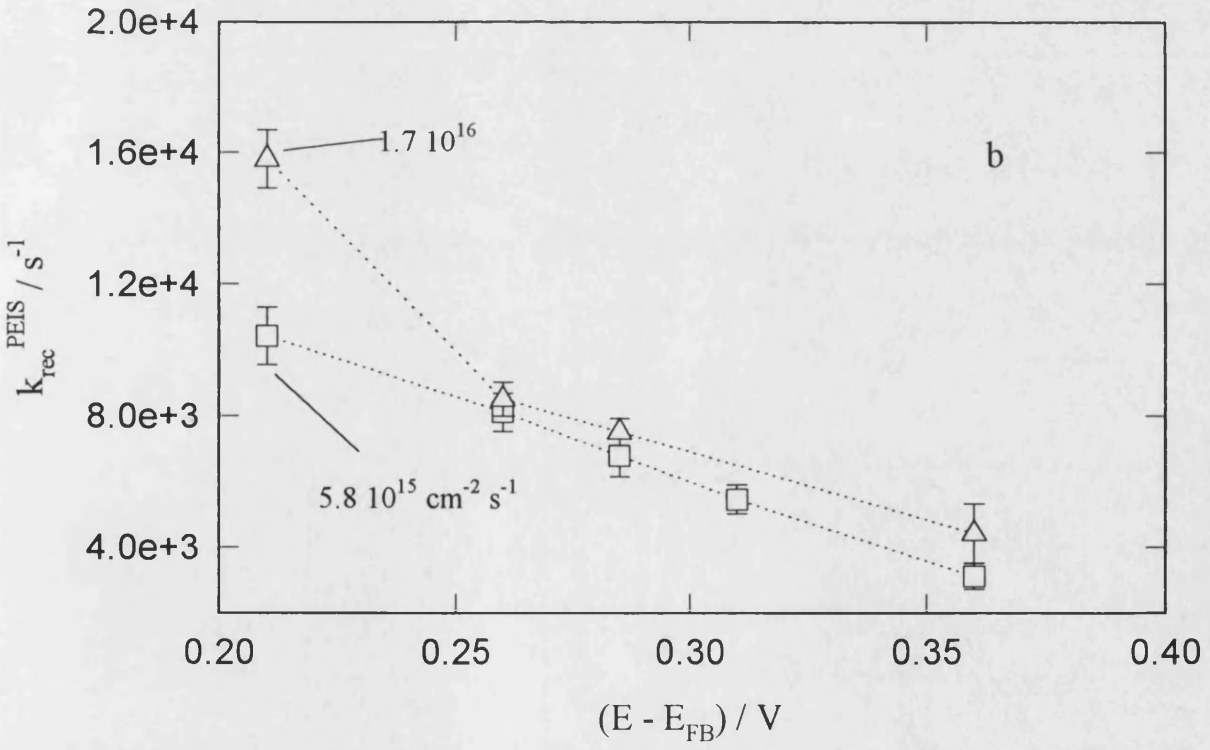

Fig. 4.11. Phenomenological (a) k_{tr}^{PEIS} and (b) k_{rec}^{PEIS} as a function of potential at two different photon fluxes.

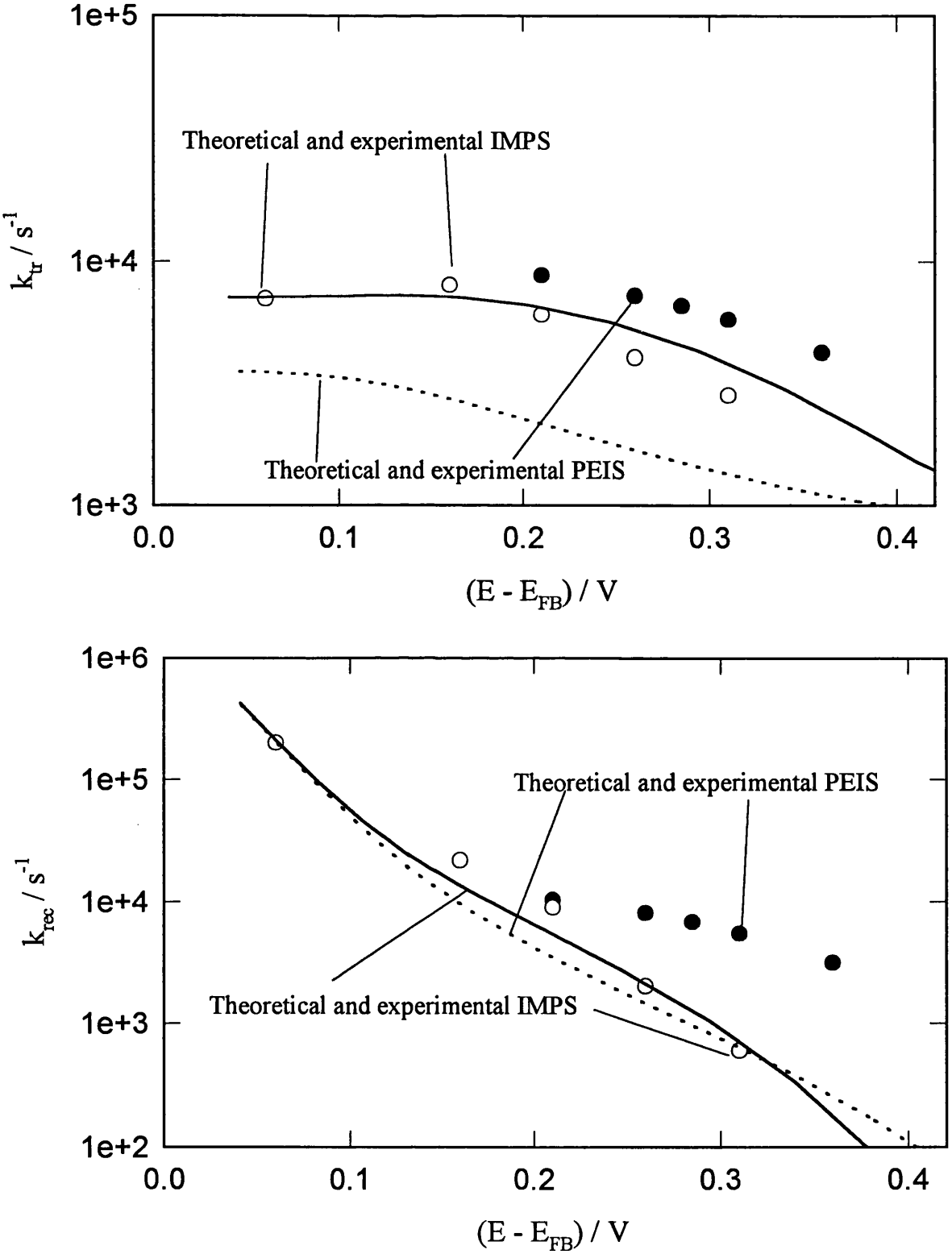

Fig. 4.12 Comparison between phenomenological parameters from IMPS (hollow circles) and PEIS (filled circles) at 5.9 10^{15} cm^{-2} s^{-1}. Full and dotted lines are calculated from eqs. (4.10)-(4.13) and (4.26)-(4.27) respectively. Rate constants as in **table 3.**

Although quantitative agreement was not achieved between the IMPS and PEIS analysis, both techniques confirm that the photodissolution of CdS occurs via a reaction of holes with the photogenerated intermediate X. It is also suggested that recombination occurs effectively through this intermediate.

4.5.3. On the photocorrosion mechanism

The estimation of the rate constants associated with the elementary steps (4.2) to (4.4) allows the calculation of the capture cross sections of each of the species involved. Firstly, let us consider the kinetics of the first and second hole transfer. The generation of the intermediate X features a first order rate constant of the order of 10^{10} s^{-1}, giving a capture cross section ${}^{T}\sigma_p$ of 10^{-17} cm^2 (see eq. (2.11)). At low light intensities, the second hole transfer is a considerably faster process, $k_2 \sim 0.1$ cm^2 s^{-1}, resulting in a ${}^{X}\sigma_p$ as high as 10^{-13} cm^2. This very large difference between the two capture cross sections points to fundamental aspects of the activated states involved in the photo-dissolution process.

The low value of ${}^{T}\sigma_p$ with respect to ${}^{X}\sigma_p$ suggests that the reorganisation energy (λ_1) is considerably higher for the first hole transfer. The *initial state* involves a hole in the valence band and a neutral surface crystal site CdS (T), which becomes the charged species $Cd^{+\bullet}S$ (X). The formation of this intermediate species may already imply a large degree of bond breaking and cation solvation. If this is the case, the second hole transfer may only require a smaller reorganisation energy (λ_2) in order to complete the dissolution process. It could be also argued that the solvation shell of $Cd^{+\bullet}S$ decreases the net positive charge of the intermediate species, thus the coulombic work for the second hole transfer is also negligible.

The photogenerated sulfur can play a double role in the photodissolution kinetics. At low light intensities, the generation of the first sulfur nuclei involves the collision of a critical number of S atoms. This step can introduce an initial activation energy for the second hole transfer. After these nuclei are formed, the subsequent S atoms will readily be attached to them, and the activation energy will then decrease. However, a large build up of sulfur at the surface can hinder access of electrolyte to the $Cd^{+\bullet}S$ species. Under these conditions, the cation solvation could be affected and the rate of charge transfer decreased. This effect could be responsible for the decrease

of k_2 as the light intensity is increased. Although the experimental study in this work does not provide specific information about the role of sulfur in the photocorrosion process, techniques such as Photoelectrochemical Surface Imaging may prove to be a more direct approach [47,48]

Considering a value of 10^7 cm s^{-1} for the thermal velocity of electrons in CdS [32], the capture cross section for the *recombination reaction*, ${}^{X}\sigma_e$, can be estimated to be of the order of 10^{-17} cm^2 (see eq. (2.13)). This low value for ${}^{X}\sigma_e$ is one order of magnitude smaller than the geometrical capture cross section, suggesting that *surface recombination also involves an activated state*. Coincidentally, a ${}^{X}\sigma_e$ of the same order was reported by Schoenmakers et al. for the photodissolution of ZnO [43]. In order to rationalise the nature of the activated state, it should be considered that the recombination reaction is not the reverse step of the first hole transfer. This can be clearly seen if reactions (4.2) to (4.4) are rewritten as:

$$CdS \xrightarrow{k_1^0} Cd^{+\bullet}S + e^-_{VB} \qquad (4.34)$$

$$Cd^{+\bullet}S + e^-_{CB} \xrightarrow{k_3^0} CdS \qquad (4.35)$$

Although the initial state of (4.34) and the final state of (4.35) are formally the same, the electrons involved in each reaction have different energies (in fact the difference approaches 2.4 eV). Therefore, the intermediate $Cd^{+\bullet}S$ will have two energy levels associated with the *quasi-Fermi level of holes* and the Fermi level. This is represented schematically in **fig. 4.13**, from where the activation energy of the recombination reaction can be visualised. It is then expected that the reorganisation energy λ_r will include contribution from the desolvation of the intermediate species and the re-accommodation of the CdS site into the crystal lattice. This conceptual analysis highlights the importance of the interaction between the cation and the electrolyte. In the case of Cl^-, the large affinity of the anion for Cd ions is expected to destabilise the semiconductor surface. It could be interesting to extend this analysis to other electrolytes, in order to compare the dissolution kinetics for various complexing agents and anionic species.

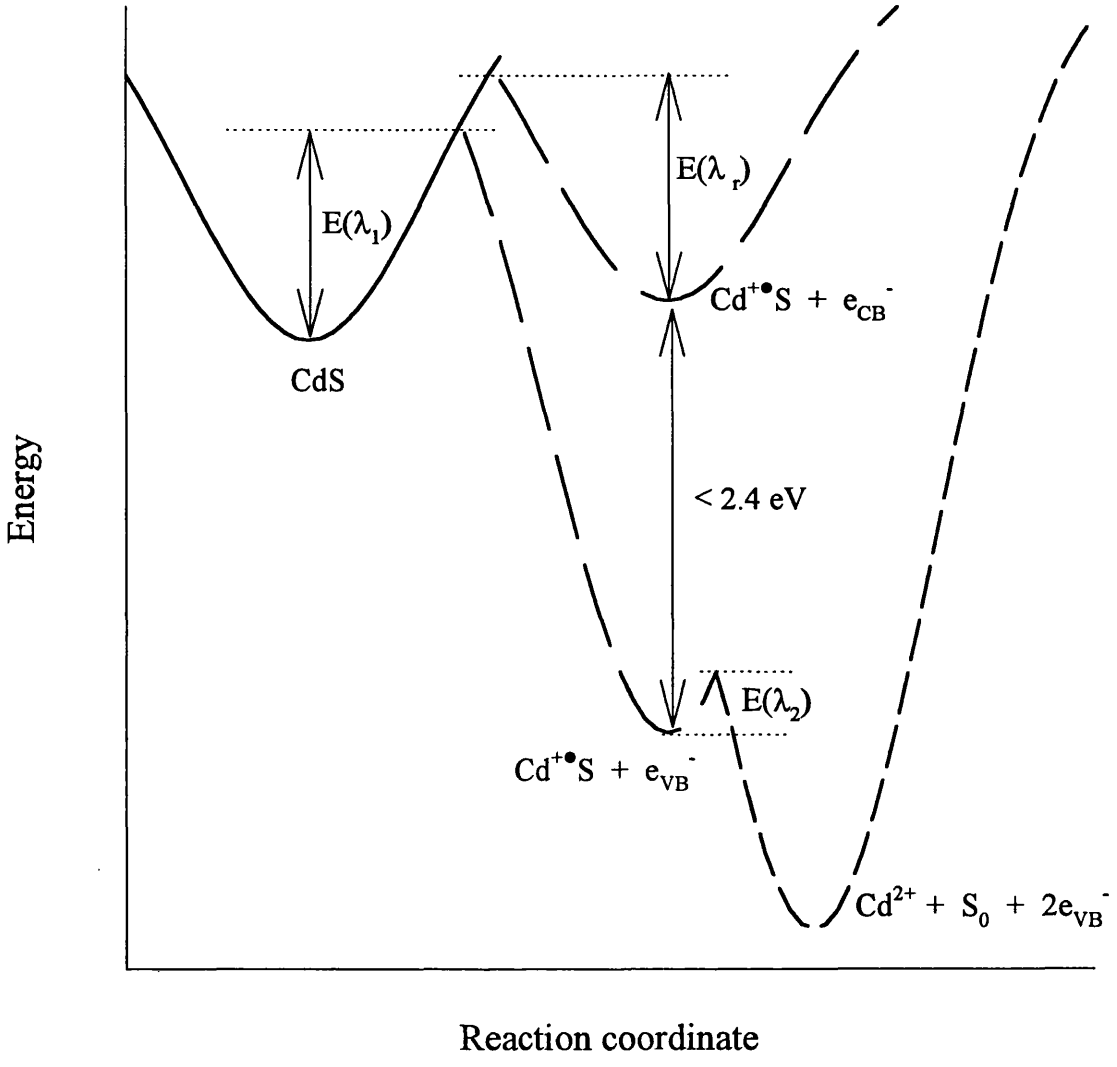

Fig. 4.13. Schematic energy diagram of the photocorrosion mechanism. Note that the activation energy for the first hole transfer, $E(\lambda_1)$, is higher than for the second step, $E(\lambda_2)$.

4.6. Conclusion

The kinetics of the elementary steps involved in the photodissolution of CdS were analysed by steady state measurements, IMPS and PEIS. It was confirmed that the basic mechanism can be described in terms of a first hole capture by an active site, generating an intermediate which can either capture a second hole to complete the dissolution, or recombine with an electron from the conduction band.

The accumulation of photogenerated sulfur affects the behaviour of the interface under illumination. Among the most relevant effects is the decrease of k_2, giving rise to a surface accumulation of charged intermediates. This surface charging introduces a light intensity dependent concentration of majority carriers.

IMPS spectra at various light intensity provide information about the rate constant of each of the elementary steps. It was estimated that the capture cross section for the first hole transfer is four orders of magnitude smaller than for the second step. This result was conceived in terms of a higher reorganisation energy for the generation of the intermediate, which include a large degree of bond breaking and cation solvation. The recombination process was also found to involve an activated state, which also corresponds to "pushing out" the solvent molecules from the cation and re-allocate the site in the crystal lattice.

Appendix 4.1

Derivation of the PEIS for two hole transfer mechanism.

It follows that from eqs. (4.18) and (4.19), the ac component of the charge accumulated in the space charge region ($Q_{(t)}$) is:

$$i\omega Q_{(t)} = -j_1 - k_3 X_1^{(I)} - \Delta k_3 X_0^{(I)} \tag{4.36}$$

where j_1 is the amplitude of the ac component of the external current. Combining eqs. (4.18) to (4.20) and (4.36), gives

$$V_0\left(i\omega C + AX_0^{(I)}k_3\right) = j_0 + k_3 X_1^{(I)} \tag{4.37}$$

Eqs. (4.36) and (4.37) allow the derivation of $X_1^{(I)}$:

$$X_1^{(I)} = \frac{Ak_3X_0^{(I)}V_0\left(k_1 + k_2X_0^{(I)} + i\omega\right)}{2k_1k_2p_0^{(I)} + k_1k_3 + k_2k_3X_0^{(I)} - \omega^2 + i\omega\left(k_1 + k_2\left(X_0^{(I)} + p_0^{(I)}\right) + k_3\right)} \qquad (4.38)$$

and finally the impedance is given by eqs. (4.37) and (4.38),

$$Z^{(I)} = \frac{1}{i\omega C_{SC} + Ak_3X_0^{(I)} \dfrac{2k_1k_2p_0^{(I)} - \omega^2 + i\omega\left(k_1 + k_2\left(X_0^{(I)} + p_0^{(I)}\right)\right)}{2k_1k_2p_0^{(I)} + k_1k_3 + k_2k_3X_0^{(I)} - \omega^2 + i\omega\left(k_1 + k_2\left(X_0^{(I)} + p_0^{(I)}\right) + k_3\right)}} \qquad (4.39)$$

Eq. (4.39) describes the frequency dependent impedance under illumination. Eqs. (4.26) and (4.27) are obtained assuming that $k_1 >> k_3$. This assumption is valid for the set of rate constants use in this work.

4.7. References

1 J. Reichman, Appl. Phys. Lett., **93** (1980) 574.

2 W.J. Albery, P.N. Bartlett, A.N. Hamnett and P. Dare-Edwards, Electrochem. Soc., **128** (1981) 1492.

3 F. El Guibaly, K. Colbour and B.L. Funt, J. Appl. Phys., **53** (1981) 3480.

4 R.H. Wilson, in A.J. Nozik (Ed.), *Photoeffects at Semiconductor-Electrolyte Interfaces*, ACS Symposium Series 146, Americal Chemical Society, Washington, 1981, p. 103.

5 J.J. Kelly and R. Memming, J. Electrochem. Soc., **129** (1982) 730.

6 J.-N. Chazalviel, J. Electrochem. Soc., **129** (1983) 963.

7 L.M. Peter and R. Peat, J. Electroanal. Chem., **165** (1984) 29.

8 J. Li, R. Peat and L.M. Peter, J. Electroanal. Chem., **165** (1984) 41.

9 L. M. Peter, in D. Pletcher (Ed.), *Specialist Periodical Report*, Vol. 9, 1984, The Royal Society of Chemistry, London, Ch. 2.

10 L.M. Peter, Chem. Rev., **90** (1990) 753.

11 D. Mao, K.-J. Kim and A. Frank, J. Electrochem. Soc., **142** (1995) 1869.

12 J. Li and L.M. Peter, J. Electroanal. Chem., **193** (1985) 27.

13 R. Peat and L.M. Peter, J. Electroanal. Chem., **228** (1987) 351.

14 A.R. de Wit, D. Vanmaekelbergh and J.J. Kelly, J. Electrochem. Soc., **139** (1992) 2508.

15 E.A. Ponomarev and L.M. Peter, J. Electroanal. Chem., **396** (1995) 219.

16 E.A. Ponomarev and L.M. Peter, J. Electroanal. Chem., **397** (1995) 45.

17 L.M. Peter, E.A. Ponomarev and D.J. Fermin, J. Electroanal. Chem., submitted.

18 D. Lincot and J. Vedel, J. Electroanal. Chem., **220** (1987) 179.

19 D. Vanmaekelbergh, A.R. de Wit and F. Cardon, J. Appl. Phys., **73** (1992) 5049.

20 D. Vanmaekelbergh and F. Cardon, Electrochim. Acta, **37** (1992) 837.

21 J. Schefold, J. Electroanal. Chem., **341** (1992) 111.

22 J. Schefold, J. Electroanal. Chem., **394** (1995) 35.

23 G. Schlichtorl, E.A. Ponomarev and L.M. Peter, J. Electrochem. Soc., **142** (1995) 3062.

24 H. Gerischer and W. Mindt, Electrochim. Acta, **82** (1968) 1329.

25 A.B. Ellis, S. Kaiser and M.S. Wrighton, J. Am. Chem. Soc., **98** (1976) 1635.

26 B. Miller and A. Heller, J. Electrochem. Soc., **124** (1977) 697.

27 H. Gerischer and J. Goebrecht, Ber. Bunsenges. Phys. Chem., **82** (1978) 520.

28 R.H. Wilson, J. Electrochem. Soc., **126** (1979) 1187.

29 J.R. Wilson and S.-M. Park, J. Electrochem. Soc., **129** (1982) 149.

30 A.R. de Wit and J.J. Kelly, J. Electroanal. Chem., **336** (1992) 125.

31 R.D. Rauh, in H.O. Finklea, *Semiconductor electrodes*, ch. 6, Elsevier, Amsterdan, 1988.

32 R.H. Bube, *Photoelectronic properties of semiconductors*, Cambridge University Press, 1992, ch.5, p 82.

33 W.P. Gomes and H.H. Goosens, in H. Gerischer and C.W. Tobias (Eds.), *Advances in Electrochemical Science and Engineering*, vol. 3, VCH, Weinheim, 1994, p.1.

34 H. Gerischer and M. Lübke, Ber. Bunsenges. Phys. Chem., **87** (1983) 123.

35 H. Gerischer, J. Electroanal. Chem., **82** (1977) 133.

36 R.A. Marcus, J. Chem. Phys., **24** (1956) 966.

37 R.A. Marcus, J. Phys. Chem., **43** (1965) 679.

38 See S.R. Morrison, *Electrochemistry at Semiconductors and Metal Oxidized Electrodes*, Plenum Press, New York, 1980.

39 D.J. Fermin and L.M. Peter, unpublished results..

40 B. Meyer, M. Gouterman, D. Jensen, T.V. Oommen, K. Spitzer and T. Stroyer-Hansen, in R.F. Gould (ed), *Sulfur Research Trends*, ACS, 1972, ch. 4

41 W.J. Albery, N.L. Dias and C.P. Wilde, J. Electrochem. Soc., **134** (1987) 601.

42 D. Meissner, R. Memming and B. Kastening, J. Phys. Chem., **92** (1988) 3484.

43 G. H. Schoenmakers, D. Vanmaekelbergh and J.J. Kelly, J. Phys. Chem., **100** (1996) 3215.

44 H. Erbse, K. Hauffe and J. Range, Z. Phys. Chem. N.F., **74** (1971) 248.

45 A.J. Bard and L.R. Faulkner, *Electrochemical Methods*, John Wiley & Sons, N.Y., 1980, ch.9.

46 D.D. Macdonald, *Transient Techniques in Electrochemistry*, Plenum Press, N.Y., 1977.

47 R. Peat, A. Riley, D.E. Williams and L.M. Peter, J. Electrochem. Soc., **136** (1989) 3352.

48 R.S. Hutton and D.E. Williams, Electrochim. Acta, **39** (1994) 701.

CHAPTER 5

Characterisation of the n-CdS/Na_2SO_3 interface

Abstract

The CdS/sulfite interface under illumination was studied by steady state photocurrent and capacitance, as well as by photo-capacitance transients, Intensity Modulated Photocurrent Spectroscopy (IMPS) and Photoelectrochemical Impedance Spectroscopy (PEIS). It was confirmed that alkaline sulfite solutions effectively suppress photocorrosion of single crystals electrodes. A nearly ideal photocurrent-potential behaviour was observed even up to the flat band potential, indicating that surface recombination is negligible. This was confirmed by IMPS and PEIS spectra. Ideal behaviour was also observed even in pre-corroded surfaces, suggesting that recombination is suppressed not only by stabilisation of the surface but also due to a fast charge transfer. Chemical Bath Deposited (CBD) films exhibited recombination losses at all potentials, evidencing the strong influence of grain boundaries. IMPS responses on CBD films suggested that the oxidation mechanism involves the transfer of a single hole to SO_3^{2-}, generating radical species which undergo a disproportionation reaction. Photo-ionisation of donor states in the space charge region was also observed in single crystal electrodes. Two processes were associated with this observation: (i) a fast excitation related to shallow donors, and (ii) a slow excitation linked to hole traps located at 0.8 eV above the valence band.

5.1 Introduction

The correlations between structure and kinetics of interfacial processes at illuminated semiconductor-electrolyte junctions have been studied for a large variety of materials [1-3]. The influence of surface states on these processes may take place in several fashions: (i) by promoting the charge transfer to redox species, (ii) or enhancing the photocorrosion process, or (iii) acting as recombination centres. These states are physically introduced by grain boundaries, strongly adsorbed species and crystal dislocations generated by surface reconstruction or corrosion pits. However, one of the major obstacles to the characterisation of surface states is their critical dependence on the surface treatment.

The photoelectrochemistry of cadmium sulfide has been studied in a wide range of electrolytes, and fundamental aspects of charge transfer, corrosion and surface recombination have been addressed [4-12]. Alkaline sulfide electrolyte has proved to be one of the most efficient corrosion suppressors for CdS single crystals [5,11-13]. Although the detailed mechanism is not fully understood, the oxidation of sulfide in strong alkaline solution is generally described as:

$$2S^{2-} + 2h^{+} \rightarrow S_2^{2-} \qquad (5.1)$$

Capacitance measurements have shown that sulfide anions adsorb strongly on the semiconductor surface and the photocurrent onset is shifted to very low band bending. In order to rationalise these observations, Wilson [11] envisaged two types of roles for adsorbed sulfide anions; (i) inactivation of recombination centres and (ii) fast hole scavenging

The first approach considers that adsorbed sulfide anions can effectively passivate surface recombination centres [11]. In the absence of a corrosion suppresser, the kinetics of charge transfer are controlled by surface recombination in the photocurrent onset potential range [14, see also chapter 4]. The mechanism can be expressed as:

$$CdS + h^+ \longrightarrow Cd^{+\bullet}S \quad (5.2)$$

$$Cd^{+\bullet}S + h^+ \longrightarrow Cd^{2+} + S \quad (5.3)$$

$$Cd^{+\bullet}S + e^- \longrightarrow CdS \quad (5.4)$$

It has been determined that the first hole capture in the CdS photocorrosion is slower than the second, due to the activation energy involved in the formation of the radical species (chapter 4). The sulfide ions may interact with the radical species, hindering the capture of the second hole (dissolution) or an electron (recombination).

The second approach is based on a very efficient hole transfer to adsorbed sulfide species directly via the valence band. In this case, the adsorbed species introduce an energy level near the band edge, therefore the shift of the photocurrent onset to lower band bending is due to an increase in the charge transfer rate and not to a decrease in the recombination rate [11].

Herrasti et al. studied the CdS/sulfide-polysulfide interface by Intensity Modulated Photocurrent Spectroscopy (IMPS) [12]. They confirmed that surface recombination can be effectively suppressed in concentrated sulfide solutions. It was found that surface charging associated with the accumulation of charged intermediates is also negligible. These results seem to support the second approach, as the absence of surface excess charge under illumination can only be explained in terms of a very fast charge transfer rate. However, it is not possible from IMPS to quantify the charge transfer rate if there are no competing reactions.

Inoue et al. [15] reported that CdS is also stabilised in the presence of sodium sulfite in alkaline solutions. Photocorrosion suppression of nearly 100% was found at concentrations higher than 0.1 M. This electrolyte has been used in other studies where stable CdS single crystal surfaces were reported [6,13,16,17]. Two reactions have been associated with the sulfite oxidation [15]:

$$SO_3^{2-} + 2OH^- + 2h^+ \rightarrow SO_4^{2-} + H_2O \quad (5.5)$$

$$2SO_3^{2-} + 2h^+ \rightarrow S_2O_6^{2-} \quad (5.6)$$

The mechanisms associated with these reactions are considered later in section 5.4.

The present chapter describe studies of the CdS/sodium sulfite interface. Measurements of Steady state photocurrent and capacitance as well as photo-capacitance transients, IMPS and PEIS were performed. It was observed that the interface behaves similarly to the sulfide junction, however no evidence was obtained for sulfite adsorption. It is concluded that photocorrosion, recombination and surface charging are negligible due to a fast charge transfer rate, probably via the valence band.

5.2. Experimental

The surface preparation of the n-CdS single crystals electrodes was carried out according to the procedure discussed in section 3.4. A doping density of (1.16 ± 0.03) 10^{16} cm^{-3} and a flat band potential of -0.78 ± 0.01 V were obtained from capacitance measurements in 1.0 mol dm^{-3} Na_2SO_3 pH 12.

The counter-electrode and the reference electrode were a platinum disk and a Ag/AgCl electrode respectively. A three compartment electrochemical cell supplied with quartz windows was employed. Monochromatic illumination was provided by a blue Light Emitting Diode NLPB 500 from Nichia Chemical Industries (425 nm). Steady state photocurrent and capacitance measurements as well as capacitance transients were performed with a 5210 EG&G PAR lock in amplifier. IMPS and PEIS spectra were recorded with a fast home built potentiostat in conjunction with a Solartron 1250 Frequency Response Analyser (Schlumberger), allowing reliable measurements up to 30 kHz.

5.3. Results

Normalised photocurrent-potential curves for the Cd-face electrode are displayed in **fig. 5.1**. It is observed that the fall of the quantum efficiency occurs very close to the flat band potential, where considerable photocurrent can still be measured. These results resemble the behaviour reported by Herrasti et al. in sodium sulfide/polysulfide [12]. Another interesting observation is the unusual structure of the photocurrent-potential curves between -0.5 to -0.85 V at low illumination levels. This feature is only detected at photocurrent densities below 1 μA cm^{-2}. The S-face electrode did not show this behaviour at any light intensity. Similar features can be also observed in current potential cycles of the Cd-face electrode in the dark. **Fig. 5.2** exhibits continuous

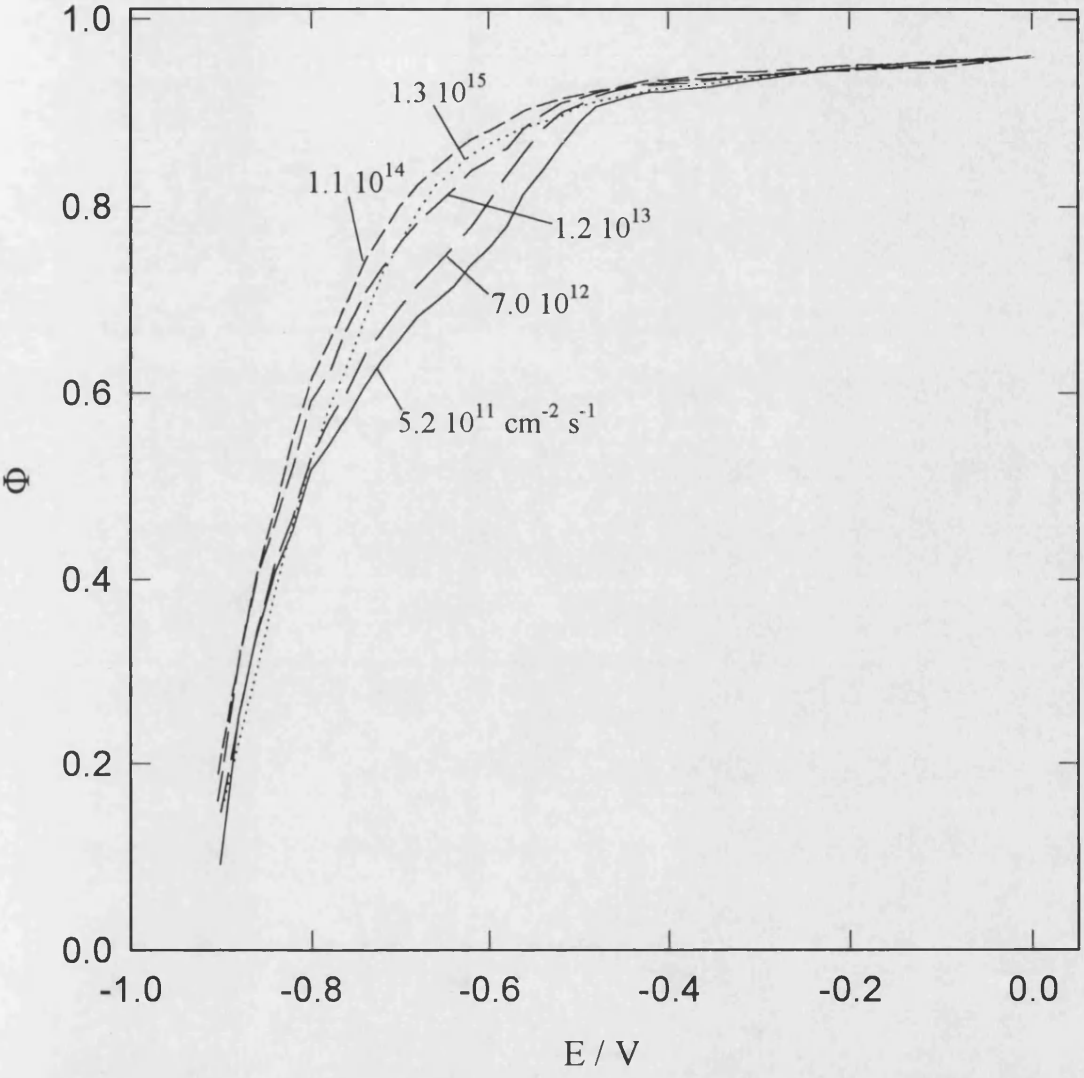

Fig. 5.1 Normalised photocurrent-potential curves of the n-CdS single crystal (Cd-face) electrode in 1.0 mol dm^{-3} Na_2SO_3 pH 12 at various holes fluxes.

current-potential cycles at various negative potential limits, taking 0.0 V as the starting potential. The anodic reverse scan shows a similar structure to the observed in the photocurrent potential curve only when the potential limit was shifted to more negative than -0.6 V. This evidence suggest that this feature could be associated with surface redox species involving Cd^{2+} ions.

It is also seen in **fig. 5.1** that the photocurrent potential relation is nearly unaffected by the light intensity. This result contrasts quite clearly with the behaviour observed in KCl at low pH (cf. **fig. 4.4**). Moreover, it also disagrees with the analysis carried out in section 2.3, where it was demonstrated that as long as the intermediates species are involved in the surface recombination process, the steady state photocurrent-potential relationship depends on the light intensity.

Photocurrent-potential curves for chemically bath deposited (CBD) CdS thin films are displayed in **fig. 5.3**. The film thickness was ca. 100 nm [18], as estimated from the geometrical capacitance. Low conversion efficiencies (without correction for reflection and transmission losses) and potential dependent photocurrents were recorded at all potentials. It can be also observed that photocurrent curves depend on light intensity especially at high band bending. Clearly, the behaviour of the photocurrent-potential curves on CBD films is different to those derived for *Cases I and II* (see section 2.3). Firstly, curves at various light intensity tend to a common photocurrent onset potential range. It is expected for *Case I and II* that the photocurrent onset shifts to more negative potentials as the light intensity is increased. Secondly at high band bending, the normalised photocurrent decreases with increasing light intensities. These results indicate that recombination is effectively present at all potentials, showing the important effect of the surface structure on the kinetics of charge transfer. For thin films, it could be expected that recombination occurs at the surface and also in the space charge region.

Fig. 5.4a shows photocurrent-potential curves obtained in concentrated and dilute sulfite solutions. In dilute solutions, no photocurrent saturation is observed and the photocurrent falls almost to zero at potentials close to the flat band. By contrast, capacitance measurements in the dark were independent of sulfite concentration. The photocurrent behaviour in dilute sulfite solution suggests the presence of photocorrosion process and surface recombination. The independence of the space

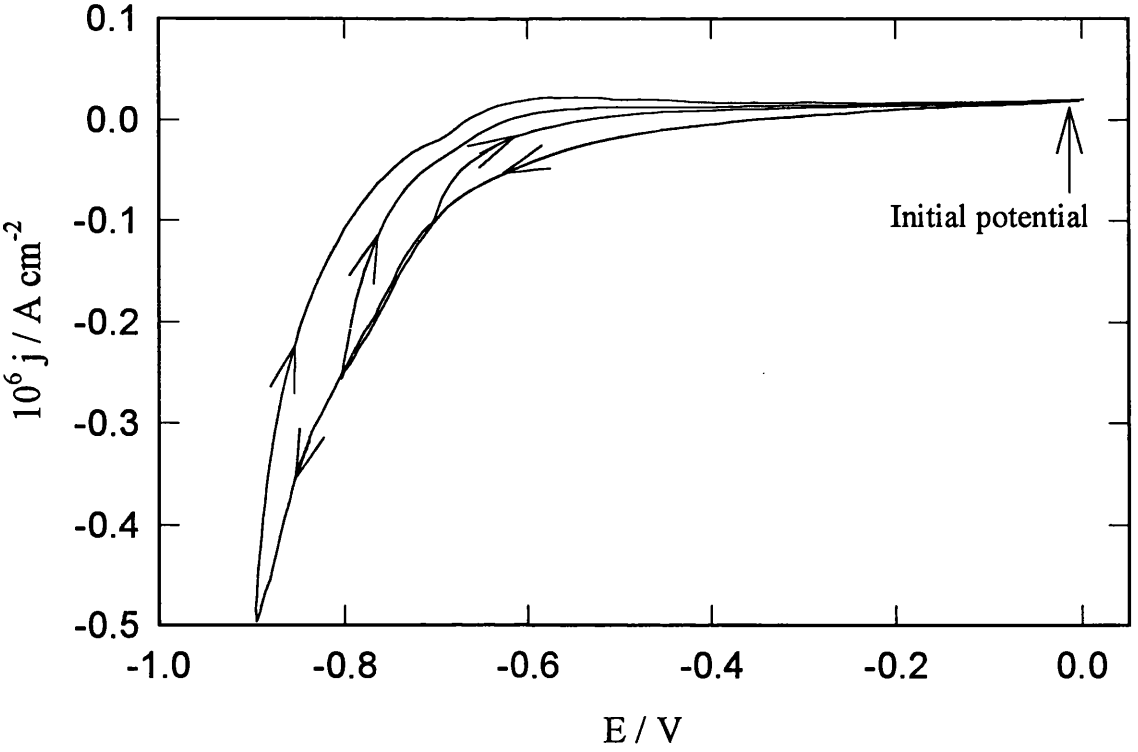

Fig. 5.2 Dark current-potential curves of the n-CdS (Cd-face) electrode in 1.0 mol dm^{-3} Na_2SO_3 pH 12. Scan rate 10 mV s^{-1}. Note the structure in the anodic cycle when the potential is swept to very negative potentials.

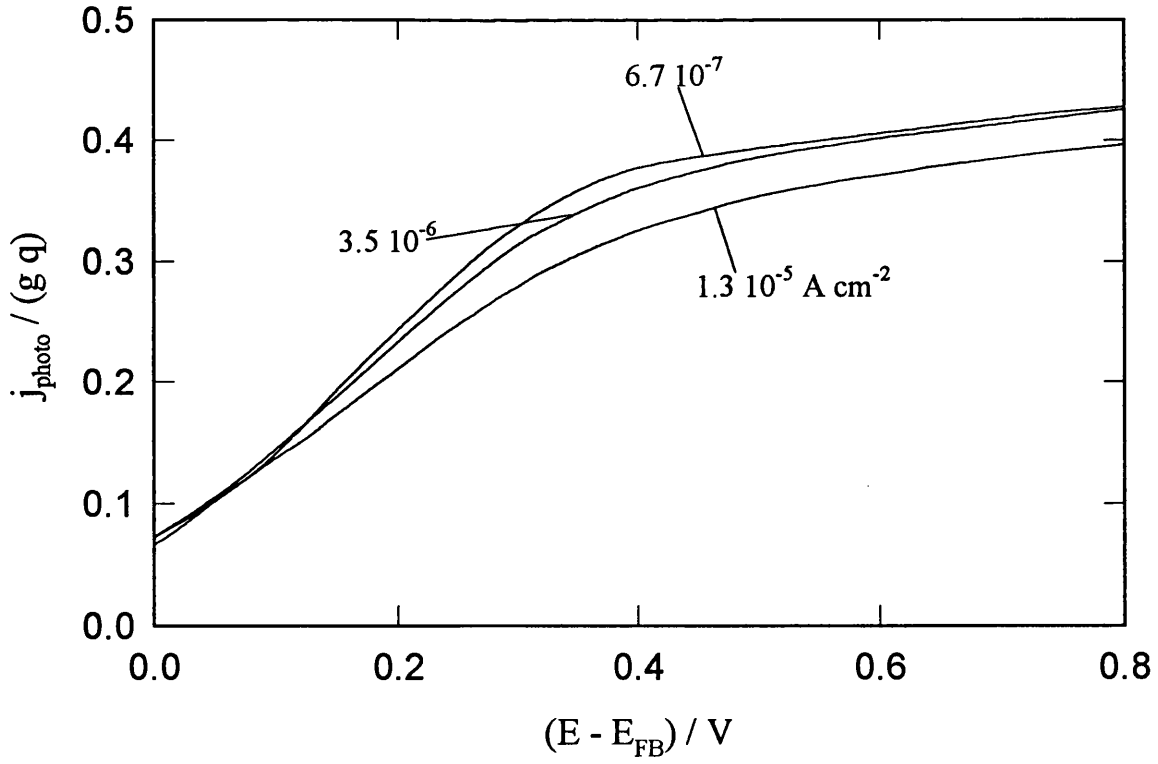

Fig. 5.3. Normalised photocurrent-potential curves for CdS CBD thin film electrodes at various light intensity (given in photocurrent density). Reflection and transmission losses are not considered.

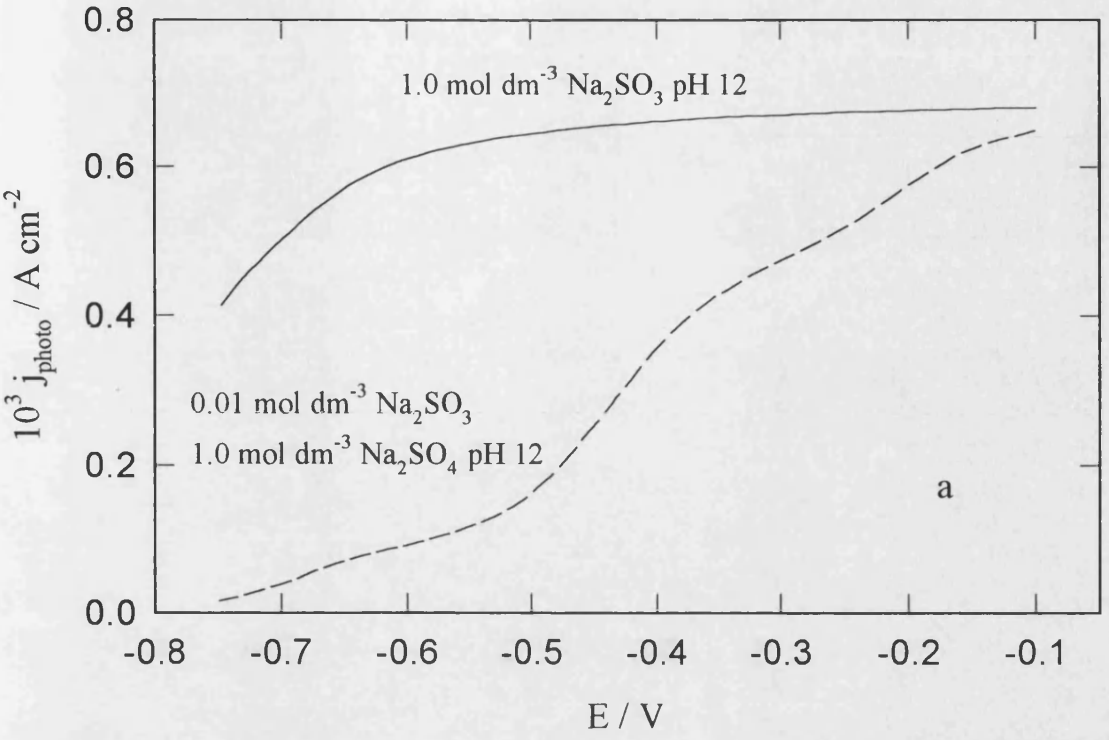

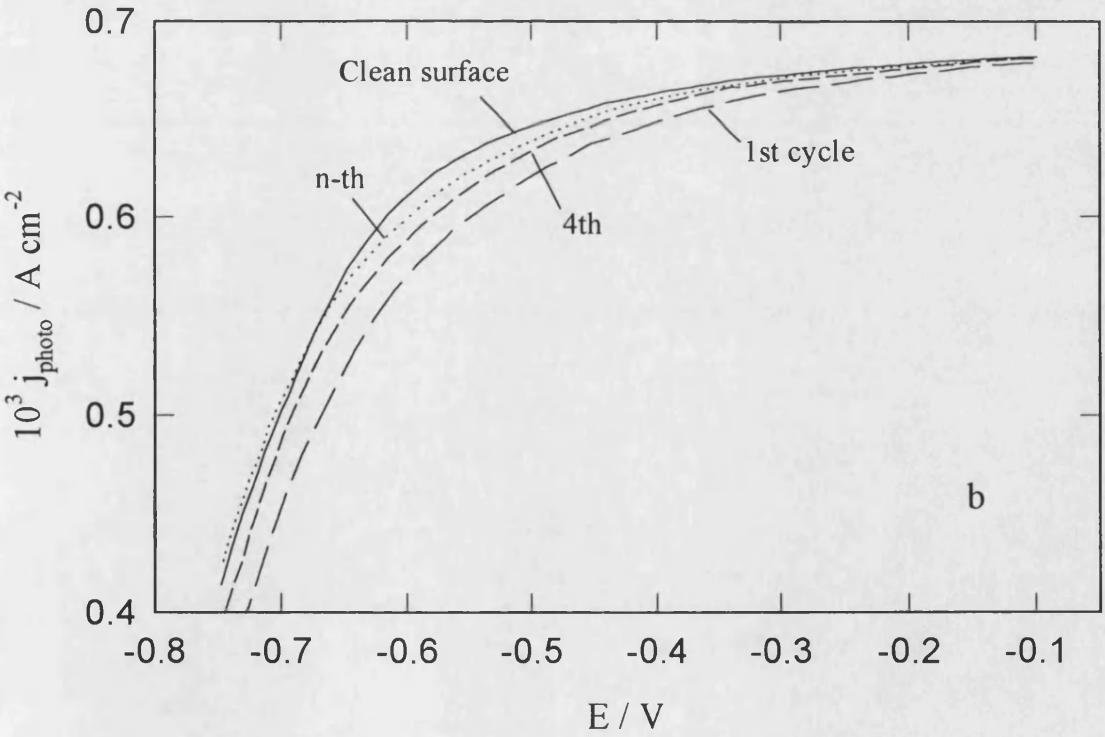

Fig. 5.4. (a) Photocurrent-potential curves of n-CdS single crystal in different sulfite concentrations. After the experiment in dilute sulfite solution, the electrode was reintroduced into 1.0 mol dm^{-3} Na_2SO_3, and the subsequent evolution of the photocurrent is shown in (b).

charge capacitance with the sulfite concentration also indicates that the anion is not strongly adsorbed on the semiconductor surface.

Fig. 5.4b contrasts the photocurrent-potential behaviour of photo-corroded and freshly etched surfaces in concentrated sodium sulfite solution. After recording the experiment in the dilute sulfite solution shown in **fig. 5.4a**, the electrode was rinsed with distilled water and immersed in the concentrated sulfite electrolyte. Initially, it can be seen that the photocurrent decay in the corroded electrode occurs at slightly higher potentials, but, the behaviour of the clean surface is almost restored after several cycles. This surprising results shows that, even in the presence of surface defects, charge transfer at the single crystal/sulfite junction is still very efficient.

Mott-Schottky plots at various illumination levels are shown in **fig. 5.5a**. Only a small shift of the flat band potential toward more negative values was observed under illumination. This effect is nearly independent of the hole flux, indicating that band edge shifts associated with surface charging is almost negligible [19-22]. On the other hand, **fig. 5.5b** shows the apparent doping density as a function of the hole flux. The increment of the doping density with increasing illumination levels has also been observed in sulfate solutions (see **fig. 4.5**) and in alkaline sulfide solutions. As the surface processes are different for each of these electrolytes, this effect can be attributed to space charge-bulk properties.

The behaviour of the capacitance under illumination suggests the presence of hole trapping centre. Steady state photocapacitance spectroscopy in the visible region did not provide clear information about energy states related to this phenomenon. Analysis of the change in capacitance as a function of time after a supra band gap illumination pulse proved to be a more successful approach. **Fig. 5.6** shows the capacitance measure at 10 kHz after interrupting an illumination intensity of $7.2\ 10^{-4}$ A cm^{-2} (425 nm) at various potentials. Two time domains are observed for the capacitance relaxation after switching off the illumination, (i) a very fast decay virtually in phase with the light perturbation, and (ii) a slow relaxation over a few seconds. These result reveals that the origin of the photocapacitance is rather complex, involving at least two different trap centres.

IMPS spectra were recorded in the potential dependent photocurrent region. **Fig. 5.7** exhibits only clustering points on the real axis even at potentials very near to

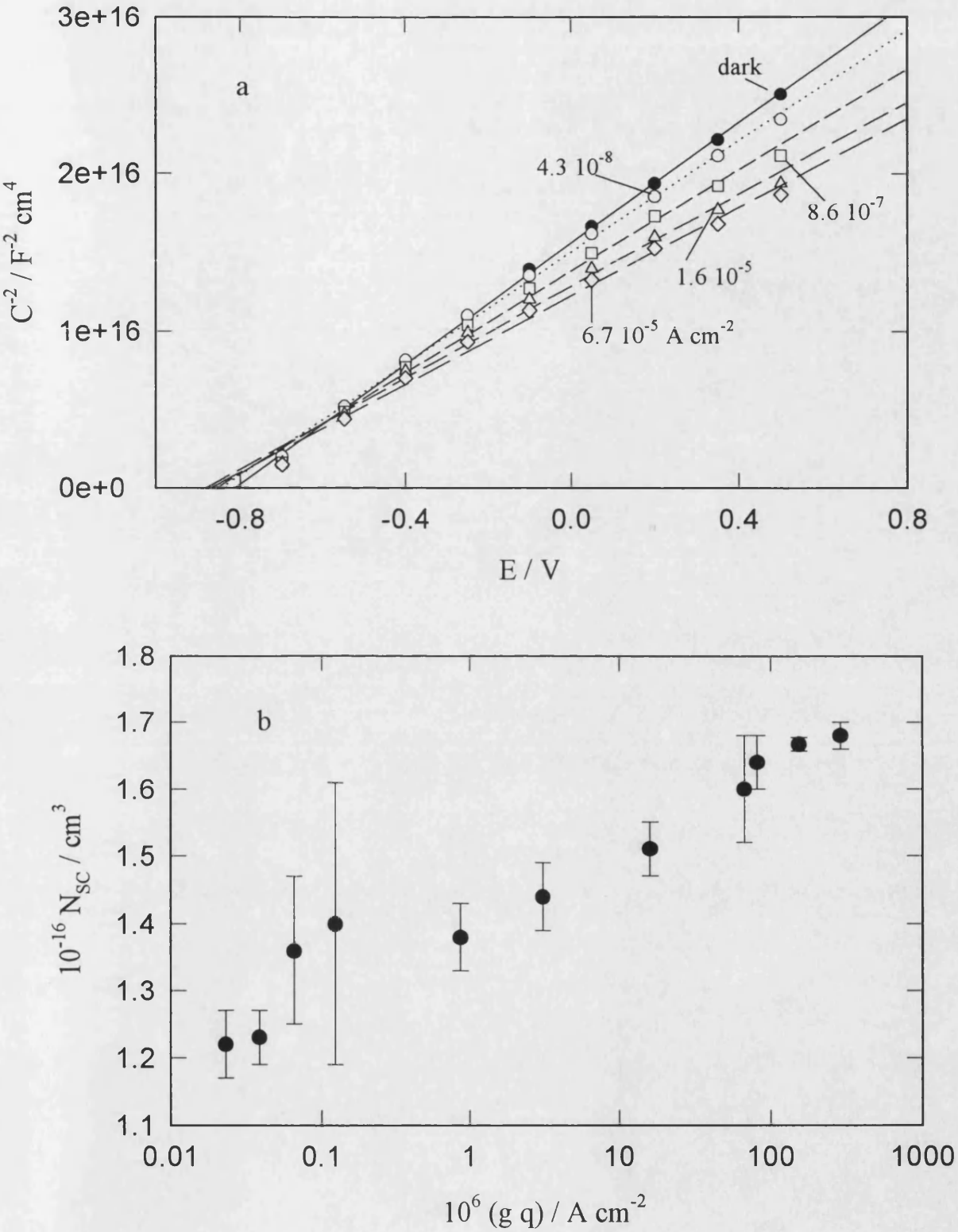

Fig. 5.5 (a) Mott-Schottky plots of the CdS /1.0 mol dm^{-3} Na_2SO_3 pH 12 interface in the dark and at various light intensities (given in photocurrent density units). Note that the E_{FB} does not change under illumination, while (b) N_{SC} increases with increasing g.

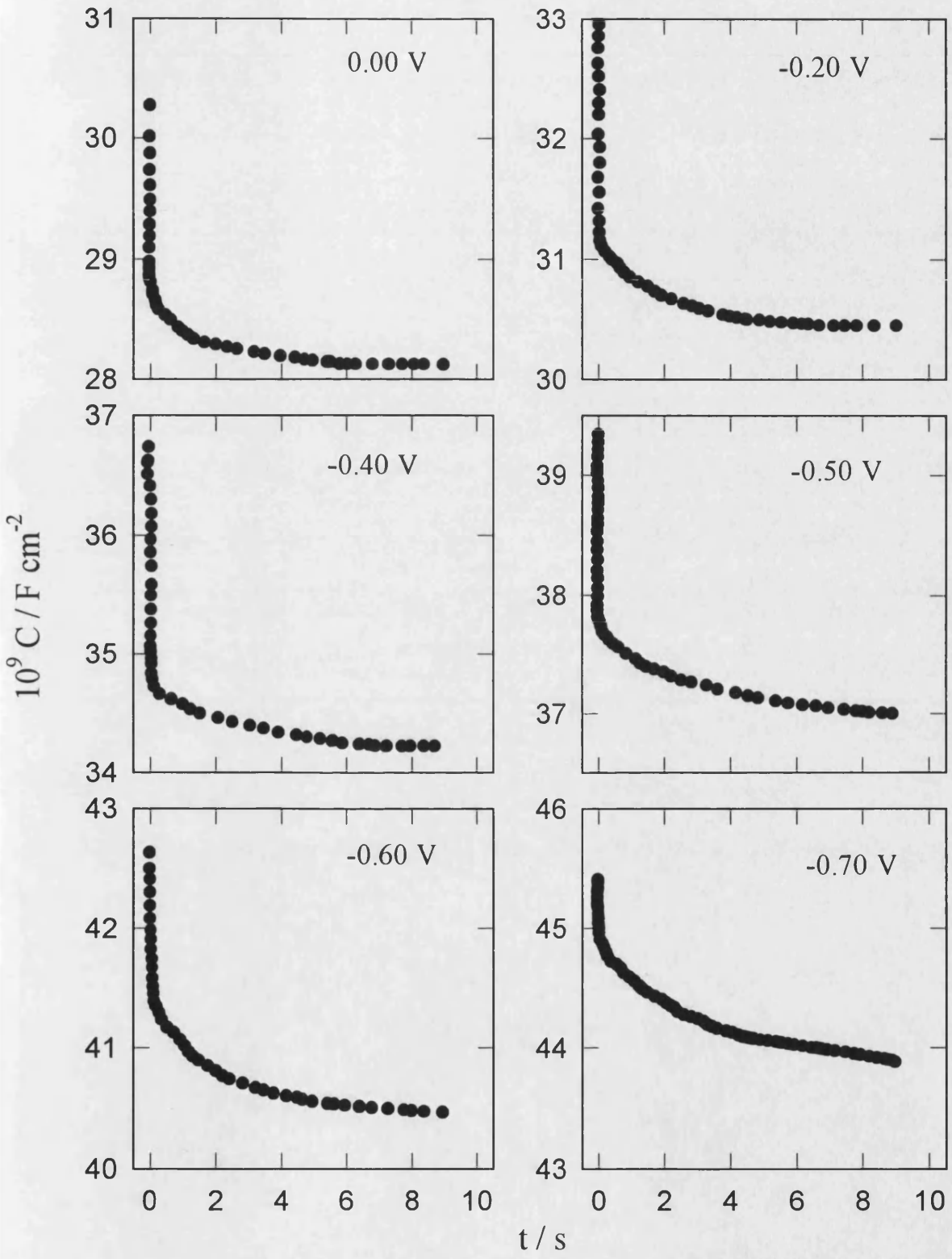

Fig. 5.6. Photo-capacitance decay after interrupting an illumination intensity of 7.2 10^{-4} A cm^{-2} at various potentials.

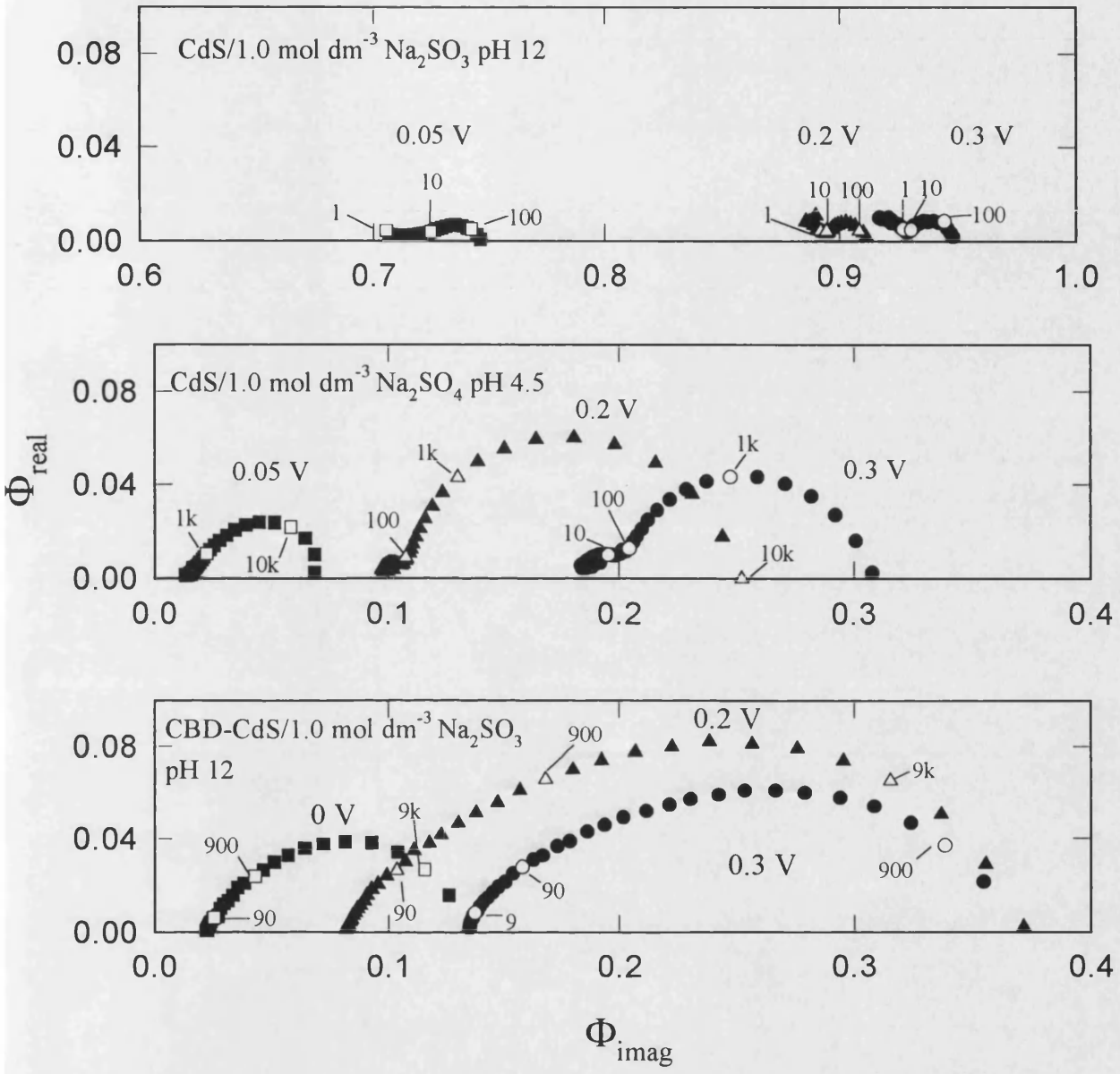

Fig. 5.7. IMPS spectra of CdS single crystal in alkaline sulfite and acid sulfate solutions, and also of CBD thin films in sulfite solutions at various band bending.

the flat band. These results are contrasted with the behaviour obtained in 0.1 mol dm^{-3} Na_2SO_4 pH 4.5 (slightly acidic solutions were used in order to avoid the formation of cadmium hydroxide on the surface) and in CBD films in concentrated sulfite solutions. A high modulation depth of light was used (50%) in order to increase the magnitude of the ac photocurrent. Under identical experimental conditions, it is clearly seen that the CdS/SO_4^{2-} and the $CdS_{(CBD)}/SO_3^{2-}$ junctions exhibit recombination processes, in contrast to the CdS/SO_3^{2-} interface which behave almost ideally.

Fig. 5.8 shows the striking differences in the steady state normalised photocurrent-potential curves of the three junction previously mentioned. The strong decay of the photocurrent with decreasing potential for the CdS single crystal in the presence of sulfate contrasts with the high conversion efficiencies observed in sulfite even at the flat band potential. The photocurrent in CdS thin film also exhibits a weak potential dependence. In the case of the single crystal/sulfite interface, it is interesting to note that the conversion efficiency of the steady state curve coincides with the values of the real axis in the IMPS measurements (**fig. 5.7**).

Further differences between sulfate and sulfite electrolytes are revealed in the potential dependence of the PEIS responses shown in **fig. 5.9**. In the presence of sulfite, a single semicircle in the lower quadrant is observed. In the absence of the corrosion suppressor, two maxima are recorded as a function of the frequency at potentials near the photocurrent saturation region. In chapter 4, it was demonstrated that two maxima in the PEIS response can be interpreted in terms of a charge transfer-recombination competition. Consequently, the single time constant registered in sulfite solutions provides additional evidence for the absence of surface recombination at this interface. The semicircular PEIS response in this electrolyte is associated with the space charge capacitance and the depletion layer resistance.

5.4. Discussion

5.4.1. Cadmium sulfide/sulfite as an ideal interface

In principle, the independence of the photocurrent-potential relationship with the light intensity (c.f. **fig. 5.1**) is a rather unexpected behaviour for a multi-electron transfer process. However, IMPS and PEIS responses clearly point the fact that surface recombination in single crystal electrodes is effectively negligible in sulfite solutions.

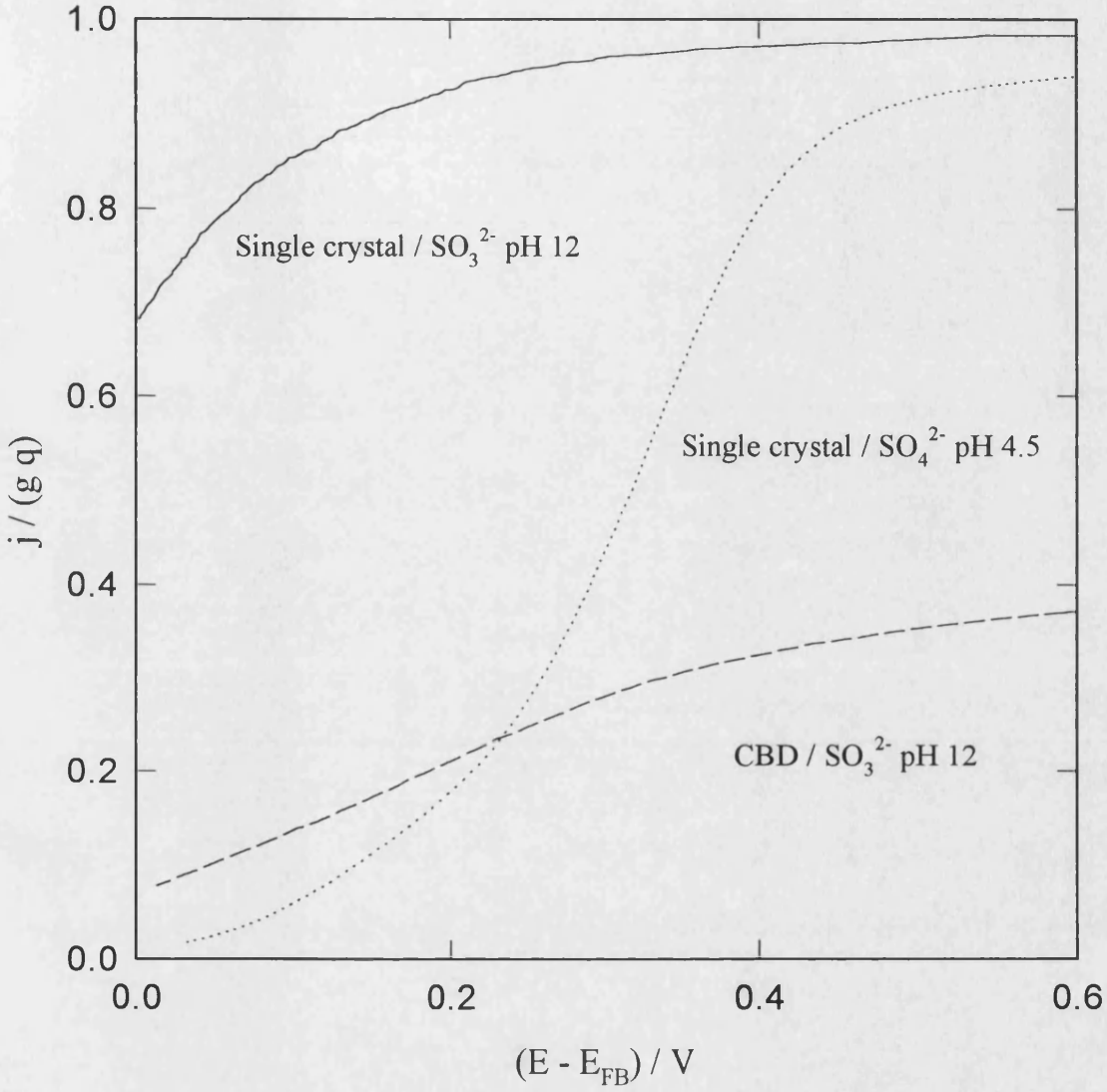

Fig. 5.8 Steady state photocurrent of the CdS single crystal and CBD thin film electrodes in various electrolytes.

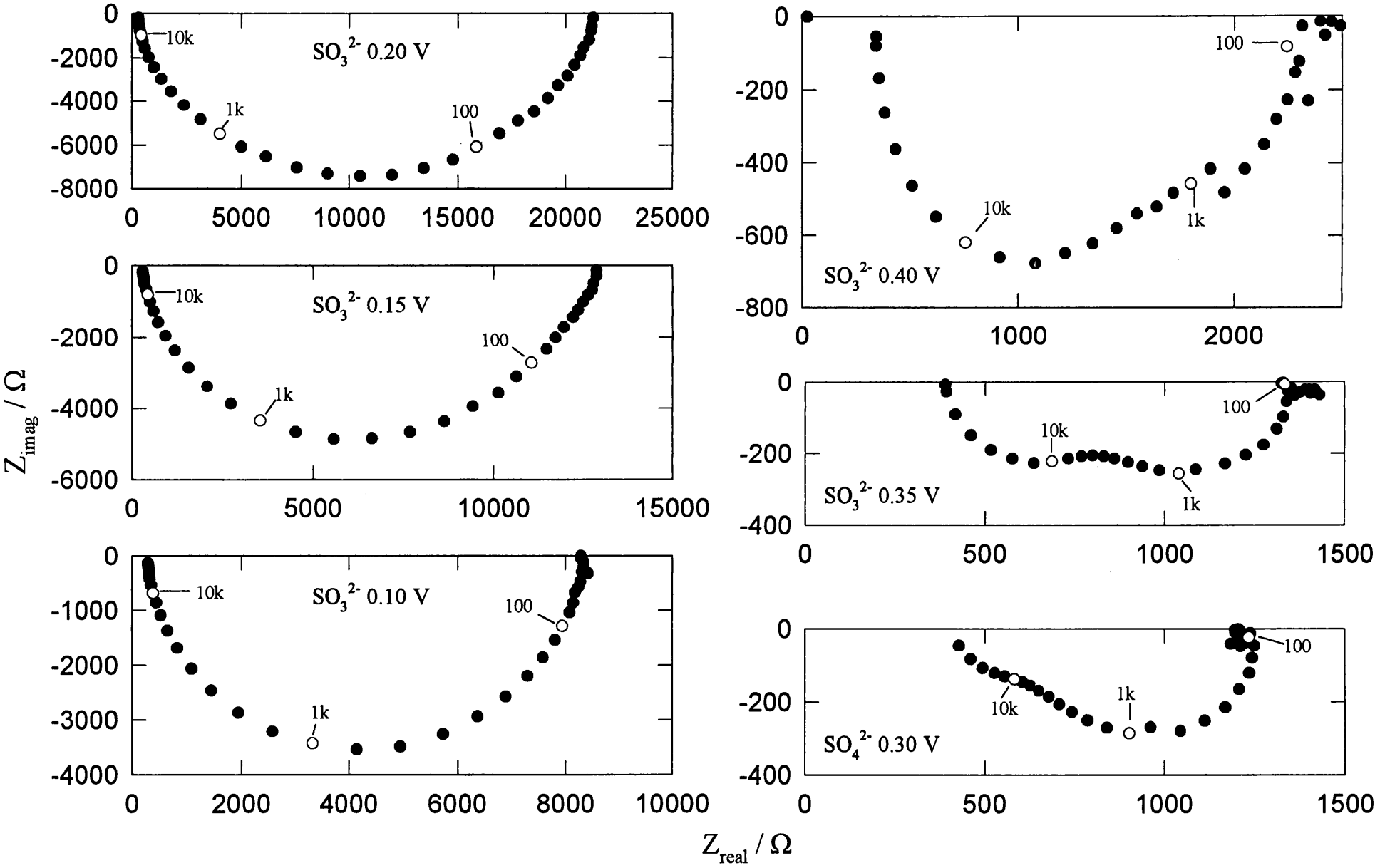

Fig. 5.9. PEIS spectra of the n-CdS single crystal electrode in 1.0 mol dm^{-3} Na_2SO_3 pH 12 and 0.1 mol dm^{-3} Na_2SO_4 pH 4.5 at various ($E - E_{FB}$). (gq) was 3.2 10^{-4} A cm^{-2}.

Under these conditions, the charge transfer is only determined by the number of holes reaching the surface. Furthermore, Mott Schottky plots under illumination (**fig. 5.5**) suggest that surface charge accumulation is also negligible, indicating that the absence of recombination is not only attributed to surface stabilisation but also to fast charge transfer. The same conclusion can be drawn from the photocurrent potential behaviour of partially corroded surfaces (**fig. 5.4**). After being exposed to photocorrosion conditions, the single crystal surface undergoes a stabilisation process in the presence of sulfite (notice the changes in the initial cycles), and after several cycles, the photocurrent-potential relation typical of freshly etched surfaces is restored.
Although the studies on single crystal electrodes did not provide direct information regarding the charge transfer mechanism, later analysis of the IMPS responses on CBD films suggest that the oxidation undergoes a *single* charge transfer step.

As mentioned previously, the photocurrent in single crystal electrodes is determined by the flux of holes to the surface, which is given by the Gärtner expression introduced in section 1.3 (see eq. (1.6)). **Fig. 5.10** shows a fit of the Gärtner equation to a steady state photocurrent-potential curve, using the doping density calculated from the Mott-Schottky plot at the same illumination level. Reasonable agreement was obtained for $\alpha = (1.4 \pm 0.2)10^5$ cm^{-1} and $L_p = (9.0 \pm 0.2)10^{-6}$ cm. The value of α coincides with that reported by Chmiel and Gerischer at 488 nm [23], while an identical estimation for L_p was reported by Herrasti et al. [12].

The independence of the steady state capacitance on the concentration of sulfite shows that these species are not chemically adsorbed on the semiconductor surface. Wilson [11] reported a shift of the flat band potential to more negative values and an increase of the density of donor states of CdS single crystal electrodes upon increasing concentration of sodium sulfide in the electrolyte. These effects occur as a result of an increase in the surface concentration of electrons associated with the chemisorption of S^{2-} and HS^- species. These phenomena are not observed in the case of SO_3^{2-}, which is an outstanding hole scavenging non-adsorbed electrolyte.

In contrast to the ideal behaviour of single crystal electrodes, CBD thin film features recombination losses, evidencing the importance of grain boundaries. The fact that the normalised photocurrent is dependent on light intensity even at very high band bending (**fig. 5.3**) suggests that recombination occurs at all potentials. The IMPS

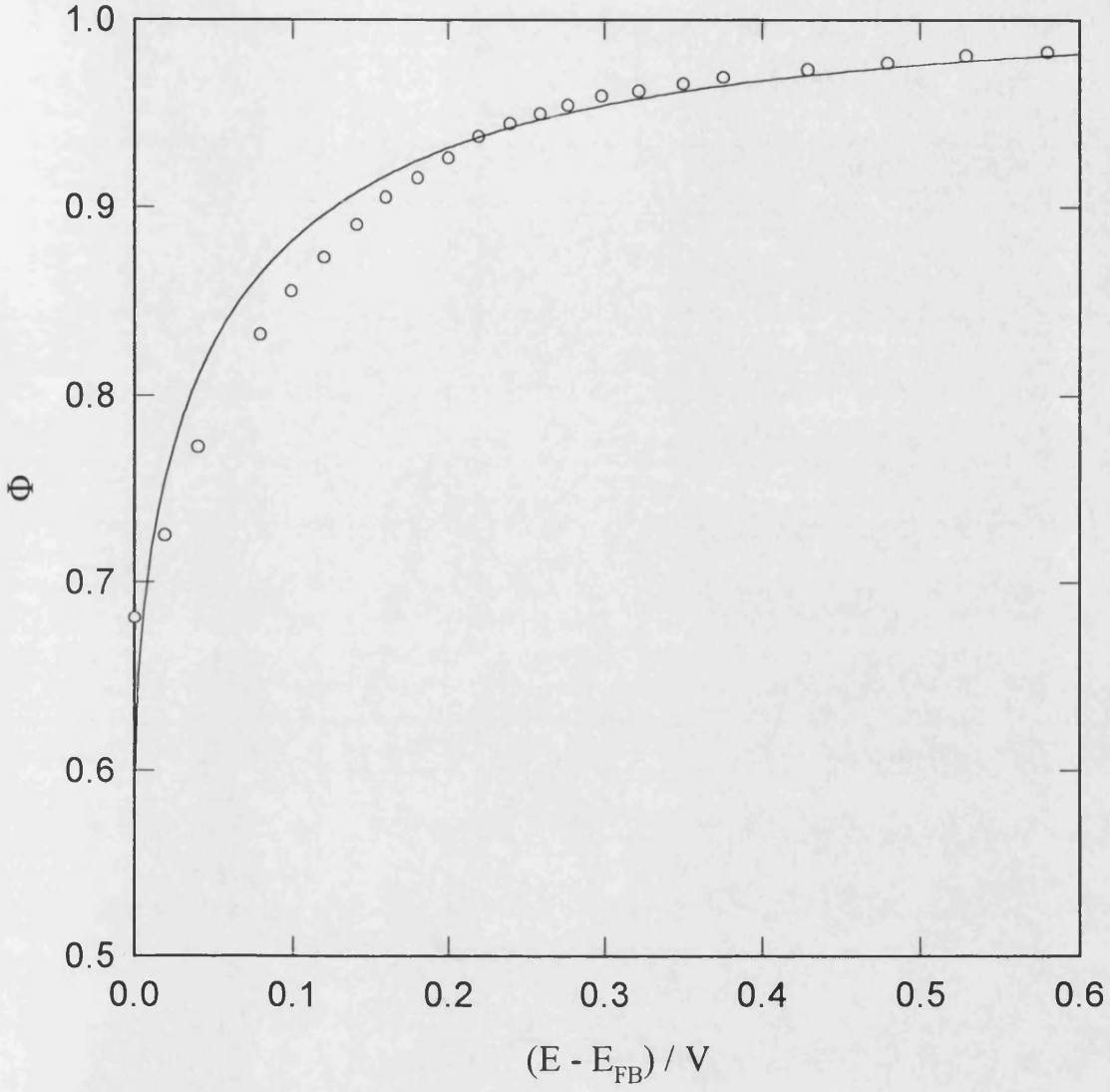

Fig. 5.10. Fit of the normalised photocurrent-potential curve of the CdS/Na_2SO_3 interface (corrected for reflection losses) to the Gartner expression (eq. 1.6). α and L_p were taken as $1.4\ 10^5\ cm^{-1}$ and $9\ 10^{-6}$ cm respectively.

responses shown in **fig. 5.7** exhibited very flattened semicircular responses. This interesting result resemble the theoretical response for a space charge recombination process according to the model of Vanmaekelbergh et al. [24]. The average grain size of this type films is of the same order of the film thickness [18], therefore recombination at grain boundaries is in fact a *volume* rather than surface recombination.

Fig. 5.11 displays the potential dependence of ω_{max} obtained from IMPS spectra of CdS CBD films (**fig. 5.7**). It can be seen that ω_{max} decreases weakly as the potential is increased, until it reaches a plateau at a critical value of E - E_{FB} of 0.6 V (E_c). At this potential, the space charge region becomes as thick as the semiconducting film. This result agrees with steady state capacitance measurements, where C_{SC} reaches its geometrical limit at E_c. The phenomenological k_{tr} and k_{rec} can be estimated from the low frequency intercept ($j_{(\omega=0)}$) and ω_{max}:

$$j_{(\omega=0)} = \frac{k_{tr}}{k_{tr} + k_{rec}} \tag{5.7}$$

$$\omega_{max} = k_{tr} + k_{rec} \tag{5.8}$$

Fig. 5.12 shows the potential dependence of k_{rec} and k_{tr}. k_{rec} decreases as the potential is increased until the critical potential E_c. This behaviour also reflects the potential independence of the interfacial concentration of electrons at potential higher than E_c. On the other hand, k_{tr} is potential independent over the whole potential range. The interesting behaviour of the phenomenological parameters resembles the response for a single charge transfer mechanism, where k_{rec} and k_{tr} are effectively the real recombination and charge transfer rate constants. It should be also note that the potential dependence of k_{rec} is rather weak, indicating Fermi Level pinning effects at the interface. This effect is probably associated with charge trapping at grain boundaries and surface defects.

The IMPS responses on CBD thin films can be interpreted in terms of a mechanism initiated by the transfer of a hole to generate a radical intermediate $SO_3^{\bullet-}$, which can dimerise to $S_2O_6^{2-}$. This mechanism can be represented as:

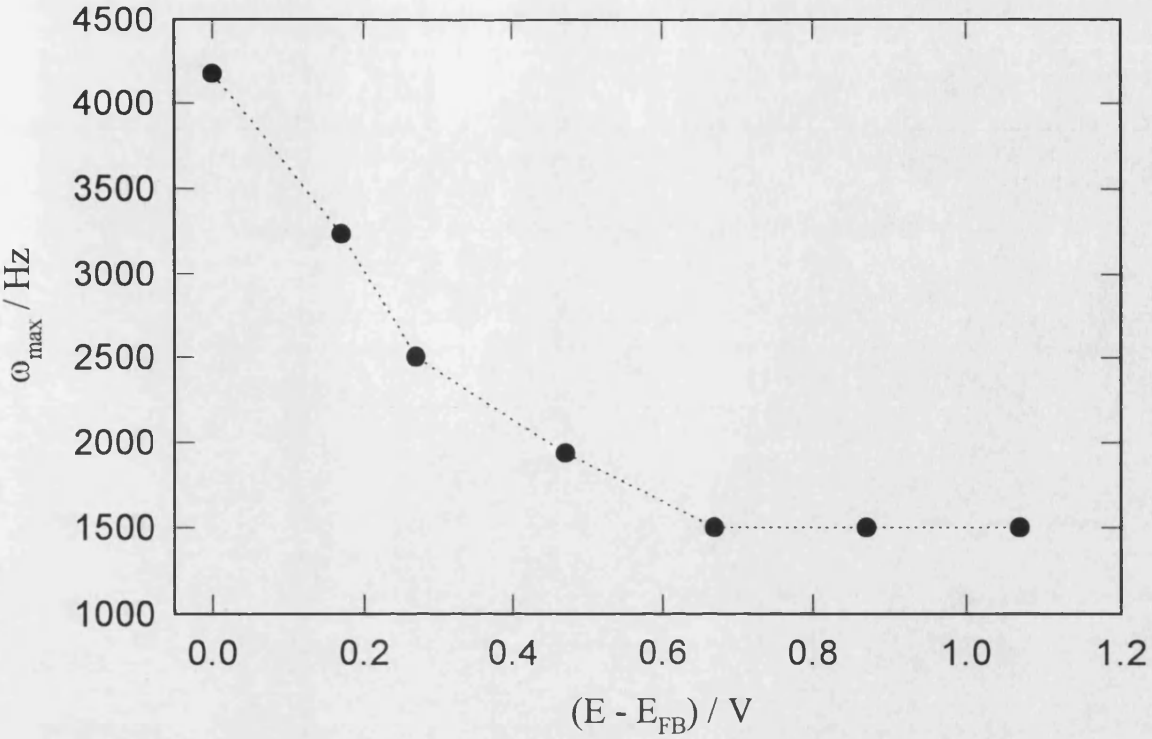

Fig. 5.11. ω_{max} as a function of the potential obtained from IMPS at the CdS CBD thin film electrode in 1.0 mol dm^{-3} Na_2SO_3 pH 12.

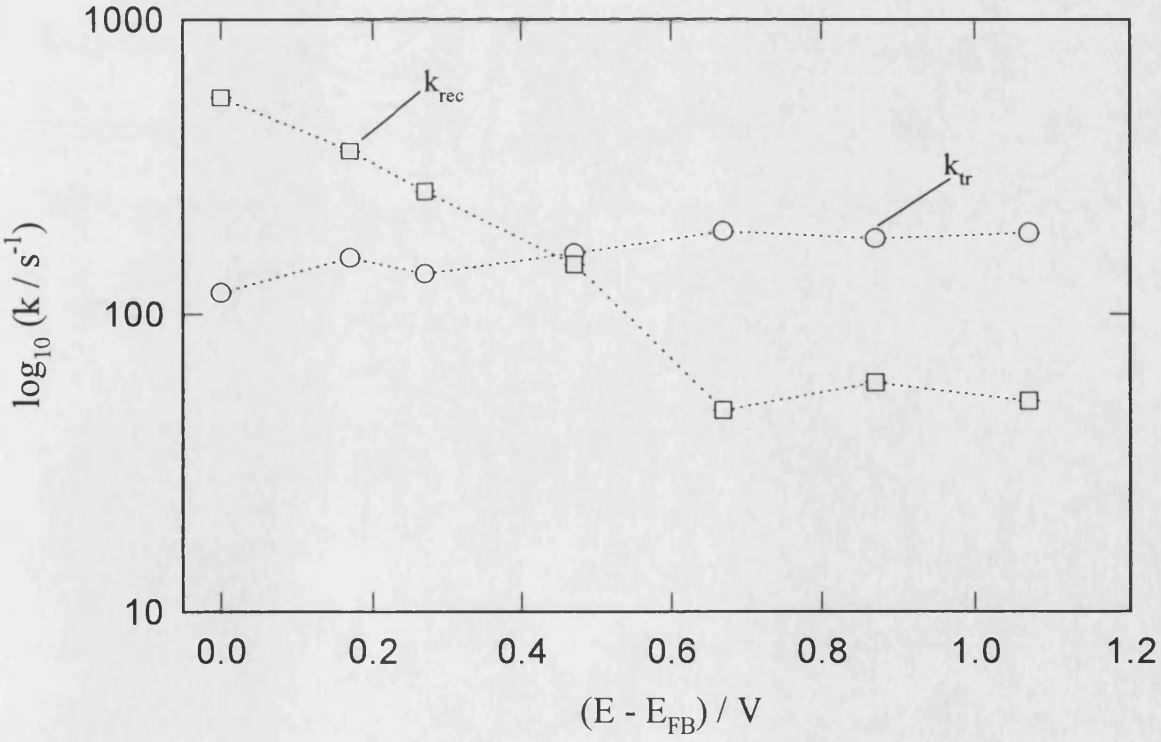

Fig. 5.12. Phenomenological k_{tr} and k_{rec} calculated from ω_{max} and the low frequency intercept of IMPS measurements at CdS CBD thin films electrodes. Note that k_{tr} is nearly independent of potential and k_{rec} decreases as the band bending is increased.

$$SO_3^{2-} + h^+ \rightarrow SO_3^{\bullet-} \quad (5.9)$$

$$2SO_3^{\bullet-} \rightarrow S_2O_6^{2-} \quad (5.10)$$

Gutiérrez and Heinglein also concluded that the oxidation of SO_3^{2-} on colloidal CdS particles involves a single electron transfer process [25]. They also suggested that the radical species can disproportionate by:

$$2SO_3^{\bullet-} \rightarrow SO_3^{2-} + SO_3 \quad (5.11)$$

$$SO_3 + H_2O \rightarrow SO_4^{2-} + 2H^+ \quad (5.12)$$

Although the single electron mechanism may look similar to a *Case II* type mechanism, the main difference lies in the fact that recombination does not involve the $SO_3^{\bullet-}$ species. The observation that the photocurrent potential relationship on single crystal electrodes is independent of the light intensity is also consistent with the single electron transfer mechanism.

The ideal behaviour of the illuminated CdS single crystal/sulfite interface is based on the fast charge transfer kinetics involved. Evidence for the absence of recombination even in partially corroded surfaces suggests that the charge transfer may occur directly via the valence band. Surprisingly, there is no clear indication that sulfite species are strongly adsorbed, which makes it even more remarkable that this electrolyte scavenges holes so effectively. However, polycrystalline thin films do exhibit recombination losses, indicating the strong influence of grain boundaries on the photoelectrochemical properties of these materials.

5.4.2 Space charge capacitance as a function of illumination

The change in the slope of the Mott-Schottky plots under illumination is attributed to internal processes in the semiconductor electrode, as it is effectively independent of the electrolyte. The increase in the capacitance can be linked to hole trapping in the space charge region. Capacitance transients measurements showed two relaxation times associated with these states (**fig. 5.6**). In the time scale of the measurements, an instantaneous decay was observed followed by a very slow process in the order of few

seconds. The fast relaxation can be associated with shallow states near the valence band, while the slow decay is attributed to states deep in the band gap.

The total change in capacitance (ΔC_{tot}) and the fraction corresponding to the fast relaxation process (ΔC_{fast}) are displayed in **fig. 5.13**. In both cases the change in capacitance passes through a maximum at around -0.3 V, which suggests a complicated non-uniform trap distribution in the space charge region. It is also seen that there is a considerable contribution of the shallow states to the total change in capacitance.

Fig. 5.14a shows the first order decay of the slow transient response at various potentials. The rate constant calculated from the slope also exhibited a potential dependence similar to ΔC_{tot} and ΔC_{fast}, as shown in **fig. 5.14b**. The relation between the rate constant and the charge trapping activation energy E_{act} is given by:

$$k = A\exp\left(-\frac{E_{act}}{kT}\right) \tag{5.9}$$

Assuming a pre-exponential factor in the order of 10^{13} s^{-1} and 0.1 s^{-1} for k, an E_{act} of 0.8 eV can be estimated. These estimations confirm that the trapping site associated with the slow time constant is located deep in the band gap region. Similar charge trapping activation energies has been obtained from optical quenching and thermally stimulated current measurements [26,27].

5.5 Conclusion

The CdS/sulfite interface behaves almost ideally over a wide potential range. Sulfite is an efficient corrosion inhibitor, and virtually no surface recombination or charge accumulation were detected. Steady state photocurrent potential plots were fitted to the Gärtner equation, yielding an absorption coefficient of $(1.4 \pm 0.2)\ 10^5$ cm^{-1} and a diffusion length of holes of $(9.0 \pm 0.2)\ 10^{-6}$ cm.

The suppression of recombination was observed even in the presence of corrosion induced dislocations, indicating the rapid nature of the charge transfer. The results obtained in single crystals and CBD thin films seem to indicate that the photo-oxidation process occurs by transfer of a single hole to SO_3^{2-}, followed by a

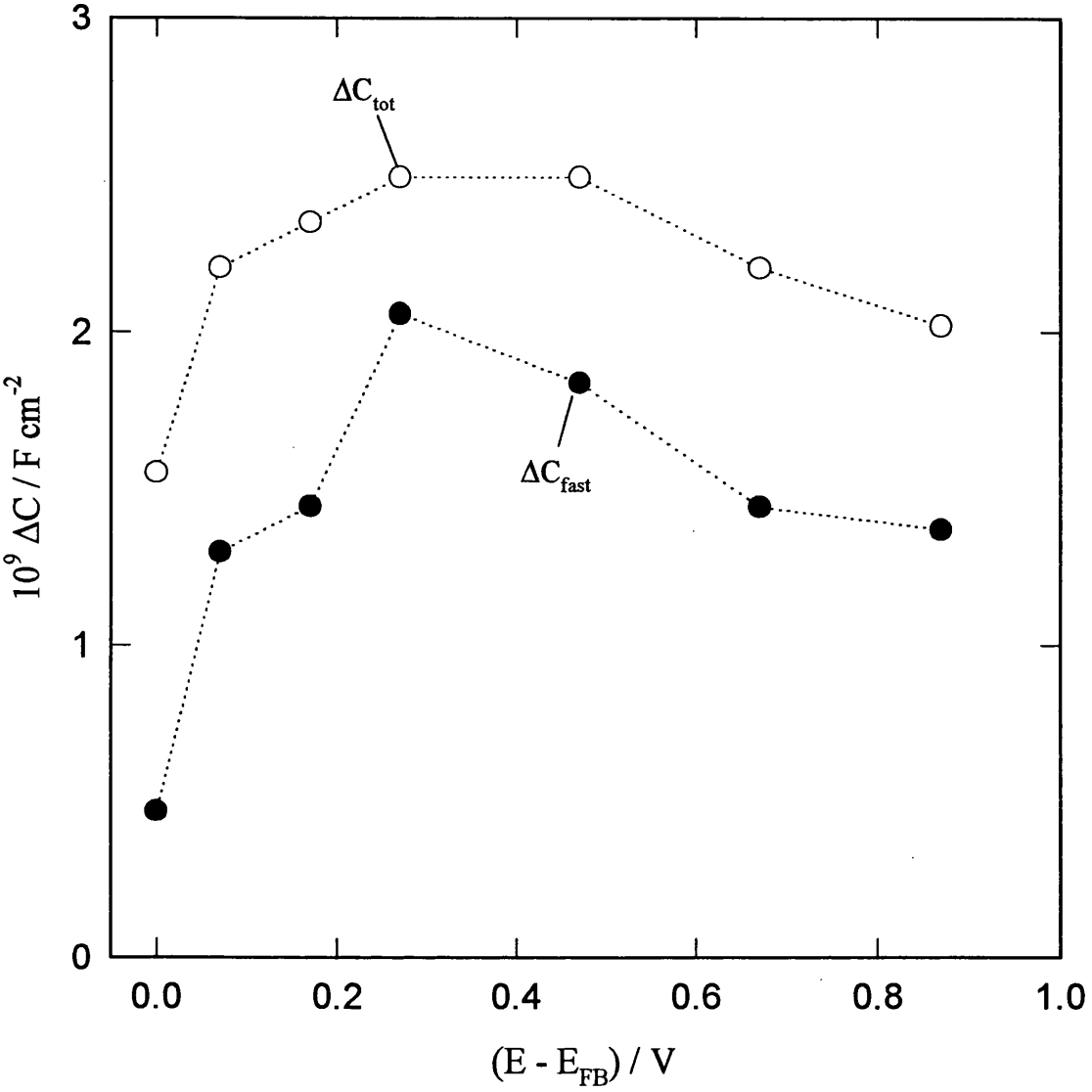

Fig. 5.13. Steady state photocapacitance, ΔC_{tot}, and the instantenous component, ΔC_{fast}, as function of the potential.

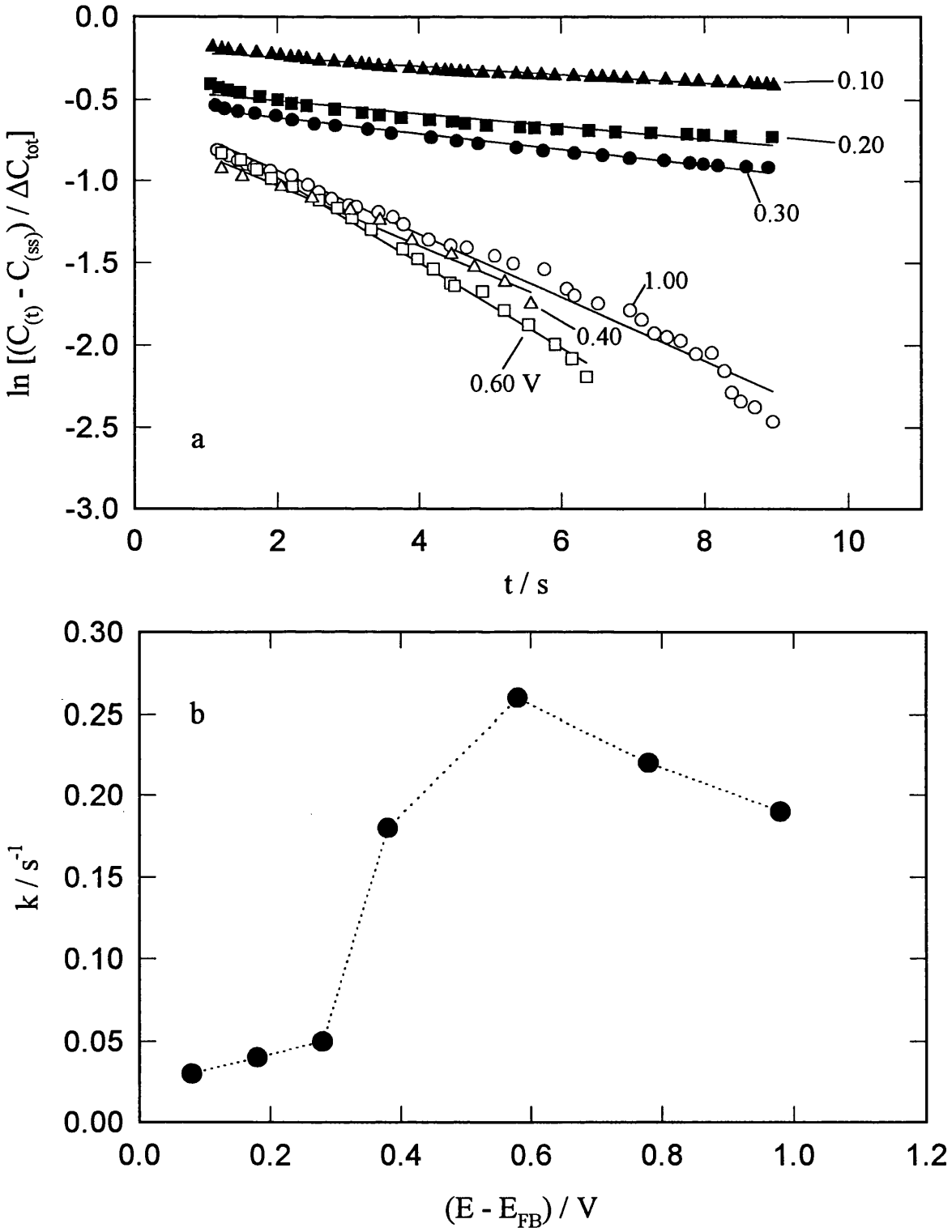

Fig. 5.14. (a) First order decay of the photocapacitance upon interruption of illumination (7.2 10^{-4} A cm^{-2}) at various ($E - E_{FB}$). $C_{(t)}$ and $C_{(ss)}$ stand for time dependent and steady state capacitance in the dark. (b) Photocapacitance rate constant decay as a function of ($E - E_{FB}$).

disproportionation process of the radical intermediate. Chemical bath deposited films exhibited recombination at all potentials, which probably takes place at grain boundaries.

In spite of the almost ideal photocurrent behaviour of single crystals, the photo-capacitance measurement presented rather complicated features attributed to hole traps in the space charge region. Two processes were associated with the increment of the capacitance under illumination: (i) a fast trapping related to shallow hole acceptor levels, and (ii) a slow process linked to hole traps located at 0.8 eV above the valence band.

5.6 References

1 A. Nozik (ed), *Photoeffects at semiconductor-electrolyte interfaces*, ACS Symposium Series 146, Washington D.C., 1981.

2 S.R. Morrison, *Electrochemistry at Semiconductor and Oxidized Metal Electrodes*, Plenum Press, New York, 1980.

3 H.O. Finklea (ed), *Semiconductor Electrodes*, Elsevier, Amsterdan, 1988.

4 H. Gerischer and W. Mindt, Electrochim. Acta, **82** (1968) 1329.

5 A.B. Ellis, S. Kaiser and M.S. Wrighton, J. Am. Chem. Soc., **98** (1976) 1635.

6 B. Miller and A. Heller, J. Electrochem. Soc., **124** (1977) 697.

7 H. Gerischer and J. Goebrecht, Ber. Bunsenges. Phys. Chem., **82** (1978) 520.

8 R.H. Wilson, J. Electrochem. Soc., **126** (1979) 1187.

9 J.R. Wilson and S.-M. Park, J. Electrochem. Soc., **129** (1982) 149.

10 A.R. de Wit and J.J. Kelly, J. Electroanal. Chem., **336** (1992) 125.

11 R.H. Wilson in A. Nozik (ed), *Photoeffects at semiconductor-electrolyte interfaces*, ACS Symposium Series 146, Washington D.C., 1981, ch. 6.

12 P. Herrasti, R. Peat and L.M. Peter, J. Electroanal. Chem., **334** (1992) 133.

13 B. Miller and A. Heller, Nature, **262** (1976) 680.

14 L.M. Peter, E.A. Ponomarev and D.J. Fermin, J. Electroanal. Chem., submitted.

15 T. Inoue, T. Watanabe, A. Fujishima, K. Honda and K. Kohayakawa, J. Electrochem. Soc., **124** (1977) 719.

16 I.J. Ferrer and P. Salvador, Ber. Bunsenges. Phys. Chem., **91** (1987) 374.

17 S. Nakabayashi and A. Kira, J. Phys. Chem., **95** (1991) 9961.

18 M.E. Özsan, D.R. Johnson, M. Sadeghi, D. Sivapathasundaran, G. Goodlet, M.J. Furlong, L.M. Peter and A. Shingleton, J. Mat. Sci., 7 (1996) 119.

19 J.J. Kelly and R. Memming, J. Electrochem. Soc., **129** (1983) 963.

20 D. Lincot and J. Vedel, J. Electroanal. Chem., **220** (1987) 351.

21 P. Allongue and H. Cachet, J. Electrochem. Soc., **132** (1985) 45.

22 A.R. De Wit, D. Vanmaekelbergh and J.J. Kelly, J. Electrochem. Soc., **139** (1992) 2508.

23 G. Chmiel and H. Gerischer, J. Phys. Chem., **94** (1990) 1612.

24 D. Vanmaekelbergh, A.R. de Wit and F. Cardon, J. Appl. Phys., **73** (1993) 5049.

25 M. Gutiérrez and A. Heinglein, Ber. Bunsengen. Phys. Chem., **87** (1983) 474.

26 B. Ray, *II-VI Compounds*, Pergamon Press, Edinburgh, 1969.

27 R.H. Bube, *Photoconductivity of Solids*, John Wiley, New York, 1960.

CHAPTER 6

Study of the water photo-oxidation on n-TiO_2 rutile single crystal electrodes by Intensity Modulated Photocurrent Spectroscopy

Abstract

The kinetics of water photo-oxidation on highly doped n-TiO_2 rutile single crystal electrodes was studied by steady state photocurrent and Intensity Modulated Photocurrent Spectroscopy (IMPS). The light intensity dependence of the photocurrent potential curves suggests a mechanism involving second order surface reaction of photogenerated intermediates (*Case II*). Moreover, the analysis of the phenomenological charge transfer and recombination parameters as a function of potential is consistent with a mechanism initiated by the generation of radical hydroxyl species ($\cdot OH_s$). These species are consumed at the surface, in the absence of other electroactive species, (i) by reacting with another mobile $\cdot OH_s$ or (ii) by trapping an electron from the conduction band. The magnitude of the rate constants associated with these two processes suggest that both reactions involve substantial activation energies. The photo-responses were also studied in aqueous solutions of formic acid and methanol at low pH. The photocurrent doubling effect was confirmed for both species. Surface recombination was effectively suppressed in the presence of the organic species, and the photocurrent doubling ratio increased with increasing illumination intensity. Analysis of the experimental evidences supports the argument that photo-oxidation of organic compounds on TiO_2 electrodes is mediated by radical species generated during the water oxidation. The effect of high space charge capacitance on IMPS responses was also analysed.

6.1. Introduction

The n-TiO_2/electrolyte interface has been subject of extensive study in the last 25 years since the pioneering work of Fujishima and Honda [1]. Detailed analyses have been reported on photo-processes from the time-scale of 10^{-12} s [2] to few seconds [3-6]. Although it is commonly accepted that the collection of photo-generated charge carriers in the space charge region occurs in the scale of picoseconds, the processes responsible for slower relaxation phenomena are still the subject of debate. These slow processes (10^{-6} to 10 s) determine the kinetics of interfacial reactions. For instance, it is not clear whether the oxidation of species in aqueous electrolyte proceeds via direct interfacial transfer of holes [7,8] or involves generation of highly oxidising hydroxyl radicals as an intermediate step [9-11].

The photo-oxidation of water is not a subject free of controversy either. It has been extensively studied by Salvador et al. using mainly photocurrent transient measurements [3,12,13]. These authors postulated a mechanism based on the transfer of holes to adsorbed hydroxyl groups, generating radical species which react subsequently on the surface to produce hydrogen peroxide:

$$H_2O + h^+ \xrightarrow{k_1} \cdot OH_s + H^+ \tag{6.1}$$

$$\cdot OH_s + \cdot OH_s \xrightarrow{k_2} (H_2O_2)_s \tag{6.2}$$

$$\cdot OH_s + e^-_{cb} \xrightarrow{k_3} OH^-_s \xrightarrow{H^+} H_2O \tag{6.3}$$

$$(H_2O_2)_s + \cdot OH_s \xrightarrow{k_4} \cdot O_2H_s + H_2O \tag{6.4}$$

$$\cdot O_2H_s + \cdot OH_s \xrightarrow{k_5} O_2 + H_2O \tag{6.5}$$

where the sub-index "s" stands for surface confined species. Step (6.3) corresponds to the surface electron-hole recombination which is believed to occur mainly via the intermediate $\cdot OH_s$. It is also reported that the rate constant for hydrogen peroxide formation (k_2) is dependent on the doping density of the crystal. This was interpreted in terms of a link between $\cdot OH_s$ and oxygen vacancies [3,14]. These authors also attempted to identify intermediate species using rotating ring-disk electrodes, but no evidence of hydrogen peroxide was obtained [15]. This result can be interpreted in terms of (i) a fast (efficient) oxidation of the peroxide to oxygen, or (ii) or confinement

of the intermediate species to the surface. However, Nogami et al. [10] reported the detection of the oxidation of ferrocyanide by H_2O_2 on a rotating ring-disk electrode. Indeed, it was claimed that all reactions beyond the generation of $\cdot OH_s$ can occur in homogeneous phase. Strong evidence for the presence of $\cdot OH_s$ and $HO_2\cdot$ radicals was also reported by Jaeger and Bard from spin trapping and ESR detection [16].

Chapter 2 examined the intensity modulated photocurrent responses for multi-electron transfer reactions. The analysis shows that the potential dependence of the charge transfer and recombination parameters can provide mechanistic information on the photoelectrochemical processes. In this chapter, this analysis is extended to the photo-oxidation of water on n-TiO_2 rutile single crystal electrodes. In principle, this approach can be related to the photocurrent transient studies by Salvador et al. [3,12,13]. However, frequency response analysis provide a more complete description of the time dependent photocurrent, which could be rather complicated in highly doped semiconductors [17]. The IMPS responses obtained in solutions containing organic compounds are also analysed in this chapter.

6.2. Experimental

The TiO_2 rutile single crystals (Pikem) electrodes were prepared as described in section 3.2. The electrochemical cell was provided with quartz windows. The cell also had separate compartments for the secondary (platinum disk) and reference electrodes (Ag/AgCl).

'Steady state' photocurrents were recorded under chopped illumination using a 5210 EG&G PAR lock in amplifier. Two illumination sources were employed for the IMPS measurements: (i) a Liconix 4207 NB HeCd laser (λ = 325 nm) and (ii) a Mercury Arc Mercury Lamp (Oriel) combined with a Bausch and Lomb high intensity monochromator. The laser intensity was modulated by an UV acousto-optic modulator A.A.MQ.10 from A.A. Opto-Electronics, controlled by a Solartron 1250 FRA (Schlumberger). The bias light was provided by the mercury line at 365 nm. The total modulation depth of light was 10-50%. Further information on the IMPS set up has been reported elsewhere [18].

6.3. Results and discussion

6.3.1. Steady state analysis

Steady state normalised photocurrent-potential curves in 0.1 mol dm^{-3} $NaClO_4$ pH 1 and at various light intensities are shown in **fig. 6.1**. It can be seen that the photocurrent onset region is shifted to more negative potentials by approximately 30 mV per decade of photocurrent density. This trend resembles the theoretical response expected for a *Case II* type of mechanism, i.e. the generation of an intermediate in the first step followed by the surface reaction of two mobile intermediates. In this respect, steps (6.1)-(6.3) can be considered as the model reaction studied in section 2.3.2. However, the photocurrent potential dependence range is considerably broadened, indicating a non-ideal potential distribution across the interface.

Mott-Schottky plots of the n-TiO_2/$NaClO_4$ 0.1 mol dm^{-3} pH 2 interface are displayed in **fig. 6.2**. The capacitance was calculated from the quadrature component of the admittance, C_p, (see section 3.2). The strong frequency dependence of the Mott-Schottky plots introduced difficulties in the determination of the flat band potential and the doping density. At low frequencies, the plots converge to a single intercept. However, as the frequencies is increased over 1.5 kHz, the slope decreases and the plot shifts to more negative potentials. This effect arises from the large space charge capacitance, which leads to a time constant in the order of 0.1 ms (the uncompensated resistance was estimated to be 125 Ω, see section 3.2). Another source of non-ideal response could be non-homogeneous crystal doping. The hot sulfuric acid etching (section 3.2) can partially re-oxidised the crystal, decreasing the doping density toward the semiconductor surface [19]. The flat band potential and the doping density of the crystal were estimated from the Mott-Schottky plots at low frequencies, and summarised in **table 6.1**. It can be seen the expected 59 mV increment of the E_{FB} per unit of pH [20].

The results shown in **fig. 6.1** also exhibits a potential dependence of the photocurrent at very high band bending. Under these conditions, surface recombination is expected to be negligible and the photocurrent density is given by the Gärtner flux of holes [21] (see section 1.3). In **fig. 6.3**, the photocurrent density corrected for

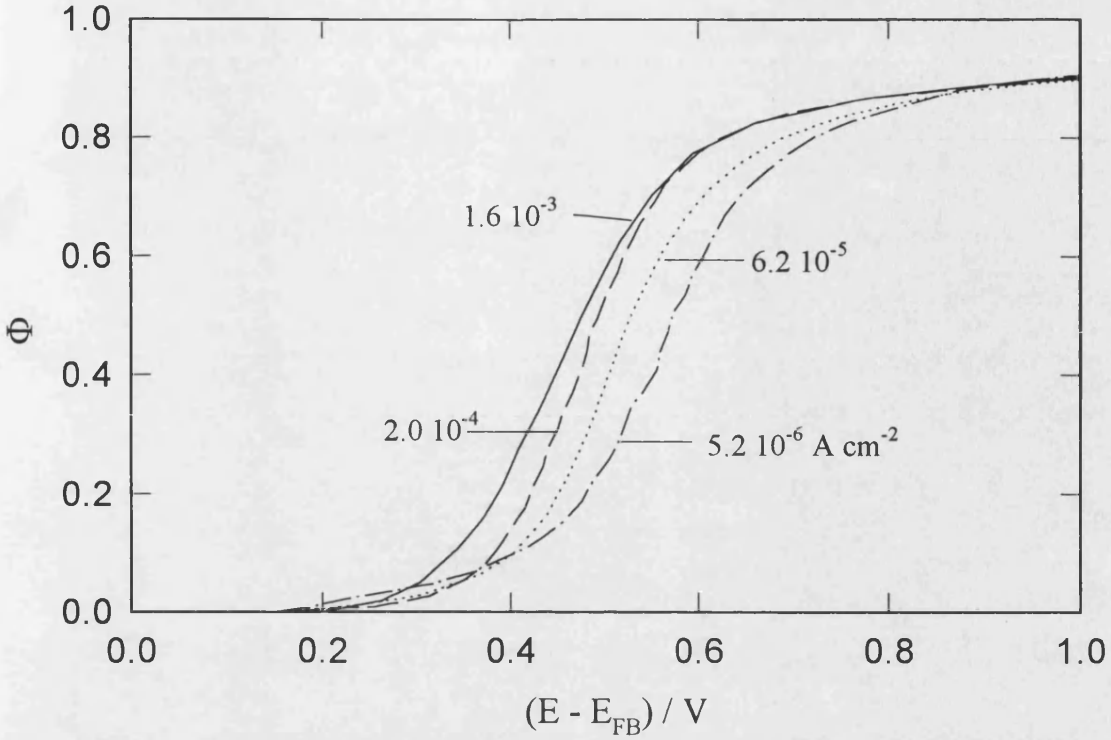

Fig. 6.1 Normalised photocurrent-potential curves of the n-TiO_2 rutile single crystal electrode in 0.1 mol dm^{-3} $NaClO_4$ pH 1 at various light intensities (given in photocurrent density units).

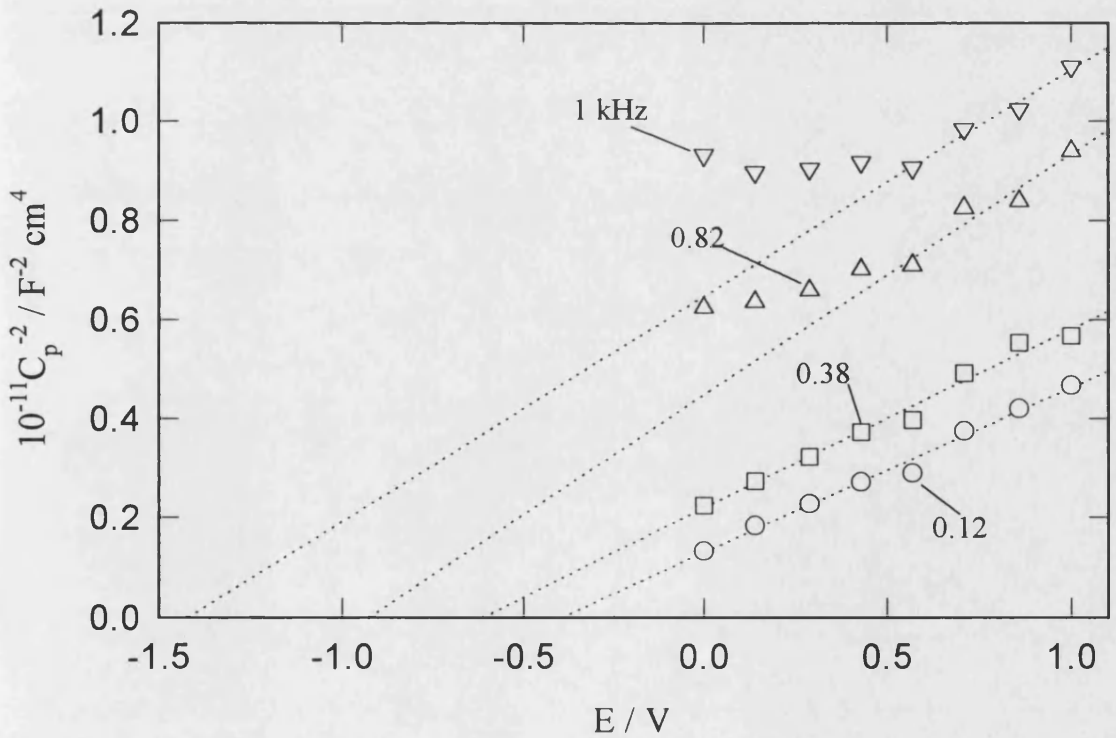

Fig. 6.2. Mott-Schottky plots of the n-TiO_2 / 0.1 mol dm^{-3} $NaClO_4$ pH 2 interface at various frequencies. The amplitude of potential modulation was 10 mV. Note the strong frequency dependent of C_p (see text). E_{FB} and N_{SC} were estimated at 120 Hz.

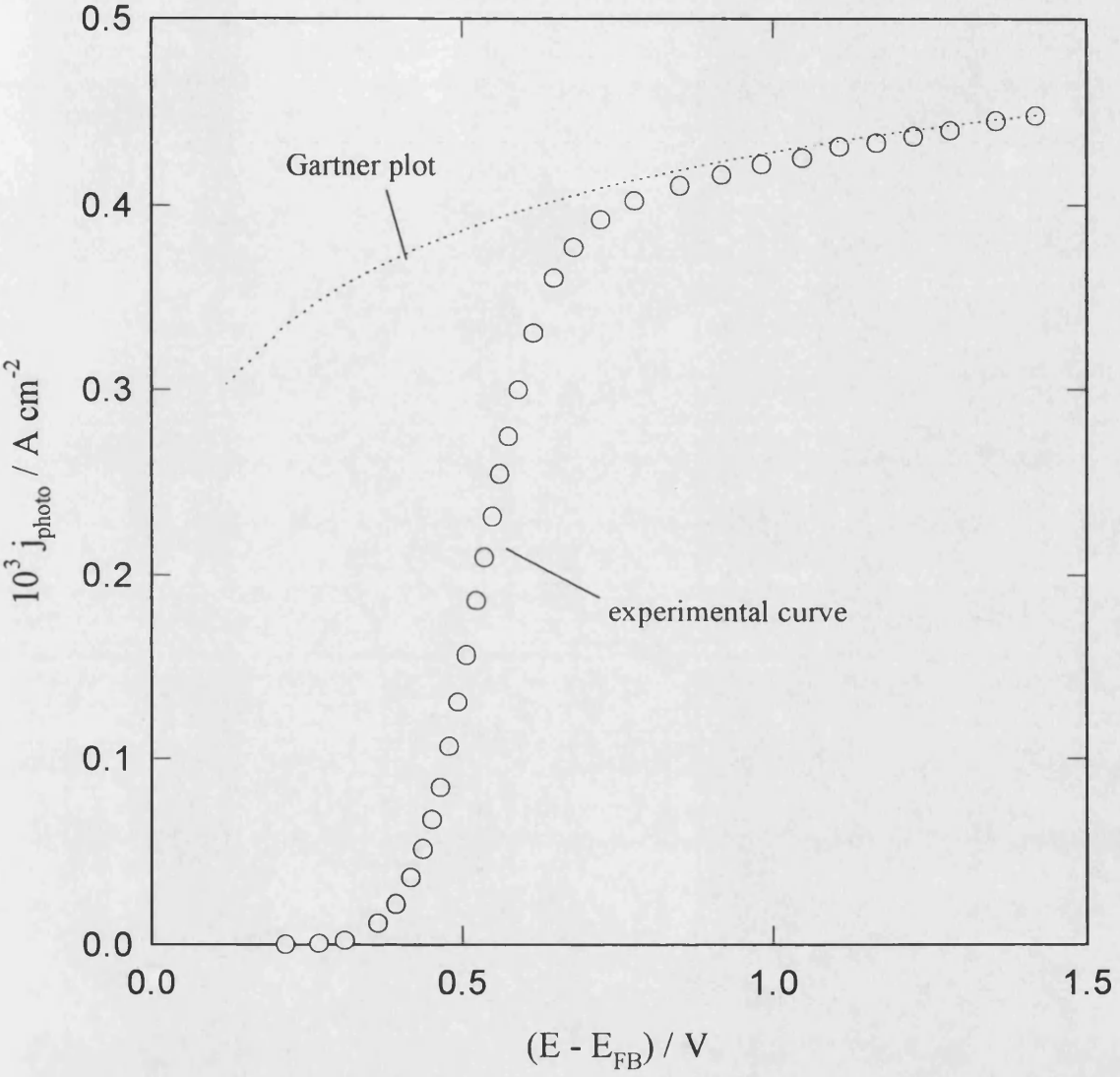

Fig. 6.3. Comparison beetwen the experimental photocurrent (0.1 mol dm^{-3} $NaClO_4$ pH 2) and the Gartner expression. Constants used: $\alpha = 5\ 10^5$ cm^{-1}, $L_p = 10^{-6}$ cm and $N_{SC} = 2.5\ 10^{19}$ cm^{-3}.

reflection losses is fitted to the Gärtner expression eq. (1.6), obtaining an absorption coefficient of (5 ± 2) 10^5 cm^{-1} and a diffusion length of holes (1.0 ± 0.5) 10^{-6} cm. These values fall into the wide range of values reported in literature [20]. It is also seen that the effect of surface recombination is evident at E - E_{FB} below 0.7 V.

Table 6.1. Flat band potentials and doping density of n-TiO_2 electrodes at various pH.

E_{FB} / V (vs. Ag/AgCl)	pH
-0.89	9.2
-0.41	2.0
-0.36	1.0
-0.31	0.0
N_{SC} / cm^{-3}	(2 ± 1) 10^{19}

6.3.2. Intensity Modulated Photocurrent Spectroscopy

IMPS spectra at various potentials are displayed in **fig. 6.4**. At potentials below 0.20 V, semicircular responses are observed in the first quadrant of the complex plane and, as the frequency is increased, a signal in the fourth quadrant is also developed. The low frequency signal is determined by the competition between the charge transfer and surface recombination, while the high frequency response is determined by the RC attenuation of the cell [17]. R is determined by the uncompensated resistance between the reference electrode and the back ohmic contact of the crystal. In highly doped semiconductors, the equivalent capacitance C is given by the space charge region and Helmholtz capacitance:

$$C = \frac{C_{SC} C_H}{C_{SC} + C_H} \qquad (6.6)$$

The frequency dependent current associated with the RC attenuation should tend to the origin as the frequency is increased. However, the responses shown in **fig. 6.4** are

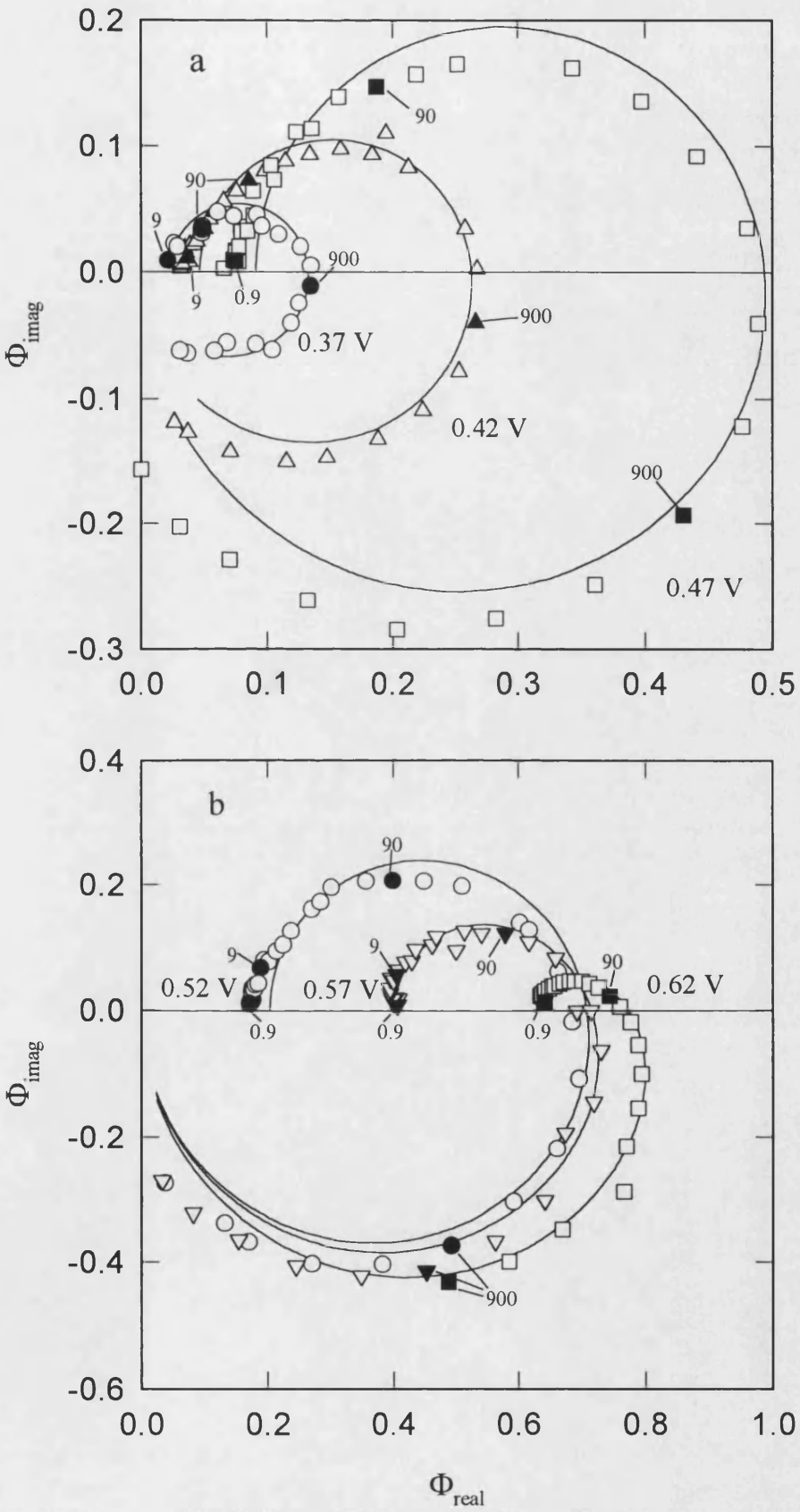

Fig. 6.4. IMPS spectra of the n-TiO_2 electrode in 0.1 mol dm^{-3} $NaClO_4$ pH 2 at a bias illumination of 1.8 10^{-5} A cm^{-2} and various ($E - E_{FB}$). Solid lines correspond to fits to eq. (6.7) (see text).

rather flat at frequencies higher than 1 kHz. This effect could be associated with the anomalous behaviour of the interface at high frequencies.

Another interesting feature of the IMPS spectra is related to the high frequency intercept with the real axis. The limiting case described by eq. (2.27) and eq. (4.6) indicates that this frequency intercept is given by the Gärtner flux of holes (g_l). **Fig. 6.5** shows that the high frequency intercept photocurrent is attenuated in comparison to the Gärtner flux given by eqs. (1.6). This attenuation arises from two components, the RC attenuation and the *interfacial charging current.* The latter contribution is determined by the surface accumulation of charge which can perturb the potential drop across the Helmholtz layer. The general IMPS expression which account for these two effects has been derived by Ponomarev and Peter [17]:

$$\frac{j_{(\omega)}}{g_l} = \frac{k_{tr} + i\omega \dfrac{C}{C_{SC}}}{k_{tr} + k_{rec} + i\omega}\left(\frac{1}{1+i\omega RC}\right) \qquad (6.7)$$

where the terms in brackets corresponds to the RC response and the ratio C/C_{SC} in the numerator is associated with the interfacial charging current.

Fig. 6.4 also displays the fitting of eq. (6.7) to the IMPS spectra at various potentials (continuous line). The ac component of the photon flux, g_l, was calculated from the Gärtner expression (1.6), while C_{SC} was obtained from the Mott-Schottky equation (1.5). The fitting parameters were k_{tr}, k_{rec} and C_H. An average value for C_H $(28 \pm 10)\ 10^{-6}$ F cm^{-2} was obtained, although the fitting of the lower quadrant response was rather poor. This limitation come as a result of the complicated high frequency response of the system discussed previously. The response in the first quadrant was successfully fitted by eq. (6.7).

The potential dependence of k_{tr} and k_{rec} is displayed in **fig 6.6**. It is seen that k_{tr} increases and k_{rec} decreases as the applied potential is increased. *This result provides further evidence to support a Case II type mechanism for the photo-oxidation of water on TiO_2 electrodes.*

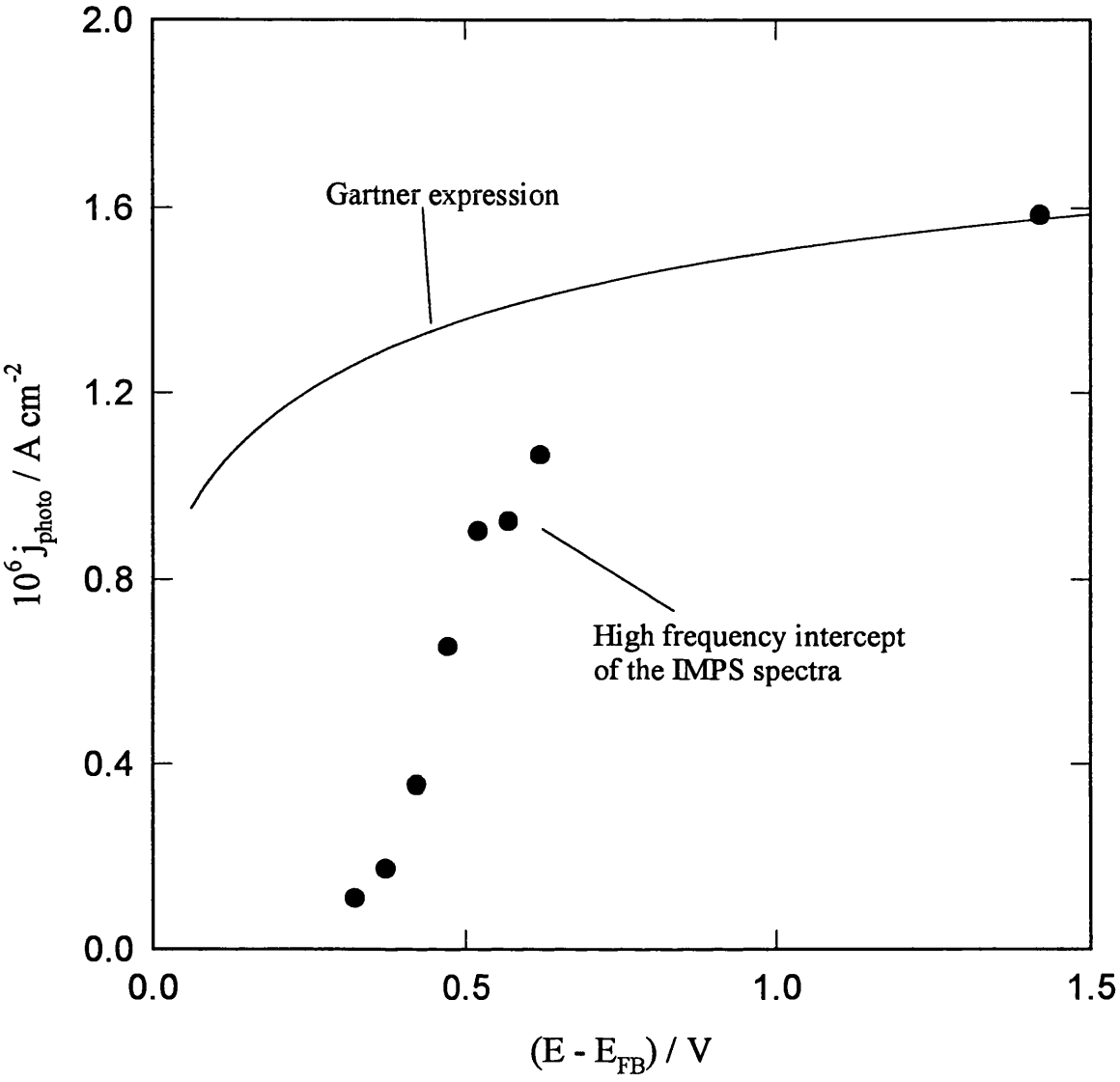

Fig. 6.5. Comparison of the Gartner limit and the high frequency intercept of the IMPS spectra (see fig. 6.4) as a function of (E - E_{FB}). The deviation arises from the effects of the RC attenuation and the interfacial charging current.

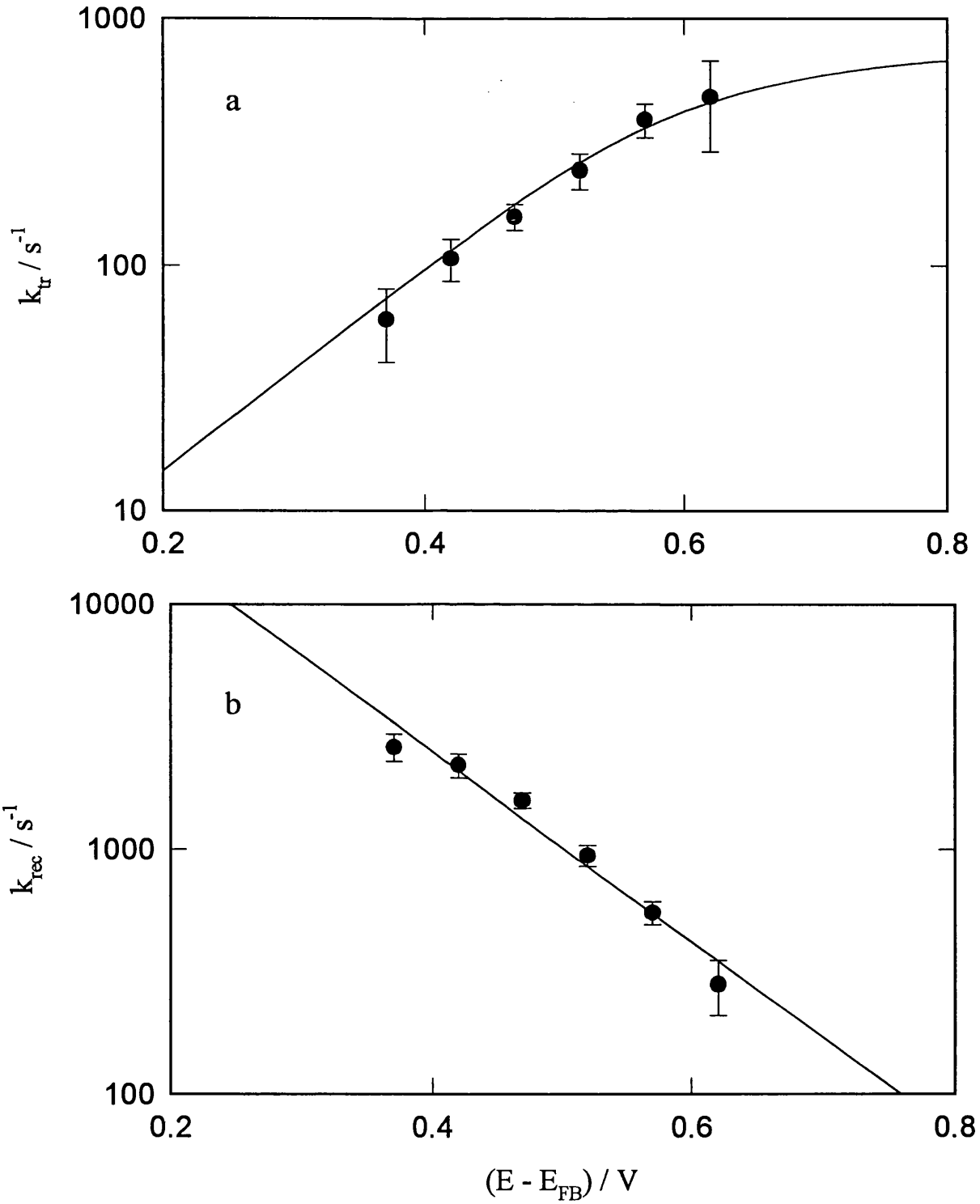

Fig. 6.6. Phenomenological k_{tr} (a) and k_{rec} (b) as a function of (E - E_{FB}) obtained from the analysis of the IMPS spectra in fig. 6.4. The increment of k_{tr} with increasing potentials is consistent with a *Case II* type mechanism.

Assuming that the steps (6.4) and (6.5) are in equilibrium, the phenomenological parameters associated with the mechanism (6.1) to (6.5) can be obtained following a similar derivation to that outlined in section 2.4 [22]:

$$k_{tr} = \frac{8k_1k_2OH_0}{k_1 + 8k_2OH_0 + k_3} \tag{6.8}$$

$$k_{rec} = \frac{k_1k_3}{k_1 + 8k_2OH_0 + k_3} \tag{6.9}$$

$$OH_0 = \frac{-k_3 + \sqrt{k_3^2 + 16k_2g_0}}{8k_2} \tag{6.10}$$

where OH_0 is the steady state concentration of the radical $\cdot OH_s$. It follows from eq. (6.9) that for $k_1 >> k_3$ and k_2OH_0, k_{rec} is essentially determined by k_3. **Fig. 6.6(b)** shows a logarithmic dependence of k_{rec} with the applied potential, which reflects a modified Boltzmann distribution of electrons in the space charge region:

$$k_3 = k_3^0 \exp\left(-\beta q(E - E_{FB})/kT\right) \tag{6.11}$$

where β is an empirical factor associated with Fermi-Level pinning effects. From the linear regression fit of k_{rec} vs. $(E - E_{FB})$, the parameters k_3^0 and β are readily accessible. The very low value of β, 0.25 ± 0.02, indicates an almost "metal-like" behaviour of the electrode. This behaviour can be connected to the large electron concentration, especially at potentials near E_{FB}. It could be also due to a large surface excess charge associated with the population of interband surface states. This surface charge also introduces a potential drop across the Helmholtz layer. The presence of surface states on TiO_2 electrodes has been studied quite extensively by various methods [23-26].

The recombination rate constant, $k_3^0 = (1.2 \pm 0.8)\ 10^5\ s^{-1}$, was also obtained from **fig. 6.6(b)**. Similarly, the rate constant for step (6.2), $k_2 = (2 \pm 1)\ 10^{-8}\ cm^{-2}\ s^{-1}$, was calculated from fitting eq. (6.8) to the potential dependence of k_{tr} **(fig. 6.6(a))**. This simple approach does not allow estimations of k_1. It can be seen in eqs. (6.8)-(6.10) that as long as k_1 is large, IMPS responses are rather insensitive to this rate

constant. On the other hand, steps (6.4) and (6.5) are assumed to be in equilibrium, therefore these reactions do not affect the kinetics of the process. It is also possible that the last two steps do not involve surface processes, but only disproportionation of the hydrogen peroxide in solution [20].

The values obtained for the rate constants k_2 and k_3^0, as well as β consistently describe the steady state photocurrent potential behaviour at various illumination intensities. An illustrative fit is displayed in **fig. 6.7**.

In section 2.3.2, an approximate expression for the second order rate constant for *Case II* was presented based upon a random walk approximation. Recalling eq. (2.19), the activation energy (E_{act}^{tr}) for the step (6.2) can be estimated of the order of 40 kJ mol^{-1}. This estimation is close to values reported for the recombination of hydrogen atoms on metal surfaces [27]. In this sense, the step (6.2) can be envisaged as the effective combination of two surface mobile $\cdot OH_s$ generating hydrogen peroxide.

Assuming a thermal velocity of electrons to be 10^5 cm s^{-1}, the capture cross section for the recombination step (6.3), σ_e, can be estimated in the order of 10^{-19} cm^{-2} (see eq. (2.13)). Considering $\cdot OH_s$ as the electron trapping species, the magnitude of σ_e is small, which suggests that this step also involves an activated process. If the capture cross section for a non-activated process is assumed to be 10^{-16} cm^{-2}, the activation energy for the recombination (E_{act}^{rec}) is estimated in 170 kJ mol^{-1}. This is an interesting result considering the strong oxidising nature of this radical. As discussed previously, the recombination step is not the reverse reaction of the first hole transfer, eq. (6.1). The first reaction involves charge carriers from the quasi-Fermi level of holes, while the recombination, and so E_{act}^{rec}, is associated with electrons from the Fermi level. This rather slow recombination process not only allows the surface reaction between two mobile $\cdot OH_s$ species, but also the reaction of this intermediates with electrolyte species. This possibility is discussed in the next section.

6.3.3 Photoelectrochemical responses in the presence of organic species

The photo-oxidation of organic compounds on TiO_2 has been widely studied on single and polycrystalline substrates [28], as well as on powders and colloidal suspensions [29]. In the case of small organic molecules, quantum efficiencies higher than one have been associated with the presence of radical species capable of injecting electrons into

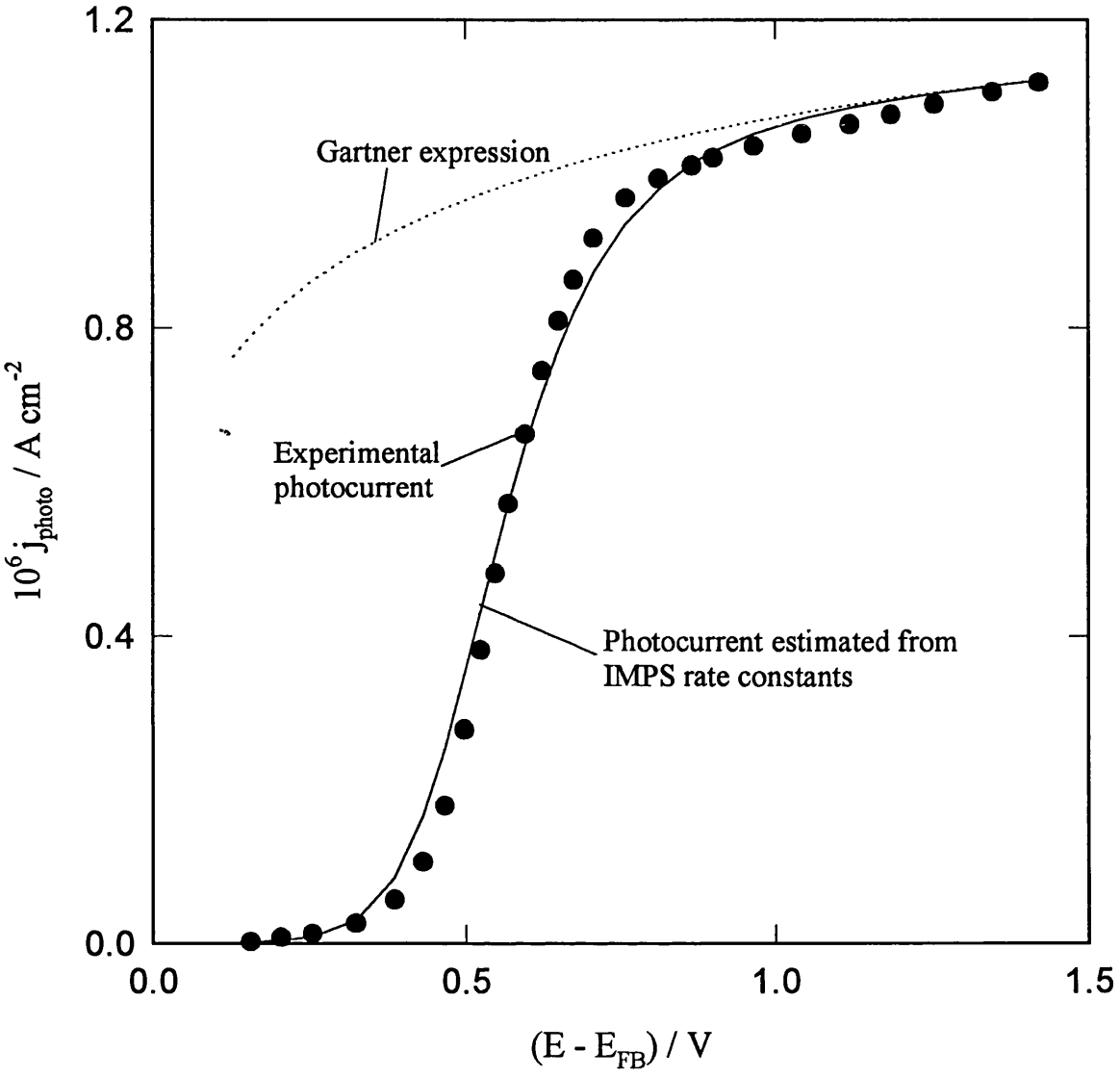

Fig. 6.7. Comparison of the experimental photocurrent with the Gartner limit and the calculated photocurrent using the parameters obtained from IMPS spectra (see also eq. (2.15)). $k_2 = 2\ 10^{-8}$ cm^{-2} s^{-1}, $k_3^0 = 10^5$ s^{-1} and $\beta = 0.25$.

the conduction band of the TiO_2 [7]. This phenomenon is referred to as photocurrent doubling. Despite the enormous amount of research on this area, there is still debate whether holes are directly transferred into the electrolyte species, or whether the oxidation is initiated by radical species generated during the oxygen evolution.

Fig. 6.8 displays the photocurrent-potential curves of the n-TiO_2 electrode in the presence and absence of formic acid and methanol. The photocurrent density is higher in the presence of the organic species over the whole potential range, which is connected to the photocurrent doubling reaction. This reaction can be represented in a simplified way as:

$$RH_2 + h^+ \xrightarrow{k_6} RH^{\cdot} + H^+ \qquad (6.12)$$

$$RH^{\cdot} \xrightarrow{k_7} R + e^-_{CB} + H^+ \qquad (6.13)$$

These two reactions will determine that two electrons flow in the external circuit per photon absorbed in the semiconductor. The first electron arises from hole transfer (6.12) and the second from the injected carrier in the conduction band (6.13). Obviously, there are competing parallel reactions which set the conversion efficiency between one and two. **Fig. 6.9** shows the injection ratio for formic acid, i.e. $j_{photo}^{HCOOH} / j_{photo}$, as a function of the photocurrent in the absence of the organic species. It is clearly seen that the ratio increases from almost one to two as the illumination intensity is increased. A similar trend was obtained for methanol, although the overall injection ratio was smaller. These results contrast quite dramatically with the behaviour observed for the photo-oxidation of formic acid on other semiconductors [30,31], where the conversion efficiency *decreases* as the light intensity is increased.

Conversion efficiencies between one and two have been explained in terms of competition between reaction (6.13) with the direct transfer of a second hole [30]:

$$RH^{\cdot} + h^+ \xrightarrow{k_8} R + H^+ \qquad (6.14)$$

This competition will be determined by the surface concentration of holes, therefore it is expected that the ratio $j_{photo}^{HCOOH} / j_{photo}$ will decrease as the light intensity is increased [30,31]. Evidently, the behaviour observed in **fig. 6.9** indicates that the transfer of a

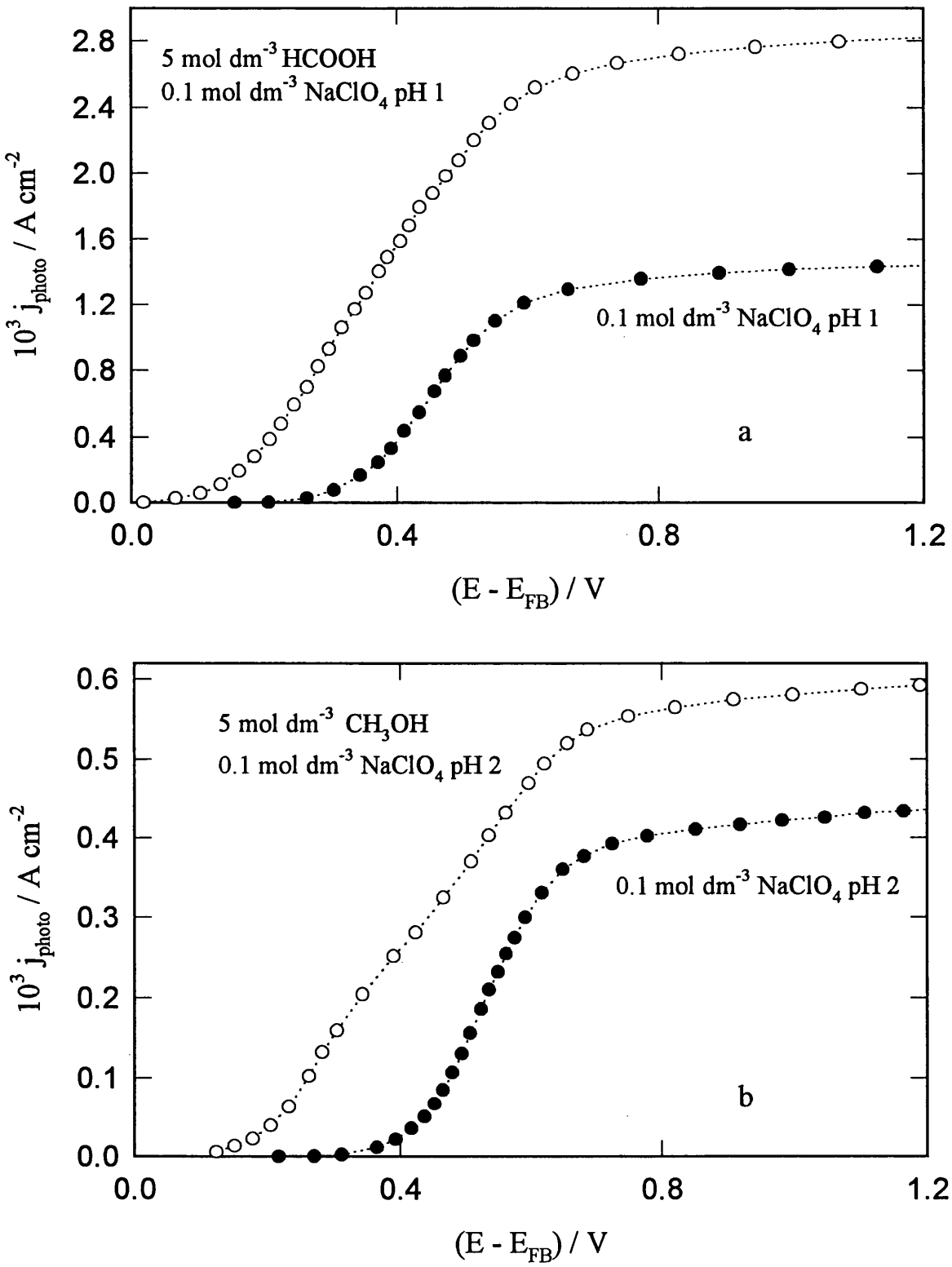

Fig.6.8. Photocurrent-potential curves of n-TiO_2 electrodes in the presence and absence of (a) formic acid and (b) methanol.

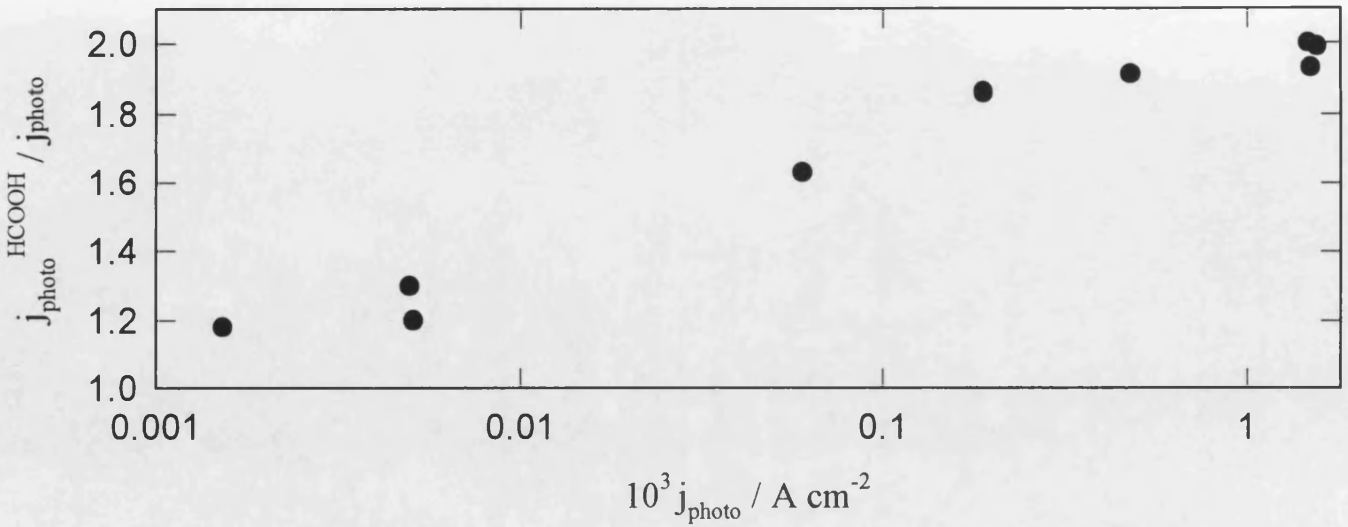

Fig. 6.9. Injection ratio $j_{photo}^{HCOOH} / j_{photo}$ in 5 mol dm^{-3} HCOOH pH 1 at 3 V, as a function of the photocurrent in the absence of organic species. Note the nearly perfect doubling of the photocurrent at high light intensities.

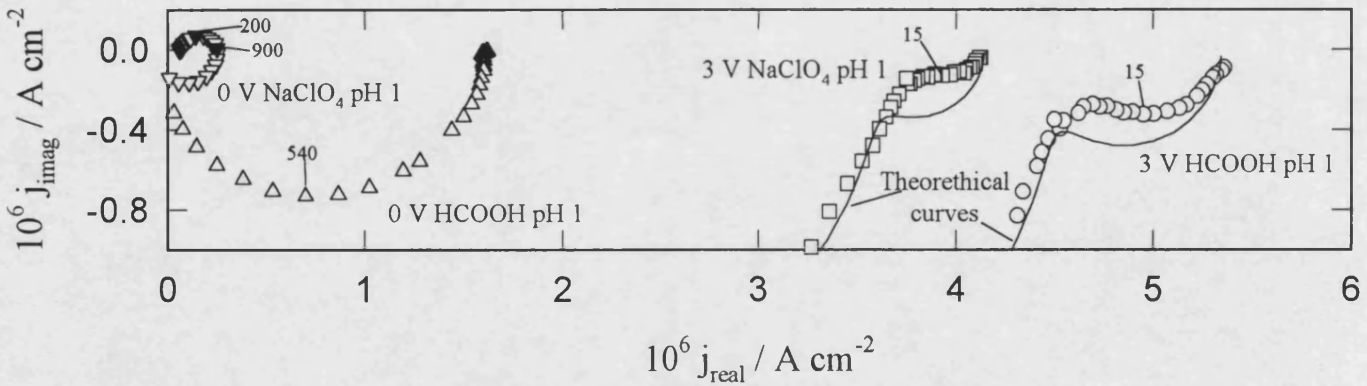

Fig. 6.10. IMPS spectra of n-TiO_2 in the presence and absence of formic acid. The electrolyte was 0.1 mol dm^{-3} $NaClO_4$ pH 1. Solid lines in the high potential curves depict the theorethical behaviour of eq. (6.7).

second hole to the injecting species is not part of the mechanism. In consequence, this evidence seems to support the idea that there is no direct charge transfer between the organic species and the solid. Alternatively, the photo-oxidation process may occur via a complicated sequence of reactions involving intermediate species of the water oxidation process.

Fig. 6.10 shows IMPS spectra in the presence and absence of formic acid. Two interesting features can be distinguished at high and low band bending: (i) the development of a low frequency signal in the fourth quadrant in both electrolytes and (ii) the suppression of the recombination semicircle in the presence of the organic species. Although electron injection processes are characterised by a semicircle in the lower quadrant[1] [30-34], the relaxation observed in **fig. 6.10** cannot be related to the photocurrent doubling reaction for two obvious reasons: firstly it also appears in the absence of organic species, and secondly the frequency of the minimum imaginary part is far too low for an injecting species ($\omega_{min} \sim 15$ Hz). Previous studies on ZnO and CdS electrodes have concluded that the injecting species lifetime is in the order of 10^{-5} s [30,31,35,36], therefore it is very unlikely that this process can occur four orders of magnitude slower on TiO_2 photoelectrodes.

The fact that the low frequency response at high band bending is common to all electrolytes indicates that it is connected to an inherent property of the n-TiO_2/aqueous interface. From eq. (6.7), it follows that at low frequencies ($\omega < 1/RC$) and high band bending ($k_{rec} \sim 0$), the frequency dependent photocurrent is given by:

$$j_{(\omega)} = g_1 \frac{k_{tr} + i\omega \dfrac{C}{C_{SC}}}{k_{tr} + i\omega} \qquad (6.15)$$

Providing that C_{SC} is comparable to C_H, eq. (6.15) describes a semicircle in the lower quadrant with $\omega_{min} = k_{tr}$ [17]. As $k_3 \approx 0$, the value of k_{tr} only depends on k_2 and g_0 (see eqs. (6.8-10)). In **fig. 6.10**, it can be seen that the ω_{min} is effectively independent of the electrolyte, suggesting that the photo-oxidation kinetics remains "unaffected".

[1] The rate constant for the electron injection is also readily accessible from the frequency of minimum imaginary part, i.e. $\omega_{min} = 1/k_{inj}$.

Furthermore, it is also shown that eq. (6.7) describes a similar behaviour to the experimental plot (see solid lines). The parameters used in these calculations were identical for both electrolytes except for the hole flux g_l. This can be interpreted as an evidence that the kinetics of both processes is similar, but the measured photocurrent is "higher" in the presence of formic acid. Although this result suggests that k_{tr} is identical in both electrolytes, it does not provide information about the mechanism for the consumption of $\cdot OH_s$ at the surface. However, it seems clear that the generation of radical species occurs at the same rate in both electrolytes.

The remarkable quenching of recombination in the presence of methanol and formic acid (**fig. 6.10**) provides strong evidence of the interactions between the $\cdot OH_s$ radical and the organic species. This interesting result indicates that the $\cdot OH_s$ species can capture an electron more readily from the organic species than from the 'conduction band' of the solid. Another interesting result is that the space charge capacitance is not affected by the presence of the organic species, suggesting that theses species are not chemically adsorbed at the surface.

In summary, the experimental evidence analysed in this section showed that the oxidation of organic species occurs via $\cdot OH_s$ radicals generated from the oxidation of water, however, it is not clear yet what is the real nature of this radical. It is seen that the intermediate interacts with the electrolyte, to induce the oxidation of the organic species, but also interacts with the semiconductor since it is involved in the recombination process. In the review by Finklea [20], it is suggested that the radical species can be chemisorbed or physisorbed. The conversion from chemi- to physisorbed is expressed as:

$$Ti - OH^{\bullet} + H_2O \rightarrow Ti - OH^{-} + OH^{\bullet} + H^{+} \qquad (6.16)$$

Spectroscopic analysis may provide an alternative approach for the understanding of these processes.

6.4. Conclusions

Steady state and dynamic responses of the water photo-oxidation on TiO_2 electrodes corresponds to the *Case II* type mechanism. The photocurrent potential

curves shift by approximately 30 mV per decade of light intensity toward more negative potentials. Analysis of IMPS spectra revealed an increase of k_{tr} and a decrease of k_{rec} as the potential is increased. The potential dependence of the kinetic parameters was largely affected by strong Fermi-Level pinning associated with a high surface charge. The mechanistic model was based upon the generation of radical $\cdot OH_s$ species which can either (i) react with another mobile $\cdot OH_s$, or (ii) capture an electron from the conduction band [3,10,12-16]. It was observed that both processes involved significant activation energies.

Photoresponses in the presence of small organic compounds were also studied. It was found that the photocurrent doubling ratio increases as the light intensity was increased. Surface recombination was also effectively suppressed in the presence of the organic species (formic acid and methanol at low pH). The analysis of the experimental evidence supports the argument that the oxidation of these molecules is mediated by radical species generated during the water oxidation [9-11]. However, further research is required in order to clarify the interactions between hydroxyl radicals and organic species.

6.5. References

1 K. Honda and A. Fujishima, Nature, **238** (1972) 37.

2 A.L. Linsebigler, G. Lu and J.T. Yates, Chem. Rev., **95** (1995) 735.

3 D. Tafalla, P. Salvador and R.M. Benito, J. Electrochem. Soc., **137** (1990) 1810.

4 J.M. Lantz and R.M. Corn, J. Phys. Chem., **98** (1994) 4899.

5 E.A. Ponomarev and S.D. Babenko, J. Electroanal. Chem., **371** (1994) 27.

6 N.S. Foster, C.A. Koval, J.G. Sczechowski and R.D. Noble, J. Electroanal. Chem., **406** (1996) 213.

7 E.C. Dutoit, F. Cardon and W.P. Gomes, Ber. Bunsengen. Phys. Chem., **80** (1976) 1285.

8 R.B Draper and M.A. Fox, Langmuir, **6** (1990) 1396.

9 J. Li, L.M. Peter and R. Potter, J. Appl. Eletrochem., **14** (1983) 495.

10 G. Nogami, Y. Nishiyama and H. Nakamura, J. Electrochem. Soc., **135** (1988) 877.

11 C.S. Turchi and D.F. Ollis, J. Catal., **119** (1989) 483.

12 P. Salvador and M.L.G. Gonzalez, J. Electroanal. Chem., **325** (1992) 369.

13 P. Salvador, J. Phys. Chem., **89** (1985) 3863.

14 M.L.G. Gonzalez and P. Salvador, J. Electroanal. Chem., **325** (1992) 369.

15 P. Salvador and F. Decker, J. Phys. Chem., **88** (1984) 6116.

16 C.D. Jaeger and A.J. Bard, J. Electrochem. Soc., **83** (1979) 3146.

17 E.A. Ponomarev and L.M. Peter, J. Electroanal. Chem., **396** (1995) 219.

18 L.M. Peter, Chem. Rev., **90** (1990) 753.

19 M.P. Dare-Edwards and A. Hamnett, J. Electroanal. Chem., **105** (1979) 283

20 H.O. Finklea, in H.O. Finklea (ed.), *Semiconductors Electrodes*, Elsevier, Amsterdan, p. 43.

21 W.W. Gärtner, Phys Rev., **116** (1959) 84.

22 L.M. Peter, E.A. Ponomarev and D.J. Fermin, J. Electroanal. Chem., submitted.

23 E.C. Dutoit, R.L. Van Meirhaeghe, F. Cardon an W.P. Gomes, Ber. Bunsengen. Phys. Chem., **79** (1975) 1206.

24 W. Siripala and M. Tomkiewicz, Phys. Rev. Lett., **50** (1983) 443.

25 K.H. Liao and D.H. Waldeck, J. Phys. Chem., **99** (1995) 4569.

26 Y. Nakato, H. Akanuma, J.-I. Shimizu and Y. Magari, J. Electroanal. Chem., **396** (1995) 35.

27 R.J. Madix, in D.A. King and D.P. Woodruff, *The Chemical Physics of Solids Surfaces and Heterogenous Catalysis*, Vol. 4, Elsevier Scientific Publishing Company, Amsterdan, 1982, ch. 1.

28 J. Augustynski, *Structure and Bonding, vol. 69*, Springer-Verlag, Berlin, p.1, and reference there in.

29 M. Schiavello (ed), *Photocatalysis and Enviroment, Trends and Applications*, NATO ASI, Dordrecht, 1988.

30 P. Herrasti and L.M. Peter, J. Electroanal. Chem., **305** (1991) 241

31 G. Schonmakers, *PhD thesis*, Utrecht, 1996

32 R. Peat and L.M. Peter, J. Electroanal. Chem. **147** (1986) 1931

33 L.M. Peter, A.M. Borazio, H.J. Lewerenz and J. Stumper, J. Electroanal. Chem., **290** (1990) 229

34 J.J. Kelly, B.P. Minks, N.A.M. Verhaegh, J. Stumper and L.M. Peter, Electrochim. Acta, **37** (1992) 909

35 F. Cardon and W.P. Gomes, J. Electroanal. Chem., **144** (1983) 135

36 F. Cardon and W.P. Gomes, Surf. Sci., **27** (1986) 201